A THEORETICAL AND NUMERICAL STUDY OF THE USE OF GRID EMBEDDED AXIAL MAGNETIC FIELDS TO REDUCE CHARGE EXCHANGE ION INDUCED GRID EROSION IN ELECTROSTATIC ION THRUSTERS

DISSERTATION

Presented in Partial Fulfillment of the Requirements for

the Degree Doctor of Philosophy in the Graduate

School of The Ohio State University

By

Ian R. Claypool, M.S.

****

The Ohio State University
2007

Dissertation Committee:

Professor Thomas M. York, Adviser

Professor Michael G. Dunn

Professor Igor V. Adamovich

Approved by

____

Adviser
Aeronautical and Astronautical
Engineering Graduate Program

ABSTRACT

Decay of ion thruster grids due to impact by charge exchange ions is the main life limiting factor in ion propulsion systems. Any system which can reduce the number or energy of ions impacting the grids will add to the life expectancy at current power levels. One possible technique for reducing damage from charge exchange ions would involve the incorporation in the grids of axial aligned embedded “micro-solenoid” magnetic fields. These fields, generated by currents running around the grid apertures would form mini magnetic nozzles guiding beam ions through the aperture while diverting charge exchange ions from directly impacting the grids. Evaluation of different grid geometries, grid fields, or the use of external or internal auxiliary fields as means to limit charge exchange induced grid erosion is difficult to accomplish either experimentally or computationally. For the sole purpose of quickly testing and evaluating different arrangements of grid geometry and fields a simpler computational model which only evaluates the motion of charge exchange ions would be useful in arriving at a reduced set of potential improved configurations that can then be evaluated by more sophisticated computational and eventually experimental means. A simple computational simulation of the environment within a single set of ion thruster grids has been created for use in evaluating the response of single charge exchange ions to many different grid geometries and field arrangements. This effort involved the development of the ionLite code which simulates the grid geometries, fields, and ion beam charge distribution while allowing individual charge exchange ions to be created at any point and their trajectories and eventual fates to be determined. Using this code the use of auxiliary magnetic fields was examined. This analysis shows that energy transfer to a simulated accelerator grid from charge exchange ions can be reduced by approximately 20%, but only at vary large magnitude magnetic field strengths (order of 100 T). It was found that for the configurations investigated the optimum performance resulted when the applied magnetic field was just enough to cause the particle Larmor radius to be approximately equal to the grid aperture radius. The use of lower mass propellants such as neon or helium allow for this benefit at fields on the order of 20 T. The potential impact of the embedded magnetic fields is shown to be very sensitive to grid geometry, and therefore it is probable that a different configuration could provide even greater reduction in kinetic energy transfer at moderate field levels.

Dedicated to my mother whose love of science set my course.

ACKNOWLEDGEMENTS

I would like to take this opportunity to thank the many people who have aided me in this effort. First and foremost I would like to thank Professor Thomas York who planted the seed of this idea and whose patient guidance has been my most important resource. I would also like to acknowledge the support and input I have received from the other members of my committee, Professor Michael Dunn and Professor Igor Adamovich.

I would like to thank Steve Zammit of Boeing Satellite Development Center for advice on C++ coding and for allowing me to use him as a springboard for many ideas which were eventually incorporated into the ionLite code.

I would like to gratefully acknowledge Dr. Carsten Scharlemann for helping me during my time at The Ohio State University and for his contribution to the brainstorming session which led to the concept behind this work.

Finally, I would like to thank Tracy Roquemore for her patience during two summers and more that I spent working on this effort, if not for her I probably never would have finished.

VITA

November 25, 1960………………………..	Born, Sacramento, California, USA
1984………………………………………..	B.S. Astronautical Engineering, United States Air Force Academy, Colorado Springs, Colorado, USA
1984-1990………………………………….	Commissioned Officer, United States Air Force
1991-1994………………………………….	Galileo Mission Planning Engineer, NASA, Jet Propulsion Laboratory, Pasadena, California, USA
1992………………………………………...	M.S. Mechanical Engineering California State University Northridge, Northridge, California, USA
1995………………………………………..	Assistant Science Coordinator, NASA, Jet Propulsion Laboratory, Pasadena, California, USA
1996-2000………………………………….	Staff Engineer, Hughes Electronics, El Segundo, California, USA
2000-present………………………………..	Senior Staff Engineer, Boeing, El Segundo, California, USA
2000-present………………………………..	Graduate Student, The Ohio State University, Columbus, Ohio, USA

PUBLICATIONS

1. Claypool, I.R., “Galileo Gaspra Encounter Notebook”, NASA-JPL Publication #1625-488, October 1991.

2. Claypool, I.R., “Detection of Organic Activity on Europa with Galileo” Graduate Project/Thesis, California State University Northridge, December 1993.

3. Martin, T.Z., Orton, G.S., Travis, L.D., Tamppari, L.K., Claypool, I.R., “Observations of Shoemaker-Levy Impacts by the Galileo Photopolarimeter Radiometer”, Science, June 1998, Volume 268, p 1875 – 1879.

FIELDS OF STUDY

Major Field:	Aeronautical and Astronautical Engineering
Specialization:	Advanced Propulsion, Electric Propulsion, Fluid Dynamics
Other Areas of Study/Research:	Simulation Development, Remote Sensing, Biogenesis and Achaean Biology, Spacecraft Operations and Mission Planning

TABLE OF CONTENTS

LIST OF TABLES

LIST OF FIGURES

CHAPTER 1

INTRODUCTION

Current gridded electrostatic ion propulsion systems suffer from gradual decay and failure of the ion optics due to sputter erosion of the grid material. New materials are being tested which provide some relief to this problem. [1,2,3] Additionally, thrusters with thicker accelerator grids have been examined as a means of increasing lifetime by increasing the amount of material in the grid most susceptible to erosion. [4] In this paper an active system is for reducing grid erosion still further is examined. This system involves the inclusion in the grid material of a "micro-solenoid" magnetic field generation system. This system creates solenoid magnetic fields within each grid aperture. The generated magnetic fields form a miniature magnetic nozzle reducing the velocity vector normal to the grid surface, while allowing the ions in the beamlets to pass largely unaffected. The proposed system is described in more detail later in this paper and an example of the initial high level analysis justifying this work is presented. This system is then evaluated in detail using a new simple computer model as a means of both demonstrating the usefulness of the code and as a theoretical study of the usefulness of the embedded magnetic field system for limiting thruster grid erosion.

Evaluating methods for reducing grid erosion and thereby increasing thruster life are generally costly and time consuming. Current computational methods for modeling electrostatic thrusters require considerable computer power and time to reach steady state and therefore limit what can be done with regard to modeling multiple configurations. A model which only examines charge exchange ions and the damage they impart to the thruster grids, and which is less computationally intensive than the more sophisticated codes currently in use would aid in the evaluation of techniques and technologies for limiting grid erosion and extending thruster life. Such a simplified electrostatic thruster model has been created and is described in this paper.

The simplified model is titled “ionLite” and can be rapidly run and reconfigured to test multiple configurations of grid geometry, grid potentials, and supplemental fields to compare kinetic energy transferred to the grids and the Isp of the configuration. This provides a pair of metrics for use in determining the suitability of any postulated system for mitigating grid erosion for further evaluation using the available more sophisticated codes and eventually through experimentation.

This code is used to examine the proposed system for inclusion in the grid material of "micro-solenoid" magnetic fields for reducing grid erosion. The program is used to compare several configurations of magnetic field and the resultant grid damage as determined from the total kinetic energy transferred to the grid material and the net Isp of the system.

1.1 Ion Thruster Grid Erosion Mechanism and Problems

In an electrostatic thruster the optics provide for the extraction of ions from the discharge chamber plasma and acceleration of these ions to exhaust velocities required for the desired thrust and Isp levels. The optics are made up of at least two grids, a screen grid held at a potential near that of the discharge chamber plasma, and an accel grid held at a potential much less than the discharge chamber plasma. In most operational systems a third, decel grid, is used which is held at approximately the spacecraft bus potential. Each grid is a very thin plate with the bulk of its surface area open in small individual round apertures. Each grid has the same number of apertures and the apertures for all grids are aligned to form a "Pierce-Gun" like ion acceleration system. [5]

The grids are typically made of molybdenum though as discussed earlier other materials are becoming available. The grids are frequently domed or dished to provide structural stability over a wide range of operating temperatures. Each grid is separated from the other grids by narrow gaps on the order of the grid aperture size. The screen grid is adjacent to the discharge chamber and in contact with the discharge plasma. The accel grid is separated from the screen grid and comes next in the sequence of grids proceeding from the discharge chamber to the thruster exit (the direction of the expelled thrust plume will be referred to as "aft" while anything in the direction of the discharge chamber will be referred to as "forward"). The last grid, in a three grid thruster is the decel grid.

The operation of the grid system is fairly straightforward. The positive potential of the screen keeps ions in the discharge plasma away from the grid surface (ideally) and contained within the discharge chamber. At regions near the apertures of the screen grid ions in the discharge chamber sense the lower potential of the accel grid and are accelerated toward it. The potential of the screen grid focuses the ions as they pass through the apertures in the screen, forming beamlets that then pass through the apertures in the accel grid and, if present, the decel grid. The decel grid serves to bring the overall potential of the exhaust plume back to near the spacecraft bus potential. It also helps minimize electron back-streaming. Of chief interest for this paper is that the higher potential of the decel grid helps to reduce the erosion of the accel grid by charge exchange ions. [6] A more thorough discussion of electrostatic thrusters is contained in Chapter 2.

Ion sputtering induced damage can occur throughout an ion thruster. Erosion of the accel grid is usually cited as the main life limiting factor for ion thruster; however, erosion of the screen grid and the decel grid occur and can also contribute to diminished thruster performance. [6, 7] There are two principal sources of ion impact sputter induced grid erosion. The primary source is the impact of charge exchange ions on the grid material. A lesser erosion mechanism is the direct impact of non-focused ions from the discharge plasma. In all ion thrusters some portion of the propellant remains un-ionized and can pass through the screen grid, even exiting the thruster eventually. In addition sputtered grid material can be in the exhaust plume. These sputtered neutral particles are available to undergo charge exchange collisions. [8] Most neutrals in the exhaust beam originate within the main thruster body. It was found on the DS-1 spacecraft, for example, that un-ionized gas leaving the neutralizer cathode was not a significant source of charge exchange ions. The NSTAR thruster on DS-1 was also observed to have a time variability to charge exchange ion flux (at the detector) which could not immediately be explained. [9]

When a neutral atom within or near the exit of the thruster grid system comes in contact with a fast moving propellant ion it can undergo charge exchange and become an ion. The now neutral propellant particle will continue on with its trajectory largely unaffected by the collision. The resultant charge exchange ion remains in the thruster grid system or just outside. It is, initially, slow moving and therefore susceptible to electrostatic acceleration toward the low potential of the accel grid. These charge exchange ions can eventually impact the accel grid or the decel grid with energies that are the difference between the potential at the point where they were created and the potential of the surface they eventually contact. [9]

Erosion of the accel grid by charge exchange ions is the fundamental life limiting factor in all ion thrusters. [5] Charge exchange results because some percentage of propellant atoms remains un-ionized and can diffuse into the grid system. Ions from the discharge chamber, accelerated to high velocities can interact with these neutrals. The fast moving ion removes an electron from the neutral and continues on its previous trajectory. The formerly neutral propellant atom is now a charge exchange ion with only a small velocity deep in the grid system potential. It will be drawn to the accel grid and can impact at high velocities. Figure 1.1 shows the basic configuration of a three grid system in the vicinity of one of the beamlets, where charge exchange can occur, and the possible trajectories of the resultant ions. Charge exchange which occurs outside the ion beam is insignificant and is not addressed in this investigation. [9]

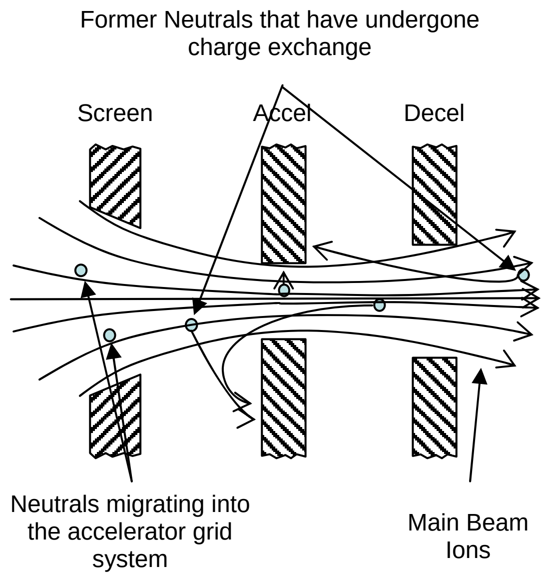

Figure 1.1: Locations where charge exchange ions are created and their likely trajectories. [10]

The secondary mechanism for ion impact grid erosion is the direct impact of ions from the discharge plasma or of unfocused discharge plasma ions passing through the grid system. Direct impact of discharge chamber plasma ions effects primarily the screen grid which is in direct contact with the plasma. Over time erosion of the grids due principally to charge exchange ions, can lead to the beamlets becoming less focused. This will then lead to an increase in direct impacts of high energy unfocused beam ions with the accelerator grid in particular. Kaufman noted that with their much higher energies these ions would result in significant impact damage to the accelerator. Kaufman also noted that direct impact of the accelerator grid would be more likely from the beginning of operation for a high perveance system. [10] The flux of these ions impacting the grids is part of the overall accel grid current. [11]

The impact of both charge exchange and discharge chamber plasma ions with the grids results in a number of damage mechanisms that limit thruster life and performance. These damage types are enlargement of the grid apertures by the impact of charge exchange ions, "pit and groove" erosion of the accel grid surface by charge exchange ions, erosion of the upstream surface of the screen grid by the direct impingement of discharge plasma ions, and enlargement of grid holes by the direct impact of discharge chamber plasma ions. [1]

The nature of charge exchange ions, their tendency to be created between the grids or near the thruster exit, leads to their impacting the accel grid preferentially. [7] As described earlier, these ions are most likely to be created where both the neutral and ion beam densities are highest, and that is within the grid holes, or in line with the axis of the hole. With low initial energies they are preferentially attracted to the regions of the hole edges, thus sputtering material from those locations. Many charge exchange ions actually impact on the inside of the accelerator grid holes causing erosion there. [5] Both impacts on the surface near the holes and within the holes result in the sputtering of grid material from those areas and enlargement of the apertures in the accel grid. In a three grid system some charge exchange ions created just aft of the decel grid may impact the edges of the decel grid apertures. This is because the ions are drawn to the low potential of the accel grid but are relatively unfocused and may not make it through the decel grid holes. Charge exchange ions impacting the edges of the decel grid aperture could result in enlargement of the apertures.

Not all charge exchange ions impact in or on the edge of the accel grid apertures. Many also strike the surface of the grid. Most surface damage to the accel grid occurs on the downstream side of the grid. [5] Surface erosion of the accel grid results in regular pattern of "pits" and "grooves" on the downstream surface. This wear pattern has been seen repeatedly in ion thruster system ground testing. [7]

Erosion of the surface and apertures of the screen grid is caused mainly by direct impingement of the discharge chamber plasma. [7] Although the screen grid is held at a potential only slightly lower than the discharge chamber the density of the plasma and its overall energy spread inevitably result in high energy ions contacting the grid surface. While the number of discharge plasma ions contacting the screen grid may be small compared to the number of charge exchange ions contacting the accel grid, their higher energies result in significant erosion. The resultant grid erosion is concentrated on the upstream surface of the screen. [11] Screen grid erosion can be relatively accurately predicted as it is a function of ion energy and current. [7]

The erosion of grid material as described in the previous paragraphs leads to a number of performance loss and failure mechanisms. Additionally, the sputtered material can become a source of contamination for other spacecraft systems. Enlargement of the accel grid holes in particular leads to a gradual loss of performance throughout thruster life due to the consequent reduction in beam current. [10] Another consequence of the enlargement of accel grid apertures is the increased tendency for electrons from the neutralizer to "back-stream" into the thruster. This additional current must be handled by the power supply, but a point can be reached where the power supply can no longer compensate and thruster operation is no longer possible. [7] Finally, the erosion of the grid material can lead to structural failure. This failure is typically manifested in the accel grid first since it bears the brunt of the charge exchange impacts. [7]

1.2 Description of the Micro-Solenoid B Field Concept

As described above, the decay of ion thruster grids due to impingement by propellant ions is the main life limiting factor in ion propulsion systems. Any system which can reduce significantly the kinetic energy of ions impacting the grids will add to the life expectancy at current power levels. More importantly however, with reduced susceptibility of the grids to ion strikes, higher grid voltages can be used thereby achieving higher thrust and Isp levels. While new materials will reduce the sputter yield, the ultimate solution would be to implement an active system which prevents both charge exchange ions and direct impingement ions from striking the grids. Such an active system is what is examined here.

The creation of magnetic fields aligned principally with the ion flow through the holes would act in much the same way as a magnetic nozzle system such as those used experimentally on Magneto-Plasmadynamic Thrusters. [14] In the MPD application the magnetic nozzle serves the purpose of directing and optimizing the plasma flow. [14] The intent of the micro-solenoid fields is to protect the thruster material from damage caused by the plasma, in this case the charge exchange ions. This is more like experimental work done at The Ohio State University on use of magnetic nozzles to protect thruster components from damage due to the extremely dense high energy exhaust plume from a fusion propulsion system. [15] In the ion thruster grid use, the micro-solenoid fields will act to guide ions through the apertures and thereby reduce ion impact induced grid erosion. This system should be effective against all of the ion strike grid erosion types. The magnetic fields can be created by a current running around each individual grid hole. The current runs through a loop of grid material separated from the main grid material by a thin layer of solid insulation. The insulation need be neither thick or of particularly high insolating character since the voltage difference between the current carrier loop and the remaining grid material is very small (order of 1 Volt). Each grid (Screen, Accel, and Decel if used) will have similar current carrying loops. The loop around each hole will be connected to the loop around the next hole in the same row of holes, through to the end of the row. The next row of holes will then carry current back the other way. The regions carrying current between holes will run right next to that carrying current to the next row of holes, thus reducing the stray magnetic field between holes. The fields for each grid can be oriented such that a nearly continuous solenoid type field permeates each sequence of holes an individual ion would pass through or they may be alternated between grids.

Consider an individual grid aperture as depicted in Figure 1.2. The orientation of the electric field is such that ions are attracted to the grid. If magnetic filed lines are added as depicted, particles will experience an additional force which, due to the orientation of the field lines, will be principally parallel to the grid surface whether within the aperture or along the grid plane. (The reasons for this are described in more detail in the next section.) The desired trajectory for ions is along the axis, and those particles with trajectories principally along the **z** axis will be almost completely unaffected by the

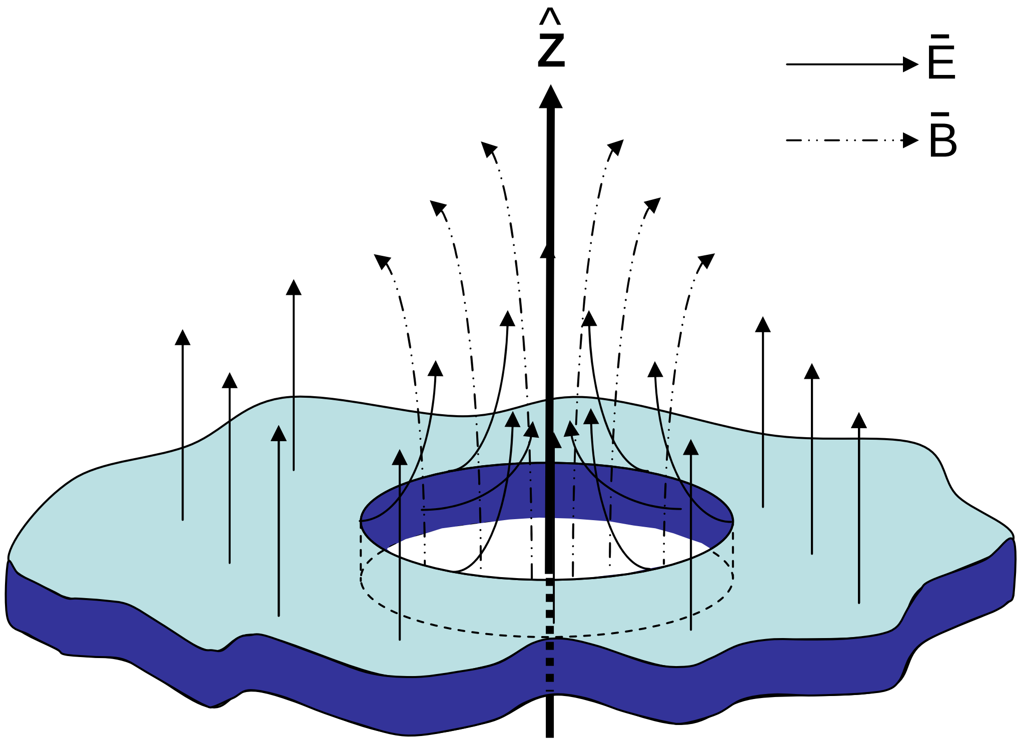

Figure 1.2: Example Grid Aperture Showing Orientation of Electric and Proposed Magnetic Field.

addition of the magnetic field. This can be seen by a simple examination of the force acting on a moving charged particle:

$$\mathbf{F} = q(\mathbf{E} + \mathbf{u} \times \mathbf{B}) \tag{1.1}$$

where bold font identifies vector quantities. Clearly, the change in force experienced by the particles traveling within the system due to the addition of a magnetic field is:

$$\Delta\mathbf{F} = q(\mathbf{u} \times \mathbf{B}) \tag{1.2}$$

If **u** and **B** are both along the **z** axis this quantity will be zero. Therefore most particles in the beamlet will experience no new force with the addition of the magnetic field.

Particles traveling along trajectories that cross magnetic field lines will however experience an additional force that, in a cylindrical coordinate system, would be primarily in the **R** or **θ** direction. Judicious selection of the field orientation can lead to a reduced acceleration toward the grids.

Away from the immediate vicinity of the aperture the field lines will obviously be more along the radial direction than the **z** direction. In this case a particle with a trajectory crossing the field lines initially traveling primarily along **z** will experience a force principally in the **θ** direction. This imparts a velocity component that lends to a negative Z acceleration slowing the particle's impact velocity. The new magnetic field therefore protects the grid material from erosion at the apertures and along the surface.

These "micro-solenoid" fields can be created by incorporating in the grids themselves a series of "loops". There is one loop around each grid aperture. The current is provided to each loop from the preceding loop by additional grid material acting as a "wire". The loops and wires are separated from the remaining grid material by a thin layer of high temperature low sputter yield material such as boron-nitride. The voltage difference between the loops and wires and the remaining grid material is small, on the order of a single volt, so only minimal insulation is required. Figure 1.3 gives a general schematic of how the system may be implemented. The voltages quoted in the figure are for general reference, each row pair of apertures would require a slightly different voltage (as each has a different number of holes) in order to maintain approximately equal fields for each grid hole. The figure of +/- 1 Volt for the difference across the system is intended to indicate that the voltage difference between the loop and wire system and the remaining grid material is small.

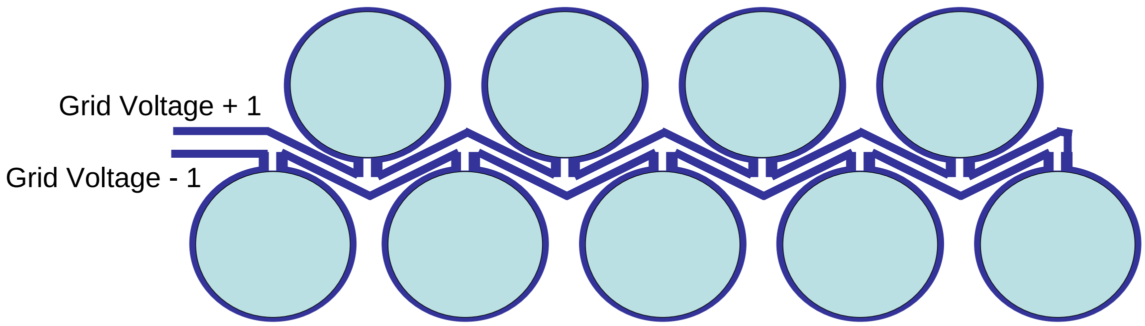

Figure 1.3: General layout of solenoid field forming loops and wires

The actual voltage across the system will probably be less than this. The figure also exaggerates the distance between the wires. The wires are intentionally placed very close to each other to minimize the stray magnetic field generated by the current passing through them.

The field strength generated by such a system can be calculated simply. As an example, a 13 cm diameter grid with holes of 1.3 mm diameter (this approximates current Boeing flight thrusters) with a loop current of 1 A will see a magnetic field strength at the center of the aperture of approximately 10 Gauss. For this type of thruster, magnetic field strength within the discharge chamber itself is on the order of 25 to 100 Gauss. [14] The field strength that particles passing through the grids will see is therefore not insignificant. In the analysis, image currents in the grid material are neglected. These will obviously work to reduce the overall magnetic field strength, however there are several techniques that can be used to minimize their impact. For the purpose of this work it can be assumed that the effects of image currents have been accounted for in the current used to produce the stated field strength.

In the described configuration, all magnetic field lines have **Z** or **R** components, but never a **θ** component. Particles moving along the magnetic field lines (the desired situation within grid apertures) will experience little if any force due to the inclusion of the magnetic field. Particles moving in trajectories that cross the field lines will feel a force turning them in the **θ** direction and changing their **R** component.

Consider charge exchange ions created in the exhaust plume aft of the decel grid. They may sense the accel grid potential and be drawn to it. In many cases these ions will come up against the magnetic field running primarily along **R** on the aft surface of the decel grid. This will cause their trajectory to turn them away from the grid apertures and into a region where the higher potential of the decel grid predominates. Now, consider a charge exchange ion created within the grid system, or which enters from the exhaust plume. It will be closer to the accel apertures and will therefore be in a region where the magnetic field is primarily along **Z**. As it accelerates toward the accel grid it will be turned in the direction parallel to the interior wall of the aperture. Finally, the magnetic field on the screen grid will help to funnel discharge plasma ions through the screen grid apertures, while deflecting them away from the screen grid surface.

1.2.1 Basic Analysis of a Few Typical Situations

Starting with the simplest case of particle trajectory along the **z** axis inside the grid aperture as depicted in Figure 1.4. (Note that in Figures 1.4 through 1.7 the dotted curves represent the magnetic field lines, the solid lines represent the approximate electric field lines, and the heavy solid line represents the initial particle trajectory.) Here the desire is

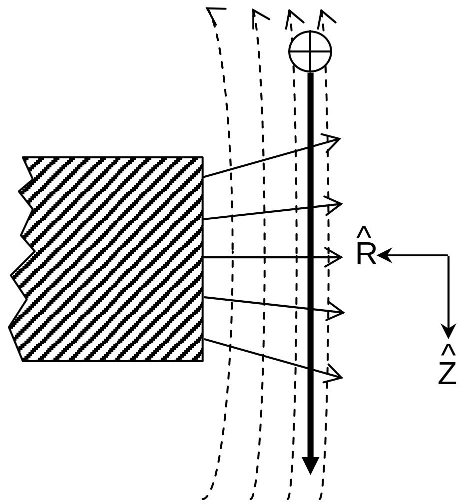

Figure 1.4: Particle Trajectory Along B Field Lines Inside Grid Aperture

that the additional magnetic field has little or no impact on the nominal particle trajectory. The total force experienced by a charged particle in an electric and magnetic field is defined as the Lorentz Force given by the Lorentz Force Equation [15]:

$$\mathbf{F} = q(\mathbf{E} + \mathbf{u} \times \mathbf{B}) \tag{1.3}$$

So the additional force due to the presence of the magnetic field is:

$$\Delta\mathbf{F} = q(\mathbf{u} \times \mathbf{B}) \tag{1.4}$$

The configuration being examined lends itself to the use of cylindrical coordinates. In cylindrical coordinates the cross product of two vectors ($\mathbf{u} \times \mathbf{B}$) where $\mathbf{u}$ is:

$$\mathbf{u} = u_R\hat{\mathbf{R}} + u_\theta\hat{\boldsymbol{\theta}} + u_z\hat{\mathbf{z}} \tag{1.5}$$

and $\mathbf{B}$ is:

$$\mathbf{B} = B_R\hat{\mathbf{R}} + B_\theta\hat{\boldsymbol{\theta}} + B_z\hat{\mathbf{z}} \tag{1.6}$$

is:

$$\mathbf{u}\times\mathbf{B} = \frac{1}{R}\left(u_\theta B_z - Ru_z B_\theta\right)\hat{\mathbf{R}} + \left(u_z B_R - u_R B_z\right)\hat{\boldsymbol{\theta}} + \frac{1}{R}\left(Ru_R B_\theta - u_\theta B_R\right)\hat{\mathbf{z}} \tag{1.7}$$

For the situation indicated in Figure 1.4 it is assumed that the B field in is entirely along the **z** axis:

$$\mathbf{B} = B\hat{\mathbf{z}} \tag{1.8}$$

and since the trajectory is principally along the **z** axis:

$$\mathbf{u} = u\hat{\mathbf{z}} \tag{1.9}$$

These two assumptions allow for the simplification of the general result to zero. This can also be arrived at by observation since for the two reduced vectors the additional force felt due to the magnetic field is:

$$\Delta\mathbf{F} = q\left(u\hat{\mathbf{z}}\times B\hat{\mathbf{z}}\right) \tag{1.10}$$

which is zero by definition. Therefore $\Delta\mathbf{F} = 0$ for particles traveling along the field lines. We can conclude from this also that for most ions in the main ion beam the net new force is approximately zero.

Now consider the case of a particle in the grid aperture traveling toward the side of the aperture as depicted in Figure 1.5. In this case once again assume that **B** is entirely along the Z axis:

$$\mathbf{B} = B\hat{\mathbf{z}} \tag{1.11}$$

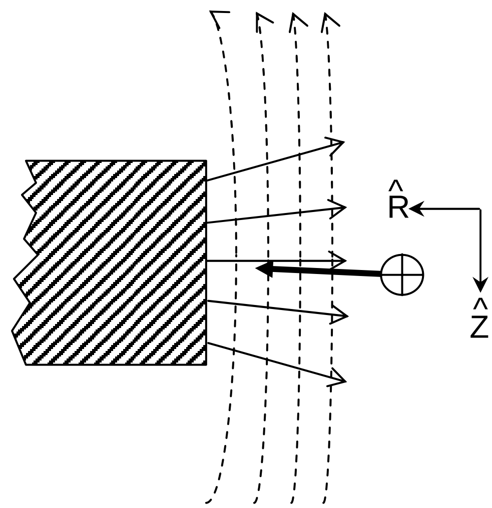

Figure 1.5: Particle Trajectory Across B Field Lines Inside Grid Aperture

To begin with examine an arbitrary trajectory represented by:

$$\mathbf{u} = u_R\hat{\mathbf{R}} + u_\theta\hat{\boldsymbol{\theta}} + u_z\hat{\mathbf{z}} \tag{1.12}$$

Taking the cross product of **u** and **B** gives Δ**F** as:

$$\Delta\mathbf{F} = q\left(-\frac{u_\theta B_z}{R}\right)\hat{\mathbf{R}} + qu_R B_z\hat{\boldsymbol{\theta}} \tag{1.13}$$

This means that the additional force experienced by a particle traveling across magnetic field lines within a grid aperture adds an acceleration in the **θ** direction and an acceleration component in the **R** direction which opposes the acceleration due to the E field.

Next consider regions of the grid surface where the magnetic field lines are more or less parallel to the surface as depicted in Figure 1.6.

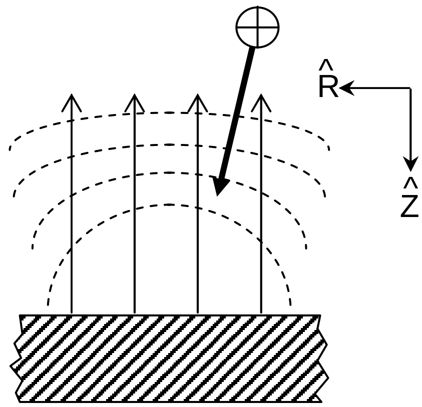

Figure 1.6: Particle Trajectory Across B Field Lines Along Grid Surface

This case represents both charge exchange ions which might otherwise cause pit and groove erosion of the grid surface and the upstream surface of the screen grid in contact with the discharge plasma. In this case assume that the magnetic field lines are entirely in the **R** plane such that:

$$\mathbf{B} = B_R \hat{\mathbf{R}} \tag{1.14}$$

Leaving the trajectory of the particle unrestricted for now:

$$\mathbf{u} = u_R \hat{\mathbf{R}} + u_\theta \hat{\boldsymbol{\theta}} + u_z \hat{\mathbf{z}} \tag{1.15}$$

Taking the cross product of these to solve for $\Delta\mathbf{F}$ gives:

$$\Delta\mathbf{F} = q\left(u_z B_R \hat{\boldsymbol{\theta}} - u_\theta B_R \hat{\mathbf{z}}\right) \tag{1.16}$$

Once again the additional force is only in the **θ** direction which is parallel to the surface of the grid and in the negative **Z** direction adding an acceleration counter to that imposed by the electric field.

Finally consider a particle traveling on any trajectory which would cause it to impact the grid in the vicinity of an aperture such that it crosses the magnetic field lines were they have both **z** and **R** components as depicted in Figure 1.7. In this case the magnetic field can be described as:

$$\mathbf{B} = B_R\hat{\mathbf{R}} + B_\theta\hat{\boldsymbol{\theta}} + B_z\hat{\mathbf{z}} \tag{1.17}$$

and once again the trajectory is:

$$\mathbf{u} = u_R\hat{\mathbf{R}} + u_\theta\hat{\boldsymbol{\theta}} + u_z\hat{\mathbf{z}} \tag{1.18}$$

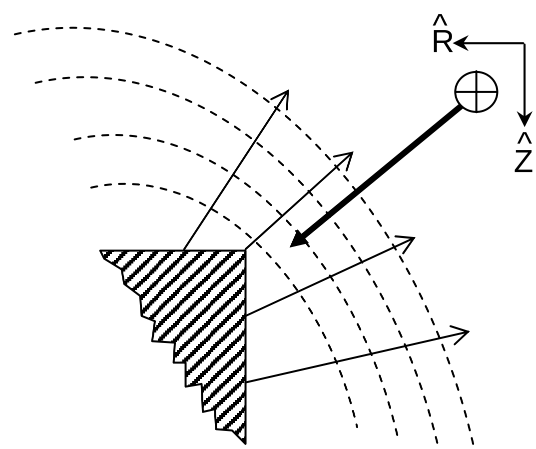

Figure 1.7: Particle Trajectory Across B Field Lines Near Grid Aperture

The cross product of these two arbitrary vectors gives the general case for the additional force of:

$$\Delta\mathbf{F} = \frac{q}{R}\left(u_\theta B_z - Ru_z B_\theta\right)\hat{\mathbf{R}} + q\left(u_z B_R - u_R B_z\right)\hat{\boldsymbol{\theta}} + \frac{q}{R}\left(Ru_R B_\theta - u_\theta B_R\right)\hat{\mathbf{z}} \tag{1.19}$$

The B field will still have no **θ** component and as such will reduce to:

$$\mathbf{B} = B_R \hat{\mathbf{R}} + B_z \hat{\mathbf{z}} \tag{1.20}$$

which gives a final additional force of:

$$\Delta\mathbf{F} = \frac{q}{R}\left(u_\theta B_z\right)\hat{\mathbf{R}} + q\left(u_z B_R - u_R B_z\right)\hat{\boldsymbol{\theta}} + \frac{q}{R}\left(-u_\theta B_R\right)\hat{\mathbf{z}} \tag{1.21}$$

If B_z is made to be counter to **Z** (i.e., B_z = -B**z**) then there is an additional acceleration along **Z** and an acceleration counter to that caused by the E field in **R**. This would tend to push the particle away from and through the grid.

1.2.2 Areas of Further Study

Before any hardware development of this system can be justified a number of important areas require further, more detailed investigation. The mathematical analysis presented indicating the new forces imparted to particles in the vicinity of the grids just scratches the surface. It also does not actually delve into the nature of the individual particle motion within the system. Further analytic investigation of the particle motion provides an indication of just how much the trajectories are affected and whether there will be a significant enough change in motion to reduce grid erosion. Ultimately, a detailed computational analysis of effects on not just grid erosion rates but also on ion extraction, electron back-streaming and beam divergence should be performed. In the interim however, the ionLite code described in Chapter 3 offers an opportunity to model the impact of various field configurations and determine the viability of the concept.

There is the potential for there to be an impact on ion extraction from the discharge plasma due to the addition of the screen grid magnetic field. The implications of the additional fields on ion extraction are not addressed in this work.

Another factor affecting thruster performance and life is electron back-streaming. It may be possible that the field will help limit back-streaming in the same way it helps to reduce grid erosion, by altering the electron trajectories. This question can not be addressed with the ionLite code since relativistic effects that come into play with electron motion are not accounted for by the current version of the program.

Finally there is the question of how the "ingestion" of charge exchange ions into the discharge chamber, if any were to occur, impacts cathode life and performance. Ion sputtering of cathode components is another life limiting factor in ion propulsion. [16] In current designs the damage to the cathode from ion impacts can be limited and cathodes tend to outlive the accel grid. Analysis will be required however to determine if the additional charge exchange ions entering the discharge chamber change this and lead to a shortening of cathode life. This is beyond the scope of the current analysis.

CHAPTER 2

FUNDAMENTAL PHYSICS OF ELECTROSTATIC THRUSTERS

Ion propulsion systems are complex amalgamations of many subsystems including power supplies, propellant storage, propellant regulators, valves, switches, and of course the ion thruster itself. Likewise, the thruster is also a complex assembly incorporating a cathode for generating electrons, a discharge chamber for ionizing propellant, an accelerator system for accelerating the ions, and a neutralizer for maintaining spacecraft potential. In spite of all the complexity of the complete system and the thruster however, the actual structure and mechanism behind the production of thrust, i.e., the acceleration of ions, is relatively simple. As described briefly in the introduction, parallel charged plates with aligned apertures cause the acceleration and ejection of the ionized propellant. The physics behind this process is also relatively simple. In fact the mechanism of electrostatic acceleration of ionized gas was proposed as a means of achieving spaceflight almost as long ago as the similar use of chemical rockets was first being investigated. [17] The basis of the science behind the production of thrust in an ion thruster is based on the fundamental laws of electrostatics and magnetostatics. It is not for the most part even necessary to delve too far into electrodynamics, magnetodynamics, or electromagnetic waves. These impart only secondary effects. In order to fully understand the use of grid embedded magnetic fields for minimizing charge exchange induced grid erosion, it is however necessary to understand the basic physics of both the electrostatic acceleration and the impact of applied magnetic fields.

This chapter is intended to provide a background in the physics and operation of gridded electrostatic thrusters. It consists of two sections. The first addresses the basic physics while the second goes into detail on the architecture and operation of the electron bombardment ion thruster. This is the type of thruster used by NASA for the Deep Space 1 mission and by Boeing for commercial satellite orbit raising and station-keeping. This material is provided to refresh the reader’s knowledge of the subject and as a reference for evaluating the remainder of this work.

2.1 Physics of Charged Particle Motion

This Section provides a high level discussion of the physics and mathematics involved in the electrostatic acceleration of charged particles as seen in ion thrusters and the influence of magnetic fields on those particles. It is intended as a ready summary of the material and will be referred to frequently in the remainder of this work. It is assumed that the reader has an in-depth knowledge of this material, but is presented here as a partial description of the logical path which leads to this investigation of the use of magnetic fields to reduce grid erosion in electrostatic propulsion systems.

Three types of particles play a role in the operation of ion propulsion systems. These three particle types are: neutral atoms, atoms which are missing one or more of their electrons and are thus positively charged ions, and electrons which are negatively charged. The behavior, and most importantly the motion, of neutral atoms is governed by a subset of fluid dynamics known as free molecular flow. A discussion of free molecular flow is beyond the scope of this effort and is not required as the contribution of neutral atoms to the problem of grid erosion only begins when they become ionized. The discussion of the physics of the thruster will therefore be limited to the behavior of the charged particles. At this point it is not necessary to differentiate between the positively charged ions and the negatively charged electrons.

Particles move under the influence of forces that are applied to them as defined by Newton's 2nd Law. [18] The predominant forces operating on charged particles in an ion thruster are electric or magnetic. The basis for this assertion will be discussed in Chapter 3. The source of the electric force is the electric field generated by all charges. [15] The force which occurs between charges is defined by Coulomb's Law. [18] Coulomb's Law can be expressed in several ways, for the purposes of this discussion the two important mathematical descriptions are: [19]

$$F = \kappa \frac{|q_1||q_2|}{r^2} \tag{2.1}$$

where κ is Coulomb's constant and q_1 and q_2 are the charges of particle 1 and particle 2 respectively, and: [15]

$$F = \frac{q_1 q_2}{4\pi\varepsilon_0 r^2} \tag{2.2}$$

In both cases r is the separation distance between the two charges. In the case of equation 2.1, F is the magnitude of the force acting on either particle 1 or 2, no direction is implied. In equation 2.2, F is a magnitude, however directionality can be discerned by the sign of the result which only comes from the nature of the charges themselves. If F is positive the direction will be such as to try to separate the two particles. If F is negative the force will be such as to attempt to move the two particles closer together. Coulombs Law gives rise to the concept of Electric Field. This can be seen from the fact that there is no inherent directionality to the force between charges, except the line connecting them. A charged particle will experience the same magnitude of force at any point of equal separation from a second charged particle. It is therefore possible to define a field emanating from particle 1 which extends radially in all directions. The magnitude of this field is such that the resultant force can be found by multiplying it by the charge of any particle placed within it. [15]

$$E = F/q = \frac{\kappa Qq}{qr^2} = \frac{\kappa Q}{r^2} \tag{2.3}$$

In this equation E is the magnitude of the Electric Field, Q is the charge of the source particle or assembly of particles. [19] The direction of the electric field is defined such that if the source particle is positively charged all of the field lines extend radially outward from it. If the source particle has a negative charge the field lines can be viewed as originating at infinity and converging uniformly toward, and terminating on the particle. [19]

From equation 2.3 it is clear that if a charged particle is placed in an electric field it is accelerated by a force that is the product of to the electric field and the charge of the particle. [18] The direction of the resultant force is determined by the direction of the electric field at the location of the particle. This can be expressed as: [18]

$$\mathbf{F} = q\mathbf{E} \tag{2.4}$$

where $\mathbf{E}$ and $\mathbf{F}$ are now vectors representing not just the magnitude of the field and force, but also its orientation.

As stated earlier, the motion of a particle in an electric field is controlled by Newton's 2^{nd} Law. [18] When the particles in question are moving at significantly less than the speed of light the non-relativistic acceleration can be found from: [18]

$$m\mathbf{a} = m\frac{d\mathbf{v}}{dt} \tag{2.5}$$

which for a charged particle is

$$m\mathbf{a} = q\mathbf{E} \tag{2.6}$$

however, the total energy of a charged particle is the sum of both its kinetic and potential energies. The potential energy of a particle in an electric field is the product of the charge of the particle and the difference in electric potential between the particles location and some defined ground state. Because electric potential must always be defined relative to some other electric potential it is usually best to consider it in terms of a change of potential seen by the particle as it moves from one point to another. If V_c is used to define the difference in potential between two points (as contrasted by the use of V to indicate the potential at a specific point relative to ground) then an initially at rest particle will have an energy of:

$$W = qV = \tfrac{1}{2}mv^2 \tag{2.7}$$

which indicates that the total change in the magnitude of velocity is determined by the difference in potential between the starting and ending points of the particles trajectory.

[18] A more convenient form for this equation provides the final velocity of an initially resting particle that passes through a potential difference V_c: [18]

$$v = \left[\frac{2qV_c}{m}\right]^{1/2} \tag{2.8}$$

The motion of a charged particle in the presence of a magnetic field (absent any electric field other than that produced by the particles charge) is determined from the Lorentz Force Law. [15] This Law describes the force on a single charged particle moving in a magnetic field and is given by: [18]

$$\mathbf{F} = q(\mathbf{v} \times \mathbf{B}) \tag{2.9}$$

This is a vector equation which shows that the components of the force are proportional to the components of the cross product of the particles velocity vector at any point and the magnetic field vector at that point. From this equation it is immediately obvious that if a charged particle with zero velocity is subjected to a steady magnetic field nothing happens. [18] Additionally, if the particle trajectory is in the same direction as **B** it experiences no acceleration due to the magnetic field. [15] Conversely, the maximum magnitude of force will be achieved for a charged particle with a velocity that is perpendicular to the local magnetic field lines. In the case of a charged particle with a velocity component perpendicular to the magnetic field the force due to equation 2.9 will result in acceleration at a right angle to the velocity vector and the magnetic field. [18]

The “archetypical” motion of a charged particle in a magnetic field is circular, the magnetic field providing the centripetal acceleration. [15] Expressing equation [2.9] in terms of the resulting acceleration gives: [18]

$$m\mathbf{a} = q(\mathbf{v} \times \mathbf{B}) \tag{2.10}$$

A particle in a uniform magnetic field with no **E** field and an initial velocity **v** exhibits a simple "cyclotron gyration" the equation of motion for which is: [20]

$$m\frac{d\mathbf{v}}{\mathbf{dt}} = q\mathbf{v} \times \mathbf{B} \tag{2.11}$$

The magnitude of the force experienced by a charged particle moving at right angles to a magnetic field, and the resulting acceleration is:

$$F = ma = qvB \tag{2.12}$$

This force imparted is balanced by the centrifugal force

$$F = {mv^2}/{r_L} \tag{2.13}$$

where r_L is the radius of the resulting path. Equating [2.12] and [2.13] gives an equation for the radius of the resulting motion: [18]

$$r_L = {mv}/{qB} \tag{2.14}$$

This motion has a natural frequency known as the "cyclotron frequency" which is defined by: [20]

$$\omega_c = \frac{|q|B}{m} \tag{2.15}$$

The radius of motion of a particle in a uniform magnetic field is known as the Larmor Radius. The more commonly used equation for defining it is: [20]

$$r_L = \frac{v_\perp}{\omega_c} = \frac{mv_\perp}{|q|B} \tag{2.16}$$

From equation [2.16] it is clear that the larger the velocity of the particle or the larger its mass the larger its radius of motion. Conversely, the greater the charge or the magnetic flux density the smaller the radius. [18]

If the particle has an initial velocity component parallel to **B** as well as a component perpendicular to **B** the path of the particle is helical with the axis parallel to **B**. [18] This is because the component of velocity parallel to **B** is unchanged resulting in a path which is the combination of the circular motion of the particle and the linear motion of the center of the circle. This center of motion of a charged particle moving under the influence of a magnetic field is known as the "Guiding Center". [20] In many circumstances it is the motion of the guiding center of the particle which is of interest. The nature of the guiding center gives rise to the "Guiding Center Drift" concept. [20] The importance of this will be discussed later.

If there are both an electric and a magnetic field present the total force on the particle is the total Lorentz Force given by: [18]

$$\mathbf{F} = q\left[\mathbf{E} + \left(\mathbf{v} \times \mathbf{B}\right)\right] \tag{2.17}$$

The motion of a charged particle is therefore a combination of the motion due to the electric field which acts directly on the particle and the motion due to the magnetic field which acts indirectly on the particle through the particle's velocity vector. When summed together the key factor is that the particles acceleration at any point is a factor of its own velocity. The Electric field acts to change the magnitude and direction of the velocity vector. The Magnetic field acts to change just the direction of the velocity vector. This combination of interacting components of motion results in some interesting behavior. For example, if a particle is placed in a region where the magnetic field is at a right angle to the electric field the particle travels along a path known as a "cycloid" with the net velocity vector orthogonal to both **E** and **B**. [15] This cycloid motion is very important in the use of grid embedded magnetic fields to limit charge exchange induced grid erosion.

For a particle in a crossed **E** and **B** field the equations of motion take the form:

$$\ddot{y} = \omega_c \dot{z} \tag{2.18}$$

and

$$\ddot{z} = \omega_c \left(E/B - \dot{y} \right) \tag{2.19}$$

where ω_c is the cyclotron frequency. These equations assume **E** = E_z and **B** = B_x. [15] If the particle starts at rest these differential equations of motion have closed form solutions of: [15]

$$y(t) = E/\omega_c B \left(\omega_c t - \sin \omega_c t \right) \tag{2.20}$$

and

$$z(t) = E/\omega_c B \left(1 - \cos \omega_c t \right) \tag{2.21}$$

Cycloid motion due to the presence of a component of **E** orthogonal to **B** is one type of the behavior known as guiding center drift mentioned earlier. In this case however the velocity magnitude is not constant and the Larmor radius for the particle changes throughout its journey. Generally, guiding center drift results whenever there is an additional force acting on the charged particle (other than the magnetic field). Guiding center drift also occurs whenever the magnetic field is not constant. [20]

2.2 Operation of Electrostatic Ion Thrusters

This section describes how the fundamental physics of charged particle motion are employed in an electrostatic ion propulsion system. As with the previous section it is intended to be a summary for those already knowledgeable in the field and as a reference for the discussion in the remainder of this work. The type of device described represents the class of ion propulsion system currently used for station keeping and orbit raising on commercial and experimental satellites and for primary propulsion on several interplanetary scientific spacecraft. While the general description being provided here concentrates on the Kaufmann type thruster used by Hughes/Boeing, the basic components and behavior, particularly of the acceleration system, is common to other types of electrostatic ion thrusters. While sometimes referred to as ion thrusters, Hall Effect propulsion systems are not discussed here as they have no grids.

2.2.1 Background

The idea of using electric fields to accelerate an ionized gas as a from of propulsion has been under discussion for nearly a century. Rocket pioneer Robert Goddard referenced it as far back as the 1920's. [17] There are several forms that ion propulsion systems can take. These different forms basically break down according to the type of ion source used. There are three basic types of ions sources that have been used over the years; surface ionization (contact engine), high pressure arcs (plasmatrons), and low pressure arcs (bombardment engines). [21] A fourth type exists known as the Radio Frequency Ion Thrusters or RITs. In Radio Frequency Ion Thrusters the propellant is ionized by electromagnetic fields. An RF coil surrounding the ionization chamber induces an axial magnetic field. The primary magnetic field induces a secondary circular electric field in which free electrons gain energy for impact ionization. [22] In both bombardment thrusters and RITs, after any impact ionization a xenon ion and at least one more free electron is generated. [22] In this way an RIT may also be considered a cathodeless bombardment thruster. Once the ionization process is triggered a self-sustaining plasma discharge is formed. [22] In order to limit the scope of the following sections only the electron bombardment type thruster will be discussed. In a standard bombardment thruster ionization is produced in a magnetically constrained arc operating at a low gas pressure, typically on the order of 10 torr. [21]

Electron bombardment thrusters have a long history for space applications, though only in the last ten years (since 1996) have they been used for primary propulsion or stationkeeping on satellites not dedicated to the testing or evaluation of the thrusters themselves. The first electron bombardment thruster was operated in the laboratory in 1960. [10] The first time an electron bombardment ion thruster was actually operated in space came four years later in July 1964 on the SERT 1 spacecraft. [17] In fact the first ion thruster to operate in space was a mercury electron bombardment thruster. [17]

Early ion thrusters used mercury or cesium as propellants. [10] Both mercury and cesium fed ion thrusters were developed to flight status. [23] Since the late 1980s however, ion propulsion development has concentrated on xenon propellant. [23] Xenon's ease of handling has made it the propellant of choice for all current commercially available ion propulsion systems.

One of the principle benefits of using electron bombardment ion thrusters for space propulsion is that they generate low but reasonable thrust (order of tenths of

Newtons) at very high I_{sp}. Currently used commercial ion thrusters operate between 2500 and 4000 seconds I_{sp} but research has shown that I_{sp} values of greater than 100,000 sec are attainable using gridded ion thrusters. [24] Preliminary work by Fearn has shown that a combination of reduced atomic mass propellant, an improved ion extraction grid system, and a much increased extraction potential could lead to I_{sp} values of 150,000 sec. [24]

2.2.2 Overview

At its most fundamental level an ion thruster is a device which converts electric power into kinetic energy of an essentially collisionless neutral beam of propellant ions and electrons. [17] An ion propulsion system is made up of three principle subsystems. [5] A propellant storage and handling subsystem provides a steady flow of clean propellant gas at low pressure. A power subsystem supplies conditioned power to all subsystems involved in the propulsion system. Finally, the thruster subsystem including the neutralizer, converts the electric power from the power subsystem and the gas from the propellant handling subsystem into thrust for the spacecraft. [5]

The electrostatic nature of ion thrusters separates them from other electric propulsion systems. Electrostatic thrusters are characterized by separate acceleration of positive and negative charged particles. [5] All other electric propulsion systems use a single mechanism to accelerate positive and negative charges together. [17]

At its most basic level an electron bombardment ion thruster incorporates three basic components. Each electron bombardment thruster system includes an ion source, ion accelerator, and a neutralizer. [5] In the thruster these three basic elements are divided into the three principle structural components of the thruster. The ion source has the conceptually simple task of providing a source of ions and is composed of the bulk of the structure of the thruster usually called the discharge or ion chamber. The accelerator system consists of an accelerator electrode which provides the electric field for accelerating the ions. The final and physically smallest component is the neutralizer. It is responsible for neutralizing the exhaust beam by injecting free electrons in numbers that exactly equal the number of ions accelerated by the accelerator system. [21]

The combined purpose and function of the thruster is to provide a source of high efficiency thrust for the spacecraft for use in orbit raising, station-keeping, or primary propulsion. The design of the thruster itself is dependant on the intended operating conditions and limitations, starting with the required thrust to be provided by the system. The thrust produced by an ion thruster is given by the equation:

$$T = \frac{d}{dt}\left(m_p v_p\right) = \dot{m}_p + v_p = \dot{m}_p + I_{SP}{}' g \tag{2.22}$$

where $\dot{m}_p$ is the expelled mass of propellant flow rate, v_p is the propellant ion exhaust velocity, $I_{sp}{}'$ is the effective specific impulse. g is the force of gravity at the surface of the Earth. [5]

The thrust requirement determines the propellant handling requirement, specifically the propellant flow rate. The propellant flow rate necessary to produce the desired thrust is given by:

$$\dot{m}_p = \frac{T}{I_{SP}{}' g} \tag{2.23}$$

in mass/sec. This can be further reduced down to

$$\dot{m}_p = 1.04 \times 10^{-5} M I_i \quad gms / \sec \tag{2.24}$$

where I_i is the total ion current due to the flow of $\dot{n}_i$ ions per second of charge q needed to produce the desired thrust. M is the atomic weight of the propellant. [5]

The power supply design is driven by the total ion current required by the thrust requirement. The electric power imparted to the ion beam to achieve the final exhaust velocity is equal to the ion flow rate $\dot{n}_i$ multiplied by the kinetic energy per ion: [5]

$$\mathrm{P}_j = \left(\tfrac{1}{2} m_i v_p^2\right)\dot{n}_i \tag{2.25}$$

The total ion current required to produce the required thrust is given by:

$$I_i = n_i q = \frac{\dot{m}_p^{+}}{m_i} q = \frac{\dot{T}}{I_{SP}} \frac{q}{m_i g} \text{ in Amps} \tag{2.26}$$

where m_i is the ion mass. [5]

The physical dimensions of the thruster are likewise determined by the thrust requirement and driven by the ion current and current density deliverable from the power supply. These constrain the minimum ion source area which to a large degree defines the physical grid size and hence the thruster size. The total ion source area required to produce the desired thrust is:

$$A_i = \frac{I_i}{J_i} \tag{2.27}$$

where J_i is the source current density. [5]

In this way are the fundamental design parameters for the thruster assembled to achieve the desired result. Figure 2.1 shows a diagram of a typical electron bombardment thruster. In practice there are many more complex issues involved, some of which will be discussed in the following three sections which address in turn each of the three basic components, starting with the ion source, the discharge chamber.

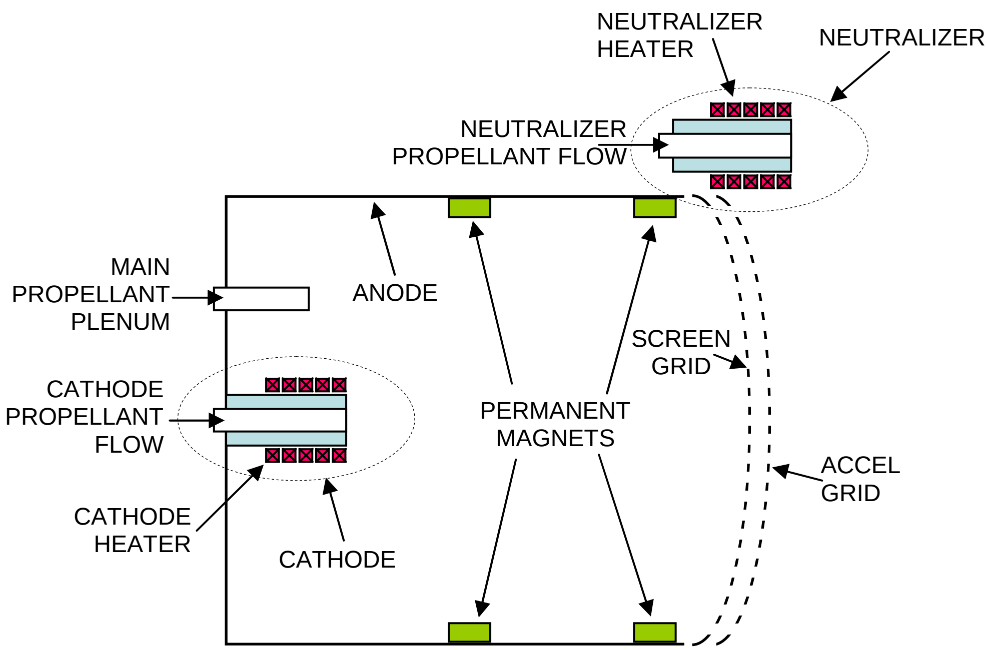

Figure 2.1: Functional Diagram of a Typical Electron Bombardment Thruster

2.2.3 Discharge Chamber

In an electron bombardment thruster the production of ions for acceleration to produce thrust occurs in the discharge chamber. [10] The principle function of the discharge chamber is to generate an ion current of moderate, but nearly uniform current density and do this with low losses of energy and neutrals. [10] For most electron bombardment thrusters the basic configuration of the discharge chamber is a cathode at the center of a cylindrical anode with a roughly axial magnetic field. In early thruster designs a fully axial magnetic field was imposed by a solenoid outside the anode. [21] Most modern thrusters employ a ring-cusp magnetic field to maximize electron residence time in the chamber.

The basic design of the discharge chamber is usually composed of a cylinder with the propellant introduced and an electron source provided at one end, and an ion extraction system at the other end. [5] Electrons emitted by the electron source interact with propellant atoms. Ionizing collisions between electrons and propellant atoms result in a plasma continuously supplied with ions and electrons. [5]

Many different electron sources have been testes for use in electron bombardment thrusters though most have generally been some form of cathode. The most commonly used electron source in use today is hollow cathodes. In most gridded electrostatic thrusters, a single, centrally located hollow cathode supplies the electrons. [25] Hollow cathodes are used as a both as a source of primary electrons for the discharge chamber and as the neutralizer to provide electrons to neutralize the thrust beam. [26]

The basic design of a hollow cathode consists of an outer refractory metal tube, frequently tantalum. This tube is covered on its downstream end by an orifice plate usually made of thoriated tungsten. A refractory metal insert either coated or impregnated with materials such as barium and strontium carbonates serves to lower the work function which aids in the emission process. The emission process is started by the application of heat from an external heater. [26] Once the emission process has started, propellant ions streaming upstream through the orifice impact the insert surface with sufficient energy to heat it. The emission process is therefore self sustaining once the cathode discharge is established and the heater can be turned off. [26]

The cathode is typically operated 30 to 40 Volts negative of the anode in a mercury thruster. [10] The voltage difference between the cathode and anode is an important design consideration since it impacts the ion energies in the discharge chamber. Figure 2.2 shows a cross section diagram of a typical hollow cathode such as those used in Hughes/Boeing XIPS.

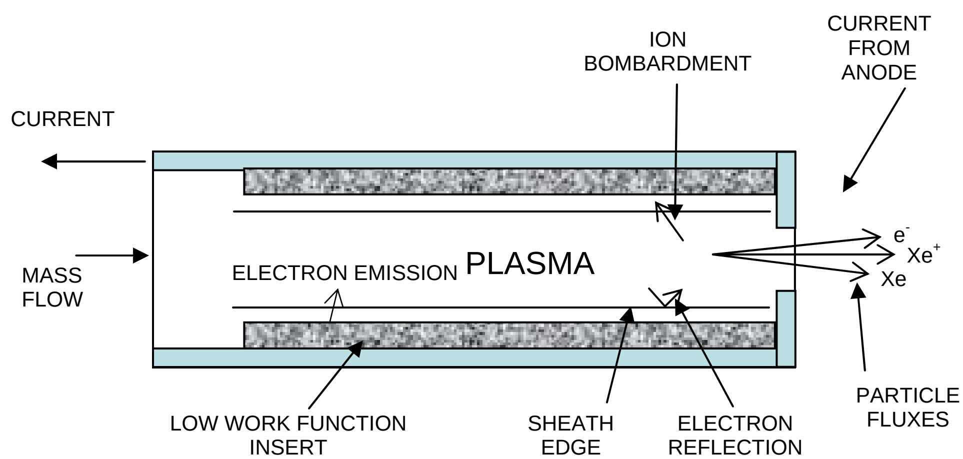

Figure 2.2: Functional Diagram of a Typical Hollow Cathode [27]

Within the discharge chamber a magnetic field is required for efficient ionization of the low density (approximately $10^{18}/m^3$) propellant atoms. [10] It is desired that primary electrons reach, without collisions and without intercepting the anode, as much as possible of the ion chamber cross section near the accelerator section. [10] In early thrusters a primarily axial magnetic field was used. This was later replaced by a field that diverged toward the accelerator system in order to more evenly spread the ions along the screen grid discharge chamber interface. Modern non RIT electron bombardment thrusters use a highly divergent form of magnetic field known as a ring-cusp field. Ring cusp thrusters have been shown to perform better than divergent field thrusters. [28] Ring cusp thrusters use permanent magnets and show substantial promise for high performance operation. [28]

In the classic thruster design the cylindrical walls of the discharge chamber serve as the anode. [5] More modern ring-cusp thrusters may have ring sections of the discharge chamber that serve and the anode with insulated sections between them. In either case the anode is maintained at a positive potential with respect to the ends of the discharge chamber so that electrons emitted by the cathode are injected through a plasma sheath which exists in front of the cathode into a region in which the potential varies with both radius and axial distance. [5] The ends of the discharge chamber are maintained at the same potential as the cathode. Ions created by the electron bombardment are therefore drawn to the cathode and chamber ends. [21]

The emitted electrons are likewise constrained by the chamber ends which are at cathode potential and by the magnetic field. [10] The magnetic field prevents electrons from flowing directly to the anode, the outer cylinder wall. [5] Electrons leaving the cathode are drawn radially toward the anode but, because of the magnetic field travel in curved paths. Collisions with propellant atoms interrupt the paths and allow the electrons to diffuse to the anode. In the process many propellant atoms become ionized. [21]

Many, but not all propellant atoms become ionized in this fashion. The residence time for neutrals in the discharge chamber is much greater than for ions though because the escape rate of ions through the accelerator is much higher than the neutral escape rate. [10] This is because neutrals move at velocities consistent with the wall temperature which is generally on the order of a few hundred degrees C, while ions move at 2-3 eV. [10]

The arc plasma behind the grid aperture is perturbed by penetration of the accelerating field into the discharge chamber, forming a concave sheath which separates positive and negative particles and provides focusing. [21] This is what is known as the plasma sheath. The plasma sheath is an important feature of the thruster simulation as will be discussed in Chapter 3.

2.2.4 Accelerator System

Extraction, focusing, and acceleration of the ions from the discharge chamber to produce thrusts is accomplished by the accelerator system. The accelerator system of an electron bombardment thruster is composed of two or three nearly parallel plates with aligned apertures. The plates are separated by gaps usually on the order of the aperture size. These plates or as they are more commonly referred to, grids, serve the function of acting upon the ions generated in the discharge chamber and producing a nearly parallel flow of ions in an exhaust beam of desired velocity. [10] The grid adjacent to the discharge chamber is called the screen grid and is usually maintained at a potential equal to that of the cathode. [21] The screen grid serves two purposes, the containment of the plasma and the focusing of ions from the plasma. [5] The accelerator grid is aft of the screen grid and is maintained at a potential lower than the screen grid in order to accelerate ions. A third grid is sometimes employed to decelerate the beam and limit electron back-streaming. The ability of the accelerator system to perform its desired function is constrained by the interaction of the accelerator system with the discharge chamber, the electric field limit to prevent electrical breakdown, cosine loss of thrust due to beam divergence, space charge limitations on the current density, and charge exchange erosion. [10] It is convenient to express the current producing characteristics of the accelerator in terms of a parameter called perveance. [5] The meaning of this concept will be discussed later. It represents a geometric quantification of the ability of the accelerator system to achieve full space charge limited flow. This in turn is limited by electrical breakdown and grid erosion due to charge exchange ions. [10]

The design of the accelerator system is driven by space charge factors and the material properties of the grids themselves. The space charge limited current density is given by

$$j = \left(\frac{4\varepsilon_0}{9}\right)\left(\frac{2q}{m}\right)^{1/2}\left(\frac{V^{3/2}}{l^2}\right) \tag{2.28}$$

where q/m is the charge to mass ratio and V is the potential at distance l from the plane of origin. [10] Since the current per hole is essentially constant for a given operating condition, the use of many small closely spaced apertures in closely spaced grids maximizes space charge performance. [10]

As was stated earlier the perveance of the accelerator system is a key parameter in the system design and evaluation. The perveance provides an indication of space charge performance for an accelerator system. [10] Perveance is defined as the total ion beam current divided by three halves power of the accelerator voltage: [5]

$$P = I_i / V^{3/2} \tag{2.29}$$

however; it is more illustrative of the role of perveance to look at how the current density is limited by space charge factors. Since I_i is just the product of the current density and the beam area the perveance can easily be expressed as:

$$P = \frac{I_i}{V_a^{3/2}} = \frac{A_i J_i}{V_a^{3/2}} \tag{2.30}$$

If J_i is defined as the space charge limited current density then from the equation for a space charge limited diode J_i can be expressed as:

$$J_i = \frac{4}{9}\varepsilon_0 \frac{V_a^{3/2}}{d^2}\sqrt{\frac{2q}{m_i}} \tag{2.31}$$

Inserting [2.31] in [2.30] shows that perveance can be expressed as:

$$P = \frac{A_i \frac{4}{9}\varepsilon_0 \frac{V_a^{3/2}}{d^2}\sqrt{\frac{2q}{m_i}}}{V_a^{3/2}} \tag{2.32}$$

which reduces to:

$$P = \frac{4}{9}\varepsilon_0 \frac{A_i}{d^2}\sqrt{\frac{2q}{m_i}} \tag{2.33}$$

Perveance is therefore a factor of the accelerator geometry, specifically the accelerator open area A_i and the grid separation distance d. [5] A high perveance accelerator system would therefore have closely spaced grids with many holes. [10]

The design of high perveance accelerator systems is limited by the material of the grids which must hold their shape under varying thermal conditions and must not erode to quickly due to charge exchange ion impacts. Additionally, the spacing of the grids is limited by the need to avoid electrical breakdown between the grids. Under ideal vacuum conditions electrical breakdown might be expected to be zero; however, flight data shows this not to be the case. [10] One source of breakdown is the growth of conductive whiskers. The whiskers can grow as a result of preferential deposition of sputtered material in regions of high electric field. [10] The presence of charge exchange ions has been discussed earlier. Their impact on the accelerator system design is to impose a limitation on the open area due to the need to maintain structural integrity of the grid. It is possible to calculate an effective charge exchange current, and then use that in the grid design process. The charge exchange current can be expressed as the product of the charge exchange cross section, the neutral density, the total beam current, and the effective length of the acceleration portion of the charge exchange current: [10]

$$J_a = \sigma_c n_o J_b l_e \tag{2.34}$$

A further design limitation comes from the need to limit as much as possible the number of electrons from the neutralizer that flow upstream into the discharge chamber. This is known as electron back-streaming. Electron back-streaming occurs when the minimum potential within the accelerator aperture is high enough to permit electrons to flow backward through the accelerator system. [10] Back-streaming electrons constitute a current drain on the power supply, distort the potential profile in the acceleration gap from the simple ion space charge configuration, and could damage the ion source and disturb the electron emission process. [17] The addition of a region of increasing potential aft of the accelerator can preclude electron migration into the acceleration gap. [17] Providing this increased potential aft of the accelerator grid is accomplished with the use of a third, decelerator grid. The decel grid is located aft of the accel grid and maintained at a potential near that of the spacecraft bus. The decelerator also provides a means of reducing ion exhaust speeds without corresponding loss in space charge current, thereby preserving higher thrust densities at lower Isp. [17]

2.2.5 Neutralizer

The final component of an electron bombardment thruster is the neutralizer. There are two functions of the neutralizer, charge neutralization of the beam to prevent space charge limitation of the beam current flow and current neutralization to prevent buildup of charge on the spacecraft. [10] In almost all current thrusters hollow cathodes, similar if not identical to those used as electron sources for the discharge chamber, are used as neutralizers. Neutralization in no way implies recombination, only the net current of the beam. [10] If current neutralization ceases, in a matter of seconds the spacecraft potential will drop to the point that ions will no longer leave. [10]

In order to ensure that the right number of electrons is inserted into the ion beam, the current provided to the neutralizer is usually tied back to the electron current arriving at the discharge chamber anode. Since every electron arriving at the anode represents an ion that has been created it serves to guide the generation of electrons for the neutralizer.

CHAPTER 3

THE IONLITE SIMPLIFIED ELECTROSTATIC THRUSTER MODEL

A computational model of a typical electrostatic thruster was developed in order to examine the behavior of individual charge exchange ions and their response to different applied fields. A model which takes into account all of the particle motion seen throughout the grids would have proven computationally intensive, and was not necessary for this effort. The primary particles of interest are only charge exchange ions and unfocused beam ions. These particles can be assumed to already exist within the grid structure, their creation is not an issue, and can be tracked as they progress along their calculated trajectories. This greatly simplifies the model, as the interactions of all particles are neglected, except insofar as the ion beam is treated as a steady charge distribution interacting with particles of interest through the net electric field. Given this simplification both the magnetic and electric fields can be treated as constant in time and calculated once, separately from the calculation of any particle trajectory.

3.1 The Advantages of a Simplified Electrostatic Thruster Model

There are several advantages to a simplified model of the typical ion thruster over the current sophisticated codes available. The simplified model can be run hundreds of times in the time that the more sophisticated codes would run to steady state once. Additionally, the simple model can be rapidly reconfigured between runs to examine slightly different fields and grid geometries. Finally, the ability to rapidly reconfigure the simple model and run it quickly allows for narrowing in on multiple different advantageous configurations that can then be examined in greater fidelity with the more sophisticated ion thruster simulations currently being used.

3.1.1 Simplified Model Can be Run Repeatedly

A model that can be run many times while the more sophisticated code runs once offers an advantage in finding techniques for limiting thruster grid erosion. Current simulations described in the literature are very computationally intensive. These simulations such as ffx [29] or IBEX-T [30] simulate many thousands of particles, each in turn representing multiple particles. Generally these simulated particles represent neutral atoms, singly charged ions from the discharge plasma, doubly charged ions from the discharge plasma, or electrons from both the discharge plasma and the neutralizer. Each particle is moved a single step under the influence of the imposed fields and the fields due to every other charged particle in the simulation. Once each particle has been moved one step the codes then recalculate the overall field within the model. This process repeats generally until a steady state condition has been reached.

The function of these sophisticated codes is therefore very computationally intensive. After each of the thousands of particles is individually stepped forward one time increment under the influence of the total potential field at time zero, the field must then be updated. This is done by solving Poisson's Equation using an iterative method such as Gauss-Siedel. This solution generally takes several thousand iterations at each of many thousand grid points to arrive at a final value for the potential throughout the model. Throughout the process the positions and velocities of each of the thousands of particles must be tracked. This requires considerable memory or frequent hard storage access which slows processing. For example, to achieve the necessary precision requires the use of double precision floating point variables, three for each particle for tracking the three dimensional position, and another three for velocity. That is six 64 bit variables for each particle or 48 bytes per particle. Unless the position and velocity of each particle are to be written to hard storage after each update the previous positions must be retained for all previous position updates. There can be expected to be many thousands of updates, but assuming a limit of one thousand position and velocity updates this still requires 48K bytes of memory for each particle. For a very limited model only considering one thousand particles this still requires 48 Meg of RAM for tracking particle position and velocity only. In reality there are many more than one thousand particles and each moves many more than one thousand times. [29] In addition, the field values at every location throughout the model must be retained in memory, or accessed when needed from hard storage.

The ionLite program is much simpler computationally. The electric and magnetic fields are assumed to be constant over time and therefore need to be solved for only once. This can be done because all of the ion beam particles are assumed to be present in a fully space charge limited current state. Fields due to charge exchange ions are orders of magnitude lower than the grid and ion beam fields. The field contribution from charge exchange ions can also be viewed as incorporated in the field contribution due to the ion beam. A Gauss-Sidel technique is used along with successive over-relaxation (SOR) to quickly determine the potential throughout the model and this is then used through the remainder of the run.

In the ionLite program particle motion is evaluated only for single particles. Particle position is iterated from an arbitrary initial position to a final position one particle at a time. This reduces the memory required considerably. The position and velocity of each particle at every step can be recorded to hard storage at the conclusion of the particles passage through the model. The program then goes on to the next particle. The initial position represents the location within the model where the charge exchange ion is created through a collision between a neutral atom and a fast ion beam ion. The final position is the point at which the particle collides with a grid or exits the model either by returning to the discharge chamber or reaching the neutralization plane. Once all desired particles have been iterated to their final outcome the program run is done. Outcomes for the individual particles are recorded at the termination of their individual motion. Totals indicating the damage potentially done to the grids are summarized in a final report documenting how the configuration evaluates for comparison to other runs for other configurations. These limits to the computational complexity allow for the ionLite program to be run hundreds of times with minor changes between runs thus providing the capability to create trend plots comparing the results for grid damage and Isp for changing field or geometric parameters.

3.1.2 Rapid Reconfiguration of Model Parameters

One of the fundamental advantages of the ionLite simplified electrostatic thruster simulation is that it can be rapidly re-configured between program runs to examine slightly different field or grid geometry configurations. This can be done because all of the parameters defining the configuration are contained in an input text file that is read at the beginning of the program run. This input file can be easily modified between runs. This characteristic makes it possible to use a shell script to run the program multiple times with slightly different input files which ultimately results in the capability to rapidly model many different configurations in an effort to develop new techniques for mitigating charge exchange ion induced grid erosion.

In the ionLite program the key parameters defining the nature of the model are all inputs to the program that are read in from a text file as one of the first functions of the program. This input text file contains the grid aperture radius, grid thickness, grid spacing, grid potentials, and any auxiliary magnetic field. The file also contains a number of other key characteristics or features of the simulation such as the neutral atom temperature, initial thermal velocity vector, particle mass, and degree of charge. Finally, the input file contains control parameters that determine how the simulation is to function such as whether to include the ion beam, where to generate the test particles, and the size of the simulation space. (An example of the input file with a full list of the parameters that are available for modification is contained in Section 3.3.7.)

The input data file can be rapidly modified or replaced between runs allowing for changes in configuration or function of the model. Changing the fundamental parameters of the simulation is as simple as changing a few values in the input file. It is also possible to pre-generate a number of input files, each with slightly different parameters, and simply replace the target file with these other files one at a time between runs. This provides a capability to automate the variation of the simulation between runs. A Run Summary file is created as one of the outputs of the program. This Run Summary file, in addition to the results of the simulation, contains the key input parameters that define the simulation. This allows for easy review and tracking of the outcome of each simulation run.

In addition to flexibility in the configuration of the model, the program builds in flexibility in the output. All of the calculated variables generated during the program execution are passed to a separate output handling utility implemented in the form of a header file. This allows for selective modification of the form and content of the output depending on the nature of the investigation. This can be implemented by minor modification to the header file, leaving the main program untouched. This eliminates the need for complete retest and validation of the primary computational portion of the code. (A full description of program function including a list of available output is contained in Section 3.3.7.)

It is possible to generate a shell script or calling program that modifies the input file or copies a different file into the input file target directory, calls the ionLite program, then repeats until the desired test configurations have been evaluated. The shell script can simply use a look-up table of a single parameter that varies between runs and copies the new parameter into the input file between runs. Alternatively the shell can access a list of input files, each with a variation in one or more parameters from the others. It would then replace the target input file with one of the alternative files between runs. The shell then runs the ionLite program with the new or modified input file. After the simulation has completed the shell then repeats the process with the next modification to the input file. This then repeats until all of the desired runs have been made. Each time the ionLite program completes the results of the run are appended to the Run Summary file. After the script completes the Run Summary contains the results for each different execution of the program indicating how many particles strike the grids and the total kinetic energy transferred to each portion of each grid. In addition the Run Summary contains the principle input parameters that define the simulation. This makes the comparison of results across multiple runs with variations of one or more parameters relatively simple.

3.1.3 Identifying Configurations for Further Study

The simple nature of the ionLite model allows for rapidly narrowing in on multiple different advantageous configurations which can then be examined in greater detail with more sophisticated codes or by experimentation. As described above the program can be run multiple times with minor modifications between each run. The results for kinetic energy imparted to the different grids and the Isp for each configuration can then be compared across many different runs. A configuration that results in a lower kinetic energy transferred to the grids but little or no reduction in Isp would then merit further more detailed investigation.

The previously described characteristics of the program allow for slightly modifying one or more parameters between runs. Consider as an example if one wanted to examine the impact of varying the grid separation distance on kinetic energy transfer to the grids. To investigate this, the input file can be modified, slightly increasing the grid separation each run.

The output of the program documents the kinetic energy imparted to each grid, the total kinetic energy conveyed to all grids, the number of particles impacting each grid, and the velocity of a particle representing an individual beam ion expressed in terms of Isp. The results for each run are documented in the Run Summary file which includes the principle input parameters which define the configuration and the kinetic energy transferred to each grid. The results for kinetic energy transfer are listed to the level of fidelity which indicates which grid surface is impacted including the kinetic energy transferred to the sides of the grid aperture. The output also includes the total number of particles impacting each part of each grid. The Run Summary file is added to each time the program is run providing documentation of the results for multiple configurations. The values in the Run Summary can then be entered into any spreadsheet or visualization software and plotted to show variation in kinetic energy transfer to the grids with changing configuration. For the example described earlier, the kinetic energy transferred to the grids can be plotted against the grid spacing and the Isp to determine if there is any advantage.

A configuration which reduces the kinetic energy imparted to the grids while minimizing the reduction in Isp would be one which merits more detailed evaluation. Staying with the grid spacing example, consider a case where increasing the grid spacing by 10% results in a 20% reduction in kinetic energy transferred to the grids but only a 2% reduction in Isp. This would be a case which would qualify for further more detailed evaluation since the decrease in Isp could be made up for with longer burn times while still leaving an expected increase in grid life of 18%. This resulting configuration could then be further evaluated with the ionLite program to consider the impact of changing other parameters such as grid voltages or the addition of auxiliary magnetic fields.

3.2 Justification for the Use of a Simplified Electrostatic Thruster Simulation

Considerable time and effort have been put into the development of the current sophisticated simulations, it is therefore necessary to spell out why the simplified model discussed here provides some capability that they do not. Additionally, it is important to note how the nature of the physics operating within the thruster makes the use of the simplified model valid for evaluating the grid erosion problem. It is a key physical characteristic of the electrostatic thruster that the particles move in response to the fields within the grid system, simulate the fields and the particle motion can be recreated with reasonable accuracy. The only other contributor to particle motion is collisions which are relatively rare. Since charge exchange ions exist within the thruster, their creation is not an issue, only where they are created and that is predominately within the ion beam. To evaluate grid erosion doesn’t require every possible particle, not even every charge exchange ion, just an evaluation of the kinetic energy transferred to the grids over a given period of time. This can then be compared to the kinetic energy transfer to the grids over time for different configurations.

3.2.1 Fields Control Particle Motion

Charged particles move in response to the fields, either electromagnetic or gravitational. It can be assumed that since the primary area of operation of any electrostatic thruster is in space that the gravitational field component is negligibly small compared to the electromagnetic fields. Therefore the simulation of the electromagnetic fields within the grid system will inevitably lead to an accurate model of particle motion within the grid system. The ionLite program inputs values for the potential for each grid and solves for the steady state charge density in the ion beam. The grid potentials and charge density can then be used to solve Poisson's Equation for the potential throughout the model.

Within an electrostatic thruster particle motion is controlled by the fields. The fundamental equation of motion for charged particles is the Lorentz force equation.

$$\mathbf{F} = q(\mathbf{E} + \mathbf{u} \times \mathbf{B}) \tag{3.1}$$

In this equation $\mathbf{F}$ is the total force acting on the particle, q is the charge on the particle, $\mathbf{E}$ is the electric field, $\mathbf{u}$ is the particle velocity, and $\mathbf{B}$ is the magnetic field. If the particle charge and initial velocity are known, or given, then the only parameters that influence the force on the particle are the fields. If the thruster is operating under steady state conditions the overall field inside the thruster will not change. Therefore under steady state operating conditions the fields can be determined once and the motions of the individual charged particles can be modeled accurately.

The ionLite program inputs the value of the potential for each grid and solves for the steady state charge density in the ion Beam. The grid potentials can be set to any reasonable value. A temporally constant charge distribution is used to represent the ion beam. The charge distribution is determined from basic equations for electrostatic thrusters operating under nominal space charge limited current conditions.

The grid potentials and charge density are then used to solve Poisson's Equation for potential throughout the model. A Gauss-Sidel iteration method is used to solve for potential at each node point. If a non-real configuration is input the iteration will not collapse to a solution. The program takes between 30 seconds and five minutes to reach a solution for the potential; however, this is done only once during the course of an individual run. It should be noted that the run times expressed here represent those seen when the program is run on a Windows PC with 1.7 GHz single Pentium 4 processor.

3.2.2 Contribution of Collisions is Minimal

The only non-field contribution to particle motion is collisions which are rare. This can be shown to be the case by examining the length of the mean free path at representative points within a typical thruster. The mean free path (MFP) can be found from one of the standard equations of kinetic theory. [31]

$$\lambda = \frac{1}{\pi\sqrt{2}d^2 n} \tag{3.2}$$

In this equation d is the molecular diameter, n is the number density of particles, and λ is the mean free path. For xenon a reasonable value of d would be 5.8Å. This value is an approximation based on high and low values of atomic radius. [32] The number density of ions in the discharge chamber plasma is on the order of $3\times10^{17}\mathrm{m}^{-3}$. [30] Using these values results in a mean free path within the discharge plasma of 2.23 meters. The density of particles within the ion beam can be determined from the beam current density. In the case of this thruster the beam current density, j_b, was found to be 4.36mA/cm^2 or 43.6 A/m^2. Assuming a realistic Isp of 3058 seconds or an exhaust velocity of 30000 m/s gives a number density of $8.98\times10^{15}m^3$. Using these numbers gives mean free path of 74.5 meters. Given that the interior dimensions of the grid apertures being considered in the model are on the order of $5\times10^{-3}m$, it is obvious collisions are relatively rare, and that the probability that a particle that has already experienced a collision will experience a second before striking a grid or exiting the model is very slim.

3.2.3 Particle Creation

It can be assumed that charge exchange ions exist within the grid system and that it is not necessary to model their generation. The fact that charge exchange ions are created within the grid system of an electrostatic thruster is well established and was discussed earlier. The only question is whether it is necessary to model their creation exactly to evaluate the benefit of any configuration intended to reduce grid erosion. It is proposed that characteristics that charge exchange ions possess that relate to how likely they are to impact the grids or the damage they do to the grids can be limited and made inputs to the program. These characteristics can then be cycled through to make a more complete evaluation of any set of grid parameters being evaluated. In this way ultimately it is not necessary to model every charge exchange ion within the system, just a representative subset.

It is already established that charge exchange ions are created and exist within the grid system of an electrostatic thruster. It is also understood that some of these charge exchange ions will impact the grids causing erosion of the grid material, and that some will exit with the ion beam. This is discussed in detail in section 2.2. It is also clear that the charge exchange ions of significance are created within the ion beam.[9] Charge exchange ions created outside of the beam will be relatively rare and could easily be neglected in an examination of the ions that cause the most grid damage.

3.2.4 Evaluation of Grid Erosion

The intent of the program is to determine whether fewer charge exchange ions strike the grids or if the ones that do impact do so with less kinetic energy transfer. A sample of charge exchange ions that represent ions generated at selected points throughout the ion beam can be used to evaluate the effectiveness of any technique aimed at mitigating grid erosion. The program can be run to evaluate the results for an even distribution of charge exchange ions throughout either the entire computational space or just throughout the ion beam, or it can be run creating only a limited number of ions starting within specific areas of the ion beam as part of examining a specific configuration in greater detail. This might be done for example if a high level examination of various configurations identified one that showed promise. It could then be investigated to determine if there was a general improvement, or if there was only an improvement for ions starting in specific regions.

Parameters relating to the characteristics that charge exchange ions possess that effect their end outcome can be limited and made inputs to the program that can be cycled through along with the thruster configuration parameters. As described in section 2.2 the source of charge exchange ions is neutral propellant atoms diffusing from the discharge chamber through the grids and out into the exhaust beam. Neutral atoms will have thermal velocities and random directions, but the general sense of the direction will be driven by the pressure difference between the discharge chamber and space. This necessitates that that most neutrals will have a velocity that is primarily in the positive axial direction. The only other characteristic that differentiates any charge exchange ion from any other charge exchange ion is the degree of ionization. The vast majority of charge exchange ions will be singly charged due to the high energy level required of a collision which produces a doubly charged ion. In either case the charge state of the ions can also be input in the program. A typical investigation of several runs at different grid separations for example would examine evenly distributed singly charged charge exchange ions with an initially axial velocity equal to the thermal velocity at the discharge chamber operating temperature.

The relative benefit to be derived from any given configuration can be analyzed by looking at the kinetic energy transferred to the grids by a relatively small sample of charge exchange ions. The damage mechanism by which charge exchange ions erode the thruster grids is the kinetic energy transferred to the grid material at impact. It is only reasonable then that any modification to the thruster architecture that limits the kinetic energy transferred to the grids will also reduce the damage done to the grids. ("Thruster architecture" refers to the physical configuration of the grids and grid apertures such as grid thickness, grid spacing, grid aperture radius, grid potentials, etc.) If one assumes that the charge exchange ions are created evenly throughout the ion beam it is also reasonable that an evenly spaced sample of those ions can be used for examining the overall grid erosion of the configuration.

The kinetic energy transferred by a charge exchange ion to the thruster grid material determines the amount of damage done by the particle to the grid material. Kinetic energy is determined from one half the mass of the particle multiplied by the velocity of the particle normal to the surface at impact, squared. The impact of the particle sputters off grid atoms. The amount of grid material sputtered out of the grid is a factor of the planar surface potential as compared to the kinetic energy of the impacting particle.[33] The higher the energy of the impacting particle normal to the surface, the more atoms that will be knocked out of the material.

Any change to the thruster configuration that reduces the kinetic energy transferred to the grids will reduce the damage done to the grids, and hence increase the life of the grids. The total kinetic energy transferred to the grids defines the total damage done to the grids. The number of particles impacting the grids is not as important as their velocity vector normal to the surface being impacted. If the charge exchange ions are created evenly throughout the beam then a sample of particles generated evenly throughout the beam should serve as a good test set representing charge exchange ions per unit of time. A configuration which reduces the kinetic energy that the evenly distributed test particles impart to the grids can be considered to be a configuration that reduces the kinetic energy imparted to the grids by all charge exchange ions.

If the charge exchange ions are created evenly throughout the beam then an evenly spaced sample represents charge exchange ions per time unit. If the charge exchange ions are not in reality created evenly throughout the beam but are concentrated in some areas, as long as some charge exchange ions are created throughout the beam, then an evenly distributed arrangement of test particles is still a legitimate method for evaluating grid damage. If charge exchange ions are created evenly throughout the ion beam and a configuration is shown by the program to reduce kinetic energy transfer to the grids, then the program is indicating that the total kinetic energy transfer to the grids per unit time is reduced by the configuration. If charge exchange ions are not created evenly throughout the beam but are instead concentrated in, for example the narrowest part of the beam, but some are still created throughout the beam, then an even distribution of test particles can still be a valid test of different configurations. In this case however, it may be necessary to compare kinetic energy transfer to grids from test particles generated in different regions. If charge exchange ions are created predominately in one or a couple of regions of the beam and test ions from these areas behave sufficiently differently to different configurations with respect to evenly distributed test particles it may be necessary to narrow the region of the test particle generation. For purposes of initial investigation using the program it is still completely valid to use an even distribution of test particles. Once an initial finding of a desired configuration which reduces kinetic energy transfer is made, further detailed analysis can be done examining the behavior of ions created in different regions. Ideally, the configuration would result in reduced kinetic energy to grid transfer from test particles created in all regions of the ion beam.

3.3 Model Description and Function

For this simulation a single set of grid apertures is modeled. The grid layout can be modified to vary the aperture size, grid spacing and the presence or absence of a decel grid. The simulation space is a cylinder created by establishing a 100 by 300 node grid system, 100 nodes radially by 300 nodes axially. For the third dimension, **θ**, the model simply tracks the particle position and does not incorporate additional gird nodes. This is possible because the electric and magnetic fields are symmetric about the **Z** axis with no **θ** component and the particles of interest are examined individually. As each particle traverses the grid system its position is tracked, but the fields change only with change in radial or axial position. The particle's location in **θ** is recorded, but the actual **θ** coordinate does not exist in the simulation. In that respect even though much of the motion of interest is along **θ**, the simulation really only has a single step thickness in **θ**. The **R** and **Z** axis can be thought of as a Cartesian system that rotates around **Z** with the motion of the particle. For simplicity this will be henceforth referred to as a “floating” coordinate system.

The potential, electric, and magnetic fields were calculated using a two dimensional coordinate system where the coordinates of interest represented the axial (**Z**) and radial (**R**) coordinates of a nominally three dimensional cylindrical system. The fields are all calculated separately from the particle motions. The electric field at each node point is generated by first solving Poisson’s Equation numerically to obtain the potential at each node. The fields are then obtained by numerical approximation of the derivative of the potential at each point. The program can be run either with or without an ion beam simulated.

The actual calculation of the particle trajectories closely follows the method described by Farnell et al [29]. The primary difference between the employed methodology and that used in the reference is that cells do not have a constant volume and are not cubes. For the calculation of particle motion within each cell the **R** and **Z** components of the fields are expressed as **X** and **Z** components. The boundaries of each cell are defined in orthogonal **X**, **Y**, **Z** coordinates and orthogonal equations of motion based on the Lorentz force equation are used to determine the motion through each cell. Time step size is continuously adjusted to make sure that at least five steps occur within each cell. Once the calculated trajectory takes a particle to the boundary of a cell the exit conditions for that cell are determined and used as the input for the next cell along the trajectory. There are four conditions which lead to the termination of the trajectory calculation. The first is that the calculated next cell to be entered is occupied by one of the grids. The second exit condition is that the particle reached the neutralization plane as defined by the axial coordinate limit. The third is that the particle can reach the axial zero limit which indicates a particle re-entering the discharge plasma. Finally, a particle that has resulted in excessive computational errors will have its trajectory terminated. These computational errors will be discussed in more detail later. Particles that reach the radial zero limit (i.e., that cross the axis of the computation space) or the extreme radial limit are reflected back into the space.

As a particle traverses the model its motion is recorded to an output file along with the final exit condition it met and velocity. If the first condition was met, the particle's kinetic energy at the time of impact is also recorded. As described earlier the kinetic energy is a good determinate of the amount of damage in the form a grid material sputtering that the particle's impact would cause to the impacted grid.

3.3.1 Layout of the Computational Space

The computational space is designed to model a single set of axial aligned grid apertures in a two or three grid electrostatic thruster. To accomplish this a cylindrical space is used with the axis of the cylinder, **Z**, being the axis of each of the grid apertures. The radius of the cylindrical space is determined to be approximately halfway between the edge of the apertures and the edge of the next aperture in the same grid in a typical thruster. Using the definition that the discharge chamber is forward and the exhaust plume is aft, the computational space begins in the discharge chamber just forward of the screen grid. The coordinate system used for defining and using the computational model is a cylindrical coordinate system with **Z** being the axial coordinate, **R** the radial, and **θ** the rotational. For determining the fields only the **R** and **Z** coordinates are needed.

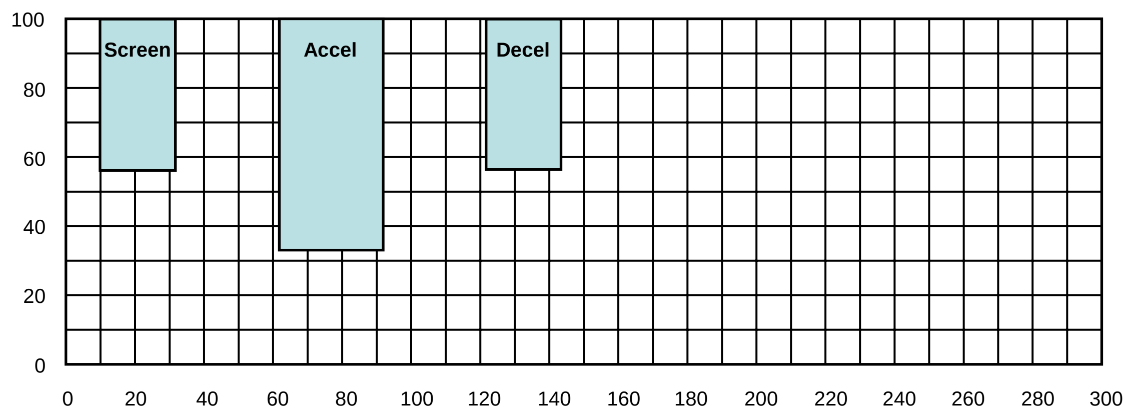

Figure 3.1: Computational Grid Layout Showing Typical Three Grid Thruster Configuration

The computational space is fundamentally a 100 by 300 grid as depicted in Figure 8. The **R** dimension is 100 grid points and the **Z** dimension is 300 grid points. This defines a slice of the computational space extending from the **Z** axis to one edge defined by the limit of the **R** axis.

For calculation of the electric and magnetic fields only the 100 by 300 grid space shown in Figure 3.1 is used. For calculation of the actual particle trajectory only a single "slice" defined by a single step in **θ** is used. In Figure 3.1 the **R** component runs vertically and the **Z** component runs horizontally. The grid points are numbered, **R** from 0 to 99, **Z** from 0 to 299. Steps in **R** are indexed by i and steps in **Z** are indexed by j. Every cell in the space is identified by its cell index, the i and j values of the forward most and inner most node of the four nodes in the cell. The cell made up by the nodes i = 10 and 11, and j = 20 and 21, is defined as cell (10,20).

The actual size of the computational space is established as one of the first calculations of the program and is set by inputting the "Radius" of the calculation. This is the distance from the **Z** axis or R = 0 to the edge of the space or R = 99 in meters. This parameter can be changed as one of the inputs to the program which will be discussed later, but for the examples in this section it is set to 1.17×10^{-3} meters. This establishes the length of the calculation as 3.51×10^{-3} meters or three times the radius. From these the step size of the grid is established. Two fundamental parameters are generated, the step size between R grid nodes, ΔR, and the step size between Z grid nodes, ΔZ. To simplify the calculation these are always kept equal to each other and are defined as one of the first actions in the program to be used throughout the run. Their values are found by dividing the calculation radius defined above by the number of radial grid nodes, 100, which results in $\Delta R = \Delta Z = 1.17\times10^{-5}$ meters.

3.3.2 Calculation of the Electric Field

The electric field is required as one of the components of the Lorentz equation. The method used for determining the electric field is to first find the potential, V, throughout the computational space. The electric field is then determined from:

$$\mathbf{E} = -\nabla V \tag{3.3}$$

In order to determine V the grids are treated as equipotential conductors maintained at the specified grid voltage. The small voltage difference due to the presence of the current used to generate the magnetic field, if one is present, is neglected. The nominal method for determining a voltage at any given point due to the presence of a charged conductor is to solve Poisson's Equation:

$$\nabla^2 V = -\frac{\rho}{\varepsilon_0} \tag{3.4}$$

where ρ is the charge distribution and ε_0 is the permittivity of free space. If the presence of the ion beam is to be neglected, the equation reduces to Laplace's equation:

$$\nabla^2 V = 0 \tag{3.5}$$

The problem of finding the electric potential in a three grid ion thruster aperture is greatly simplified by imposing axial symmetry. Since the potential does not change with any change in θ the problem can be reduced from three to two dimensions. Poisson's equation therefore can be written in its component form for the remaining two dimensions, **R** and **Z**:

$$\frac{\partial^2 V}{\partial R^2} + \frac{\partial^2 V}{\partial Z^2} = -\frac{\rho}{\varepsilon_0} \tag{3.6}$$

This equation can then be written in a finite difference form and solved numerically for the given boundary conditions. Since this is a two dimensional steady state problem it is relatively easily solved using a Successive Over-Relaxation method.

For the model the second partial differentials are expressed using central differences giving a finite difference equation of the form:

$$\frac{V_{i+1,j} - 2V_{i,j} + V_{i-1,j}}{\Delta R^2} + \frac{V_{i,j+1} - 2V_{i,j} + V_{i,j-1}}{\Delta Z^2} = -\frac{\rho_{i,j}}{\varepsilon_0} \tag{3.7}$$

In this equation the *i* subscript is used to denote a grid step in R and the *j* subscript denotes a step in Z. Each step in **R** and **Z** is the same length ($\Delta R^2 = \Delta Z^2$). This equation is then recast in a form suitable for solution using the SOR method:

$$V_{i,j}^{n+1} = \frac{W}{4}\left[\frac{\Delta R^2 \rho_{i,j}}{\varepsilon_0} + V_{i+1,j}^{n} + V_{i-1,j}^{n+1} + V_{i,j+1}^{n} + V_{i,j-1}^{n+1}\right] - [W-1]V_{i,j}^{n} \tag{3.8}$$

where *W* is the relaxation parameter.

The value for the local charge density, $\rho_{i,j}$, is set to zero throughout the computational space except for the region enclosed by a simulated beam boundary. This beam boundary is controllable and is generated by a second order polynomial which uses the radius of the screen aperture, the accel aperture and the radius of the calculation space as points and the forward side of the screen grid, the center of the accel grid and the neutralization plane as their locations to generate a smooth beam radius approximation at all points within the computation space. Initially, all points within the beam radius are assigned values of $\rho_{i,j}$ that are based on a uniform current density as arrived at using the equation for the space charge limited beam current for an electrostatic thruster:[17]

$$j = \frac{4\varepsilon_0}{9}\left(\frac{2q}{m}\right)^{1/2} \frac{(V_0 + V_a)^{3/2}}{x_a^{\;2}} \tag{3.9}$$

In this equation $V_0 + V_a$ is the net acceleration voltage drop seen between the discharge potential and the accel grid, *q* and *m* are the charge and mass of the ion, and x_a is the separation between the screen and accel grids. As the current density is defined as:

$$j = \rho v \tag{3.10}$$

The charge density therefore is found from:

$$\rho = {}^{j}\!/_{v} \tag{3.11}$$

where v is the ion velocity. This ion velocity is initially assumed to be constant, thus producing a uniform charge density. It is found from:[17]

$$v = \left[\frac{2q\left(V_0 - V_{local}\right)}{m}\right]^{1/2} \tag{3.12}$$

In this equation V_{local} is the potential at the node being evaluated. The value thus arrived at is modified by the overlay of two equations, one meant to incorporate the additional charge component of electrons near the plasma sheath and near the neutralization plane, the other meant to incorporate geometrical impacts on charge density such as beam narrowing. It should be noted that the resulting charge density profile is not intended or advertised to be accurate but rather is arrived at empirically to match the resulting potential profile to experimental results and computational output from the more sophisticated simulations documented in the literature. The purpose of this simulation not being to evaluate the ion beam or beam particles but rather the trajectories and impact induced damage to the grids caused by charge exchange ions.

The boundary conditions imposed on the model in order to determine the potential are established from the thruster grid potentials, the discharge plasma potential, the neutralization of the exhaust in the far field, and the physics of the configuration. The forward boundary condition is determined from the discharge chamber plasma potential. The grid voltages are set as uniform across the grid surface. For a typical test run the screen grid voltage was set at 1000 Volts, the accel grid voltage was set at -500 Volts, and the decel grid voltage was set at 0 Volts. These values were used to allow for comparison between the calculated results and those documented by Okawa and

Takagahara using their IBEX-T code. [30] (Note that Okawa and Takagahara do not incorporate a decel grid in their model.) The aft boundary condition is based on the assumption of complete beam neutralization. The potential at $j = 299$ is held at 0 Volts. The boundary conditions at the centerline and the outer edge of the computational space are established from the requirement that the potentials along these edges be continuous with and essentially mirror the fields that would exist beyond the boundary. This provides for a Neumann condition at these boundaries whereby the requirement is that:

$$\frac{\partial V}{\partial R} = 0 \tag{3.13}$$

To implement the Neumann conditions at the centerline and the edge of the computational space two additional points were added in i and the grid essentially shifted. These points were later taken out once the potential was determined.

All grid points within the boundaries where initially set to 0 Volts. The primary exit condition established for terminating the calculation was that the sum of the magnitude of the difference between all points at n and n+1 be less than 1.0 or symbolically:

$$\sum_{j=0}^{299}\sum_{i=1}^{100}\sqrt{\left(V_{i,j}^{n+1} - V_{i,j}^{n}\right)^2} < 1.0 \tag{3.14}$$

A secondary exit condition would come into effect if the total error was not collapsing to less than 1. In this case, when the total error as defined above changes by less than 1×10^{-2}%, the over-relaxation parameter, w, is reduced by 0.05. This is continued, with the condition being checked only after every 100 complete cycles, until the primary exit condition is met or the change in total error is less than 1×10^{-7}%. Once the exit criteria were met, the potentials at all grid points are saved in an array for use later in determining the electric field and written to a text file that can be plotted to aid in visualization. A sample of the results for a case with no beam or decel grid is shown in Figure 3.2. Figure 3.3 shows the same configuration and potentials for the discharge, screen, and accel grids with the addition of the ion beam. Figure 3.3 can be compared to Figure 3.4 which is Figure 9a of Reference 20. This allows for a comparison of the resulting potential contours from the ionLite program and the more sophisticated IBEX-T code of Okawa and Takagahara. While the resulting potential for ionLite does not exactly match the output of the IBEX-T code, it is accurate enough to be able to evaluate the passage of individual charge exchange ions, which is the intent of the ionLite code.

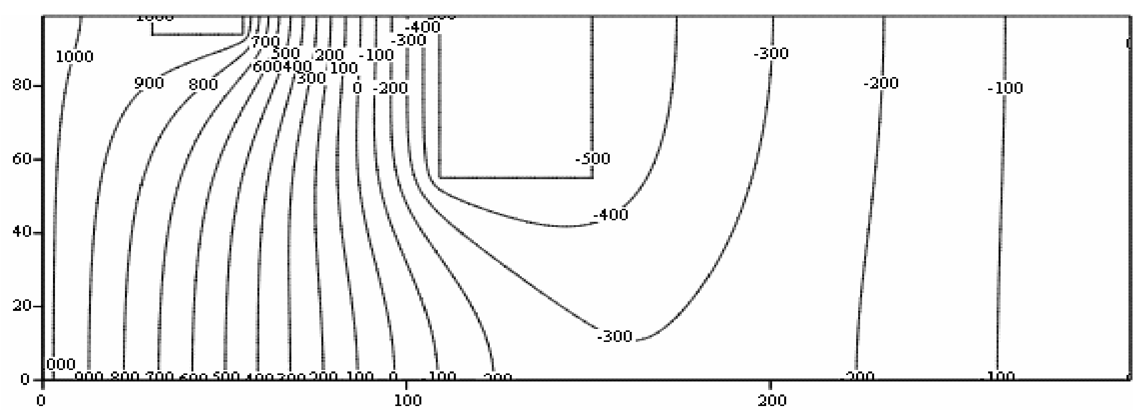

Figure 3.2: Calculated Potential throughout the Two - Dimensional Computational Space with No Ion Beam Present

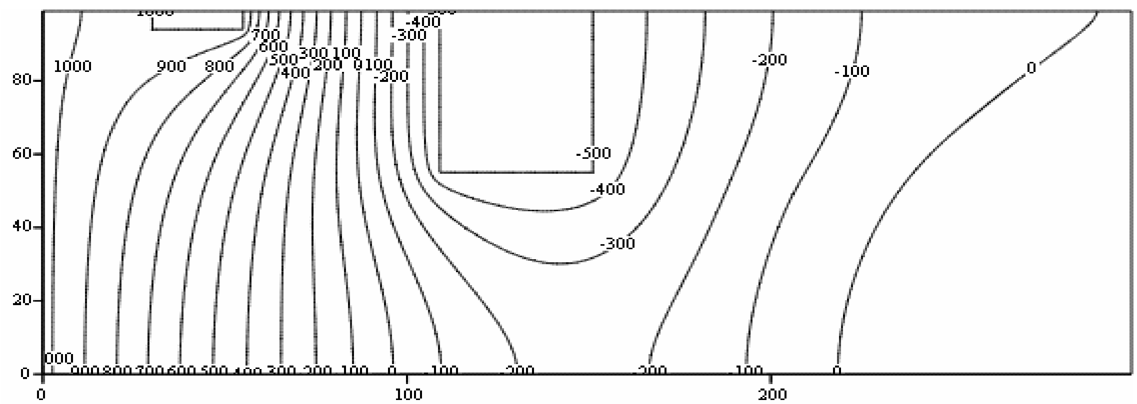

Figure 3.3: Calculated Potential Throughout the Two - Dimensional Computational Space with Simulated Ion Beam Present

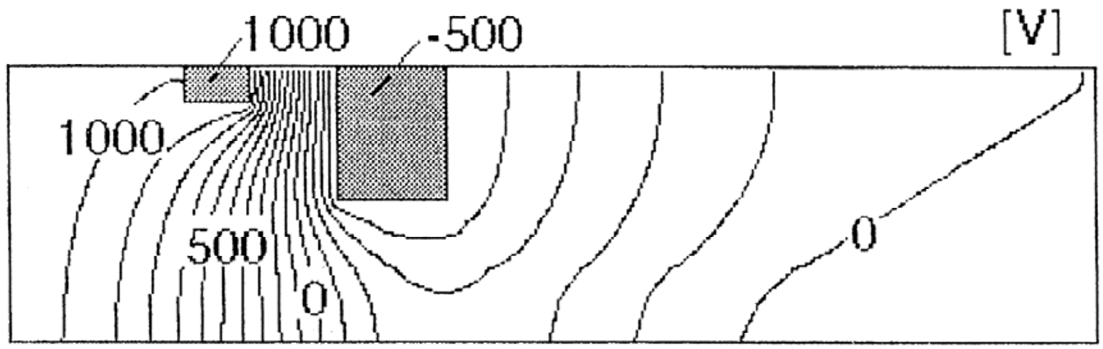

Figure 3.4: Figure 9a of Okawa and Takegahara [30] for Comparison of Potential Contours Between ionLite and IBEX-T

The electric field components throughout this region are then determined from the calculated potentials using a central difference representation of the first order partial derivative of the potential at each point in the computational space. In two dimensions the equation for determining the electric field from the potential is expressed as:

$$\mathbf{E} = -\left\{ \frac{\partial V}{\partial R}\hat{\mathbf{R}} + \frac{\partial V}{\partial Z}\hat{\mathbf{Z}} \right\} \tag{3.15}$$

This was expressed in a finite difference form by applying the method used by Farnell, Williams and Wilbur. [29] In this a four point central difference is taken to express the partial differentials.

$$E_R = -\left\{ \frac{-V_{i+2} + 8V_{i+1} - 8V_{i-1} + V_{i-2}}{12\Delta R} \right\} \tag{3.16}$$

$$E_Z = -\left\{ \frac{-V_{j+2} + 8V_{j+1} - 8V_{j-1} + V_{j-2}}{12\Delta Z} \right\} \tag{3.17}$$

The values near the centerline were calculated assuming the potential at i = -1 were the same as at i = 1, and i = -2 was the same as i = 2. For the i = 99 edge it was assumed the fields were continuous and the values of *V* at those points simply repeated the boundary value. Once all of the points in the computational space were evaluated to determine the electric field components, the **R** components and **Z** components were stored in arrays for use in calculating the particle trajectories and output to separate text files. An example of the vector field resulting from the previous potential is shown in Figure 3.5.

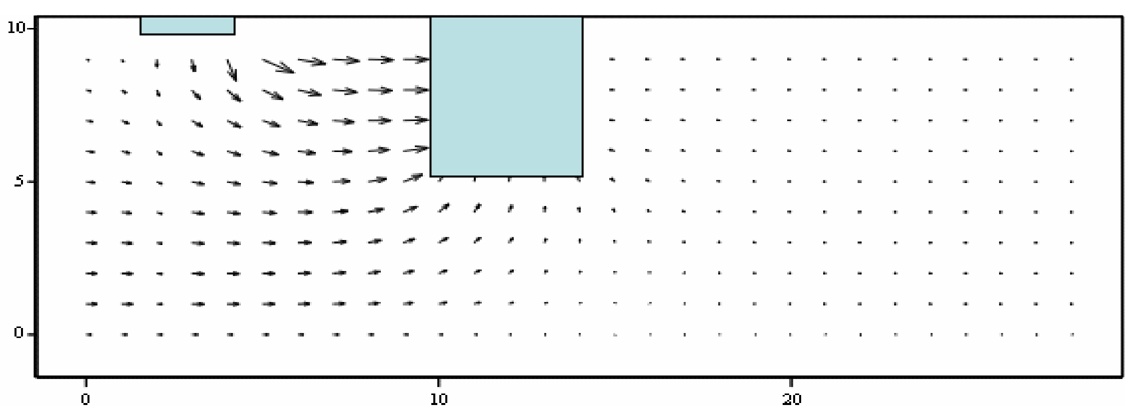

Figure 3.5: Calculated Electric Field with No Decel Grid and No Ion Beam

Figure 3.5 plots the field vectors at every tenth grid point. Since Figure 3.5 scales the magnitude of each vector based on the magnitude of the longest vector it may be difficult to visualize the field. Figure 3.6 displays the field direction throughout the computational space with all field vectors treated as unit vectors. From this plot the sense of the field throughout the grid system is clear.

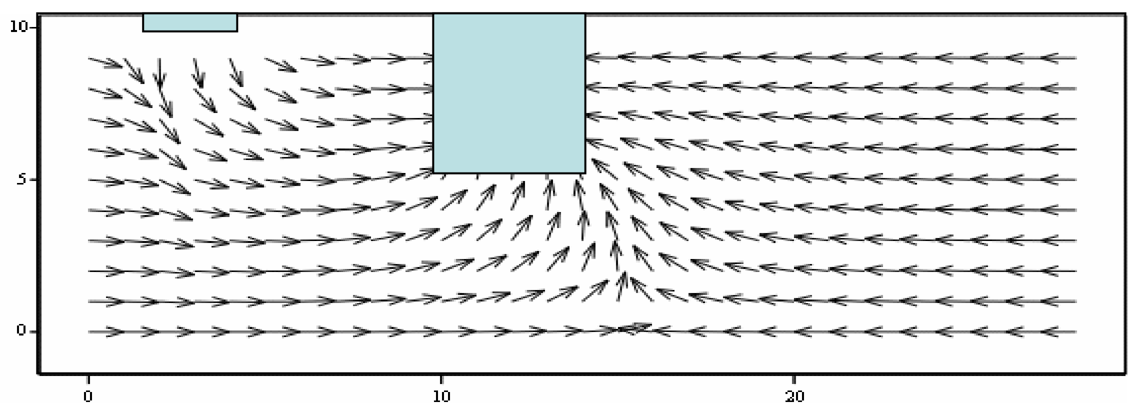

Figure 3.6: Direction of Electric Field with No Decel Grid and No Ion Beam

3.3.3 Calculation of the Magnetic Field

The magnetic field due to embedded current loops was approximated as the field resulting from a continuous loop of wire with a radius equal to that of the individual thruster grid aperture plus one half of a computational grid step in **R** and located in **Z** at the forward surface of each thruster grid. The magnetic field due to the beam current was neglected as it is negligible. The calculation of the magnetic field at any point in three dimensions is fairly complex and involves the use of elliptic integrals. Since there is no **θ** component of the field the **R** and **Z** components can be calculated for each point in the computational grid and used throughout the model. The individual **R** and **Z** components of the magnetic field are expressed by the equations: [34]

$$B_R = \frac{\mu I}{2\pi}\left\{\frac{Z}{R\sqrt{(a+R)^2+Z^2}}\right\}\left\{-K+\left(\frac{a^2+R^2+Z^2}{(a-R)^2+Z^2}\right)E\right\} \tag{3.18}$$

$$B_Z = \frac{\mu I}{2\pi}\left\{\frac{1}{\sqrt{(a+R)^2+Z^2}}\right\}\left\{K+\left(\frac{a^2-R^2-Z^2}{(a-R)^2+Z^2}\right)E\right\} \tag{3.19}$$

In these equations a is the radius of the current loop, I is the current in each loop, K is a complete elliptic integral of the first kind and E is a complete elliptic integral of the second kind. The object of these complete elliptic integrals, k, is determined from:

$$k = \sqrt{\frac{4aR}{(a+R)^2+Z^2}} \tag{3.20}$$

To determine values of the complete elliptic integrals at each grid point a look-up table/interpolation method was used. Values for K and E were stored in a look up table and a second order polynomial interpolation used for estimating the value at every instance of k.

Having determined the values of K and E at each point the value of the components of **B** at each point is made simply by inserting the values of R and Z for each grid point relative to each of the current loops. The values of the components of **B** were determined for each loop then summed throughout the computational space. These values were then stored in arrays for later use in determining the particle trajectories and output to separate text files. An example of a calculated magnetic field is displayed in Figure

3.7. Figure 3.7 displays the field vector at every fifth grid point and scales the magnitude of each vector based on the magnitude of the longest vector making it difficult to

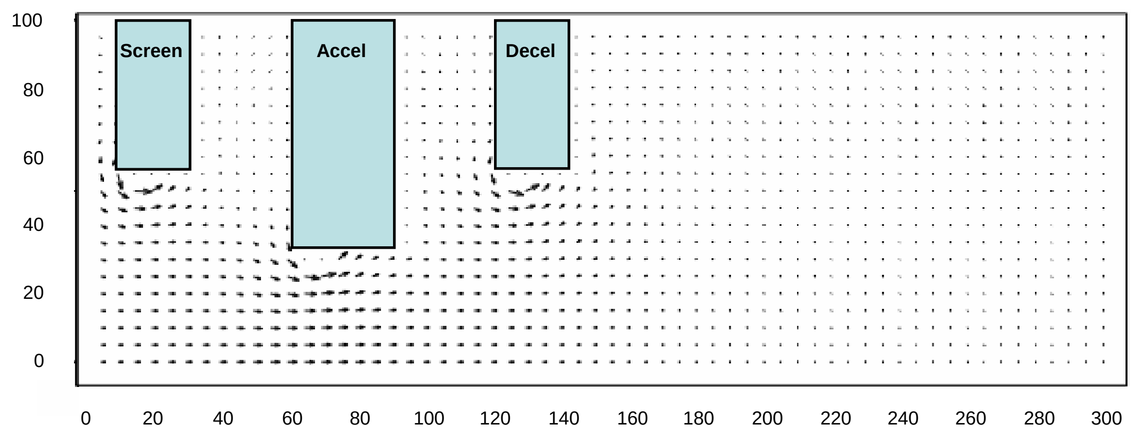

Figure 3.7: Net Magnetic Field Due to Current Loops Located at the Leading Edge of Each Grid

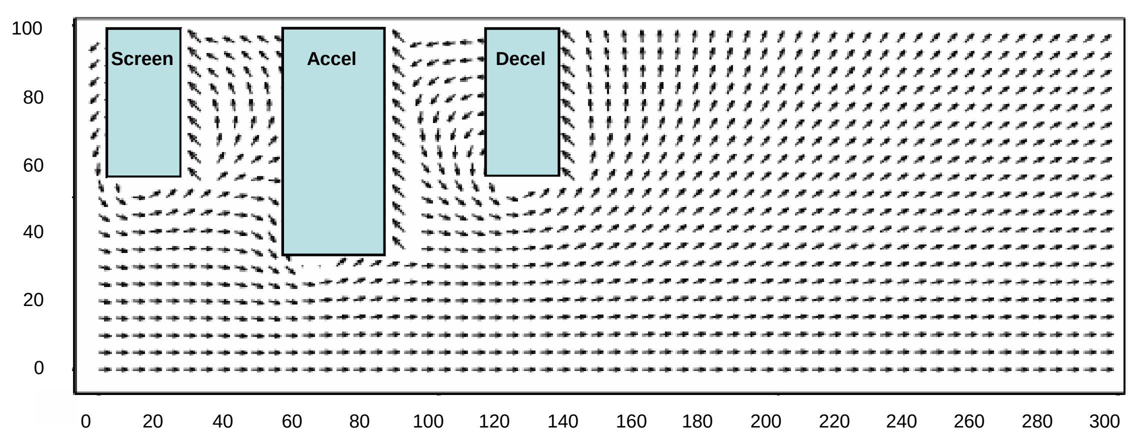

Figure 3.8: Magnetic Field Direction Due to Current Loops Located at the Leading Edge of Each Grid

visualize the field. Figure 3.8 displays the field direction throughout the computational space with all field vectors treated as unit vectors.

Since there is a singularity in complete elliptic integrals of the first type it was necessary to discard field values at **R** equals 0 and **R** equals *a*. For R equals 0 the field is entirely in the Z direction and is calculated using the field at any point on the axis of a circular current loop [15]:

$$B_Z = \frac{\mu I}{2} \frac{a^2}{\left(a^2 + z^2\right)^{3/2}} \tag{3.21}$$

Using a value of *a* greater than the aperture radius eliminates the need to find a field value at *a*. comparing the values for the field direction and magnitude between the i = 0 and i = 1 points also provides a check on the computational method. In the case shown in the figures the value of **B** at i = 0, j = 10 (location of the leading surface of the screen) was determined from the equation above to be 1.307×10^{-3} T and the value of B calculated by the program at i = 1, j = 10 is 1.307011×10^{-3} T confirming the accuracy of the solution using the equations of reference 21.

3.3.4 Calculation of the Particle Trajectories

Calculation of the particle trajectories is done assuming the only force a particle experiences is the Lorentz force. Fundamentally Newton's second law is applied repeatedly until the calculated particle trajectory caries it out of the computational domain, or into a thruster grid. When a particle enters a new cell, a new "floating cell" is created around the actual cell. The floating cell is a Cartesian (**X**-**Y**-**Z**) coordinate system. **Z** for both systems will have the same orientation. The **X**-**Y** plane will be coplanar with the **R**-**θ** plane. The floating cell is created so that all forces and fields within the computational cell can be expressed in orthogonal coordinates, greatly simplifying the calculation of the trajectory. Figure 3.9 shows an example case. When there is no magnetic field and no initial **θ** velocity the particle trajectory will always remain in the **X**-**Z** plane (same as the **R**-**Z** plane). If there is a magnetic field or an initial **θ** velocity the trajectory will have a component outside the **X**-**Z** plane.

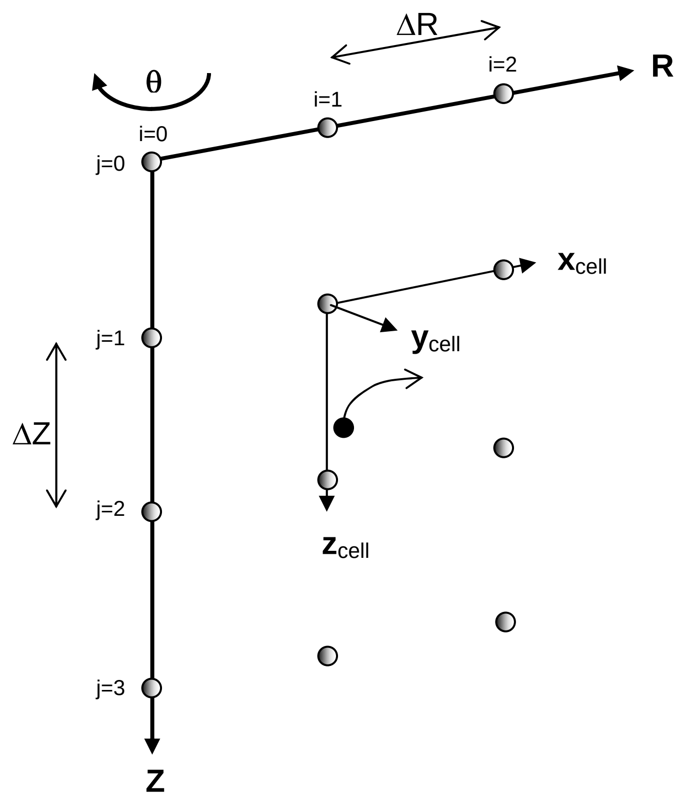

Figure 3.9: Computation Space, Floating Cell, and Example Particle Trajectory

When a particle enters a new cell its position is translated into cell coordinates. This is the Cartesian distance from the cell identification node. This is accomplished with no loss of accuracy because it is a simple subtraction exercise. The cell coordinates are established as:

$$x_{cell} = R_p - i\Delta R \tag{3.22}$$

$$z_{cell} = Z_p - j\Delta Z \tag{3.23}$$

where R_p and Z_p are the particle coordinates in **R** and **Z**. The y cell coordinate is retained from the previous cell since it used to track θ.

The equation of motion for determining the new position of a particle is:

$$x_1 = x_0 + v_x\Delta t + \frac{1}{2}a_x\Delta t^2 \tag{3.24}$$

Where x_0 and x_1 represent the initial and final positions in any dimension of the particle, v is the velocity in that dimension of the particle at the start of the time interval, and a is the acceleration in that dimension at the start of the time interval. Using the floating cell coordinate system gives three equations, one for the position in **X**, one for the position in **Y**, and one for the position in **Z**. The great simplification of using the floating cell coordinates is that these three equations are completely decoupled from each other. The acceleration comes from Newton's second law. Initially the only force considered to be acting on the particle was the Lorentz force.

$$\mathbf{F} = m\mathbf{a} \tag{3.25}$$

$$\mathbf{F} = q[\mathbf{E} + (\mathbf{v} \times \mathbf{B})] \tag{3.26}$$

$$\mathbf{a} = \frac{q[\mathbf{E} + (\mathbf{v} \times \mathbf{B})]}{m} \tag{3.27}$$

In these equations q is the charge on a single particle, and m is the mass of the particle. Particles can have any mass and ionization but were generally assumed to have a single ionization charge state and the mass was taken to be the mass of a single xenon ion. The calculated value of a is used to find an initial new value of velocity from the equation:

$$v_1 = v_0 + a\Delta t \tag{3.28}$$

Examining just the **X** component, the equation of motion is expressed as:

$$x_1 = x_0 + v_0\Delta t + \frac{1}{2}\left\{\frac{q[E_x + (\mathbf{v} \times \mathbf{B})_x]}{m}\right\}\Delta t^2 \tag{3.29}$$

In this expression $(\mathbf{v} \times \mathbf{B})_x$ represents the X component of the indicated cross product. This equation is solved for each of the three components of the change in position, then the previous equation is used to solve for the velocity vector used for the next interval. These equations of motion do not impose conservation of energy in the electrostatic environment seen in the model; therefore, it is necessary to adjust the particle acceleration and thereby its velocity vector as it traverses the computational space. The particle's energy as it moves through the system must remain a constant sum of its kinetic and potential energies. The potential energy comes from the electrostatic potential of the field. The kinetic energy comes from the velocity of the particle at any point. [29] The equation for the total particle energy is simply:

$$\mathsf{E} = \frac{1}{2}mv^2 + qV \tag{3.30}$$

After a new position is calculated based on the previous velocity vector, the new velocity vector is calculated. The magnitude of the velocity vector is adjusted to maintain the energy as a constant. Each of the components of the velocity vector are then scaled to match the relative proportions calculated from the equations of motion. Once that is done a revised acceleration is calculated from the new velocity, the previous velocity, and the time step for the calculation.

$$a_x' = {(v_1 - v_0)}/{\Delta t} \tag{3.31}$$

It is this a' acceleration that is used along with the previous velocity, the previous position, and the time step to determine the new position.

The initial energy for each particle is determined by its initial position within the potential field and its initial velocity. Each of the test particles is considered to start as a neutral atom moving at its thermal velocity. [31]

$$v_{th} = \left(\frac{2kT}{m} \right)^{1/2} \tag{3.32}$$

The initial temperature and direction of the thermal velocity are controllable parameters within the program. The temperature is nominally set to the temperature within a typical discharge chamber or around 500K. The initial direction is controlled using a direction unit vector.

Within each cell the value of the acceleration is determined from the electric and magnetic fields and the current velocity vector. The fields were calculated as described above and are expressed in cylindrical coordinates for each node which defines the limits of each cell. At each point within the cell the value of the field is interpolated from the position within the cell relative to each node. The method used is similar to that used by Farnell, though simplified by the fact that all field components are in the **R**-**Z** plane. The technique therefore becomes one of area weighting. The contribution of the field from each node of the cell is area weighted based on the area of the cell between the particle and the cell node opposite of the node in question. Figure 3.10 shows an example case. In the figure each node has been numbered 0 through 3. The particle is indicated as a solid

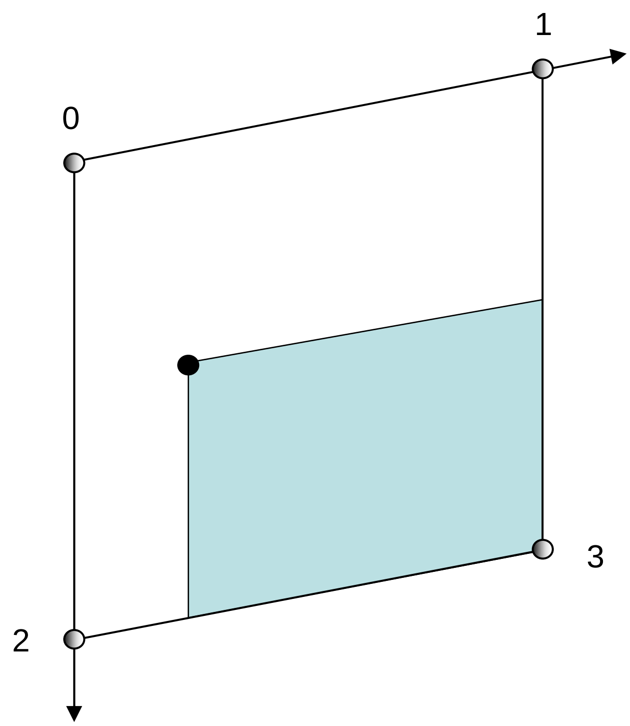

Figure 3.10: Area Weighting of Field Contributions From Each Node

black circle within the cell. The contribution of the field at node 0 is based on the area element indicated between the particle and node 3, the node opposite node 0, divided by the area of the region enclosed by the four nodes. This process is repeated for each node, and the area weighted field contributions are then summed to determine the field at the particle's location. The Area of the region between the particle and node 3 is simply:

$$Area_3 = (R_3 - R_p)(Z_3 - Z_p) \tag{3.33}$$

Where $Area_3$ is the Area element between the particle and node 3, R_p is the radius of the particle, R_3 is the radius at node 3, Z_3 is the Z location of node 3, and Z_p is the Z location of the particle. The area of the entire cell is:

$$Area_{CELL} = \Delta R \Delta Z \tag{3.34}$$

So the contribution of the field from node 0 is:

$$\mathbf{E}_0^p = \frac{Area_3}{Area_{CELL}} \mathbf{E}_0 \tag{3.35}$$

The expression to the left of the equal sign represents the contribution at the particle location due to the field at node 0. There are four of these weighted field contributions that are summed to determine the field at the particle's location.

As the particle traverses the computational space its velocity increases or decreases depending on its position within the potential field. In order to maintain the resolution of the trajectory the time-step used is adjusted each time the particle transitions from one cell to the next. The adjustment is based on the velocity vector of the particle upon entry to the cell. The program calculates the distance the particle would travel within the cell given the magnitude and direction of its initial velocity vector and determines the time of flight within the cell. It then divides that time by a constant and sets that value as the time-step used for all calculations within that cell.

At each computational step the particles position and velocity are captured and recorded to a file. If the particle trajectory intersects one of the thruster grids, the component of its velocity normal to the grid surface at the point of contact is determined. This normal velocity component is then used to calculate the kinetic energy of the impact. The program will then update a running total of the energy transferred to the thruster grids. Once the particle meets one of the exit conditions and, if necessary the grid impact parameters are determined, the program moves on to start calculating the behavior of the next particle.

3.3.5 Overall Model Function

The program begins by entering all of the input parameters which define the grid geometry, the initial particle characteristics, and auxiliary fields. This data is read from an input file that can be edited in any text editor to modify the model characteristics. It then generates the voltage profile for the entire calculation space. From this it then generates the electric field vectors at each node location. Next the program generates the magnetic field vectors at each node location. On some runs these vectors may all be zero if there is no auxiliary magnetic field present. All of these are preformed before the program starts to iterate through individual particles.

To calculate particle trajectories the program generates a charge exchange ion within a cell. Typically the program will start at $i = 0$, $j = 0$, and cycle through in a given step size through to a maximum particle at $i = 98$, $j = 298$. The increment between particles can be as low as one, however, a run which includes all node ids will require several hours to complete if all output files are being generated. If the test particle initial location is within a grid that particle is skipped and the program moves to the next particle in the sequence. The typical starting location is within the cell identified by the i and j cell id at an **R**-**Z** coordinate of $R = (i + 0.5)\Delta R$, $Z = (j + 0.5)\,\Delta Z$. The program determines the particles initial energy from its thermal velocity and the value of the potential at the particles initial position, as determined from the area weighting method described earlier. The particles position is then converted to "cell coordinates" by the formula:

$$
\begin{aligned}
x_{cell} &= R_{particle} - i_{cell} \times \Delta R \\
y_{cell} &= 0 \\
z_{cell} &= Z_{particle} - j_{cell} \times \Delta Z
\end{aligned}
\tag{3.36}
$$

The value of the field vectors, both E and B are determined at the current location and from this an initial value for the acceleration. That acceleration is used with the initial time increment, 1×10^{-9} seconds, to determine an initial velocity. This initial velocity is run through a section of code which evaluates it in light of the energy conservation requirement and adjusts the velocity magnitude to keep particle energy constant. This adjusted velocity is then used to determine an actual acceleration. It is important to note here that for the initial step for all particles the initial acceleration will always be zero as the particle is at the point at which its initial energy was determined. The initial first motion will therefore always be controlled only by the initial thermal velocity. Once the acceleration and new velocity are determined the particles position and the end of the time increment are determined using the new acceleration and the previous velocity. The new position is then tested to determine if it is still within the same cell. If it is the new velocity and new position are used to update the total R, Z and θ coordinates of the particle, with the θ being set to:

$$
\theta_1 = \theta_0 + \sin^{-1}\left(\frac{y_{cell}}{R_{0-particle}}\right) \tag{3.37}
$$

where y_{cell} is the particles new position in y. The new position and acceleration are then used to determine the position at the end of the next time increment. This process repeats until the new position is determined to be outside of current cell. The new position and acceleration are then recalculated using a smaller time step which is determined to be just long enough to put the new position just inside the boundary of the next cell. The new cell number is then checked to determine if it meets one of the exit criteria. If it does not the process repeats. If the new X position is less than zero the X position is set equal to –X and the X component of the new velocity vector, v_x, is set to $-v_x$. This has the effect of "reflecting" the particle back into the computation space.

At each step the particle's position is written to an output file which records the motion of each particle. Up to 75 particles have individual output files, one for the R position and one for the Z. These files are then available to use to plot the trajectories of multiple particles for an individual run. The particle velocities are also available in a single file. A main output file tracks the outcome for each particle indicating its final exit result and velocity. Finally there is a run summary file which indicates some of the entry parameters and the final tallies of how many particles were generated, how many impacted each grid, the cumulative kinetic energy transferred to each grid and the total transferred to all grids. This run summary file can be appended to each time thereby creating a single record of multiple runs. At the conclusion of the program the individual particle files are merged into a single flat file that can be imported into any plotting software to generate a multiple trajectory plot for the run. Generation of each of these files with the exception of the run summary is a controllable parameter and disabling their use shortens the computation time.

3.3.6 Program Data Input

Controlling the parameters of the model is accomplished by changing the input data in the inputData.txt file. This is a simple text file which is read at the beginning of program execution. This file contains two columns, the first a brief alphanumeric identifier indicating the data point on that line, the second column is the actual data. The data in the data column is a combination of integer and float data types. The configuration of the data file is fixed, the identifiers are treated as a character array of width 8 and the data is one tab from the identifier. The order of the data can not be changed. The program reads each item sequentially and does not parse it. If items are out of order they will not be interpreted correctly giving inaccurate results or a run-time error.

The data input file is 42 lines long. A sample of the inputData.txt file is shown in Table 3.1. The first two columns are what would be contained in the file, the third column is a description of the item. Line 1 contains the Radius of the calculation space. This determines the size of each grid cell. Lines 2 to 4 contain the radius of the three grids in integer grid nodes. Lines 5 to 7 contain the axial location of the leading surface of each grid in integer grid nodes. Lines 8 to 10 give the thickness of each grid in integer grid nodes. Lines 11 to 15 contain the fixed voltages as floating point data. Line 11 is the plasma potential, line 12 is the screen grid potential, line 13 is the accel grid potential, line 14 is the decel grid potential, and line 15 is the potential at the neutralization plane.

Radius	1.17e-3	Radius of calculation space
Rsc	94	Radius of the Screen Grid aperture in whole grid nodes
Rac	55	Radius of the Accel Grid aperture in whole grid nodes
Rdc	99	Radius of the Decel Grid aperture in whole grid nodes
Zsc	30	Axial location of the Screen Grid forward surface in whole grid nodes
Zac	109	Axial location of the Accel Grid forward surface in whole grid nodes
Zdc	299	Axial location of the Decel Grid forward surface in whole grid nodes
Tsc	25	Thickness of the Screen Grid aperture in whole grid nodes
Tac	42	Thickness of the Accel Grid aperture in whole grid nodes
Tdc	0	Thickness of the Decel Grid aperture in whole grid nodes
Vplasma	1030	Plasma Potential
Vsc	1000.01	Screen Grid Potential
Vac	-500.01	Accel Grid Potential
Vdc	0	Decel Grid Potential
Vnetral	0	Neutralization Plane Potential
Isc	0	Screen Grid Loop Current
Iac	0	Accel Grid Loop Current
Idc	0	Decel Grid Loop Current
i_start	5	Radial (i) index of first test particle cell
i_inter	20	Radial (i) interval for the run
i_stop	99	Radial (i) index of last test particle cell
j_start	30	Axial (j) index of first test particle cell
j_inter	20	Axial (j) interval for the run
j_stop	299	Axial (j) index of last test particle cell
Temp	500	Neutral Particle Temperature (usually discharge chamber temp.)
Uinit_r	1	R component of the initial thermal velocity of all test particles
Uinit_z	0	Z component of the initial thermal velocity of all test particles
Uinit_t	0	θ component of the initial thermal velocity of all test particles
mainF	1	Write the MainOutput.txt file (1 = Yes, 0 = No)
runNumF	1	Write the runNum.txt file (1 = Yes, 0 = No)
velF	0	Write the RTZvelocity.txt file (1 = Yes, 0 = No)
runSumF	1	Write the RunSummary.txt file (1 = Yes, 0 = No)
RposF	0	Write the Rposition.txt file (1 = Yes, 0 = No)
ZposF	0	Write the Zposition.txt file (1 = Yes, 0 = No)
TposF	0	Write the Tposition.txt file (1 = Yes, 0 = No)
RZTposF	0	Write the RZTposition.txt file (1 = Yes, 0 = No)
diagF	0	Write the diagnosticFile.txt file (1 = Yes, 0 = No)
numPosF	1	Write the numbered particle position files (1 = Yes, 0 = No)
shthOn	0	Include plasma sheath (1 = Yes, 0 = No)
beamOn	0	Include Ion Beam (1 = Yes, 0 = No)
shthTh	20	Sheath Thickness in grid points
charge	1	Particle charge state, 1 for singly charged ions, -1 for electrons
massNumber	131.0	Atomic number of the particle

Table 3.1: "inputData.txt" File Contents and Description

Lines 16 to 18 contain the grid loop currents as float data. Lines 19 to 24 contain the run iteration parameters as integers. These six integers define the cell id for the first particle in the run, the radial and axial step size between test particles, and the cell id for the last test particle. If the start and end IDs for the radial iteration are both set to “0” the program will iterate only within the simulated ion beam. The iteration will start at i = 0 and go to the edge of the beam in steps equal to the input step size. Line 25 is the neutral particle temperature in degrees K. Lines 26 to 28 store an integer representation of the initial particle velocity unit vector. Line 26 is the **R** component, line 27 is the **Z** component, and line 28 is the **θ** component. These parameters are all integers indicating the relative magnitudes of the individual components and may be positive or negative. This will later be converted to a unit vector. Lines 29 to 38 are integers, either 0 or 1 controlling the output file write process. Each line represents a different output file. If that particular output file is desired, the parameter is set to 1, otherwise it should be 0. Line 39 is an integer indicating that the plasma sheath should be included in the model. Setting this to 1 will cause the charge density model to start at the distance defined by the sheath thickness ahead of the screen grid. Setting this to 0, if the ion beam is to be modeled, will extend the charge density calculation all the way to the beginning of the computational space. Line 40 is an integer indicating that the ion beam model should be included in the run. Line 41 is an integer indicating the distance ahead of the screen grid where the plasma sheath is located. Line 42 is an integer indicating the charge state of the particle. Setting this to “1” indicates the particle is a singly charged ion while setting it to

“2” indicates a doubly charged ion. Line 42 is a double precision number indicating the Atomic mass number. Usually this is set to 131.0 for xenon.

3.3.7 Program Output

All of the calculated program variables are passed to a separate header file that generates output files that are user configurable to provide flexibility based on the nature of the investigation being undertaken. By incorporating all of the possible output parameters and output handling utilities in a header file it is possible to make significant modifications to the output format without touching the computational portion of the code.

As currently coded there are a number of output file formats that are available. The selection of which of these files are actually generated is made by modification of the inputData.txt file. The following is a list of all the parameters generated by the program that are available for output: particle position in XYZ throughout the run, particle position in RθZ throughout the run, particle velocity in XYZ throughout the run, particle impact location (grid, grid surface), particle impact velocity, particle impact energy (KE transferred to grid), total kinetic energy imparted to each grid surface, total number of particles impacting the grids, total number of particles in each particle exit category.

3.4 Example Results

This section presents a few examples of the results obtainable with this program. First, four cases are demonstrated, two with a decelerator and two without. In each of these cases one run includes the simulated ion beam and one does not. In each case a plot of the potential field and the trajectories for up to 75 particles are shown. In addition to these the run summary file indicating the particle outcomes and the main output file is shown. In each case test particles were generated at every 20th cell index from i = 0 to i = 98 and j = 0 to j = 298.

3.4.1 Example Case 1: No Decel, No Beam

The first example run includes a screen grid and accel grid but no decel grid. The screen grid is located at j = 30, has a thickness of 22 grid nodes and an aperture radius of 55 grid nodes. Given a ΔR and ΔZ of 1.17×10^{-5} meters this gives an actual grid thickness of 2.574×10^{-4} meters and an aperture radius of 6.435×10^{-4} meters. The accel grid is located at j = 92, has a thickness of 30 grid nodes and an aperture radius of 33 grid nodes. This gives a grid separation of 4.68×10^{-4} meters, an accel grid thickness of 3.51×10^{-4} meters and an aperture radius of 3.861×10^{-4} meters. The screen voltage was set to 1000 volts, the accel voltage was set to -500 volts, the plasma voltage was set to 1030 volts, and the voltage at the neutralization plane was set to zero. Figure 3.11 shows the resulting voltage profile.

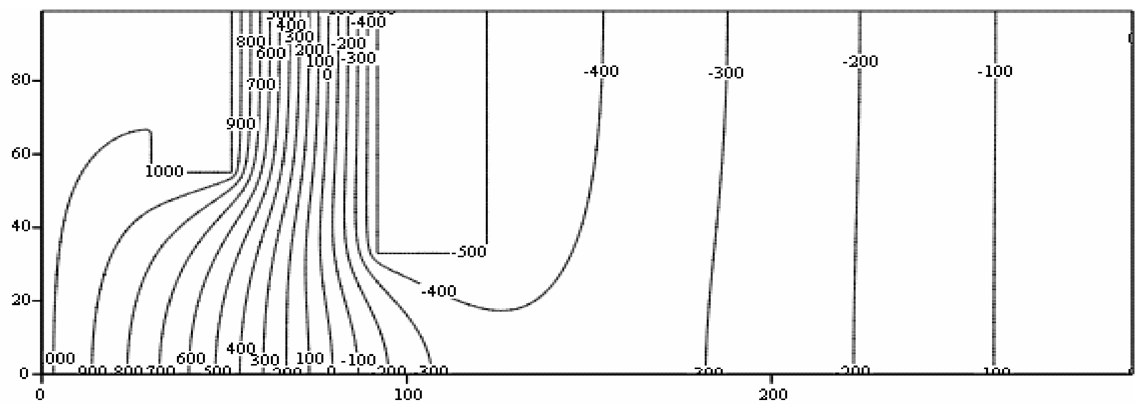

Figure 3.11: Example Case 1 Voltage Profile: No Decel Grid, No Ion Beam

The run resulted in the generation of 70 test particles, the trajectories of which are shown in Figure 3.12.

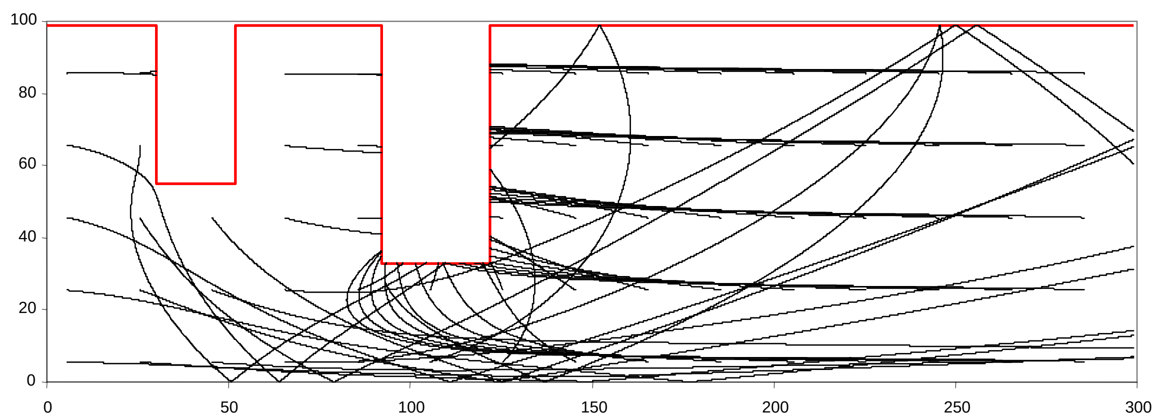

Figure 3.12: Example Case 1 Particle Trajectories

For this case the main output showing the final result for each particle is shown below.

Example Case 1 Main Output File

```
START OF PROGRAM
Particle 5,5 Final velocity Magnitude = 37531.2     Particle has exited the
neutralization plane
Particle 25,5 Final velocity Magnitude = 37705.3    Particle has exited the
neutralization plane
Particle 45,5 Final velocity Magnitude = 38051.4    Particle has exited the
neutralization plane
Particle 65,5 Final velocity Magnitude = 46759.8    Particle has exited by impacting the
accel grid in the hole Kinetic Energy imparted to Accel grid = 8.40903e-017 kg-m2/s2
Joules
Particle 85,5 Final velocity Magnitude = 5855.28    Particle has exited by impacting the
screen grid forward surface   Kinetic Energy imparted to Screen grid = 3.72163e-018 kg-
m2/s2 Joules
Particle 5,25 Final velocity Magnitude = 33486      Particle has exited the
neutralization plane
Particle 25,25 Final velocity Magnitude = 34379     Particle has exited the
neutralization plane
Particle 45,25 Final velocity Magnitude = 36464.1   Particle has exited the
neutralization plane
Particle 65,25 Final velocity Magnitude = 46439.1   Particle has exited by impacting the
accel grid in the hole Kinetic Energy imparted to Accel grid = 6.33229e-017 kg-m2/s2
neutralization plane
                      •                                            •
                      •                                            •
                      •                                            •
                      •                                            •
                      •                                            •

Particle 65,265 Final velocity Magnitude = 24313.6  Particle has exited by impacting the
accel grid aft surface Kinetic Energy imparted to Accel grid = 6.42339e-017 kg-m2/s2
Joules
Particle 85,265 Final velocity Magnitude = 24307.3  Particle has exited by impacting the
accel grid aft surface Kinetic Energy imparted to Accel grid = 6.42649e-017 kg-m2/s2
Joules
Particle 5,285 Final velocity Magnitude = 25775.4   Particle has exited by impacting the
accel grid forward surface    Kinetic Energy imparted to Accel grid = 4.51144e-017 kg-
m2/s2 Joules
Particle 25,285 Final velocity Magnitude = 25843.5  Particle has exited by impacting the
accel grid in the hole Kinetic Energy imparted to Accel grid = 4.58406e-018 kg-m2/s2
Joules
Particle 45,285 Final velocity Magnitude = 25838    Particle has exited by impacting the
accel grid aft surface Kinetic Energy imparted to Accel grid = 7.24199e-017 kg-m2/s2
Joules
Particle 65,285 Final velocity Magnitude = 25836.2  Particle has exited by impacting the
accel grid aft surface Kinetic Energy imparted to Accel grid = 7.25552e-017 kg-m2/s2
Joules
Particle 85,285 Final velocity Magnitude = 25834.4  Particle has exited by impacting the
accel grid aft surface Kinetic Energy imparted to Accel grid = 7.2598e-017 kg-m2/s2 Joules
```

This documents the outcome for each test particle. For the remaining Example cases only the run summary file will shown. The run summary file provides a concise overview of the outcome of the run. For Example Case 1 the run summary file is shown below.

Example Case 1 Run Summary File

```
Run Number 0 Cumulative Results
______________________________________________


Screen Grid: Aperture Radius = 0.6435 mm     Grid Thickness = 0.2574mm
Accel Grid: Aperture Radius = 0.3861 mm      Grid Thickness = 0.351mm
Screen Grid - Accel Grid separation = 0.468 mm

Plasma Potential = 29.99 Volts
Grid Potentials: Vsc = 1000.01 Volts  Vac = -500.01 Volts   Vdc = 0 Volts
Grid Loop Currents: Isc = 0   Iac = 0 Idc = 0

Total number of particles generated = 70
Particle runs with errors =   1
Particles that exceeded the maximum number of steps (4250Z) =      1
Particles re-entering the discharge chamber =       0
Particles exiting at the neutralization plane =     11
Particles impacting the screen grid = 2
       2      on the forward surface 0      on the aft surface    0      in the
aperture
Particles impacting the accel grid =  56
       9      on the forward surface 35     on the aft surface    12     in the
aperture
Particles impacting the decel grid =  0
       0      on the forward surface 0      on the aft surface    0      in the
aperture

Total Kinetic Energy Imparted to all Grids = 2.19257e-015
Total Kinetic Energy Imparted to Screen Grid =      4.33378e-018
Total Kinetic Energy Imparted to Accel Grid =       2.18824e-015
Total Kinetic Energy Imparted to Decel Grid =       0

Total execution time is 585 seconds
```

3.4.2 Example Case 2: No Decel, Ion Beam Simulated

The second example run maintains the same physical grid parameters and voltages as the first. In this run however the ion beam is included. Figure 3.13 shows the resulting voltage profile.

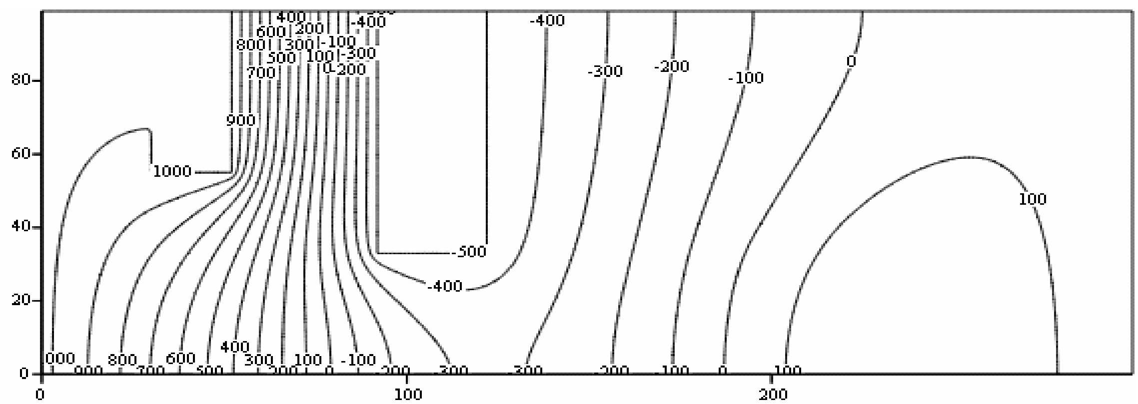

Figure 3.13: Example Case 2 Voltage Profile: No Decel Grid, Ion Beam Present

The run resulted in the generation of 70 test particles, the trajectories of which are shown in Figure 3.14.

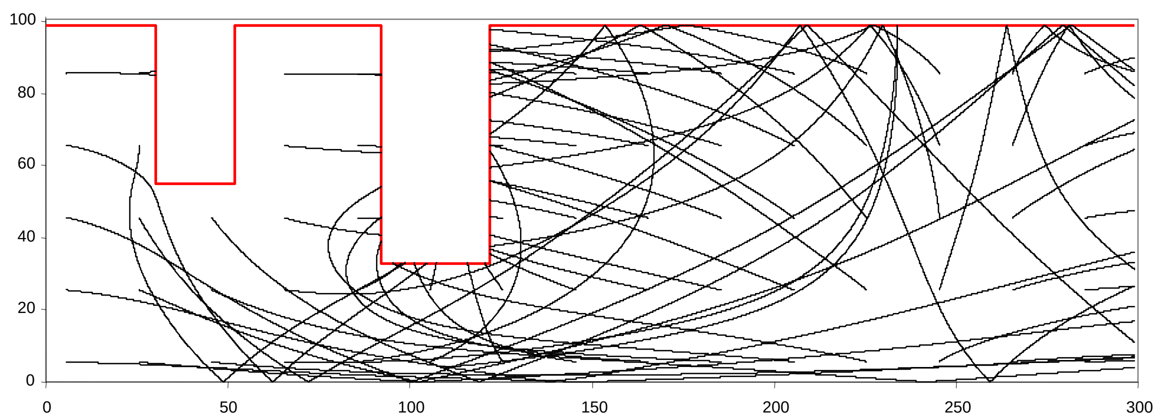

Figure 3.14: Example Case 2 Particle Trajectories

For Example Case 2 the run summary file is shown below.

```
Run Number 0 Cumulative Results
______________________________________________

Screen Grid: Aperture Radius = 0.6435 mm     Grid Thickness = 0.2574mm
Accel Grid: Aperture Radius = 0.3861 mm      Grid Thickness = 0.351mm
Screen Grid - Accel Grid separation = 0.468 mm

Plasma Potential = 29.99 Volts
Grid Potentials: Vsc = 1000.01 Volts  Vac = -500.01 Volts   Vdc = 0 Volts
Grid Loop Currents: Isc = 0   Iac = 0 Idc = 0

Total number of particles generated = 70
Particle runs with errors =   1
Particles that exceeded the maximum number of steps (4250Z) =      1
Particles re-entering the discharge chamber =       0
Particles exiting at the neutralization plane =     22
Particles impacting the screen grid = 2
       2      on the forward surface 0      on the aft surface    0      in the
aperture
Particles impacting the accel grid =  45
       9      on the forward surface 28     on the aft surface    8      in the
aperture
Particles impacting the decel grid =  0
       0      on the forward surface 0      on the aft surface    0      in the
aperture

Total Kinetic Energy Imparted to all Grids = 2.43628e-015
Total Kinetic Energy Imparted to Screen Grid =      4.32861e-018
Total Kinetic Energy Imparted to Accel Grid =       2.43195e-015
Total Kinetic Energy Imparted to Decel Grid =       0

Total execution time is 555 seconds
```

3.5 Model Validation

Thorough validation of the ionLite program was essential to ensure the accuracy of predictions for charge exchange ion behavior. While many ion thruster simulation codes can be and are verified by comparing their total output against experimental data this is not possible for the ionLite code. Since the ionLite code generates individual test particles at specific locations within an ion thruster simulation and examines their unique behavior, comparison to experiment is meaningless. Additionally, since ionLite does not attempt to model the creation of all charge exchange particles or the location of their creation, the results can not be made to correlate directly to experimental charge exchange erosion rates. What ionLite does do is provide a reasonable estimate of the trend in charge exchange induced grid erosion due to varying thruster parameters such as grid spacing, or internal magnetic field.

To validate the accuracy of the program it is therefore necessary to confirm that individual charged particles behave under very specific inputs as predicted by basic particle physics. This required setting up tests of individual particles so that equations of motion have closed form solutions, and then comparing the results from the closed form equations to the output of the program. There are three principle cases for which closed form equations of motion exist to compare against the results of the program. These three cases are: Straight line motion with change of velocity due to a given voltage drop with no magnetic field, Rotational motion of a given radius due to particle velocity perpendicular to a constant magnetic field (Larmor radius), and cycloid motion in the presence of constant uniform orthogonal electric and magnetic fields.

3.5.1 Overview of Model Validation Process

Validation of the ionLite program can be viewed as having been accomplished in three phases. The first phase was validation of the output of individual component functions of the program. The second phase, which is the principle subject of this section, was the analysis of individual particle motion under specific fixed conditions that provide for closed form solutions for comparison. The third phase was discussed in Section 3.3 and is the comparison of high level results for field composition and Isp with published experimental and sophisticated simulation data.

Most components of the ionLite program can be and were validated under limited conditions during their development. For example the function which generates the voltage profile resulting from the grid potentials was run separate from the rest of the program and its output compared to the voltage profiles documented in published papers. The validation of the linear motion of individual particles within a cell required multiple components of the program, but was accomplished during development by imposing a uniform electric field as an input condition. The resulting data was then compared against calculated results generated using the fundamental equations and rigid time increments. Evaluation of particle motion that involves transit of multiple cells within the model requires all of the program components and is fairly complex.

To test the accuracy of program simulation of particle motion three cases were set up. The first involves the straight forward linear acceleration and motion of a charged particle passing through a change in potential, or voltage drop. This motion is controlled by the conservation of energy equation:

$$\mathrm{E} = \frac{1}{2} m v^2 + qV \tag{3.38}$$

were E is the energy of the particle and is constant. For a given initial velocity and voltage drop the resulting closed for solution for the change in velocity is:

$$v_2 = \left[\frac{2q}{m} \left(V_1 - V_2 \right) + {v_1}^2 \right]^{1/2} \tag{3.39}$$

Validation of the performance of the model using this equation required setting up the input file such that the screen, accel, and decel grids had aperture radii of zero and a potential of zero at an axial location of zero, one, and two, grid cells. The neutralization potential was set to the desired change in potential (always negative for positive test particles) and the initial particle position was set to i = 0, j = 2, or just at the edge of the decel grid.

The second validation case involved an examination of the behavior of a charged particle with an initial velocity perpendicular to a constant magnetic field. As described in Chapter 2 this results in a circular orbit of fixed radius defined by the equation for the Larmor radius:

$$r_L = \frac{mv_\perp}{|q|B} \tag{3.40}$$

where r_L is the Larmor radius, m is the particle mass, $v_\perp$ is the velocity component perpendicular to the magnetic field, q is the charge, and B is the magnetic field strength. Two variations were examined. The first being movement in the R-θ (or X-Y) plane. This required hard-coding a fixed magnetic field with only Z component of various strengths into the code with the input file set for 0 potential on all grids and plasma and neutralization planes. The second variation examined motion in the R-Z (or X-Z) plane, requiring hard-coding a fixed magnetic field, with only a Y component, of various strengths. For each of these variations multiple particle velocity and magnetic field strengths were tested. The results for Larmor radius from the program were then compared to the results found directly from equation 3.40.

The third validation case investigated the program results for a particle of initial zero velocity in orthogonal constant E and B fields. This situation results in the cycloid motion discussed in Chapter 2. The closed form solution for this type of motion results in equations for position in two orthogonal coordinates y and z (for E having only a y component and B only an x component). These equations are:

$$y(t) = \frac{E}{B}\left\{t - \frac{m}{qB}\sin\left(\frac{qB}{m}t\right)\right\} \tag{3.41}$$

$$z(t) = \frac{E}{B}\left\{\frac{m}{qB} - \frac{m}{qB}\cos\left(\frac{qB}{m}t\right)\right\} \tag{3.42}$$

where *y(t)* is the y coordinate of the particle's location at time *t* and *z(t)* is the z coordinate of the particle's location at time *t*. Several test cases were run and the output of the program compared graphically to a plot generated using equations 3.41 and 3.42 in Microsoft Excel.

For each validation case comparisons were made and evaluated based on a percentage of error where the error is defined as the difference between the closed form solution and the program output for the parameter under consideration. The percentage error is then the error divided by the closed form expected result. This provides a metric for comparing the different test runs within a validation case and across validation cases. For all of the tests performed for this validation effort the particle mass number in the input file was set to 4, representing helium.

3.5.2 Examination of Linear Velocity Change Due to Specific Voltage Drop

Examination of individual particle change in velocity due to a specified voltage drop was performed as explained in section 3.5.1. Table 3.2 shows the results for a voltage drop of between 10 and 500 volts for a helium ion with initial velocity of 0.0 m/s. The "Calculated Final Velocity" column indicates the final velocity in meters per second for each voltage drop as determined from Equation 3.39. The "Program Final Velocity" column contains the results for particle final velocity for the given voltage drop as determined by the ionLite program. The final column shows the error in the program determined value as a percentage of the calculated value.

Voltage Drop	Calculated Final Velocity	Program Final Velocity	Error Percentage
10	21959.9548	21941.8	0.08267%
50	49103.9517	49062.8	0.08381%
100	69443.4745	69385.4	0.08363%
150	85050.5392	84979.2	0.08388%
200	98207.9034	98125.9	0.08350%
250	109799.774	109708	0.08358%
300	120279.626	120179	0.08366%
350	129916.845	129807	0.08455%
400	138886.949	138771	0.08348%
450	147311.855	147188	0.08408%
500	155280.33	155151	0.08329%

Table 3.2: Results for Validation of Linear Velocity Change

As can be seen from Table 3.2, the ionLite program accurately determined the particle final velocity. In each case the accuracy was better than 99.915%. This strongly indicates that the program is accurately simulating charged particle response to linear acceleration due to electric fields.

3.5.3 Examination of Larmor Radius Simulation

As described in Chapter 2 a charged particle with a given velocity perpendicular to a constant magnetic field will move in a circle with a radius that is a factor of the particle mass and velocity, and the magnetic field strength. The fixed radius is known as the Larmor radius. To validate the program's ability to simulate particle motion under the influence of magnetic fields, a comparison was made between the Larmor radius calculated for a given particle mass, velocity and applied orthogonal magnetic field using the closed form solution and that determined from the program's output for particle position over time was made. Tables were made showing the closed form calculated Larmor radius for various configurations. These tables are accompanied by tables showing the resulting Larmor radius as determined from program output. In all cases except where noted all values for Larmor radius are given in meters. These results are then used to generate an error term based on the difference between the program calculated Larmor radius for a given configuration and the closed form solution for the same configuration. This error is given in terms of a percent of calculated closed form result for Larmor radius. In all of the tables presenting data for validation of the Larmor radius the tables have four columns. The first columns lists the magnetic field strength and the next three columns list the resulting radius of motion in meters, either closed form or determined from the program output, for each of the three initial velocities.

Three sets of tests were done to validate program accuracy for circular particle motion under the influence of a uniform magnetic field. The first set examined primarily rotational motion in the X-Y plane that was confined to a single computational cell. This by its nature maximizes the accuracy of the program since the time step size is uniformly small (for this testing it was kept between 1.0×10^{-8} and 1.0×10^{-11} seconds). For this set of runs the input file was configured to a computational radius of 0.1m, This results in a cell radial size of 1mm. Initial particle velocities were entirely in Y and values of 500 m/s, 5000 m/s, and 50000 m/s were evaluated. The B field was coded into the program to be a constant value entirely in Z with values of 0.1 T, 1 T, 10 T, and 100 T. For each configuration a program result was obtained for the diameter of particle motion in the X axis and in the Y axis, both axis being orthogonal to the Z axis which was parallel to the B field. The results for the closed form calculation of these cases are shown in Table 3.3.

Bz	$R_L(v = 500)$	$R_L(v = 5000)$	$R_L(v = 50000)$
0.1	2.07366E-04	2.07366E-03	2.07366E-02
1	2.07366E-05	2.07366E-04	2.07366E-03
10	2.07366E-06	2.07366E-05	2.07366E-04
100	2.07366E-07	2.07366E-06	2.07366E-05

Table 3.3: Closed Form Solution Results for Validation of Larmor Radius on the Small Scale (<1 Computational Cell)

For each of these test cases a value of Radius along the X coordinate and along the Y coordinate was determined. Table 3.4 contains the results for the X coordinate Radius (X Radius) for the small scale examination of program accuracy in Larmor radius. Table 3.5 contains the results for Y coordinate Radius (Y Radius) for the same test cases. The values determined from running the program for each of these test cases were then compared to the expected results listed in Table 3.3 to determine the error in each case. The error is presented as a percentage of the expected value to allow for comparison between runs with orders of magnitude different expected results. For the X Radius for the small scale evaluation of the program results for Larmor radius the error for each case is shown in Table 3.6, and for Y Radius in Table 3.7.

Bz	$R_L(v = 500)$	$R_L(v = 5000)$	$R_L(v = 50000)$
0.1	2.07368E-04	2.07280E-03	2.05257E-02
1	2.07372E-05	2.07367E-04	2.07553E-03
10	2.07452E-06	2.07372E-05	2.07367E-04
100	2.04542E-07	2.07452E-06	2.07372E-05

Table 3.4: Program Results for X Radius for Positive Bz for Validation of Larmor Radius on the Small Scale (<1 Computational Cell)

Bz	$R_L(v = 500)$	$R_L(v = 5000)$	$R_L(v = 50000)$
0.1	2.07366E-04	2.07849E-03	2.15818E-02
1	2.07366E-05	2.07366E-04	2.07721E-03
10	2.07366E-06	2.07366E-05	2.07366E-04
100	2.07366E-07	2.07366E-06	2.07366E-05

Table 3.5: Program Results for Y Radius for Positive Bz for Validation of Larmor Radius on the Small Scale (<1 Computational Cell)

Bz	$R_L(v = 500)$	$R_L(v = 5000)$	$R_L(v = 50000)$
0.1	-0.00106%	0.04137%	1.01694%
1	-0.00299%	-0.00058%	-0.09028%
10	-0.04157%	-0.00299%	-0.00058%
100	1.36174%	-0.04157%	-0.00299%

Table 3.6: Program Percentage Error in X Radius for Positive Bz for Validation of Larmor Radius on the Small Scale (<1 Computational Cell)

Bz	$R_L(v = 500)$	$R_L(v = 5000)$	$R_L(v = 50000)$
0.1	-0.00010%	-0.23302%	-4.07599%
1	-0.00010%	-0.00010%	-0.17130%
10	-0.00010%	-0.00010%	-0.00010%
100	-0.00010%	-0.00010%	-0.00010%

Table 3.7: Program Percentage Error in Y Radius for Positive Bz for Validation of Larmor Radius on the Small Scale (<1 Computational Cell)

Finally, a comparison was made of the results for X and Y Radius to determine the degree to which the program generated a circle for the particle motion. This was done by differencing the X and Y Radii and dividing the result by the expected result from Table 3.3. This answer was then expressed as a percentage and the results are contained in Table 3.8.

Bz	$R_L(v = 500)$	$R_L(v = 5000)$	$R_L(v = 50000)$
0.1	0.00096%	-0.27451%	-5.14526%
1	0.00289%	0.00048%	-0.08094%
10	0.04146%	0.00289%	0.00048%
100	-1.38065%	0.04146%	0.00289%

Table 3.8: Program Percentage Difference Between X and Y Radius for Positive Bz for Validation of Larmor Radius on the Small Scale (<1 Computational Cell)

The validation described above was then repeated for negative values of B. This causes a rotation in the opposite sense from that seen in the first sequence. Results for X and Y Radius for negative values of B are contained in Tables 3.9 and 3.10.

Bz	$R_L(v = 500)$	$R_L(v = 5000)$	$R_L(v = 50000)$
-0.1	2.07368E-04	2.07371E-03	2.04842E-02
-1	2.07372E-05	2.07367E-04	2.07371E-03
-10	2.07452E-06	2.07372E-05	2.07367E-04
-100	2.04542E-07	2.07452E-06	2.07372E-05

Table 3.9: Program Results for X Radius for Negative Bz for Validation of Larmor Radius on the Small Scale (<1 Computational Cell)

Bz	$R_L(v = 500)$	$R_L(v = 5000)$	$R_L(v = 50000)$
-0.1	2.07366E-04	2.07553E-03	2.15829E-02
-1	2.07366E-05	2.07366E-04	2.07552E-03
-10	2.07366E-06	2.07366E-05	2.07366E-04
-100	2.07366E-07	2.07366E-06	2.07366E-05

Table 3.10: Program Results for Y Radius for Negative Bz for Validation of Larmor Radius on the Small Scale (<1 Computational Cell)

The results for negative B rotation were then compared to determine a percentage error in X Radius, Y Radius, and between X and Y Radii with the results displayed in Tables 3.11, 3.12, and 3.13.

Bz	$R_L(v = 500)$	$R_L(v = 5000)$	$R_L(v = 50000)$
0.1	-0.00106%	-0.00251%	1.21707%
1	-0.00299%	-0.00058%	-0.00251%
10	-0.04157%	-0.00299%	-0.00058%
100	1.36174%	-0.04157%	-0.00299%

Table 3.11: Program Percentage Error in X Radius for Negative Bz for Validation of Larmor Radius on the Small Scale (<1 Computational Cell)

Bz	$R_L(v = 500)$	$R_L(v = 5000)$	$R_L(v = 50000)$
0.1	-0.00010%	-0.09028%	-4.08129%
1	-0.00010%	-0.00010%	-0.08980%
10	-0.00010%	-0.00010%	-0.00010%
100	-0.00010%	-0.00010%	-0.00010%

Table 3.12: Program Percentage Error in Y Radius for Negative Bz for Validation of Larmor Radius on the Small Scale (<1 Computational Cell)

Bz	$R_L(v = 500)$	$R_L(v = 5000)$	$R_L(v = 50000)$
0.1	0.00096%	-0.08777%	-5.36365%
1	0.00289%	0.00048%	-0.08728%
10	0.04146%	0.00289%	0.00048%
100	-1.38065%	0.04146%	0.00289%

Table 3.13: Program Percentage Difference Between X and Y Radius for Negative Bz for Validation of Larmor Radius on the Small Scale (<1 Computational Cell)

Examination of the error percentage in each case shows that for Larmor radii that remain within a single computational cell the accuracy is quite high, on the order of 99.9% or better. The exception to this being the 500 m/s – 100 T case where the expected radius in less than 2.1×10^{-7}m. This is most likely due to the limitations of using floating point variables throughout the program to increase speed. It should be pointed out however that this represents a value of 1/5000th of a single computational cell where the normal step size is 1/20th of a computational cell. This limitation in accuracy should therefore play no significant part in the overall program function.

The next set of cases evaluated the program performance in computing the Larmor radius at larger (i.e., greater than a single computational cell) scales. This was done because the program performs additional functions when a particle moves from one cell to another and these functions impact the results for particle motion. This involved generating test cases of particle velocity and B field strength that resulted in Larmor radii of between 3 and 40 computational cells. Initial velocity values of between 10000m/s and 45000m/s were chosen. These values reflect a reasonable cross section of the velocities experienced within a typical ion thruster. To generate the desired size Larmor radius in each case B field values of between 0.025 T and 0.125 T were required. The results for Larmor radius in each case are shown in Table 3.14 which lists the output for Equation 3.40, the closed form solution for Larmor radius.

Bz	$R_L(v = 10000)$	$R_L(V = 20000)$	$R_L(v = 45000)$
0.025	1.65893E-02	3.31785E-02	7.46517E-02
0.05	8.29463E-03	1.65893E-02	3.73258E-02
0.075	5.52975E-03	1.10595E-02	2.48839E-02
0.1	4.14732E-03	8.29463E-03	1.86629E-02
0.125	3.31785E-03	6.63571E-03	1.49303E-02

Table 3.14: Closed Form Solution Results for Validation of Larmor Radius (in Meters) on the Large Scale (>1 Computational Cell)

Table 3.15 shows the same results for the closed form solution but expressed in computational cells for a cell size of 1mm. While the value for Bz = 0.025 and v = 45000 is shown in these tables, this test run was not actually evaluated since it exceeds the size of the computational space.

Bz	$R_L(v = 10000)$	$R_L(v = 20000)$	$R_L(v = 45000)$
0.025	16.59	33.18	74.65
0.05	8.29	16.59	37.33
0.075	5.53	11.06	24.88
0.1	4.15	8.29	18.66
0.125	3.32	6.64	14.93

Table 3.15: Closed Form Solution Results for Validation of Larmor Radius (in Computational Cells) on the Large Scale (>1 Computational Cell)

The computational space for this series of tests was set up similarly to that described for the small scale evaluation with the exception that the values for velocity and B were as shown in Tables 3.14 and 3.15. Once again initial velocity was entirely in the Y direction and with B entirely along Z all motion is expected to be in the X-Y (R-θ) plane. Five series of tests were conducted for each of the combinations of velocity and field, the difference in each case being the allowed number of steps per cell. This served two purposes, first, to validate the accuracy of the program over the large scale for many different cases, and second to aid in the final configuration of the program for best accuracy. The time step/cell step cases evaluated were 5 steps per cell, 10 steps per cell, 20 steps per cell, 50 steps per cell, and 100 steps per cell. It is important to point out that the step number in each case is not rigidly enforced. Upon entrance to a cell the velocity magnitude and direction are evaluated and a new time step size calculated to result in a specific number of steps in that direction and at that velocity before the particle leaves the cell. Since the particles velocity magnitude and direction are normally changing the actual number of steps that will be taken is indeterminate. What is actually being controlled is the time step size, and hence, the fidelity of the model. More steps per cell provides for higher fidelity and therefore a higher degree of accuracy. The cost is that program run times will be longer by a factor of the comparative step sizes. In addition to straight forward program validation then, this series of tests also provided for finalizing the steps per cell factor to optimize program execution.

The first series of tests for large scale program function and accuracy for determining Larmor radius examined 5 steps per cell and values for X and Y radius were determined. The results for each case for X Radius are shown in Table 3.16 and for Y Radius in Table 3.17.

Bz	$R_L(v = 10000)$	$R_L(v = 20000)$	$R_L(v = 45000)$
0.025	1.50320E-02	3.00076E-02	N/A
0.05	7.56823E-03	1.49532E-02	3.36816E-02
0.075	5.15874E-03	9.99751E-03	2.25790E-02
0.1	4.02025E-03	7.55690E-03	1.67769E-02
0.125	3.14782E-03	6.18736E-03	1.34562E-02

Table 3.16: Program Results for X Radius for Positive Bz for Validation of Larmor Radius on the Large Scale (>1 Computational Cell) with Time Adjustment Factor set for 5 Steps per Cell

Bz	$R_L(v = 10000)$	$R_L(v = 20000)$	$R_L(v = 45000)$
0.025	1.56216E-02	3.10183E-02	N/A
0.05	7.66091E-03	1.56022E-02	3.48489E-02
0.075	5.41146E-03	1.00616E-02	2.31290E-02
0.1	3.99080E-03	7.81863E-03	1.71209E-02
0.125	3.22764E-03	6.43406E-03	1.37560E-02

Table 3.17: Program Results for Y Radius for Positive Bz for Validation of Larmor Radius on the Large Scale (>1 Computational Cell) with Time Adjustment Factor set for 5 Steps per Cell

These values for Larmor radius were then compared against the computed values in Table 3.14 and expressed as a percentage error. The error for X Radius for 5 steps per cell is shown in Table 3.18 and for Y Radius in Table 3.19.

Bz	$R_L(v = 10000)$	$R_L(v = 20000)$	$R_L(v = 45000)$
0.025	9.38718%	9.55717%	N/A
0.05	8.75749%	9.86218%	9.76332%
0.075	6.70942%	9.60260%	9.26260%
0.1	3.06381%	8.89409%	10.10571%
0.125	5.12478%	6.75656%	9.87343%

Table 3.18: Program Percentage Error in X Radius for Positive Bz for Validation of Larmor Radius on the Large Scale (>1 Computational Cell) with Time Adjustment Factor set for 5 Steps per Cell

Bz	$R_L(v = 10000)$	$R_L(v = 20000)$	$R_L(v = 45000)$
0.025	5.83307%	6.51092%	N/A
0.05	7.64014%	5.95001%	6.63600%
0.075	2.13924%	9.02309%	7.05233%
0.1	3.77391%	5.73867%	8.26249%
0.125	2.71901%	3.03879%	7.86544%

Table 3.19: Program Percentage Error in Y Radius for Positive Bz for Validation of Larmor Radius on the Large Scale (>1 Computational Cell) with Time Adjustment Factor set for 5 Steps per Cell

Finally, as was done for the small scale evaluation the difference in radii predicted by the program for X and Y were compared against each other. These results are shown in Table 3.20.

Bz	$R_L(v = 10000)$	$R_L(v = 20000)$	$R_L(v = 45000)$
0.025	-3.92230%	-3.36815%	N/A
0.05	-1.22459%	-4.34021%	-3.46569%
0.075	-4.89887%	-0.64108%	-2.43589%
0.1	0.73254%	-3.46346%	-2.05044%
0.125	-2.53572%	-3.98716%	-2.22797%

Table 3.20: Program Percentage Difference Between X and Y Radius for Positive Bz for Validation of Larmor Radius on the Large Scale (>1 Computational Cell) with Time Adjustment Factor set for 5 Steps per Cell

The results show that for 5 steps per computational cell the program accuracy was between 89.9% and 97.2%. The error percentage for X and Y Radius for each case is plotted in Figure 3.15 which shows that the accuracy is slightly better in Y than in X but is overall relatively constant. Accuracy is better at smaller scales as would be expected, but levels out as the computation proceeds through more and more cells.

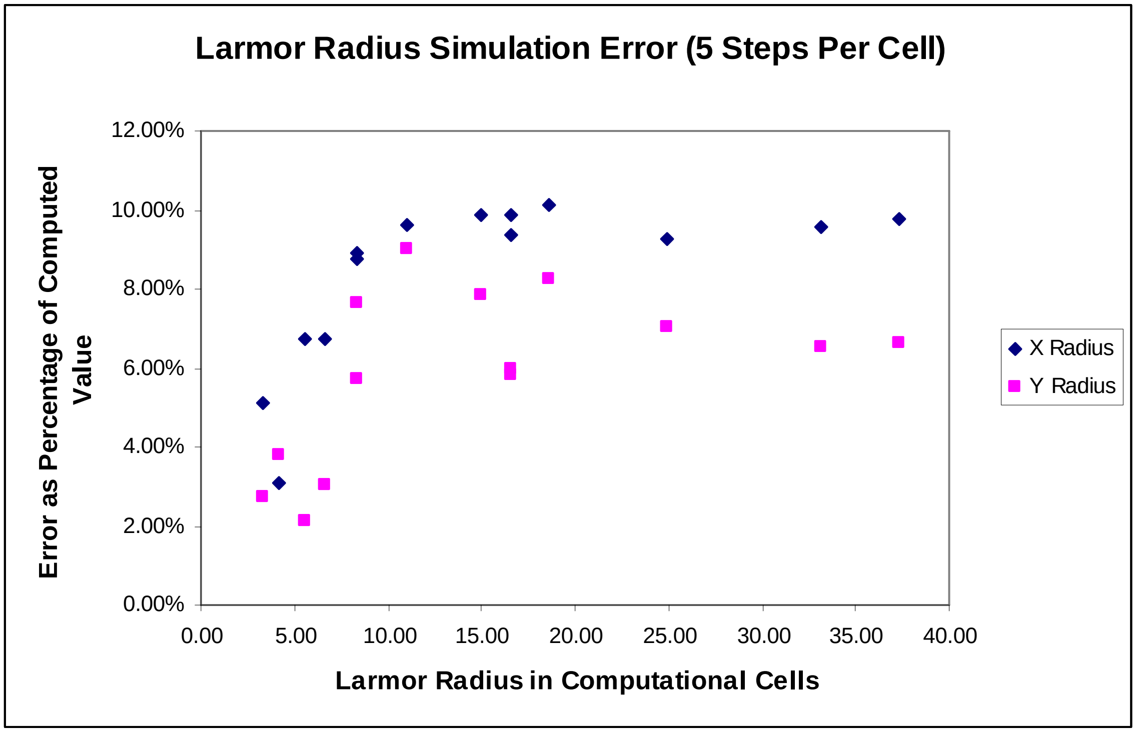

Figure 3.15: Plot of Percentage Error Between Calculated and Program Results for Larmor Radius in X-Y Plane with Time Adjustment Factor set to 5 Steps per Computational Cell

The second series of tests for large scale program function and accuracy for determining Larmor radius examined 10 steps per cell and values for X and Y radius were determined. The results for each case for X Radius are shown in Table 3.21 and for Y Radius in Table 3.22.

Bz	$R_L(v = 10000)$	$R_L(v = 20000)$	$R_L(v = 45000)$
0.025	1.58035E-02	3.17128E-02	N/A
0.05	7.91596E-03	1.57963E-02	3.56550E-02
0.075	5.35353E-03	1.05855E-02	2.36658E-02
0.1	4.00832E-03	7.90204E-03	1.78110E-02
0.125	3.21482E-03	6.46371E-03	1.41762E-02

Table 3.21: Program Results for X Radius for Positive Bz for Validation of Larmor Radius on the Large Scale (>1 Computational Cell) with Time Adjustment Factor set for 10 Steps per Cell

Bz	$R_L(v = 10000)$	$R_L(v = 20000)$	$R_L(v = 45000)$
0.025	1.54910E-02	3.21992E-02	N/A
0.05	7.85392E-03	1.57242E-02	3.58083E-02
0.075	5.19690E-03	1.06389E-02	2.39814E-02
0.1	4.07824E-03	7.79557E-03	1.74112E-02
0.125	3.30531E-03	6.45298E-03	1.43732E-02

Table 3.22: Program Results for Y Radius for Positive Bz for Validation of Larmor Radius on the Large Scale (>1 Computational Cell) with Time Adjustment Factor set for 10 Steps per Cell

These values for Larmor radius were then compared against the computed values in Table 3.14 and expressed as a percentage error. The error for X Radius for 10 steps per cell is shown in Table 3.23 and for Y Radius in Table 3.24.

Bz	$R_L(v = 10000)$	$R_L(v = 20000)$	$R_L(v = 45000)$
0.025	4.73658%	4.41770%	N/A
0.05	4.56526%	4.77998%	4.47637%
0.075	3.18684%	4.28599%	4.89511%
0.1	3.35147%	4.73308%	4.56478%
0.125	3.10540%	2.59197%	5.05104%

Table 3.23: Program Percentage Error in X Radius for Positive Bz for Validation of Larmor Radius on the Large Scale (>1 Computational Cell) with Time Adjustment Factor set for 10 Steps per Cell

Bz	$R_L(v = 10000)$	$R_L(v = 20000)$	$R_L(v = 45000)$
0.025	6.62033%	2.95169%	N/A
0.05	5.31322%	5.21460%	4.06566%
0.075	6.01934%	3.80314%	3.62682%
0.1	1.66556%	6.01668%	6.70700%
0.125	0.37804%	2.75367%	3.73158%

Table 3.24: Program Percentage Error in Y Radius for Positive Bz for Validation of Larmor Radius on the Large Scale (>1 Computational Cell) with Time Adjustment Factor set for 10 Steps per Cell

The difference in radii predicted by the program for X and Y were again compared against each other with the results contained in Table 3.25.

Bz	$R_L(v = 10000)$	$R_L(v = 20000)$	$R_L(v = 45000)$
0.025	1.97741%	-1.53377%	N/A
0.05	0.78373%	0.45644%	-0.42995%
0.075	2.92573%	-0.50446%	-1.33357%
0.1	-1.74437%	1.34737%	2.24468%
0.125	-2.81478%	0.16600%	-1.38965%

Table 3.25: Program Percentage Difference Between X and Y Radius for Positive Bz for Validation of Larmor Radius on the Large Scale (>1 Computational Cell) with Time Adjustment Factor set for 10 Steps per Cell

The results show that for 10 steps per computational cell the program accuracy was between 93.3% and 99.6%. The error percentage for X and Y Radius for each case is plotted in Figure 3.16 which shows that the accuracy is slightly better in Y than in X but is overall relatively constant. Once again, accuracy is better at smaller scales as would be expected, but levels out as the computation proceeds through more and more cells. The value for error in Y Radius for the case of B = 0.125 T and v = 10000 is out of family by an order of magnitude for this sequence of runs. If it is neglected the accuracy range is a narrower 93.3% to 98.3%.

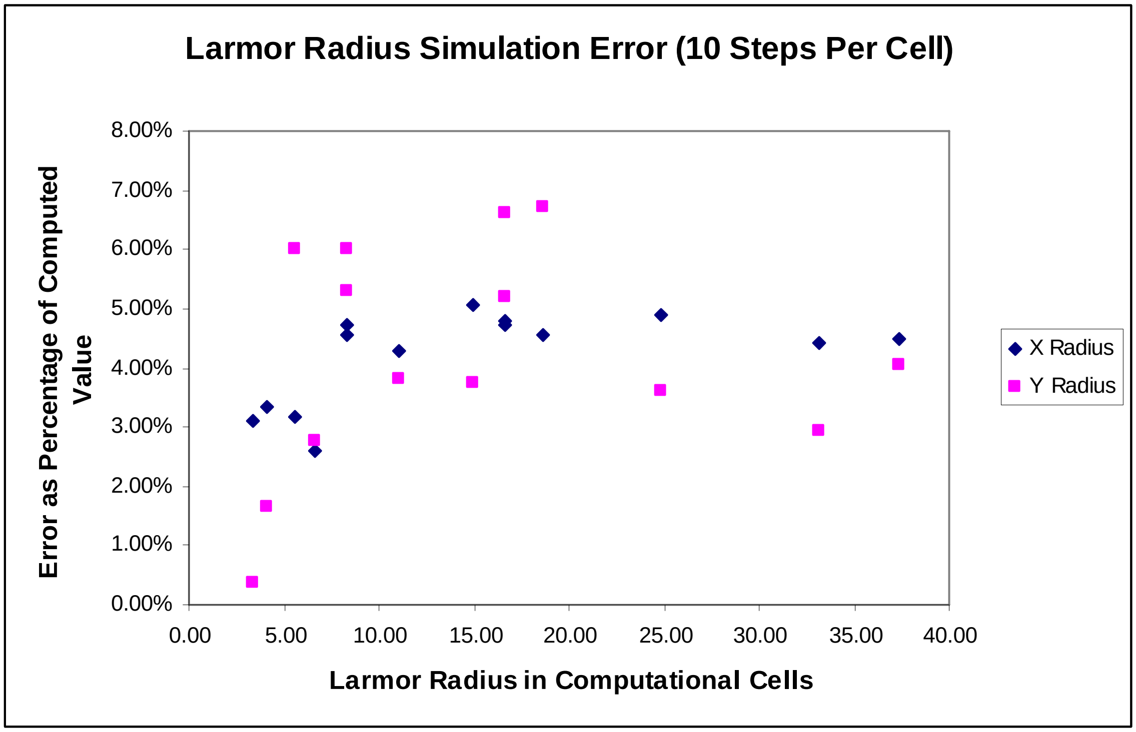

Figure 3.16: Plot of Percentage Error Between Calculated and Program Results for Larmor Radius in X-Y Plane with Time Adjustment Factor set to 10 Steps per Computational Cell

The next series of tests for large scale program function and accuracy for determining Larmor radius examined 20 steps per cell and values for X and Y radius were determined. The results for each case for X Radius are shown in Table 3.26 and for Y Radius in Table 3.27.

Bz	$R_L(v = 10000)$	$R_L(v = 20000)$	$R_L(v = 45000)$
0.025	1.61962E-02	3.22381E-02	N/A
0.05	8.12897E-03	1.61485E-02	3.63931E-02
0.075	5.37294E-03	1.07814E-02	2.43288E-02
0.1	4.07283E-03	8.11648E-03	1.82061E-02
0.125	3.26377E-03	6.49589E-03	1.45455E-02

Table 3.26: Program Results for X Radius for Positive Bz for Validation of Larmor Radius on the Large Scale (>1 Computational Cell) with Time Adjustment Factor set for 20 Steps per Cell

Bz	$R_L(v = 10000)$	$R_L(v = 20000)$	$R_L(v = 45000)$
0.025	1.62802E-02	3.22409E-02	N/A
0.05	8.15036E-03	1.62485E-02	3.62749E-02
0.075	5.37147E-03	1.05404E-02	2.42114E-02
0.1	4.12310E-03	8.18323E-03	1.83489E-02
0.125	3.29451E-03	6.50200E-03	1.45969E-02

Table 3.27: Program Results for Y Radius for Positive Bz for Validation of Larmor Radius on the Large Scale (>1 Computational Cell) with Time Adjustment Factor set for 20 Steps per Cell

These values for Larmor radius were compared against the computed values in Table 3.14 and expressed as a percentage error. The error for X Radius for 20 steps per cell is shown in Table 3.28 and for Y Radius in Table 3.29.

Bz	$R_L(v = 10000)$	$R_L(v = 20000)$	$R_L(v = 45000)$
0.025	2.36938%	2.83453%	N/A
0.05	1.99722%	2.65692%	2.49892%
0.075	2.83583%	2.51466%	2.23074%
0.1	1.79600%	2.14780%	2.44775%
0.125	1.63005%	2.10702%	2.57755%

Table 3.28: Program Percentage Error in X Radius for Positive Bz for Validation of Larmor Radius on the Large Scale (>1 Computational Cell) with Time Adjustment Factor set for 20 Steps per Cell

Bz	$R_L(v = 10000)$	$R_L(v = 20000)$	$R_L(v = 45000)$
0.025	1.86303%	2.82601%	N/A
0.05	1.73934%	2.05412%	2.81559%
0.075	2.86241%	4.69378%	2.70253%
0.1	0.58389%	1.34306%	1.68259%
0.125	0.70355%	2.01494%	2.23329%

Table 3.29: Program Percentage Error in Y Radius for Positive Bz for Validation of Larmor Radius on the Large Scale (>1 Computational Cell) with Time Adjustment Factor set for 20 Steps per Cell

The difference in radii predicted by the program for X and Y were again compared against each other with the results contained in Table 3.30.

Bz	$R_L(v = 10000)$	$R_L(v = 20000)$	$R_L(v = 45000)$
0.025	-0.51864%	-0.00878%	N/A
0.05	-0.26313%	-0.61925%	0.32479%
0.075	0.02736%	2.23533%	0.48256%
0.1	-1.23428%	-0.82240%	-0.78435%
0.125	-0.94186%	-0.09406%	-0.35337%

Table 3.30: Program Percentage Difference Between X and Y Radius for Positive Bz for Validation of Larmor Radius on the Large Scale (>1 Computational Cell) with Time Adjustment Factor set for 20 Steps per Cell

The results show that for 20 steps per computational cell the program accuracy was between 95.3% and 99.4%. The error percentage for X and Y Radius for each case is plotted in Figure 3.17 which shows the same trend for accuracy where Y is slightly better than X but is overall relatively constant. Once again, accuracy is better at smaller scales as would be expected, but levels out as the computation proceeds through more and more cells. In this case there is also an outlying result, this time toward greater error. If the value for error in Y Radius for the case of B = 0.075 T and v = 20000 is neglected the accuracy range is 97.1% to 98.3%.

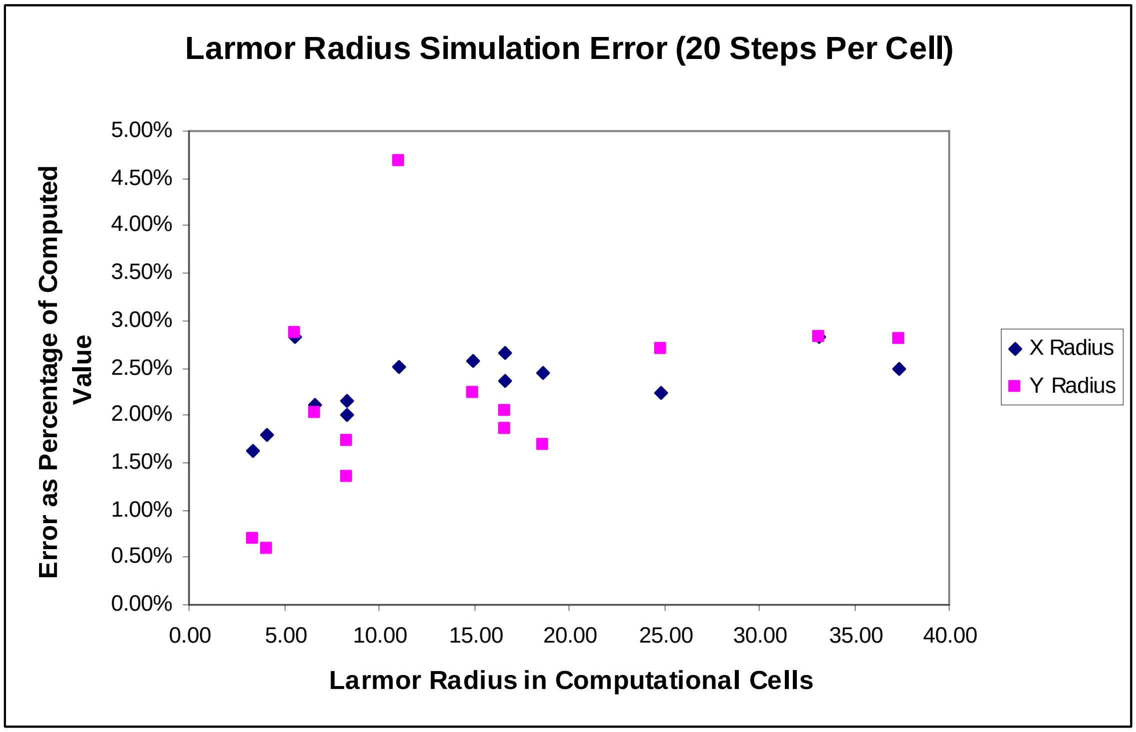

Figure 3.17: Plot of Percentage Error Between Calculated and Program Results for Larmor Radius in X-Y Plane with Time Adjustment Factor set to 20 Steps per Computational Cell

Tests for large scale program function and accuracy for determining Larmor radius for 50 steps per cell and values for X and Y radius provided the following results. For X Radius the results are shown in Table 3.31 and for Y Radius the results are shown in Table 3.32.

Bz	$R_L(v = 10000)$	$R_L(v = 20000)$	$R_L(v = 45000)$
0.025	1.64213E-02	3.28235E-02	N/A
0.05	8.21180E-03	1.63882E-02	3.69150E-02
0.075	5.49122E-03	1.09677E-02	2.45964E-02
0.1	4.10529E-03	8.21515E-03	1.84490E-02
0.125	3.28912E-03	6.56878E-03	1.47871E-02

Table 3.31: Program Results for X Radius for Positive Bz for Validation of Larmor Radius on the Large Scale (>1 Computational Cell) with Time Adjustment Factor set for 50 Steps per Cell

Bz	$R_L(v = 10000)$	$R_L(v = 20000)$	$R_L(v = 45000)$
0.025	1.63577E-02	3.28656E-02	N/A
0.05	8.24034E-03	1.63309E-02	3.69062E-02
0.075	5.49933E-03	1.09658E-02	2.46110E-02
0.1	4.13347E-03	8.22417E-03	1.85026E-02
0.125	3.26874E-03	6.59680E-03	1.46938E-02

Table 3.32: Program Results for Y Radius for Positive Bz for Validation of Larmor Radius on the Large Scale (>1 Computational Cell) with Time Adjustment Factor set for 50 Steps per Cell

The error percentage for X Radius for 50 steps per cell is shown in Table 3.33 and for Y Radius in Table 3.34. The difference in radii predicted by the program for X and Y were again compared against each other with the results contained in Table 3.35.

Bz	$R_L(v = 10000)$	$R_L(v = 20000)$	$R_L(v = 45000)$
0.025	1.01248%	1.07005%	N/A
0.05	0.99862%	1.21201%	1.10069%
0.075	0.69686%	0.83014%	1.15535%
0.1	1.01333%	0.95823%	1.14624%
0.125	0.86600%	1.00856%	0.95937%

Table 3.33: Program Percentage Error in X Radius for Positive Bz for Validation of Larmor Radius on the Large Scale (>1 Computational Cell) with Time Adjustment Factor set for 50 Steps per Cell

Bz	$R_L(v = 10000)$	$R_L(v = 20000)$	$R_L(v = 45000)$
0.025	1.39586%	0.94316%	N/A
0.05	0.65454%	1.55741%	1.12427%
0.075	0.55020%	0.84732%	1.09667%
0.1	0.33385%	0.84949%	0.85904%
0.125	1.48026%	0.58630%	1.58427%

Table 3.34: Program Percentage Error in Y Radius for Positive Bz for Validation of Larmor Radius on the Large Scale (>1 Computational Cell) with Time Adjustment Factor set for 50 Steps per Cell

Bz	$R_L(v = 10000)$	$R_L(v = 20000)$	$R_L(v = 45000)$
0.025	0.38730%	-0.12826%	N/A
0.05	-0.34755%	0.34964%	0.02384%
0.075	-0.14769%	0.01732%	-0.05936%
0.1	-0.68643%	-0.10980%	-0.29053%
0.125	0.61962%	-0.42656%	0.63096%

Table 3.35: Program Percentage Difference Between X and Y Radius for Positive Bz for Validation of Larmor Radius on the Large Scale (>1 Computational Cell) with Time Adjustment Factor set for 50 Steps per Cell

The results show that for 50 steps per computational cell the program accuracy was between 98.4% and 99.6%. The error percentage for X and Y Radius for each case is plotted in Figure 3.18 which shows for this case the error in X Radius is a fairly constant value near 1% while the Y Radius error varies between 0.3% and 1.6% before stabilizing at about 1%.

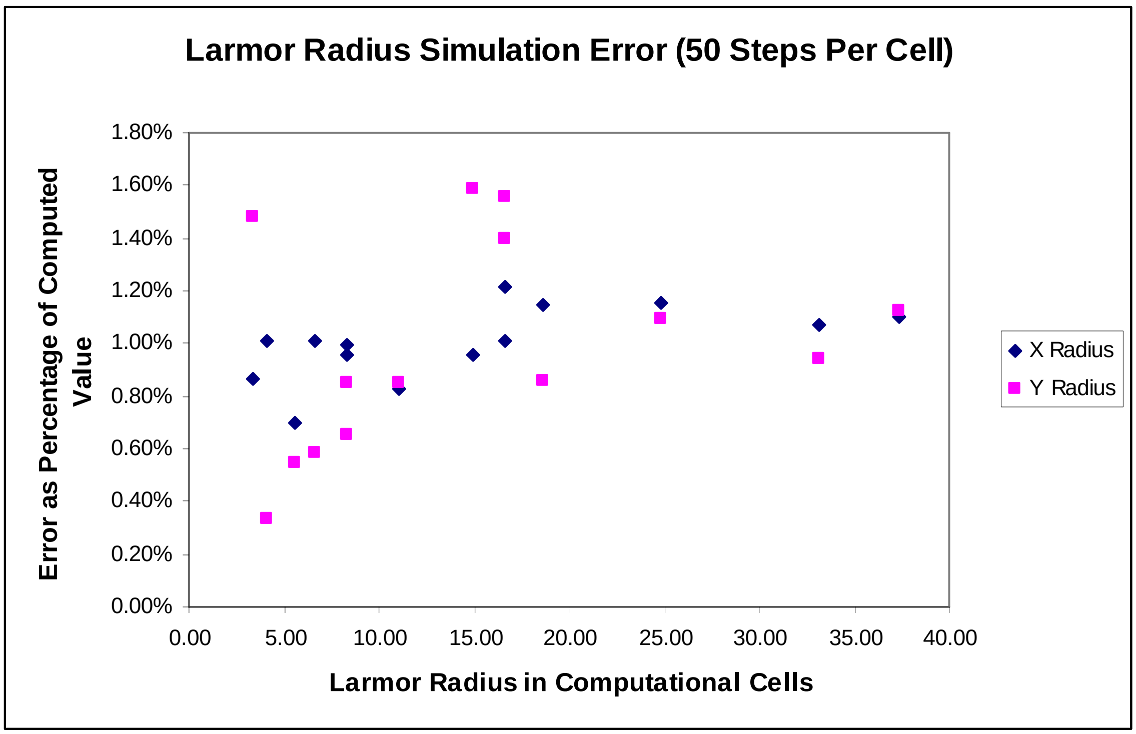

Figure 3.18: Plot of Percentage Error Between Calculated and Program Results for Larmor Radius in X-Y Plane with Time Adjustment Factor set to 50 Steps per Computational Cell

Tests for large scale program function and accuracy for determining Larmor radius for 100 steps per cell and values for X and Y radius provided the following results. For X Radius the results are shown in Table 3.36 and for Y Radius the results are shown in Table 3.37.

Bz	$R_L(v = 10000)$	$R_L(v = 20000)$	$R_L(v = 45000)$
0.025	1.65212E-02	3.30145E-02	N/A
0.05	8.30918E-03	1.65059E-02	3.71331E-02
0.075	5.54564E-03	1.10091E-02	2.47732E-02
0.1	4.15089E-03	8.29937E-03	1.85820E-02
0.125	3.33765E-03	6.60945E-03	1.48539E-02

Table 3.36: Program Results for X Radius for Positive Bz for Validation of Larmor Radius on the Large Scale (>1 Computational Cell) with Time Adjustment Factor set for 100 Steps per Cell

Bz	$R_L(v = 10000)$	$R_L(v = 20000)$	$R_L(v = 45000)$
0.025	1.65387E-02	3.29933E-02	N/A
0.05	8.29927E-03	1.65147E-02	3.71765E-02
0.075	5.53519E-03	1.10298E-02	2.47298E-02
0.1	4.15874E-03	8.28050E-03	1.86014E-02
0.125	3.33013E-03	6.64667E-03	1.48578E-02

Table 3.37: Program Results for Y Radius for Positive Bz for Validation of Larmor Radius on the Large Scale (>1 Computational Cell) with Time Adjustment Factor set for 100 Steps per Cell

The error percentage for X Radius for 100 steps per cell is shown in Table 3.38 and for Y Radius in Table 3.39. The difference in radii predicted by the program for X and Y were again compared against each other with the results contained in Table 3.40.

Bz	$R_L(v = 10000)$	$R_L(v = 20000)$	$R_L(v = 45000)$
0.025	0.41029%	0.49438%	N/A
0.05	-0.17539%	0.50251%	0.51638%
0.075	-0.28727%	0.45580%	0.44485%
0.1	-0.08618%	-0.05712%	0.43359%
0.125	-0.59669%	0.39567%	0.51196%

Table 3.38: Program Percentage Error in X Radius for Positive Bz for Validation of Larmor Radius on the Large Scale (>1 Computational Cell) with Time Adjustment Factor set for 100 Steps per Cell

Bz	$R_L(v = 10000)$	$R_L(v = 20000)$	$R_L(v = 45000)$
0.025	0.30480%	0.55827%	N/A
0.05	-0.05592%	0.44947%	0.40011%
0.075	-0.09830%	0.26863%	0.61926%
0.1	-0.27546%	0.17037%	0.32964%
0.125	-0.37004%	-0.16524%	0.48584%

Table 3.39: Program Percentage Error in Y Radius for Positive Bz for Validation of Larmor Radius on the Large Scale (>1 Computational Cell) with Time Adjustment Factor set for 100 Steps per Cell

Bz	$R_L(v = 10000)$	$R_L(v = 20000)$	$R_L(v = 45000)$
0.025	-0.10592%	0.06421%	N/A
0.05	0.11927%	-0.05331%	-0.11688%
0.075	0.18844%	-0.18803%	0.17519%
0.1	-0.18912%	0.22737%	-0.10440%
0.125	0.22531%	-0.56313%	-0.02626%

Table 3.40: Program Percentage Difference Between X and Y Radius for Positive Bz for Validation of Larmor Radius on the Large Scale (>1 Computational Cell) with Time Adjustment Factor set for 100 Steps per Cell

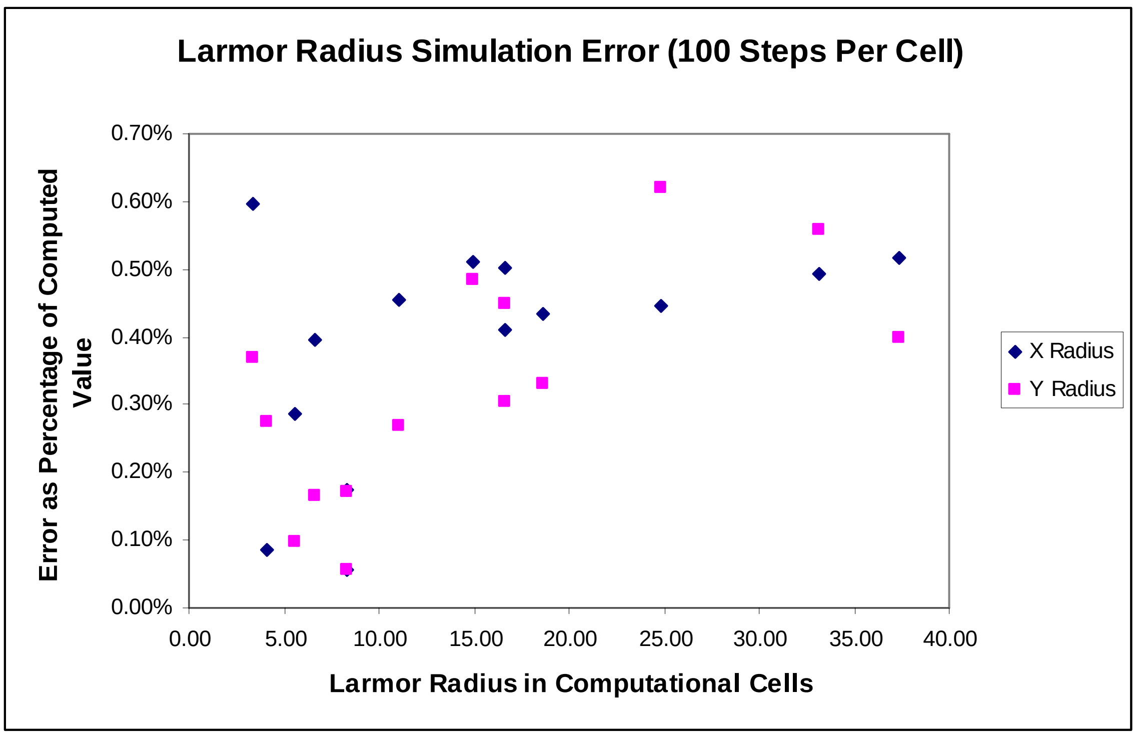

Figure 3.19: Plot of Percentage Error Between Calculated and Program Results for Larmor Radius in X-Y Plane with Time Adjustment Factor set to 100 Steps per Computational Cell

The results show that for 100 steps per computational cell the program accuracy was between 99.4% and 99.9%. The error percentage for X and Y Radius for each case is plotted in Figure 3.19 which shows for this case the error in both X and Y Radius is consistent across the test range with an average value near 0.4%.

The average error for both X and Y Radius for each series of runs for a particular number of steps per cell was calculated and the results tabulated in Table 3.41. This table

Steps per Cell	Average Larmor Radius Percentage Error – X	Average Larmor Radius Percentage Error – y
5	8.33717%	5.87022%
10	4.19583%	4.20481%
20	2.33174%	2.15129%
50	1.00199%	0.99019%
100	0.38343%	0.32509%

Table 3.41: Average Error in Larmor Radius for Different Program Execution Fidelities

shows that generally there is good agreement between the X and Y values with a slight edge in accuracy going to the Y Radius. These averages were then plotted against there representative number of steps to show the trend in accuracy versus fidelity. This information is contained in Figure 3.20. The plot clearly shows the expected increase in accuracy with increasing fidelity. This improvement, which is shown as a decrease in error, is a decaying exponential as would be expected, but this by its very nature provides an excellent metric for validating the program and for determining the most reasonable step size. The fact that for a mere 5 steps per cell the accuracy is better than 91% shows that in general the program response to circular planar motion is valid. Considering the nature of the effort (to evaluate at the highest level the benefits in terms of decreased grid erosion of various thruster configurations) 90% accuracy is probably acceptable. It would reasonably be expected that the run time for each of these cases will increase linearly with the increasing number of steps per cell. If 5 steps per cell is the baseline run duration, say 1 minute, then 10 steps per cell will require twice as long or 2 minutes, 20 steps per cell will require 4 minutes, 50 steps per cell will require 10 minutes, and 100 steps per cell will require 20 minutes. Using this estimating factor the improvement in accuracy for going from 5 steps to 10 steps is approximately a factor of 1.7. This comes

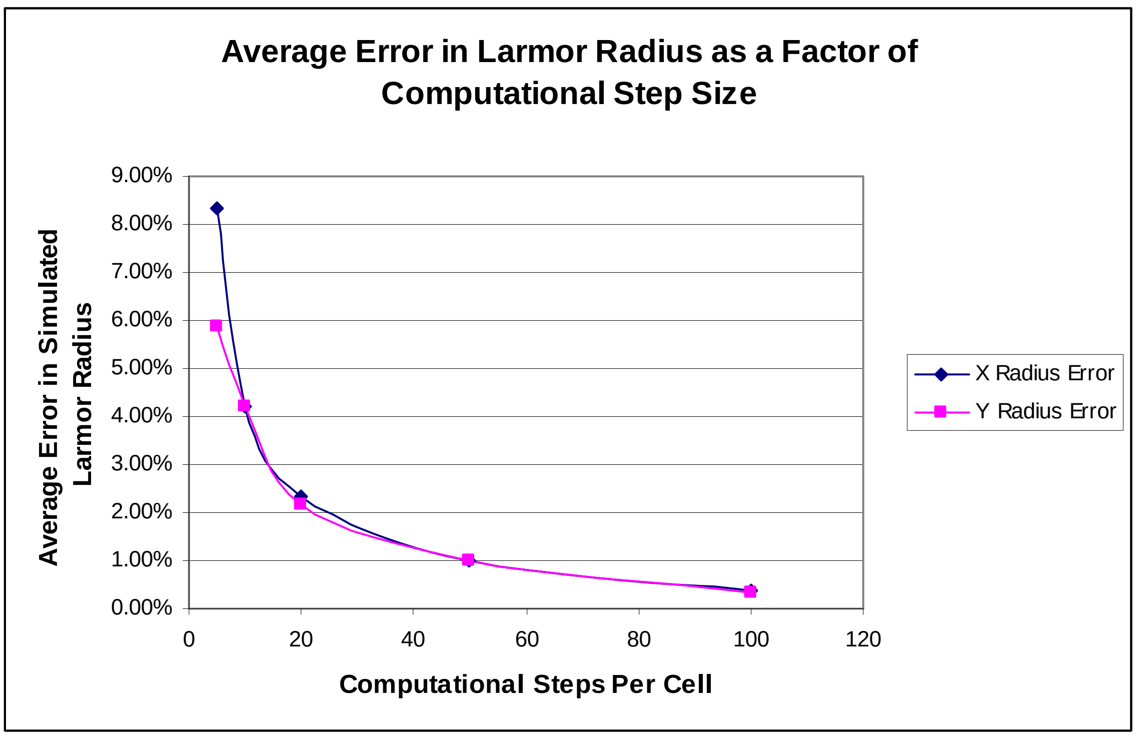

Figure 3.20: Plot of Average Error Between Calculated and Program Results for Larmor Radius in X-Y Plane for Varying Steps per Cell

at a cost of an increase in execution time of a factor of 2. The improvement in accuracy in going from 5 steps to 20 steps is approximately a factor of 3.2 at a cost in run time of approximately a 4 fold increase. The improvement in accuracy in going from 5 steps to 50 steps results in an increase in accuracy of approximately a factor of 7.1 at a cost in run time of a 10 fold increase. The improvement in accuracy in going from 5 steps to 100 steps is approximately a factor of 20 but at an increase in run time of 20 times.

Based on these results it was determined that the approximately 97% accuracy provided by using 20 steps per cell was more than sufficient for the purposes of this program and the cost in terms of run time was not overly burdensome.

Having completed the validation of program performance for Larmor motion in the X-Y plane, and determining a final value for the program fidelity factor, the next validation undertaken was of Larmor radius in the X-Z plane. This required re-orienting the magnetic field to be entirely along Y. The same test cases for velocity and field strength were run and the radius determined in X and Z. The computational results are the same as contained in Table 3.14. The results for X Radius are shown in Table 3.42 and the results for Z Radius are shown in Table 3.43.

Bz	$R_L(v = 10000)$	$R_L(v = 20000)$	$R_L(v = 45000)$
0.025	1.60747E-02	3.22183E-02	N/A
0.05	8.15113E-03	1.61449E-02	3.62092E-02
0.075	5.43185E-03	1.08226E-02	2.41521E-02
0.1	4.19616E-03	8.09580E-03	1.81468E-02
0.125	3.30593E-03	6.51375E-03	1.47203E-02

Table 3.42: Program Results for X Radius for Positive By for Validation of Larmor Radius in the X-Z Plane

Bz	$R_L(v = 10000)$	$R_L(v = 20000)$	$R_L(v = 45000)$
0.025	1.61220E-02	3.22097E-02	N/A
0.05	8.11109E-03	1.61865E-02	3.62612E-02
0.075	5.42850E-03	1.08083E-02	2.41160E-02
0.1	4.08522E-03	8.15463E-03	1.81986E-02
0.125	3.36396E-03	6.49127E-03	1.45253E-02

Table 3.43: Program Results for Z Radius for Positive By for Validation of Larmor Radius in the X-Z Plane

The error percentage for both X and Z Larmor radius were once again calculated and the results shown in Table 3.44 and Table 3.45.

Bz	$R_L(v = 10000)$	$R_L(v = 20000)$	$R_L(v = 45000)$
0.025	3.10179%	2.89412%	N/A
0.05	1.73006%	2.67862%	2.99161%
0.075	1.77050%	2.14213%	2.94084%
0.1	-1.17773%	2.39711%	2.76549%
0.125	0.35935%	1.83787%	1.40678%

Table 3.44: Program Percentage Error in X Radius for Positive By for Validation of Larmor Radius in the X-Z Plane

Bz	$R_L(v = 10000)$	$R_L(v = 20000)$	$R_L(v = 45000)$
0.025	2.81666%	2.92004%	N/A
0.05	2.21278%	2.42786%	2.85229%
0.075	1.83108%	2.27143%	3.08591%
0.1	1.49725%	1.68786%	2.48793%
0.125	-1.38967%	2.17664%	2.71285%

Table 3.45: Program Percentage Error in Z Radius for Positive By for Validation of Larmor Radius in the X-Z Plane

Finally, the X and Z Radii were compared with the results shown in Table 3.46.

Bz	$R_L(v = 10000)$	$R_L(v = 20000)$	$R_L(v = 45000)$
0.025	-0.29425%	0.02669%	N/A
0.05	0.49122%	-0.25767%	-0.14361%
0.075	0.06167%	0.13213%	0.14947%
0.1	2.64385%	-0.72667%	-0.28545%
0.125	-1.75533%	0.34512%	1.32470%

Table 3.46: Program Percentage Difference Between X and Z Radius for Positive By for Validation of Larmor Radius in the X-Z Plane

The error percentage in each case was then plotted for use in comparing overall program performance across the range of Larmor Radii tested and for comparison to results for the X-Y plane. The error in X-Z Radii is shown in Figure 3.21. This shows that not only is there good agreement between the X and Y radii, but also that these results are consistent with the accuracy found for the X-Y plane motion as shown in Figure 3.17.

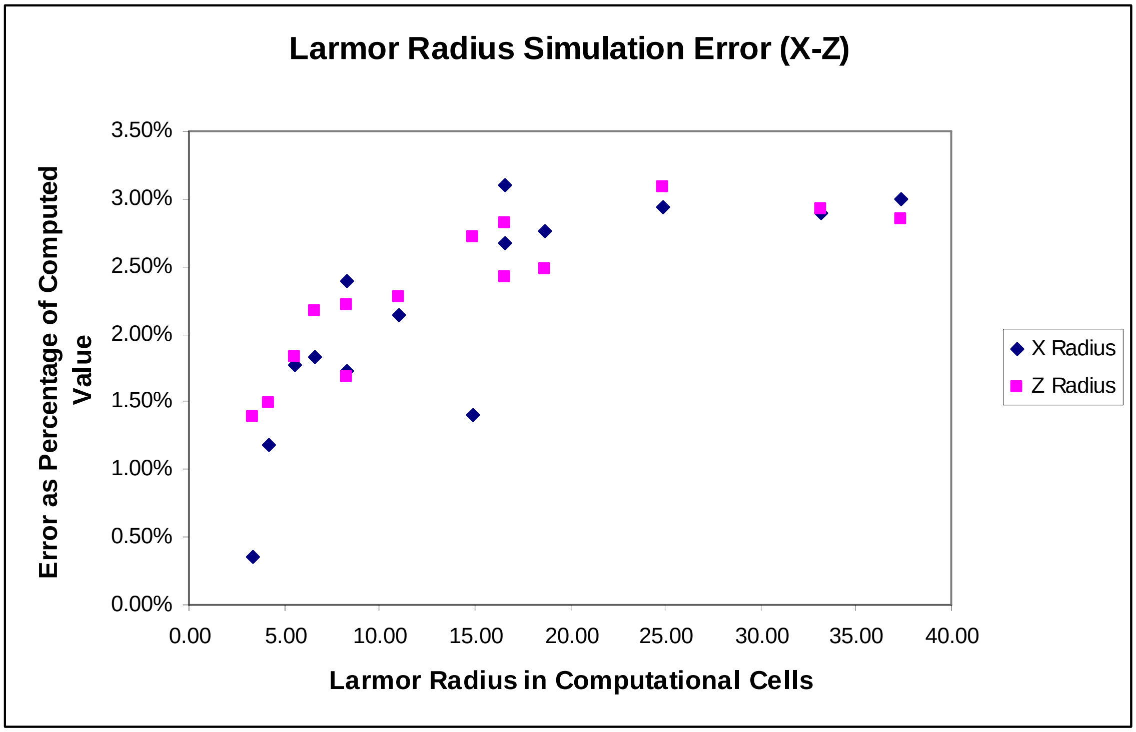

Figure 3.21: Plot of Percentage Error Between Calculated and Program Results for Larmor Radius in X-Z Plane with Time Adjustment Factor set to 20 Steps per Computational Cell

Overall the validation for repetitive circular motion showed excellent agreement between the program results and the closed form solution. Another factor in the validation which has not been mentioned, but is even more important to correct program function than the exactness of the Larmor radius, is the constancy of velocity. As described in Chapter 2, a charged particle moving in response to only a magnetic field will see no change in the magnitude of its velocity. The velocity vector will change direction, but never length. Using the program output of the final particle velocity as a metric and comparing to the input velocity gave the data required for validating this quality. In each case there was no measurable difference between the initial velocity magnitude and the final velocity magnitude. This was actually a somewhat surprising result given the number of calculations involved and the potential for round off error to creep in.

In summary, the program accurately modeled charged particle motion for an initial velocity perpendicular to a constant magnetic field.

3.5.4 Cycloid Motion Due to Orthogonal E and B Fields

The final formal validation test of the program's ability to accurately simulate charged particle motion involved an investigation of cycloid trajectories. Cycloid motion occurs when a charged particle is placed in a region of orthogonal E and B fields as described in Chapter 2. To validate the programs ability to simulate this behavior four tests were conducted, each with a variation in either E or B field strength. The performance of the program in response to this configuration is best verified graphically with plots of calculated and simulated particle motion.

The four test cases were designed to induce higher frequency cycloid motion. Higher frequency motion is a more stringent test of the program as the change in velocity vector orientation and magnitude between each time step is greater and hence the likelihood of finding instability is greater. The four cases are summarized in Table 3.47.

Case No.	B Field (all X)	E Field (all Z)
1	0.05 T	337.46 V/m
2	0.05 T	168.451 V/m
3	0.1 T	337.46 V/m
4	0.1 T	168.451 V/m

Table 3.47: Validation Cases for Cycloid Motion

For each test case the closed form solution for position was calculated using equations 3.41 and 3.42. These equations were input into MS Excel and solved for y and z position at 1.0×10^{-8} second intervals. The ionLite program input file was configured such that each cell step represented 1 mm and a constant electric field of the desired value would be created by having the potential at one end of the axis be 0 while the potential at the other end was set to either -50 or -100 volts. (With the screen and accel grids set at 1 and 2 grid position and 0 Volts and the decel grid set at 298 grid position this gives a separation distance of 296 grid cells or 0.296 meters. Thus the E field values of approximately 168 and 337 V/m.)

Test Case 1 was designed to provide cycloid motion of a limited frequency as an initial indication that the program could simulate this type of particle behavior. With a magnetic field of 0.05 Tesla and E field of 337 V/m a particle starting near the Z axis was determined from closed form results to make a little less than three complete cycles before reaching the edge of the computational space. The amplitude of the motion as determined from the closed form equations is 11.204 mm (measured in Z) and the wavelength of the motion was found to be 35.197 mm. These same values as determined from the output for position from the ionLite program are amplitude of 10.942 mm and wavelength of 33.723 mm. The results for particle motion for both calculated and simulated are shown in Figure 3.22.

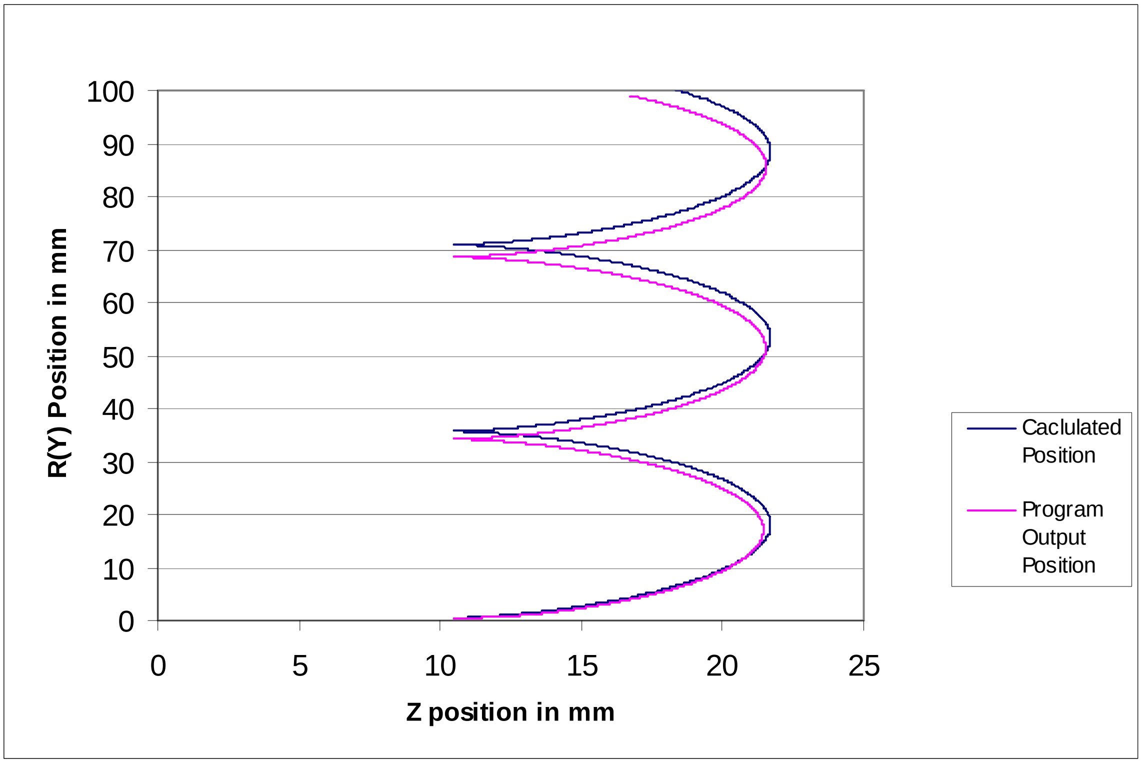

Figure 3.22: Plot of Particle Position for Cycloid Motion Validation Case 1, B = 0.05 T, E = 337.46 V/m

An important aspect, when examining this type of motion, is the amount to which errors accumulate over the distance of a particle's motion. In this case a metric for this factor is to look at the difference in radial position for the completion of the final cycle (when the particle returns to the Z min starting point). For this test case this difference between Final Z Min for the calculated and simulated results is just 3.28% of the calculated position. This is consistent with the accuracy determined for 20 steps per cell as found in section 3.5.3.

The second cycloid motion validation test case increases the frequency of the cycloid with respect to the first case. With a magnetic field of 0.05 Tesla and E field of 168 V/m a particle starting near the Z axis was determined from closed form results to make a little less than six complete cycles before reaching the edge of the computational space. The results for particle motion for both calculated and simulated are shown in Figure 3.23. The amplitude of the motion as determined from the closed form equations

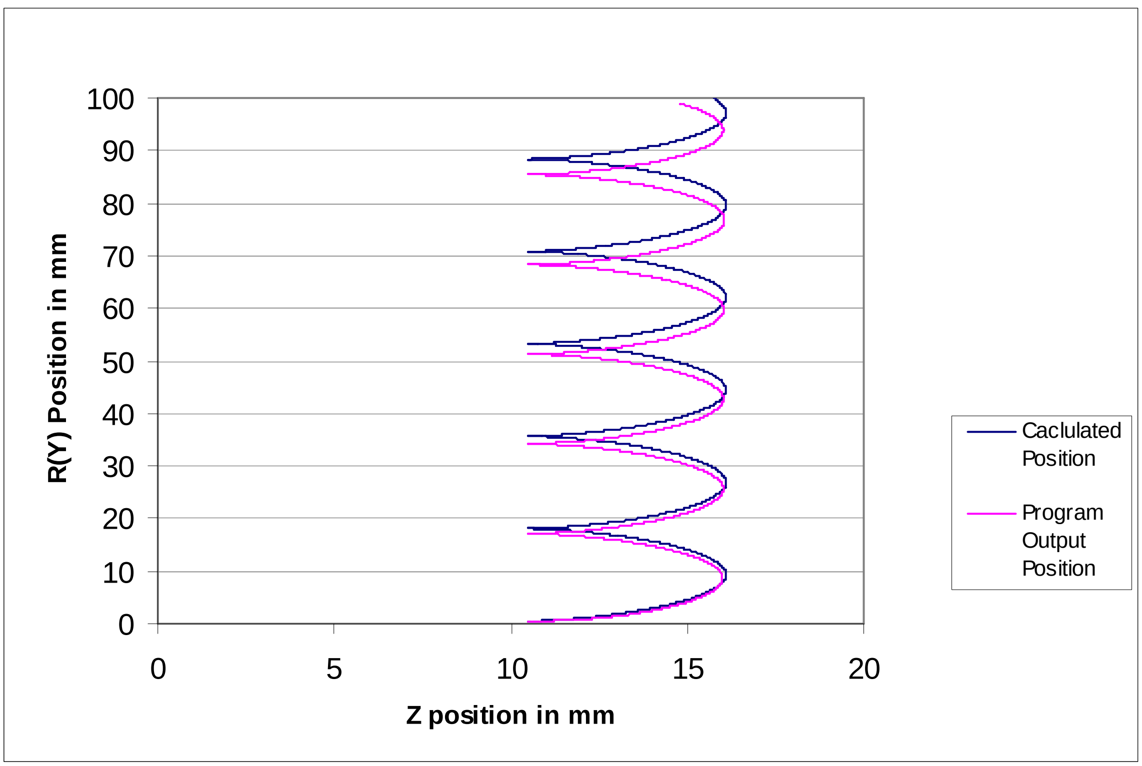

Figure 3.23: Plot of Particle Position for Cycloid Motion Validation Case 2, B = 0.05 T, E = 168.451 V/m

is 5.596 mm (measured in Z) and the wavelength of the motion was found to be 17.579 mm. These same values as determined from the output for position from the ionLite program are amplitude of 5.503 mm and wavelength of 16.601 mm.

For Test Case 2 the difference between calculated and simulated Final Z Min is 3.38% of calculated position.

The third cycloid motion validation test case increases the frequency of the cycloid even further. The results for particle motion for both calculated and simulated are shown in Figure 3.24. The magnetic field is increased to 0.1 Tesla and the E field is set to

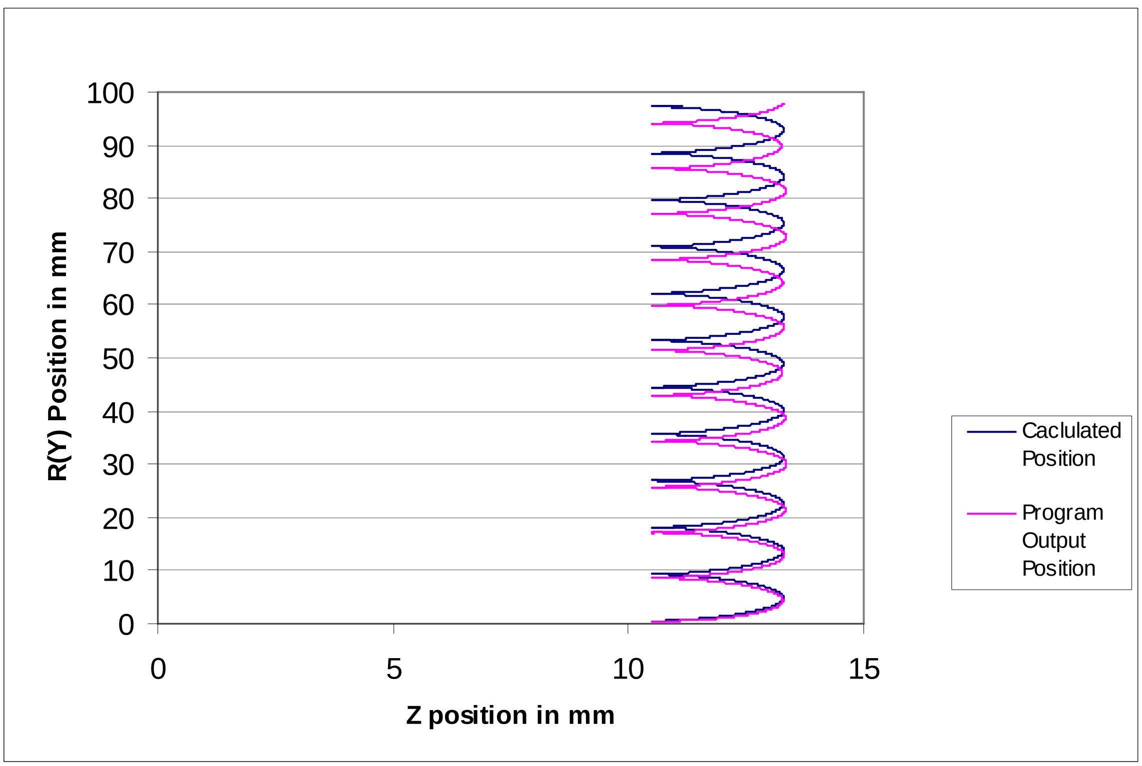

Figure 3.24: Plot of Particle Position for Cycloid Motion Validation Case 3, B = 0.1 T, E = 337.46 V/m

337 V/m. This provides for a little more than eleven complete cycles before reaching the edge of the computational space. The amplitude of the motion as determined from the closed form equations is 2.801 mm (measured in Z) and the wavelength of the motion was found to be 8.799 mm. These same values as determined from the output for position from the ionLite program are amplitude of 2.786 mm and wavelength of 8.114 mm. While in this case the difference between calculated and simulated Final Z Min is only 3.25% of calculated position, it is more significant that after eleven cycles it is off by nearly one third of a wavelength.

The fourth and final cycloid motion validation test case was intended to push the limits of the program by requiring rapid change in direction and magnitude of particle velocity. This was accomplished with the magnetic field set to 0.1 Tesla and the E field set to 168 V/m. This provides for more than twenty-two complete cycles before reaching the edge of the computational space. The amplitude of the motion as determined from the closed form equations is 1.398 mm (measured in Z) and the wavelength of the motion was found to be 4.392 mm. These same values as determined from the output for position from the ionLite program are amplitude of 1.401 mm and wavelength of 3.838 mm. The results for particle motion for both calculated and simulated are shown in Figure 3.25.

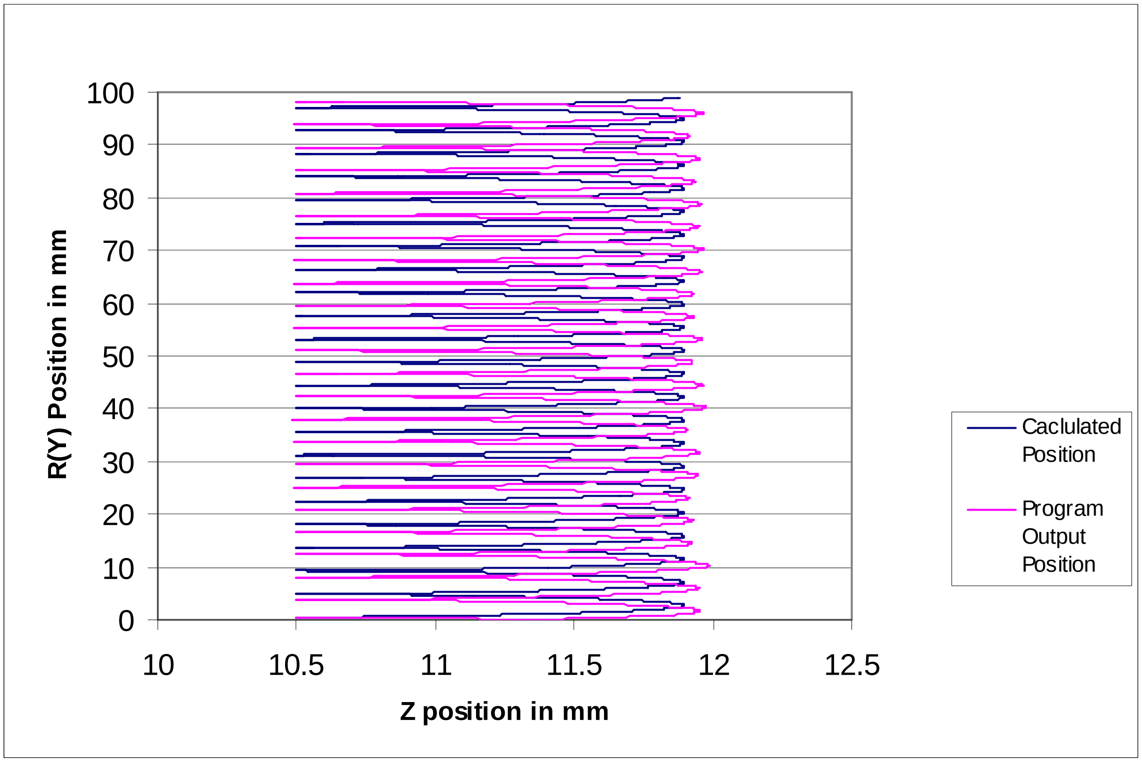

Figure 3.25: Plot of Particle Position for Cycloid Motion Validation Case 3, B = 0.1 T, E = 168.451 V/m

There are two significant differences between the outcomes of this test case and the others. First the program particle completes a full additional cycle (23 vs 22 for the closed form solution). Second is that the computed amplitude is not constant. This is however not unexpected, nor necessarily indicative a problem with the program's function. The main thing to note here is that while pressed to the limits, the results did not "blow-up" or become unstable. Final calculation of position was still better than 90% accurate in this case.

The final results for the validation of program simulation of cycloid motion are summarized in Table 3.48 which compares the calculated and simulated values for amplitude and wavelength for the four cases by once again determining an error percentage. In this case the error percentage is defined as the difference between the calculated amplitude (or wavelength) and the computed amplitude (or wavelength) divided by the calculated value.

Case	Wavelength Scale	Amplitude Error%	Wavelength Error%
Case 1	2.84	2.34%	4.19%
Case 2	5.69	1.66%	5.56%
Case 3	11.36	0.54%	7.78%
Case 4	22.77	0.21%	12.61%

Table 3.48: Cycloid Motion Program Error Percentage for Amplitude and Wavelength

In Table 3.48 a Wavelength Scale factor is introduced. This is defined simply as the number of cycles that the case motion allows for within the computational space. It gives a degree of difficulty metric for program simulation of the motion as the larger this number, the more the velocity vector must change between steps. A very interesting trend can be seen by plotting this data, specifically Error Percentage against Wavelength Scale Factor as is done in Figure 3.29.

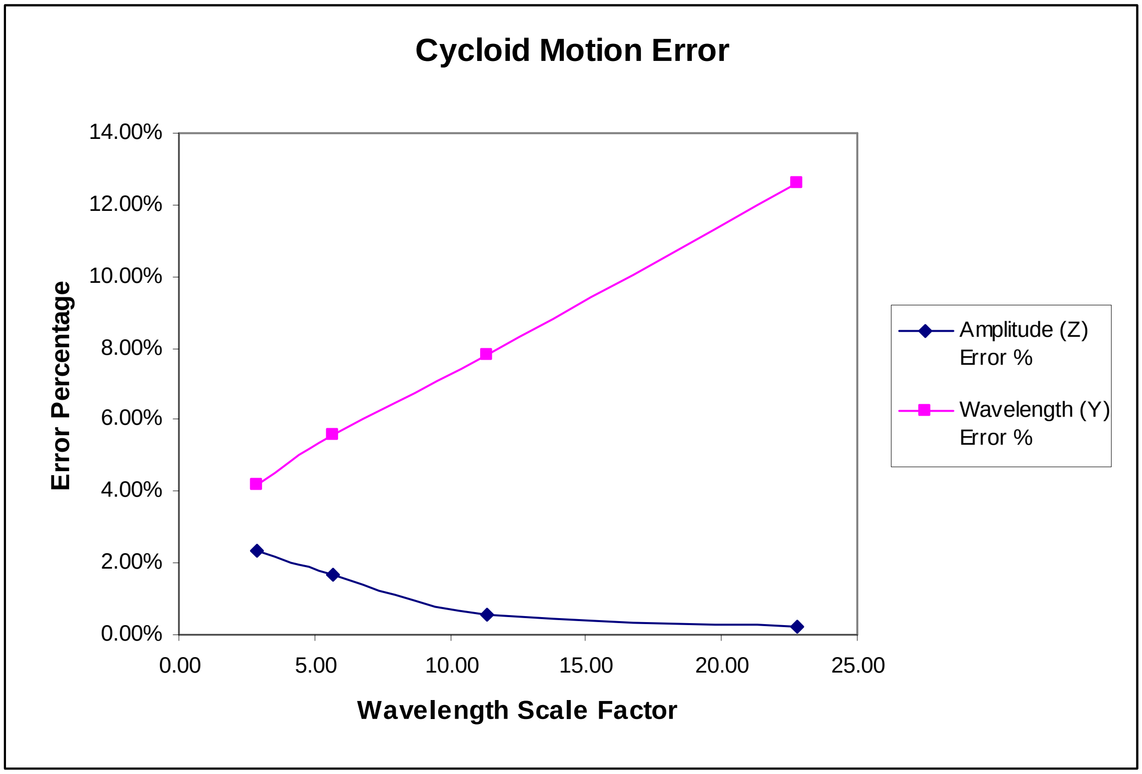

Figure 3.29: Error in Reproducing Cycloid Motion Induced Amplitude and Wavelength as Compared Against the Wavelength Scale Factor or Degree of Change in Velocity Vector with Each Step

It is clear from Figure 3.26 that while increasing the Wavelength Scale Factor causes an almost linear increase in error percentage for the wavelength, it actually causes an increase in the accuracy for the determination of cycloid motion amplitude. This is because as the particle transits its Y component goes through more and more computational cells as it transits to the edge of the computational space. The Z component however, goes through fewer and fewer computational cells as the Wavelength Scale Factor increases and the motion amplitude decreases. In other words, for the wavelength more large scale motion is seen for increasing Scale Factor, but for

Amplitude the motion becomes more small scale as the Scale Factor increases. This is consistent with the analysis of results for Larmor radius documented in the preceding section.

3.5.5 Model Validation Summary

Analysis of the performance of the ionLite simulation to specific basic particle motion shows acceptable correlation with the predictions of basic physics as expressed in the closed form equations for motion for the validation cases. The worst case for accuracy was provided by highly cycloid motion at 87.39%. Accuracy for linear acceleration for a given voltage drop was best at 99.915%, while accuracy for Larmor radius was in between at 97.67%. These values reflect a relatively high degree of accuracy for these basic particle motions and more importantly indicate that accuracy for velocity vector, on which the entire purpose of the ionLite program depends, is very accurate and should therefore provide an acceptable test of charge exchange ion behavior in the presence of or absence of magnetic fields.

CHAPTER 4

ANALYSIS OF MICRO-SOLENOID MAGNETIC FIELDS USING IONLITE

In order to determine the effect of incorporating grid imbedded magnetic fields on ion propulsion systems, three separate evaluations were undertaken using the ionLite simulation. The first of these looked at the behavior of individual charge exchange ions created within the ion beamlet of an individual set of grid apertures. Each of these individual particles was then evaluated over the range of B fields under consideration and its impact energy, if any, recorded for evaluation of the impact of the added magnetic field. The second evaluation investigated the performance of two different arrangements of grid embedded fields using multiple particles generated at even intervals throughout the ion beamlet of a single set of grid apertures of a three grid thruster. This evaluation involved the cumulative effects of many particles generated evenly throughout the grid system. The third evaluation investigated some alternative systems that might require lower magnitude B fields, or conversely generate large B fields within the grid apertures but at lower current levels, to accomplish the objective of reducing thruster grid erosion.

In each of these evaluations the key metrics used were total kinetic energy imparted to the grids and the strength of the magnetic field as measured at the centerline of the accel grid aperture at the axial location of the accel grid current loop. This provides for simple graphical evaluation of the results by plotting the kinetic energy imparted to any grid or set of grids against the peak centerline B field magnitude. The following sections provide the results of these three evaluations relying principally on graphs to convey the data.

4.1 Examination of Individual Charge Exchange Ion Motion

In order to understand the results of multiple particle runs examining the impact of the added B fields it is necessary to first examine how an individual particle behaves under the influence of the additional B field. The reason for this will be made obvious by examination of the results presented in the following sections.

Six cases are investigated for individual particle behavior. These six cases examined two basic thruster architecture differences, specifically, two vs. three grid thrusters. In each case a number of individual particles originating in narrow regions of the grid apertures are examined. Section 4.1.1 examines charge exchange ions created within the accel grid aperture of a two grid thruster. Section 4.1.2 examines charge exchange ions created between the screen and accel grids of a two grid thruster. Section 4.1.3 examines charge exchange ions created aft of the accel grid in a two grid thruster. Section 4.1.4 examines charge exchange ions created between the accel and decel grids in a three grid thruster. Section 4.1.5 examines charge exchange ions created within the decel grid aperture. Section 4.1.6 examines charge exchange ions created aft of the decel grid. The first two sections and their described investigations are not repeated for a three grid thruster as it was felt that the primary impact of the addition of the decel grid is on particles and fields aft of the accel grid. A seventh section, Section 4.1.7, examines the impact of incorporating current loops in multiple grids. The results for all section are displayed as comparisons of the energy imparted to an impacted grid (if any) and the peak axial B field magnitude. In all cases the electric fields are maintained as constant (i.e., grid potentials are the same for each case).

The specific architecture used for the individual particle examination is based on the model described by Okawa and Takegahara [30]. The specifics of the simulation are readily discernable from the input data file as shown in Table 4.1 below. This input file Table 4.2 lists the input parameters used for the program runs discussed in sections 4.1.4 through 4.1.6. It is essentially the two grid thruster from Table 4.1 but with an added decel grid. It is used to examine the impact on individual particle behavior of a grid embedded magnetic field in a three grid thruster.

The particles for the simulations in this section were given a mass consistent with xenon, a single positive charge, and initial thermal velocities based on a temperature of 500 degrees C. In each case the initial velocity vector is radial. In order to calculate over a large range of B fields, a loop was added to the program which iterated over a range of current loop multipliers to provide data over a range from 0 to 175 Tesla. For most of the individual particle examinations the simulation included only an accel grid current loop. A brief discussion of the impact of incorporating multiple current loops is contained in Section 4.1.7.

Radius	1.5e-3	Radius of calculation space
Rsc	73	Radius of the Screen Grid aperture in whole grid nodes
Rac	43	Radius of the Accel Grid aperture in whole grid nodes
Rdc	99	Radius of the Decel Grid aperture in whole grid nodes
Zsc	30	Axial location of the Screen Grid forward surface in whole grid nodes
Zac	77	Axial location of the Accel Grid forward surface in whole grid nodes
Zdc	299	Axial location of the Decel Grid forward surface in whole grid nodes
Tsc	20	Thickness of the Screen Grid aperture in whole grid nodes
Tac	33	Thickness of the Accel Grid aperture in whole grid nodes
Tdc	0	Thickness of the Decel Grid aperture in whole grid nodes
Vplasma	1030.0	Plasma Potential
Vsc	1000.01	Screen Grid Potential
Vac	-500.01	Accel Grid Potential
Vdc	0.0	Decel Grid Potential
Vnetral	0.0	Neutralization Plane Potential
Isc	-	Screen Grid Loop Current
Iac	-	Accel Grid Loop Current
Idc	-	Decel Grid Loop Current
i_start	90	Radial (i) index of first test particle cell
i_inter	10	Radial (i) interval for the run
i_stop	90	Radial (i) index of last test particle cell
j_start	210	Axial (j) index of first test particle cell
j_inter	10	Axial (j) interval for the run
j_stop	210	Axial (j) index of last test particle cell
Temp	500.0	Neutral Particle Temperature (usually discharge chamber temp.)
Uinit_r	1	R component of the initial thermal velocity of all test particles
Uinit_z	0	Z component of the initial thermal velocity of all test particles
Uinit_t	0	θ component of the initial thermal velocity of all test particles
mainF	1	Write the MainOutput.txt file (1 = Yes, 0 = No)
runNumF	0	Write the runNum.txt file (1 = Yes, 0 = No)
velF	0	Write the RTZvelocity.txt file (1 = Yes, 0 = No)
runSumF	1	Write the RunSummary.txt file (1 = Yes, 0 = No)
RposF	0	Write the Rposition.txt file (1 = Yes, 0 = No)
ZposF	0	Write the Zposition.txt file (1 = Yes, 0 = No)
TposF	0	Write the Tposition.txt file (1 = Yes, 0 = No)
RZTposF	0	Write the RZTposition.txt file (1 = Yes, 0 = No)
diagF	0	Write the diagnosticFile.txt file (1 = Yes, 0 = No)
numPosF	0	Write the numbered particle position files (1 = Yes, 0 = No)
shthOn	1	Include plasma sheath (1 = Yes, 0 = No)
beamOn	1	Include Ion Beam (1 = Yes, 0 = No)
shthTh	1.5e-3	Sheath Thickness in grid points
Charge	73	Particle charge state, 1 for singly charged ions, -1 for electrons
massNumber	43	Atomic number of the particle

Table 4.1: Input Data for Two Grid Individual Particle Runs

Radius	1.5e-3	Radius of calculation space
Rsc	73	Radius of the Screen Grid aperture in whole grid nodes
Rac	43	Radius of the Accel Grid aperture in whole grid nodes
Rdc	73	Radius of the Decel Grid aperture in whole grid nodes
Zsc	30	Axial location of the Screen Grid forward surface in whole grid nodes
Zac	77	Axial location of the Accel Grid forward surface in whole grid nodes
Zdc	137	Axial location of the Decel Grid forward surface in whole grid nodes
Tsc	20	Thickness of the Screen Grid aperture in whole grid nodes
Tac	33	Thickness of the Accel Grid aperture in whole grid nodes
Tdc	20	Thickness of the Decel Grid aperture in whole grid nodes
Vplasma	1030.0	Plasma Potential
Vsc	1000.01	Screen Grid Potential
Vac	-500.01	Accel Grid Potential
Vdc	10.0	Decel Grid Potential
Vnetral	0.0	Neutralization Plane Potential
Isc	-	Screen Grid Loop Current
Iac	-	Accel Grid Loop Current
Idc	-	Decel Grid Loop Current
i_start	90	Radial (i) index of first test particle cell
i_inter	10	Radial (i) interval for the run
i_stop	90	Radial (i) index of last test particle cell
j_start	210	Axial (j) index of first test particle cell
j_inter	10	Axial (j) interval for the run
j_stop	210	Axial (j) index of last test particle cell
Temp	500.0	Neutral Particle Temperature (usually discharge chamber temp.)
Uinit_r	1	R component of the initial thermal velocity of all test particles
Uinit_z	0	Z component of the initial thermal velocity of all test particles
Uinit_t	0	θ component of the initial thermal velocity of all test particles
mainF	1	Write the MainOutput.txt file (1 = Yes, 0 = No)
runNumF	0	Write the runNum.txt file (1 = Yes, 0 = No)
velF	0	Write the RTZvelocity.txt file (1 = Yes, 0 = No)
runSumF	1	Write the RunSummary.txt file (1 = Yes, 0 = No)
RposF	0	Write the Rposition.txt file (1 = Yes, 0 = No)
ZposF	0	Write the Zposition.txt file (1 = Yes, 0 = No)
TposF	0	Write the Tposition.txt file (1 = Yes, 0 = No)
RZTposF	0	Write the RZTposition.txt file (1 = Yes, 0 = No)
diagF	0	Write the diagnosticFile.txt file (1 = Yes, 0 = No)
numPosF	0	Write the numbered particle position files (1 = Yes, 0 = No)
shthOn	1	Include plasma sheath (1 = Yes, 0 = No)
beamOn	1	Include Ion Beam (1 = Yes, 0 = No)
shthTh	1.5e-3	Sheath Thickness in grid points
Charge	73	Particle charge state, 1 for singly charged ions, -1 for electrons
massNumber	43	Atomic number of the particle

Table 4.2: Input Data for Three Grid Individual Particle Runs

4.1.1 Charge Exchange Ions Created Within the Accel Grid Aperture

The behavior of particles representing charge exchange ions which might be created at specific locations within the aperture of an accel grid were examined over the range of peak axial B fields (0 to 175 Tesla) for the case of a two grid thruster as defined by the input data file shown in Table 4.1. Particles originating in twelve grid location within the accel aperture were examined. The particles under consideration were created at the grid locations representing approximately the aperture axis, approximately 25% of the distance from the axis to the aperture radius, approximately 50% of the distance from the axis to the aperture radius, approximately 75% of the distance from the aperture axis to the aperture radius, and at near the aperture radius. Each of the radial locations were then duplicated for particles originating at the forward surface axial location of the accel grid, at the middle of the accel grid axis, and at the aft edge of the accel grid. Each of these particles is identified by its grid origin location, for example the particle starting in the grid cell identified by inner radial node i = 10 and axial minimum node j = 77 is indicated as particle (10,77). The results for each of these particles over the range of B fields described can be broken into three major categories; exponential roll off of impact energy (ERIE), gradual increase of impact energy (GIIE), and erratic impact energy (EIE). The meaning of these category identifiers will be clarified directly.

The exponential roll-off in impact energy (ERIE) category implies that the kinetic energy of the particle impact with the accel grid decreases exponentially as the axial B field strength is increased. Particle (20,88) created at both the mid radial distance and mid axial location within the accel grid is representative of this category of behavior as can be seen in Figure 4.1.

Figure 4.1 shows that between the axial B field levels of 0 and 120 Tesla the kinetic energy imparted to the accel grid by the impact of particle (20,88) decreases exponentially from an initial maximum of 4×10^{-17} Joules to a minimum of 7.5×10^{-18} Joules. This is clearly the desired behavior as the result is an 80% reduction in the kinetic energy and hence damage caused to the accel grid.

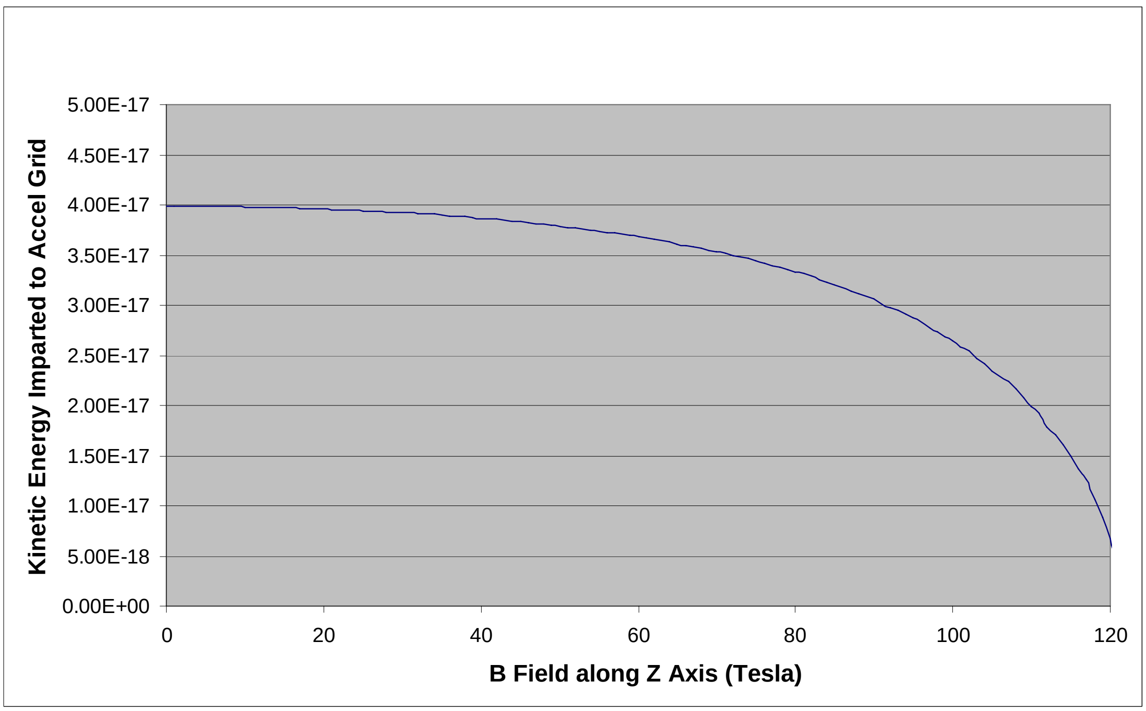

Figure 4.1: Kinetic Energy Imparted to Accel Grid by Particle (20,88)

Particles exhibiting the second category of behavior, the Gradual Increase in Impact Energy (GIIE), have impact energies that increase with increasing axial B field strength. The (GIIE) category is represented by the behavior of particle (10,99) created near the axis of and exit of the accel grid aperture. The results for this particle can be seen in Figure 4.2.

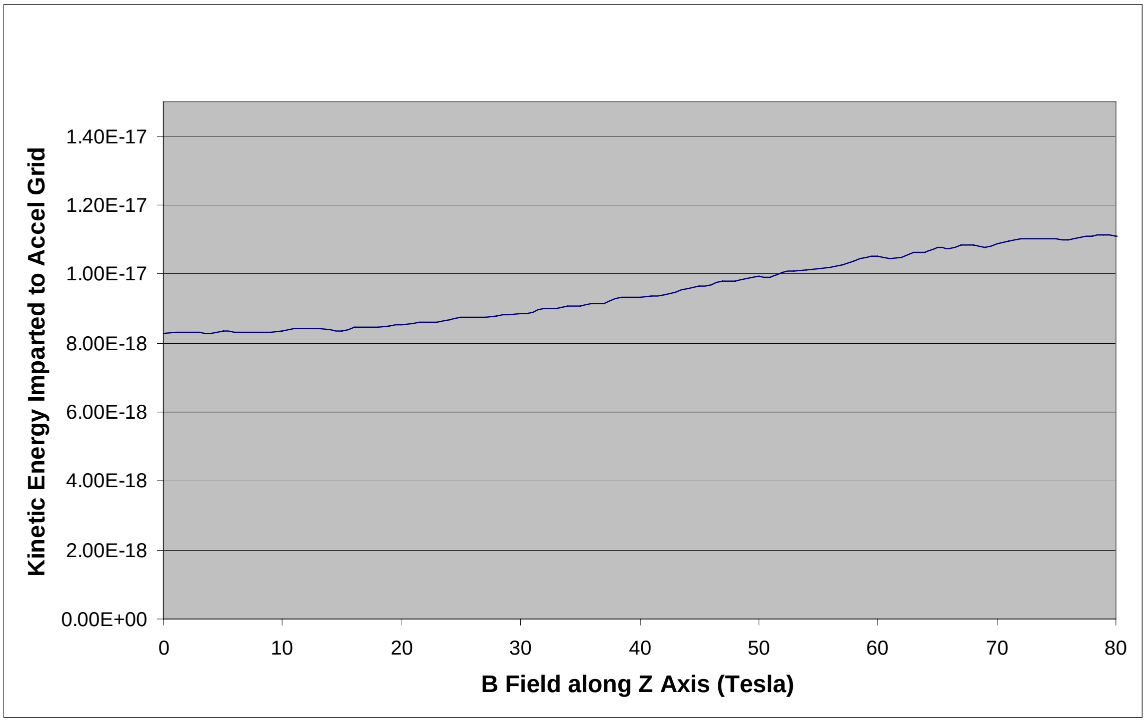

Figure 4.2: Kinetic Energy Imparted to Accel Grid by Particle (10,99)

Figure 4.2 shows that for the particle (10,99) the energy at impact, and hence the damage done to the accel grid, increases gradually with increasing axial B field strength from an initial minimum of 8.28×10^{-18} Joules to a maximum of 1.11×10^{-17} Joules over the range of axial field strengths of 0 to 80 Tesla. This is the opposite of the desired behavior as this implies that more damage is done to the accel grid as the field strength is increased. It is noteworthy however that while the energy imparted to the grid by this particle increases by 2.82×10^{-18} Joules over this range of B fields, the energy imparted to the grid by particle (20,88) decreases by 6.6×10^{-18} Joules over the same range.

The third category, Erratic Impact Energy (EIE), includes particles which impact the accel grid at widely varying energies over the range of B fields being examined. This behavior is demonstrated by particle (40,77) and is shown in Figure 4.3.

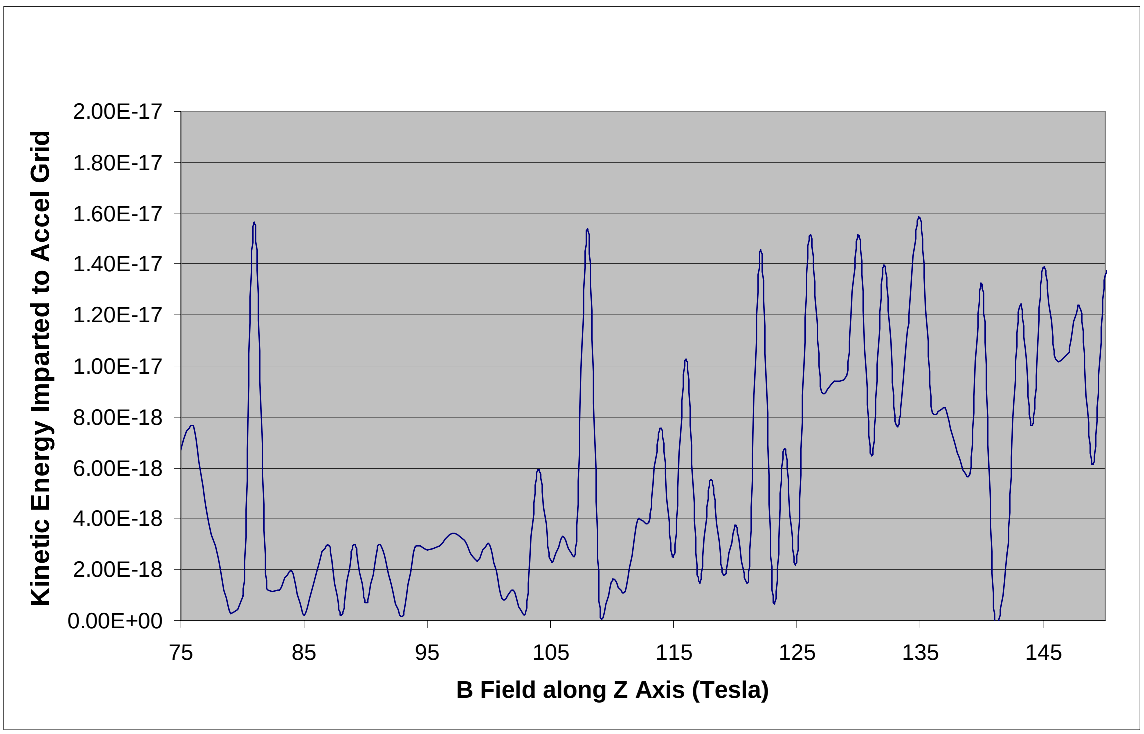

Figure 4.3: Kinetic Energy Imparted to Accel Grid by Particle (40,77)

Figure 4.3 shows that for particle (40,77) the impact energy varies rapidly both increasing and decreasing by two or more orders of magnitude over magnetic field strength changes of less than a Tesla in some cases. This behavior manifests itself due to two effects of the presence of the magnetic field. First as the field magnitude is increased the particle trajectory varies to the point where it no longer impacts the grid inside the aperture, instead passing outside the aperture to where it can continue to accelerate under the influence of the electric field and eventually impact the accel grid surface. The second effect is caused by particle mirroring due to the presence of the magnetic field. As the B field increases the particle moves into regions where the field density increases to the point where the particle is reflected. The particle is then free to be accelerated on an even longer path by the electric field resulting in larger energies at impact. However, in this case the alternate result is also possible in that a reflected particle may impact on a highly oblique trajectory with a very small normal component thus imparting very little energy to the grid.

As will be seen later, many particles exhibit only one of these behaviors over the full range of B fields under consideration; however, it is also quite common for a particle to exhibit one behavior over one range of B field and a different behavior over a different range of B field. An example of this is particle (10,99) which exhibited gradual increase in impact energy over the B field range from 0 to 80 Tesla. When this particle's behavior is examined over the full range of interest, 0 to 175 Tesla, it can be seen to exhibit all three behaviors over different B field ranges as shown in Figure 4.4. Over the previously discussed range of 0 to 80 Tesla the particle has a gradual increase in impact energy. From the range of 80 to 100 Tesla however it manifest the exponential decrease in kinetic energy at impact behavior. Finally, above 100 Tesla the behavior becomes erratic with rapid variation in impact energy.

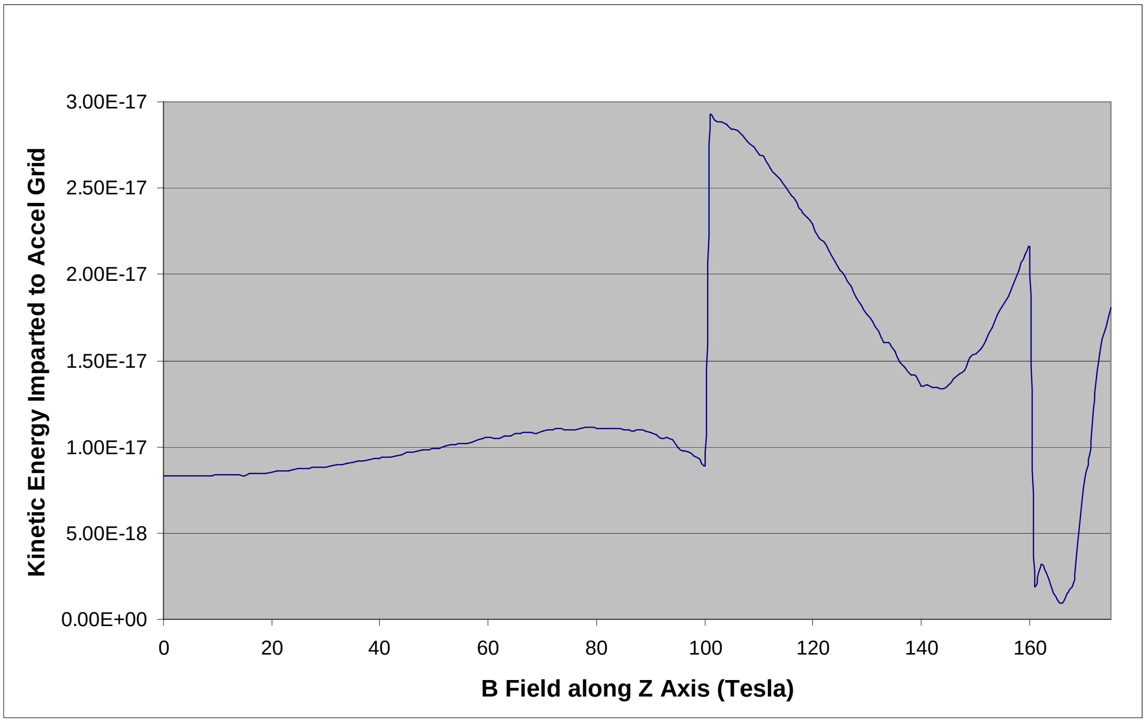

Figure 4.4: Kinetic Energy at Impact for Particle (10,99) Showing Different Categories of Behavior Over Different Ranges of Axial B Field Magnitudes.

Figures 4.5, 4.6, and 4.7 show the results for each of the particles considered in this section, specifically particles generated within the accel grid aperture of a two grid thruster. Figure 4.5 shows particles generated near the axis, at 25% of the aperture radius, 50% of aperture radius, 75% of aperture radius, and near the aperture radius of the accel grid for a starting axial location near the leading surface of the accel grid. Figure 4.6 shows particles generated near the axis, at 25% of the aperture radius, 50% of aperture radius, 75% of aperture radius, and near the aperture radius of the accel grid for a starting axial location near the middle of the accel grid. Figure 4.7 shows particles generated near the axis, at 25% of the aperture radius, 50% of aperture radius, 75% of aperture radius, and near the aperture radius of the accel grid for a starting axial location near the aft surface of the accel grid.

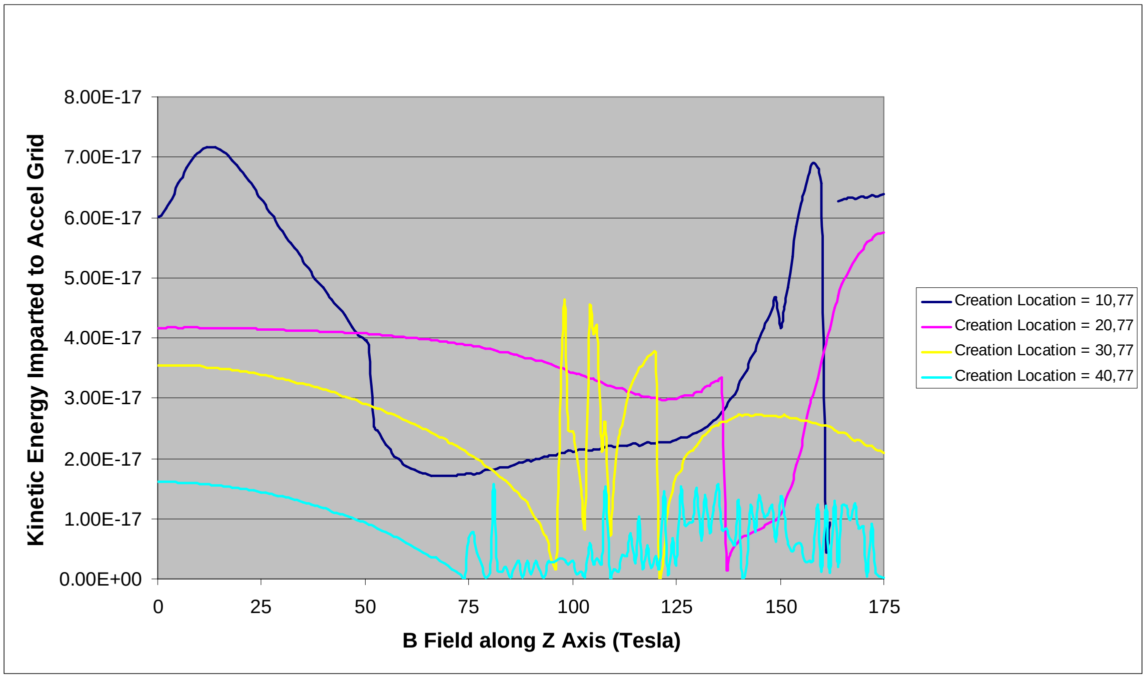

Figure 4.5: Impact Energies of Particles Created Within and Near the Forward Surface Axial Location of the Accel Grid

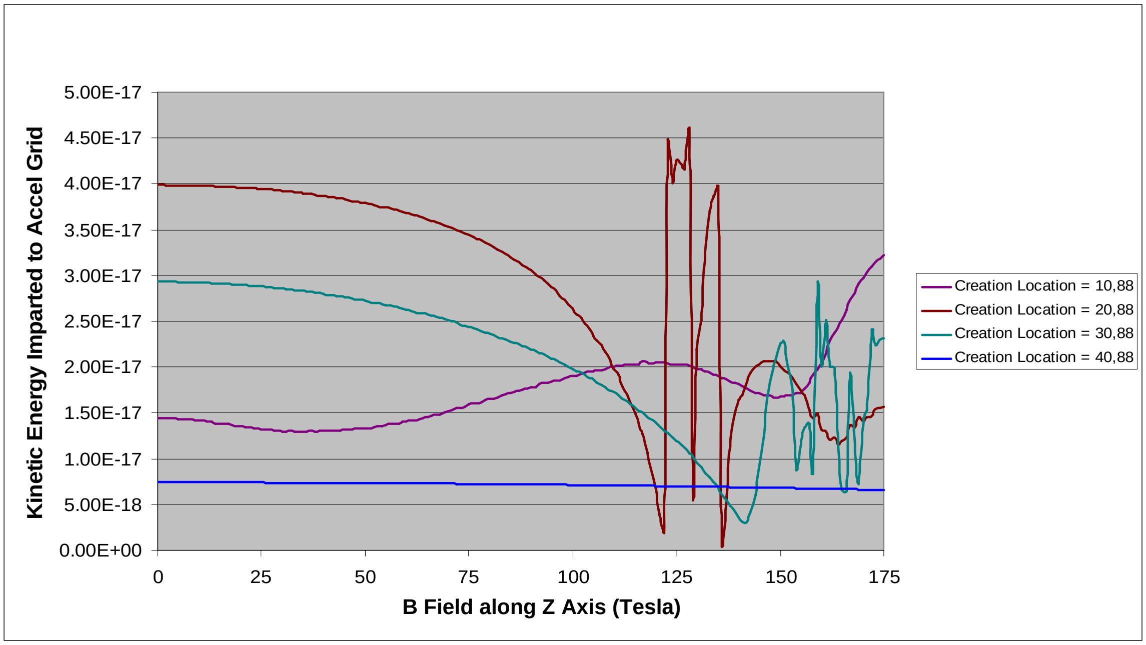

Figure 4.6: Impact Energies of Particles Created Within and Near the Axial Midpoint of the Accel Grid

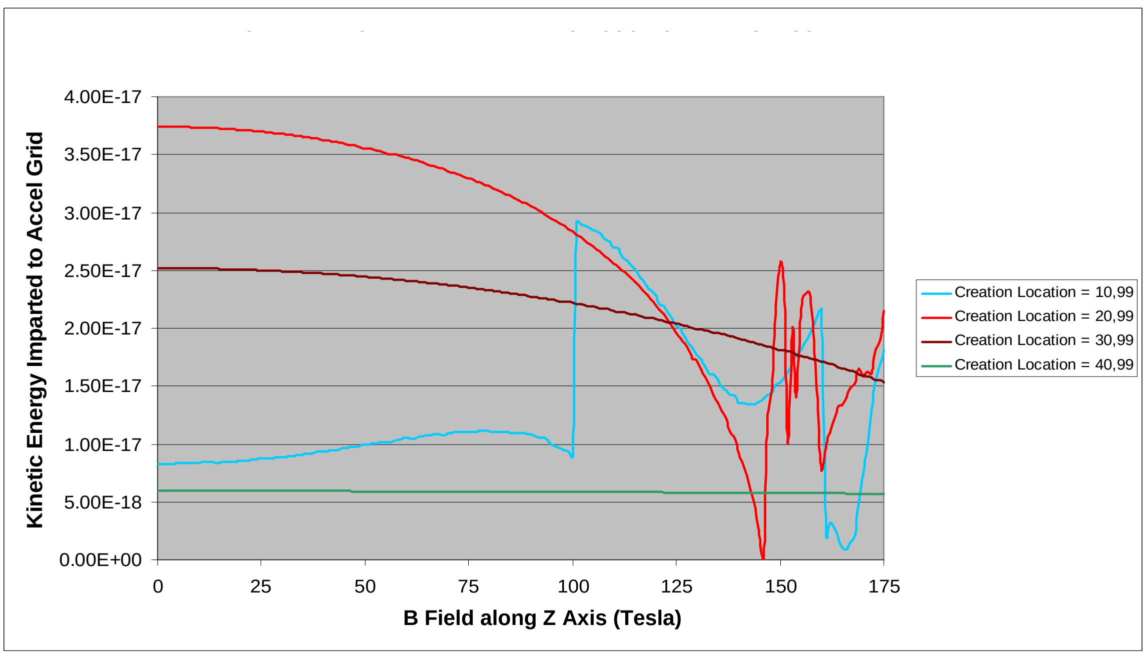

Figure 4.7: Impact Energies of Particles Created Within and Near the Aft Surface Axial Location of the Accel Grid

As can be seen from Figures 4.5 through 4.7, most of the particles examined demonstrate multiple categories of behavior over the range of axial B fields examined. A key observation on the behavior of these particles however is that between B fields of 0 to 100 Tesla, most of the particles examined show a net decrease in the impact energy. This general trend implies that the cumulative energy of impact of all charge exchange ions created within the accel grid aperture will decrease with increasing B field up to approximately 100 Tesla for the thruster configuration from Table 4.1. This tendency will become critical to evaluating the overall benefit of grid embedded magnetic fields in reducing charge exchange induced grid erosion.

4.1.2 Charge Exchange Ions Created Between the Screen and Accel Grids

The behavior of several individual particles representing charge exchange ions created both inside and outside the ion beam and between the screen and accel grid of a two grid thruster were examined over a range of axial magnetic fields with peak axial field magnitudes between 0 and 175 Tesla. Once again each of the particles examined was given the mass and charge of singly ionized xenon. The initial axial locations were selected to represent particles originating just aft of the aft surface of the screen grid, midway between the screen and accel grids, and just forward of the accel grid. The radial locations of the particles were the same as those examined for Section 4.1.1 for the particles starting entirely within the ion beam. The radial starting locations for additional particles, some starting within the beam and some starting outside the ion beam were 50, 70, and 90. These values were chosen such that for a particle starting axially near midway between the two grids a radial location of 50 will be just on the edge of the ion beam, and for a particle starting just aft of the screen grid a radial location of 70 will be just on the edge of the ion beam. In all cases a radial starting location of 90 is outside the beam.

In most cases particles originating well within the ion beam and between the two grids exited the simulation at the neutralization plane and did not contact either grid through the full range of magnetic fields considered. Particles that behaved in this fashion will not be discussed further. Some particles that originated within the beam did not impact any of the grids until the axial magnetic field became large. Two examples of this behavior are particles (10,50) and (20,50). Figure 4.8 shows the behavior of particle (10,50).

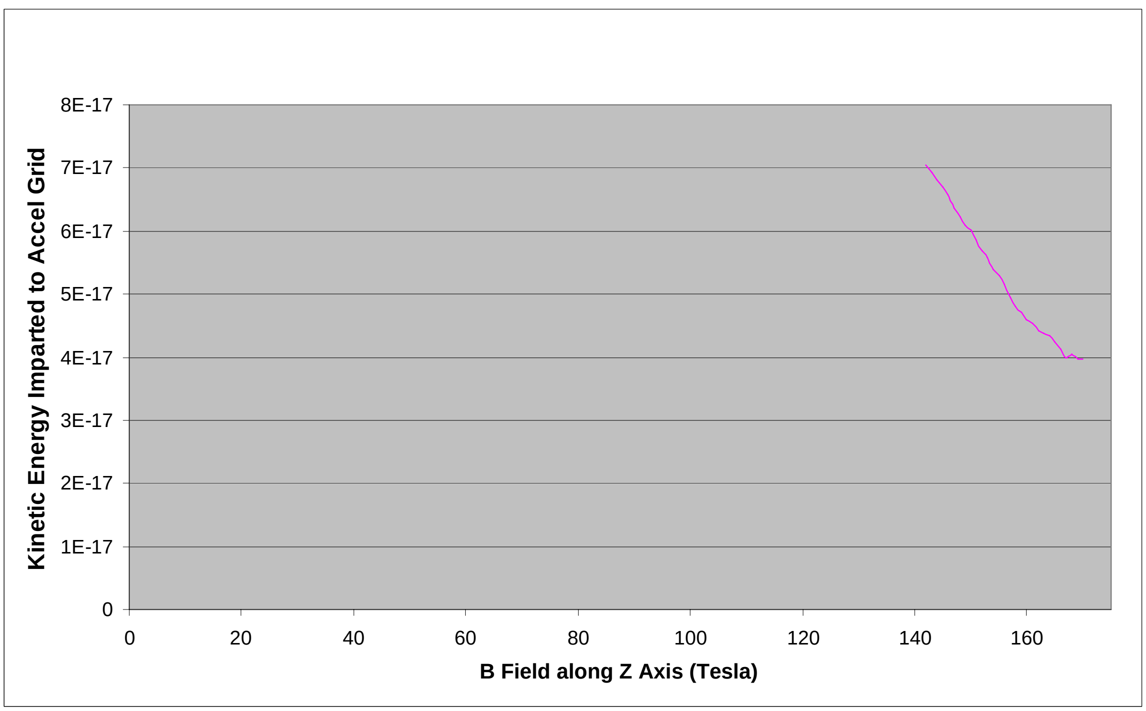

Figure 4.8: Kinetic Energy Imparted to Accel Grid by Particle (10,50)

For particle (10,50) at axial magnetic field strengths below 110 Tesla the final outcome was to exit the neutralization plane. Between 110 and 141 Tesla the particle result was to exceed the allowed number of steps for the simulation, implying that the particle became trapped due to mirroring. Between 142 and 170 Tesla the particle impacted the accel grid aft surface with energies that decreased for increasing B field. Finally, above 170 Tesla the particle once again exceeded the allowed number of steps for the simulation.

Particle (20,50) had an even more erratic behavior over the range of axial B fields examined. Figure 4.9 shows the behavior of particle (20,50). It shows that as in the case of particle (10,50) at low magnetic fields the particle does not impart any energy to the accel gird. However in this case at magnetic fields above 45 Tesla the particle exceeds the simulation step limit up to an axial field strength of 61 Tesla. Above 61 Tesla the particle has very erratic behavior, sometimes impacting the accel grid forward surface, sometimes the accel grid aft surface, and sometimes inside the accel grid aperture. Within the range of magnetic fields between 62 and 175 Tesla this particle also has ranges of fields wherein it also exceeds the simulation step limit.

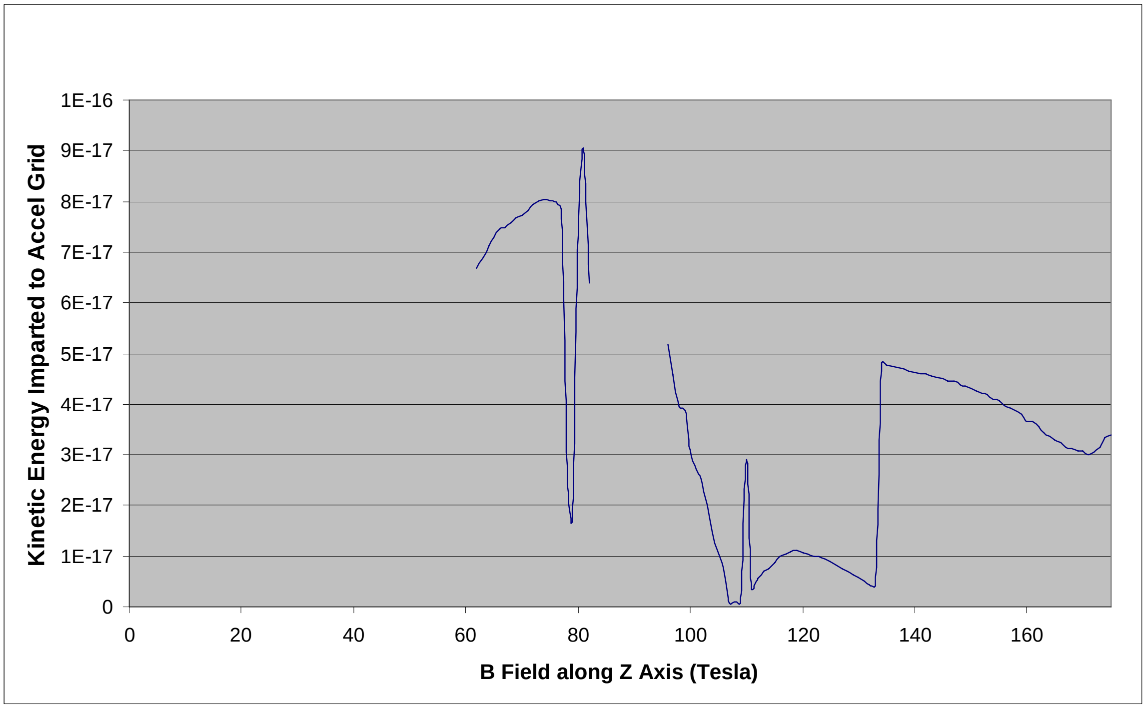

Figure 4.9: Kinetic Energy Imparted to Accel Grid by Particle (10,50)

The behavior of the remaining particles breaks down into two categories determined by whether the particle began within or outside the ion beam. Particles initially created within the beam exhibited behavior similar to that demonstrated by particles discussed in the previous section in that they were influenced by the presence of the magnetic fields. This was shown by either exponential roll off type behavior or erratic behavior. The particles which were created outside the ion beam had impact energies with the accel grid which were only modestly influenced by the increasing magnetic field, or not influenced at all. Figure 4.10 shows the cumulative results for particles that always impacted the accel grid and the impact on the kinetic energy imparted to the accel grid of axial magnetic fields between 0 and 175 Tesla.

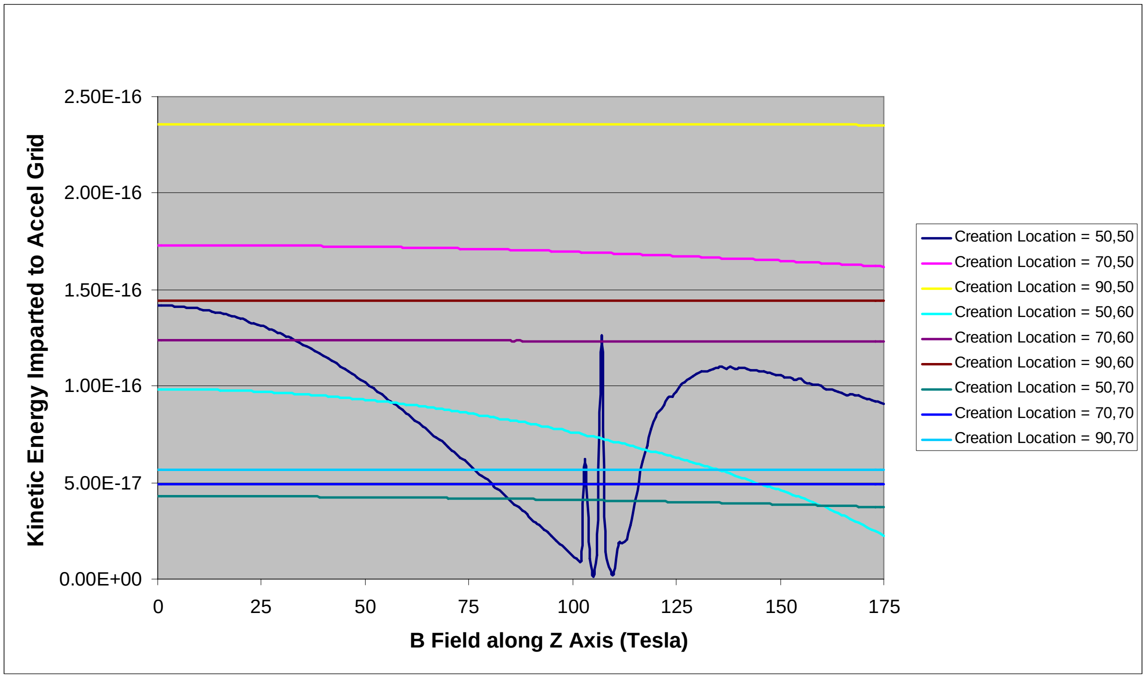

Figure 4.10: Charge Exchange Ions Created Between the Screen and Accel Grids of a Two Grid Thruster Which Always Impact the Accel Grid

4.1.3 Charge Exchange Ions Created Aft of the Accel Grid in a Two Grid Thruster

Individual particles representing charge exchange ions created both within and outside the ion beam and aft of the accel grid of a two grid thruster were simulated over the range of magnetic fields between 0 and 175 Tesla. The particles examined started at radial locations of 10, 20, 30, 40, 50, 70, and 90 and axial locations from 110 which is just aft of the accel grid to 290 in 20 cell node increments. These particles represent charge exchange ions that might be created in the exhaust plume of a two grid thruster.

Behavior of these particles breaks down similarly to that for the particles forward of the accel grid in that particles generated within the ion beam are significantly effected by the presence of the auxiliary magnetic fields while particles created outside the beam are only modestly effected or not impacted at all by the fields within the range of field strengths examined. Figure 4.11 shows the resulting impact energies for charge exchange ions examined with starting locations inside the ion beam and axial location between 110 and 130.

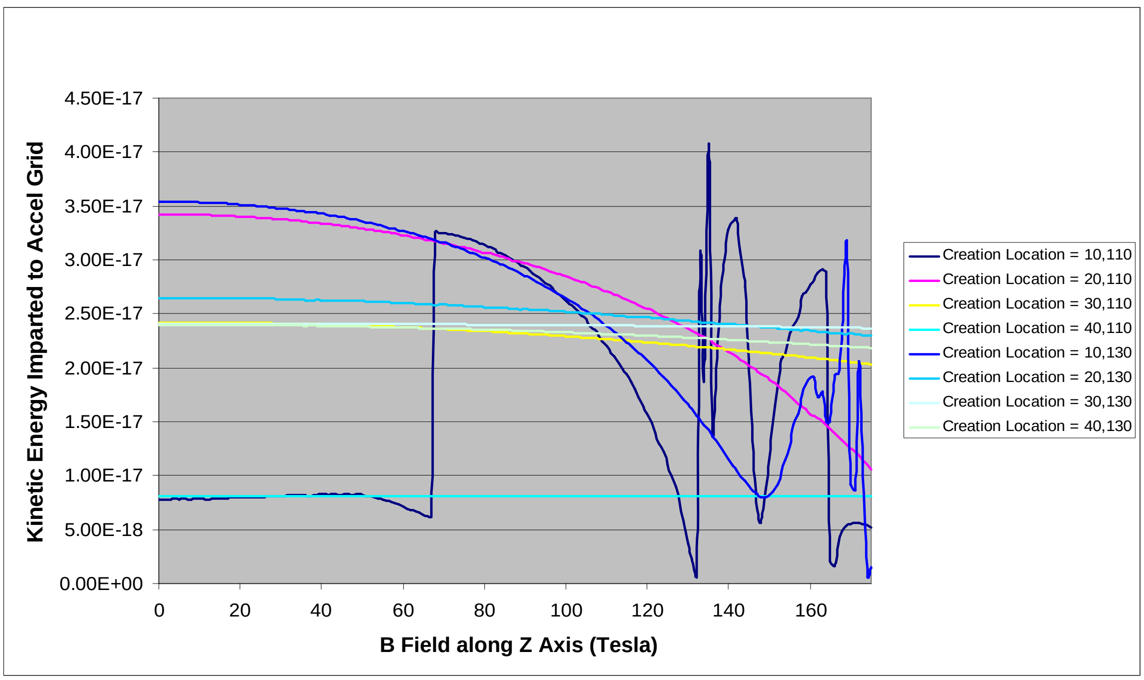

Figure 4.11: Impact Energies for Particles Created within the Ion Beam and Aft of the Accel grid for a Two Grid Thruster (Axial Locations 110 and 130)

Figure 4.11 shows the degree to which an increase in axial magnetic field impacts the energy imparted to the accel grid. The discontinuity in the graph for particle (10,110) results when the turning of the trajectory of the particle allows the particle to miss impacting the accel grid aft surface and it instead impacts the accel grid in the aperture.

Figure 4.12 shows the same information for particles originating within the ion beam and from axial locations 150 and 170.

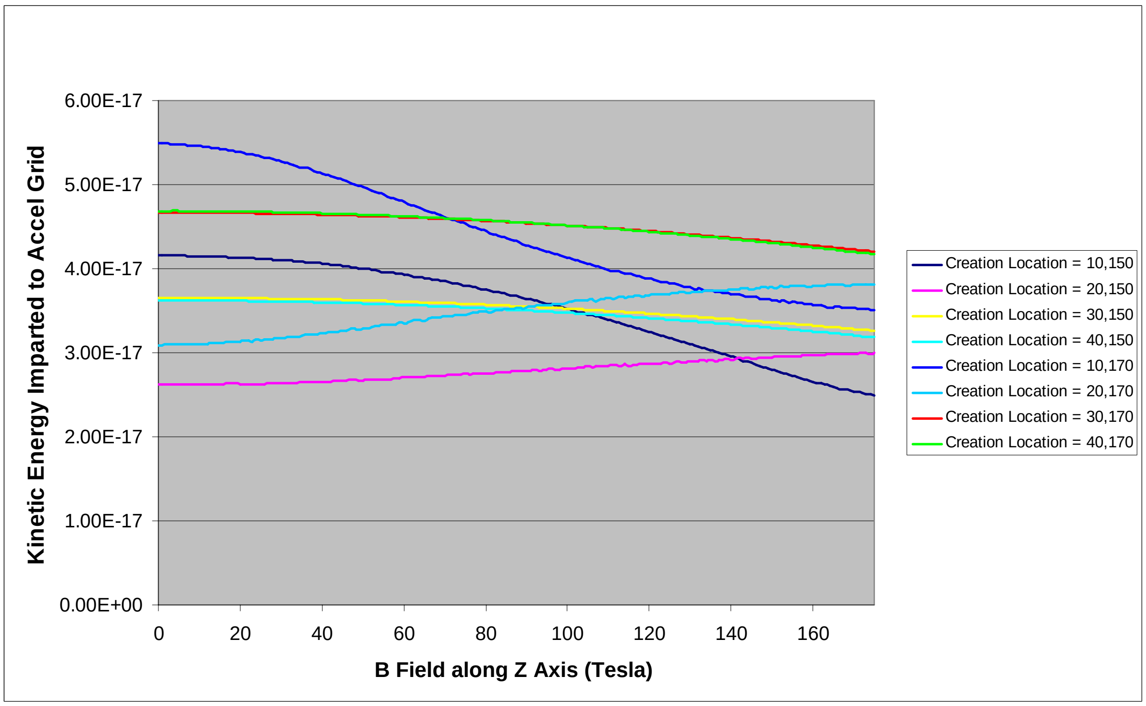

Figure 4.12: Impact Energies for Particles Created within the Ion Beam and Aft of the Accel grid for a Two Grid Thruster (Axial Locations 150 and 170)

Figure 4.12 shows the particle's behavior clearly breaking down into the Exponential Decrease category and the Gradual Increase category described in Section 4.1.1.

Figure 4.13 adds particles at radial distance 50 since by axial location 190 the beam has expanded such that radial position 50 is just on the edge of the beam. It shows data for particles created at axial locations 190 and 210.

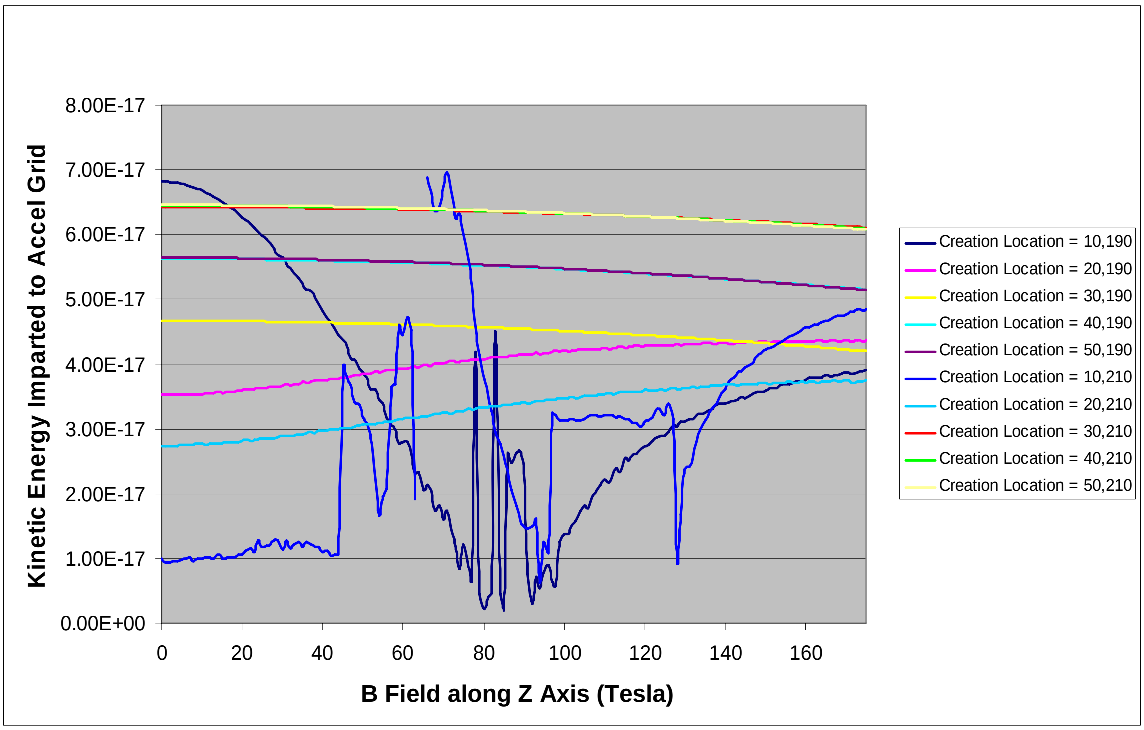

Figure 4.13: Impact Energies for Particles Created within the Ion Beam and Aft of the Accel grid for a Two Grid Thruster (Axial Locations 190 and 210)

Figure 4.13 shows that by a point approximately one accel aperture diameter aft of the accel grid particles originating near the centerline exhibit Erratic Category behavior. This indicates that modest variation in the magnetic field strength greatly changes the path and thereby impact energy of these particles.

Progressing further aft of the accel grid Figures 4.14 shows the behavior of particles from 230 to 250 grid cells from the accel grid. These particles are from within the ion beam ranging out to grid node 50 from the centerline.

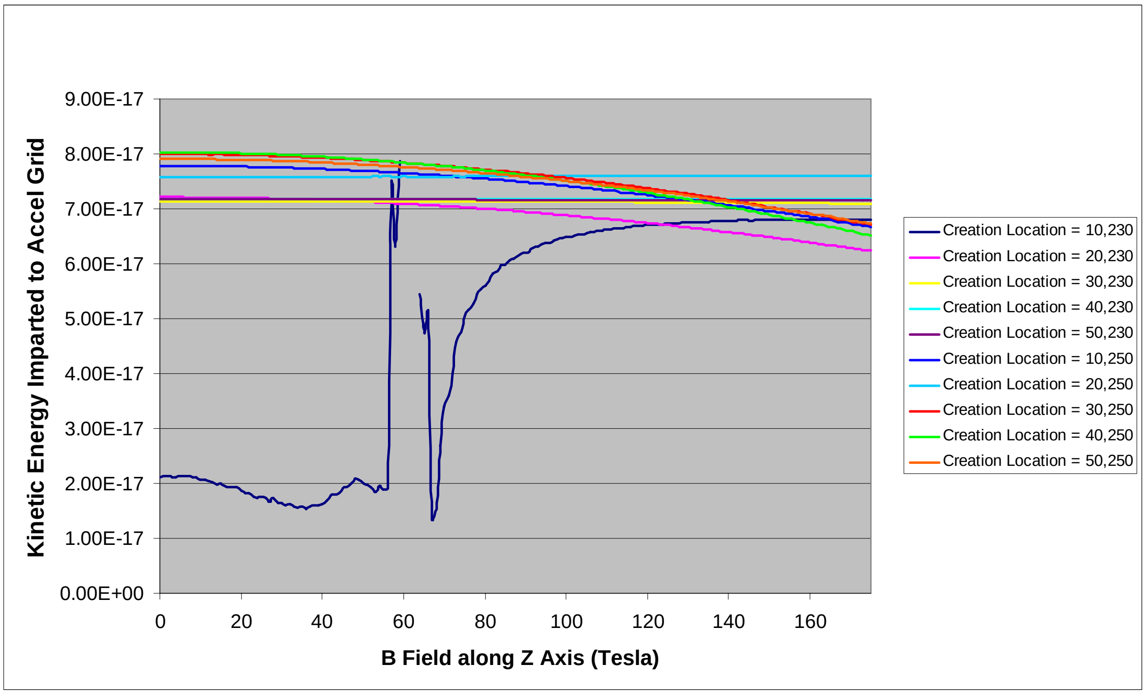

Figure 4.14: Impact Energies for Particles Created within the Ion Beam and Aft of the Accel grid for a Two Grid Thruster (Axial Locations 230 and 250)

Figure 4.14 shows that as the particle origination location moves even further aft its only modestly effected by increasing magnetic field strength. Only particle (10,230) created near the axis of the ion beam is significantly affected by changing field strength.

By a point 250 grid cells aft of the accel grid even a particle created near the centerline of the ion beam is only moderately affected at the field strengths examined here.

By a point more than 270 grid cells aft of the accel grid many charge exchange ions join the exhaust beam and exit the simulation at the neutralization plane. This simulation of course assumed full neutralization of the beam by axial grid cell 299. In a real thruster full neutralization would probably not be achieved so close to the grids, but this should only have the implication that the behavior demonstrated by the simulation is in effect an axial compression of the behavior that would be manifested in an actual exhaust plume. Figure 4.15 contains the resulting impact energies for particles created at 270 grid cells aft of the accel grid. It shows particles from the centerline to radial location 50, all inside the ion beam.

Figure 4.15 shows only particles created at axial location 270 as no particle created at axial location 290 or aft impacted the grids at any magnetic field strength. All of the particles generated at or aft of 290 exited the simulation at the neutralization plane. Most of the particles created at axial location 270 also exited the neutralization plane, only particles originating near the edge of the beam (particles (40,270) and (50,270)) impacted the accel grid. These two particles had impact energies that were only moderately affected by the increasing magnetic field strength.

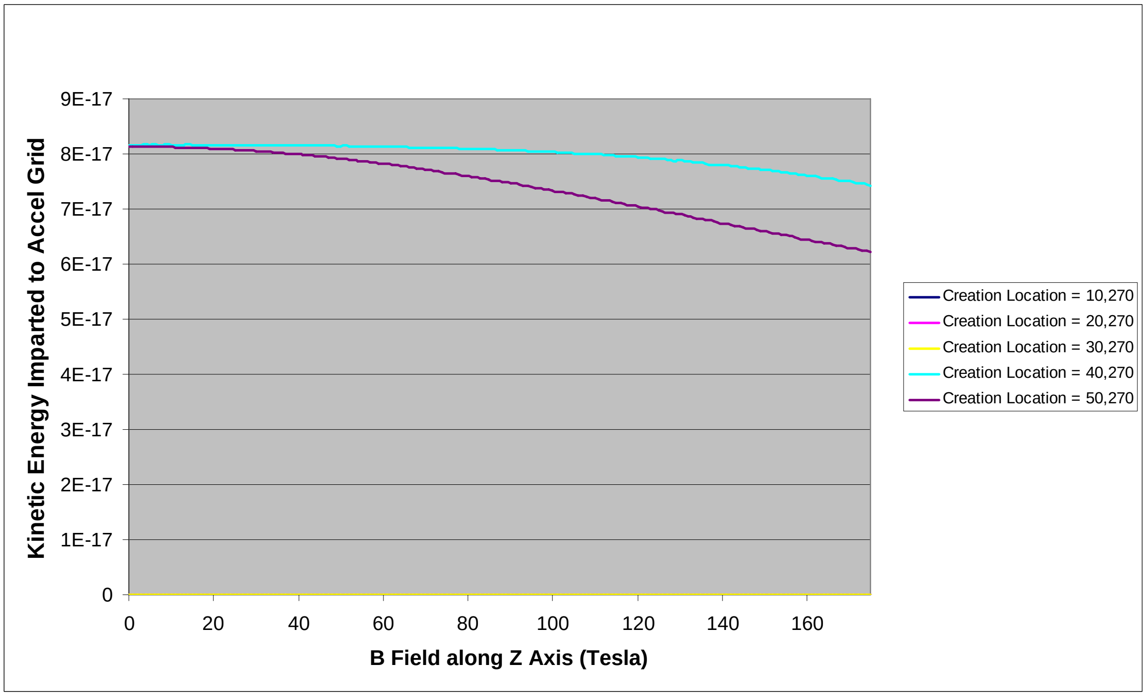

Figure 4.15: Impact Energies for Particles Created within the Ion Beam and Aft of the Accel grid for a Two Grid Thruster (Axial Location 270)

Particles generated outside of the beam and aft of the accel grid were only moderately affected by the magnetic field. This is seen in Figures 4.16, 4.17, 4.18, and 4.19. All of these figures show that the impact energy is only moderately affected by increasing magnetic field and in many cases is not affected at all. One obvious feature of the behavior of these particles is that those created near the aft surface of the accel grid demonstrate almost no influence in their impact energies as a result of the increasing magnetic field. As the axial distance from the accel grid at which the particles are created increases the influence on their impact energy of the magnetic field increases up until a grid location of about 190 or about one accel aperture diameter aft of the accel grid.

Particles created aft of this point show progressively lower sensitivity in their impact energies to the increase in the magnetic field.

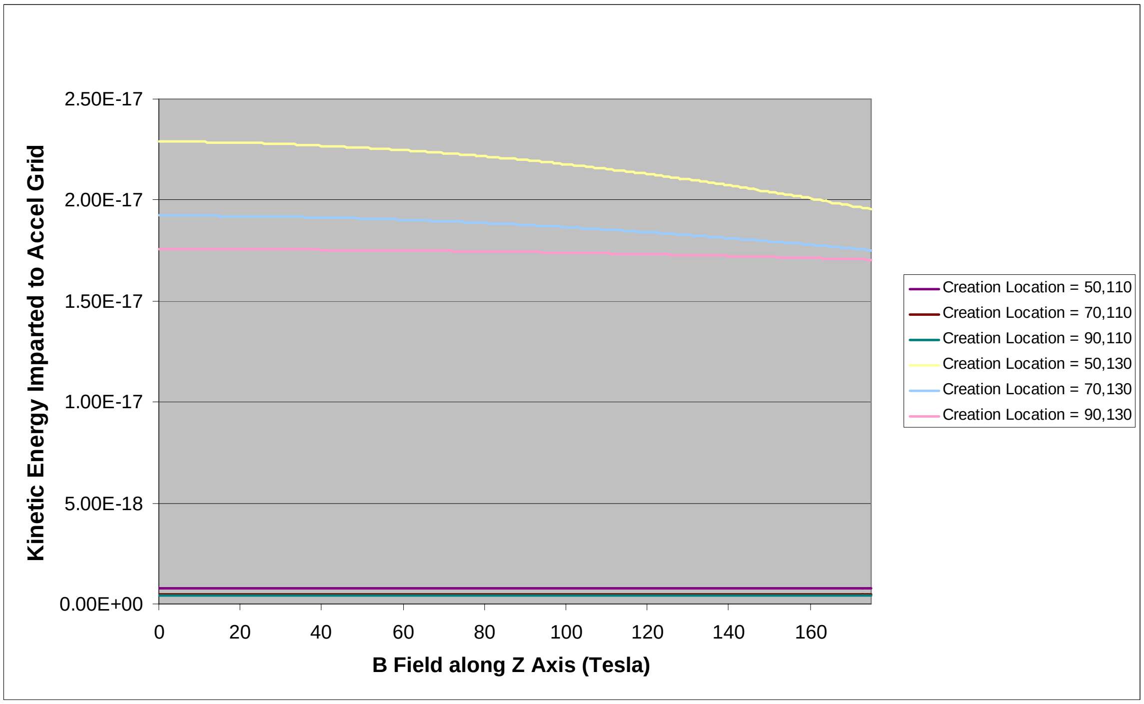

Figure 4.16: Impact Energies for Particles Created Outside of the Ion Beam and Aft of the Accel grid for a Two Grid Thruster (Axial Locations 110 and 130)

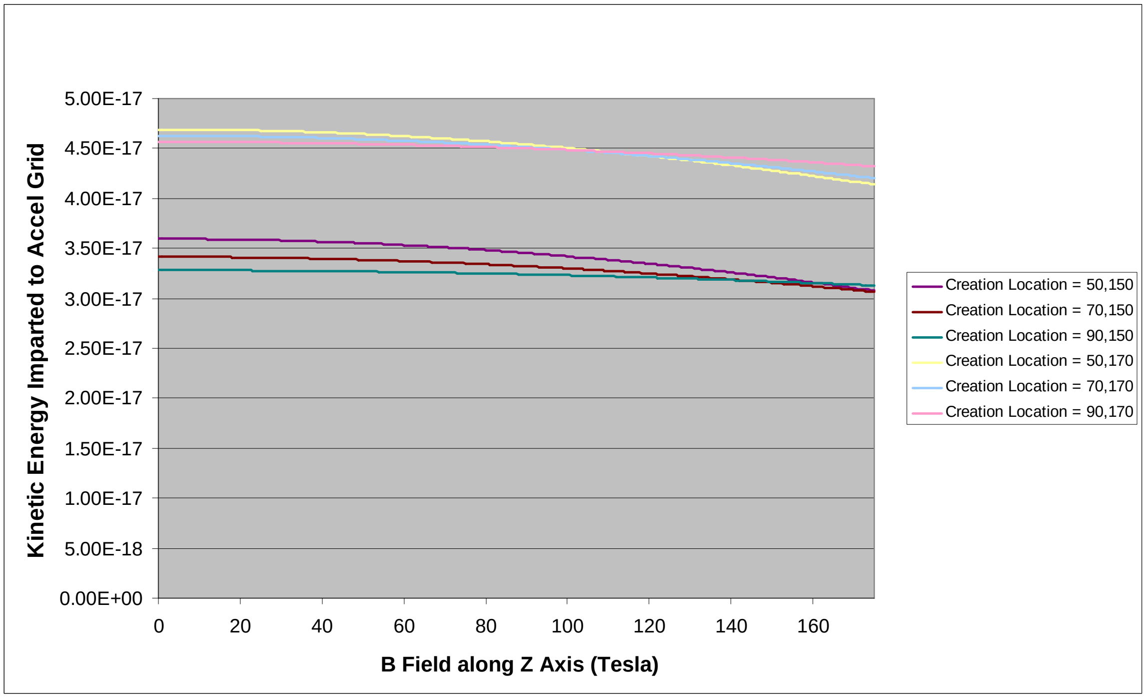

Figure 4.17: Impact Energies for Particles Created Outside of the Ion Beam and Aft of the Accel grid for a Two Grid Thruster (Axial Locations 150 and 170)

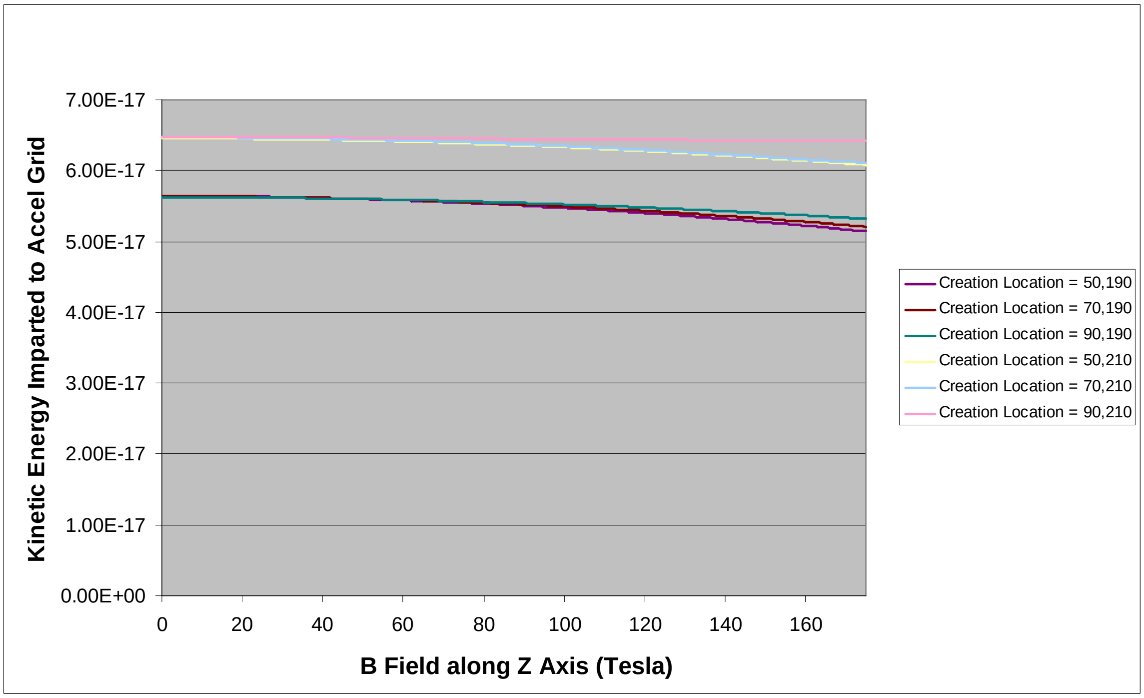

Figure 4.18: Impact Energies for Particles Created Outside of the Ion Beam and Aft of the Accel grid for a Two Grid Thruster (Axial Locations 190 and 210)

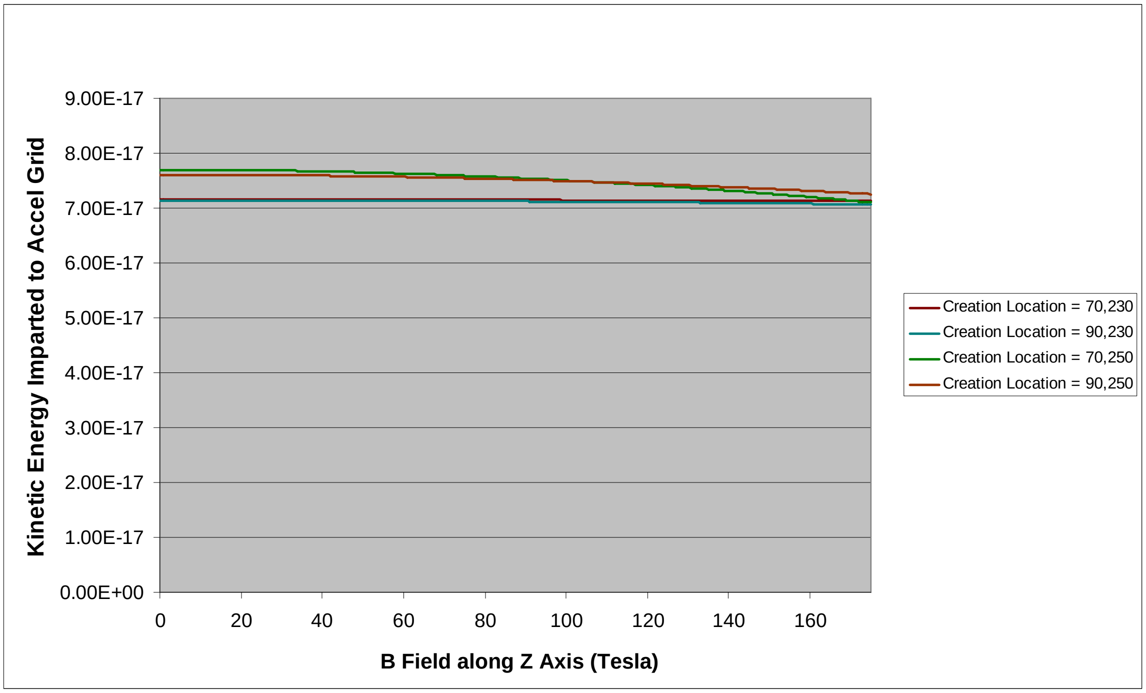

Figure 4.19: Impact Energies for Particles Created Outside of the Ion Beam and Aft of the Accel grid for a Two Grid Thruster (Axial Locations 230 and 250)

4.1.4 Charge Exchange Ions Created Between the Accel and Decel Grids of a Three Grid Thruster

Following the examination of the behavior of individual charge exchange ions in the presence of the grid embedded magnetic field in a two grid thruster an additional decel grid was added to the simulation to investigate the implications for this type of thruster architecture. The simulated thruster for this sequence of program runs was the same as for the two grid individual particle runs described in the previous sections except that a third grid was added aft of the accel grid. This third grid mirrored the screen grid in aperture size, separation distance, and thickness, but had an applied potential of +10V.

In examining the behavior of particles generated axially between the accel and decel grid the same radial distances (10, 20, 30, 40, 50, 70, & 90) were chosen and axial locations representing just aft of the accel grid and just forward of the decel grid were used. Figure 4.20 shows the resulting impact energies for particles originating inside the ion beam.

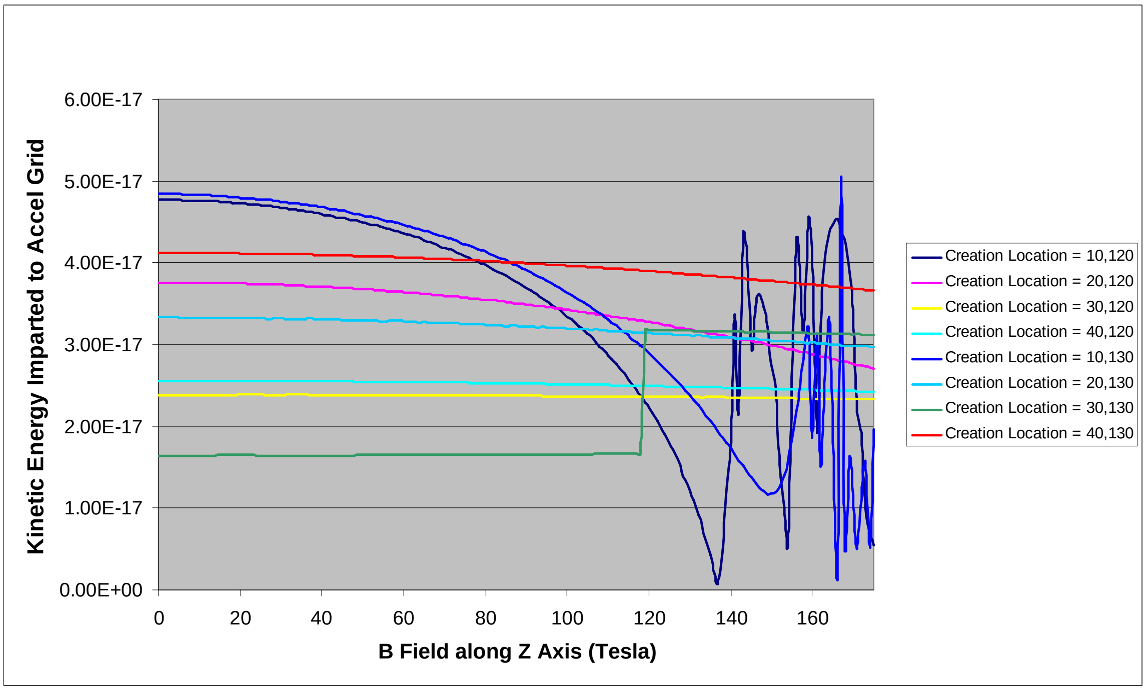

Figure 4.20: Impact Energies for Particles Created Inside of the Ion Beam and Between the Accel and Decel grids for a Three Grid Thruster

This figure indicates that particles originating near the axis of a three grid thruster and between the accel and decel grids have impact energies that are most effected by the additional magnetic field. The discontinuity in the impact energy results for particle

(30,130) happens when the trajectory of the particles changes as a result of the increased magnetic field, to impact on the aft surface of the accel grid instead of inside the accel grid aperture.

Particles originating between the accel and decel grids and outside of the ion beam have impact energy behavior as shown in Figure 4.21.

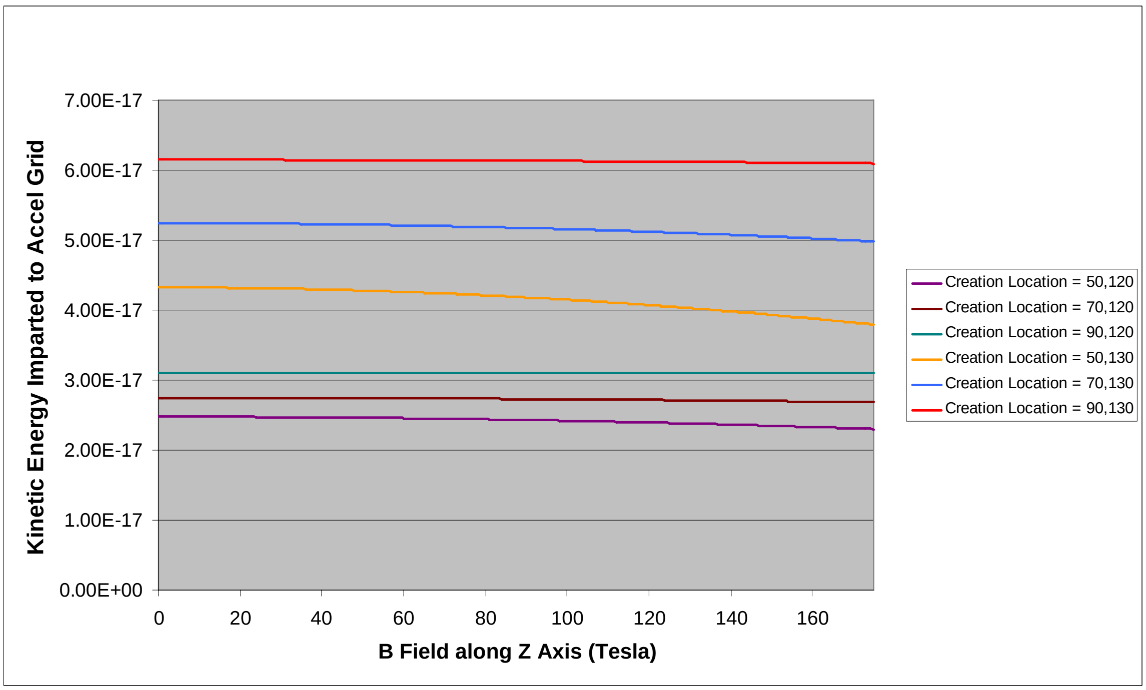

Figure 4.21: Impact Energies for Particles Created Outside of the Ion Beam and Between the Accel and Decel grids for a Three Grid Thruster

In Figure 4.21 it can be seen that the impact of the additional magnetic field on particles created outside of the ion beam is slight. Particles originating away from the current loop which is at approximately the forward edge and radius of the accel grid aperture are least effected (i.e., particle (90, 120) and (90, 130)), While particles originating near the accel grid aperture are more effected (particles (50, 120), (50, 130), (70, 130)).

4.1.5 Charge Exchange Ions Created Within the Decel Grid Aperture

Individual particles representing charge exchange ions created within the decel grid aperture of a three grid thruster were simulated over the range of magnetic fields between 0 and 175 Tesla. The particles examined started at radial locations of 10, 20, 30, and 40 representing charge exchange ions created within the ion beam inside the decel grid aperture. The axial locations selected represented points near the forward edge of the decel grid, near the middle, and near the exit of the decel grid aperture. For this set of evaluations no embedded current loop was used for the decel grid, the only magnetic field was generated at the accel grid embedded current loop.

Figure 4.22 provides the results for the individual particles impact energies over the range of Z axis magnetic fields considered. The figure shows that over the range of applied magnetic fields considered some particles impacted the accel grid with significantly lower kinetic energy as the magnetic field strength was increased. At the same time other particles had slightly increasing impact energies over the same range of magnetic fields. Particles that originated more than half way to the edge of the ion beam had impact energies that initially increased slightly as the magnetic field strength increased, then decreased quickly until a discontinuity is observed over which their impact energy increased significantly. This discontinuity occurred when the particles trajectory no longer caused it to impact inside the grid aperture and it instead impacted on the accel grid aft surface.

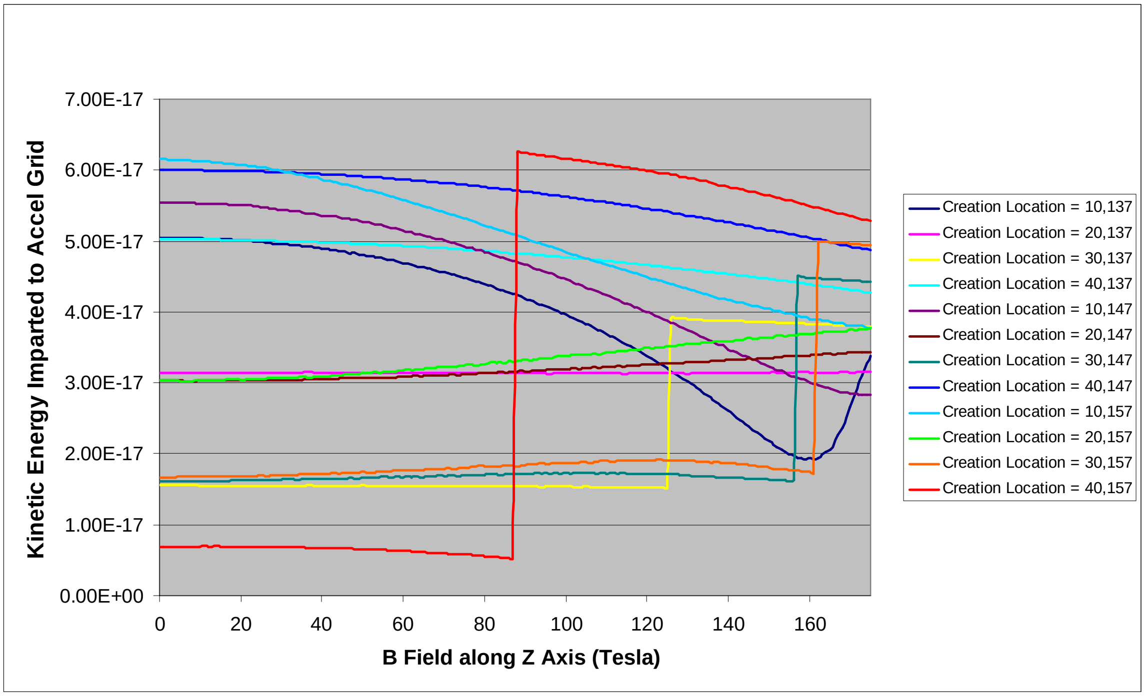

Figure 4.22: Impact Energies for Particles Created Inside of the Ion Beam and Within the Decel Grid Aperture for a Three Grid Thruster

4.1.6 Charge Exchange Ions Created Aft of the Decel Grid

Individual particles representing charge exchange ions created both within and outside the ion beam and aft of the decel grid of a three grid thruster were simulated over the range of magnetic fields between 0 and 175 Tesla. The particles examined started at radial locations of 10, 20, 30, 40, 50, 70, and 90 and axial locations from 170 which is just aft of the decel grid to 290 in 20 cell node increments. These particles represent charge exchange ions that might be created in the exhaust plume of a three grid thruster.

Figure 4.23 shows particles created within the ion beam and at axial locations 170 and 190. The behavior of these particles is more erratic in response to the increasing magnetic field than that observed for the two grid case.

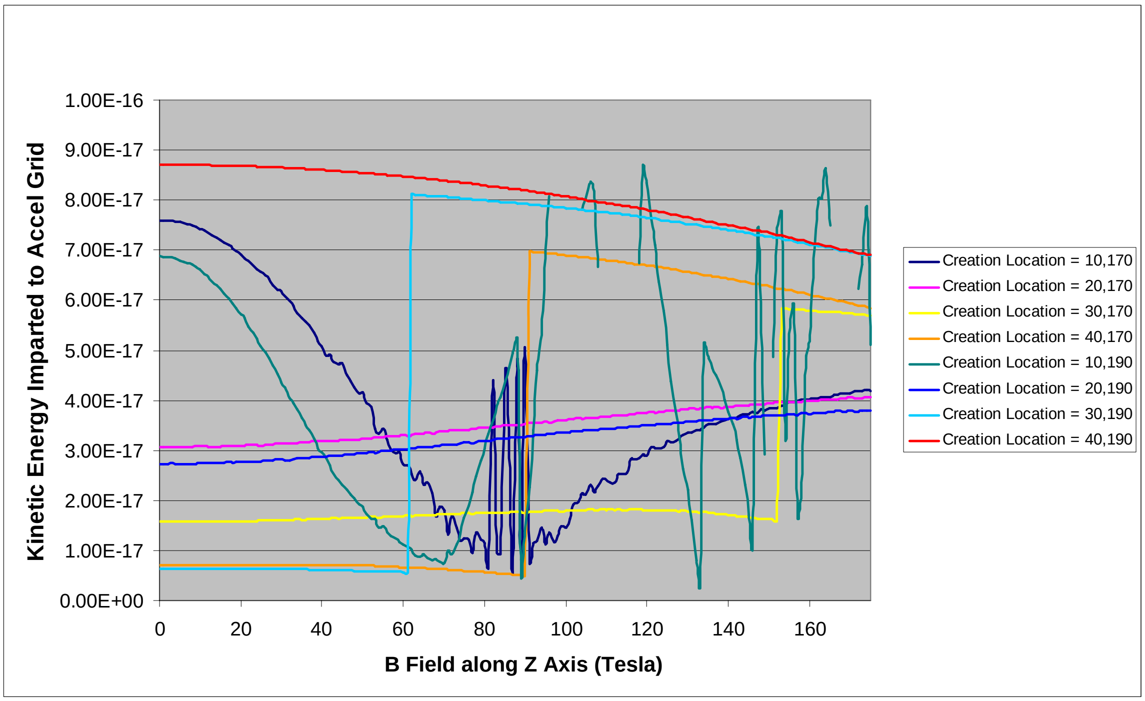

Figure 4.23: Impact Energies for Particles Created Inside of the Ion Beam and Aft of the Decel Grid for a Three Grid Thruster (Axial Locations 170 and 190)

The behavior of these particles can be seen to be highly erratic in response to the increasing magnetic field. This is similar to the behavior observed for particles created just aft of the accel grid in the two grid thruster as shown in Figure 4.11. One important feature of the behavior of these particles is that not all of the impacts are with the accel grid. In some ranges of magnetic field strength some of the particles impact the decel grid rather than the accel grid. For example, between the axial field ranges of 97 to 103 Tesla particle (10,190) impacts the decel grid aft surface. This is shown in Figure 4.23 as a gap in the data. Impacts with the decel grid will be discussed later.

Particles from within the ion beam and created between axial locations 210 and 230 have impact energies with the accel grid shown in Figure 4.24.

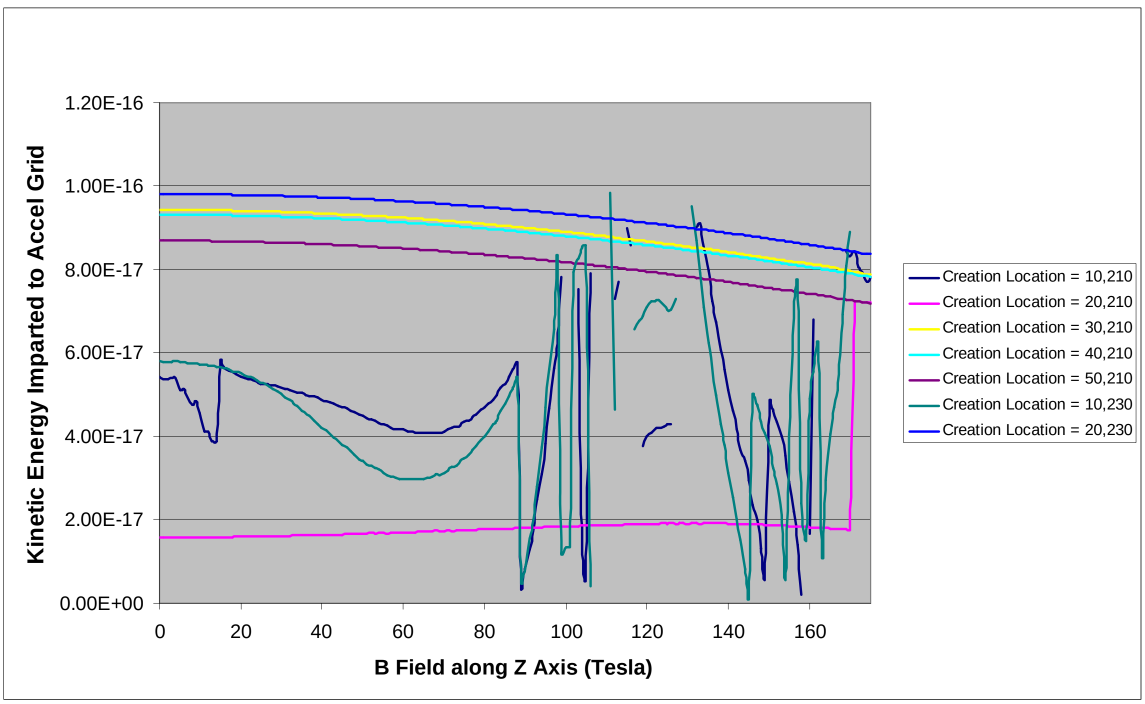

Figure 4.24: Impact Energies for Particles Created Inside of the Ion Beam and Aft of the Decel Grid for a Three Grid Thruster (Axial Locations 210 and 230)

Figure 4.24 shows only those particles that impacted the accel grid at some magnetic field strength. Many particles (particle (30,230) for example) do not impact the accel grid at any magnetic field magnitude. These particles either always impact the decel grid or never impact any grid. For particles created between axial locations 210 and 230, and near the beam axis the impact energy with the accel grid has an erratic response to the increasing magnetic field. Particles near the edge of the beam however always impact the accel grid and have a regular decreasing impact energy in response to the increasing magnetic field.

Particles created aft of the decel grid and outside of but near the ion beam generally impact the accel grid exclusively over the range of axial magnetic fields 0 to 175 Tesla. Figure 4.25 shows the resulting accel grid impact energies for particles created axially between grid locations 170 and 190 and radially from grid locations 50 and 70.

The discontinuities in the impact energy over the increasing magnetic field strength occurs as the particle's trajectories cause them to impact different surfaces of the accel grid. Particle (70,170) for example initially impacts the accel grid forward surface at low axial magnetic fields. At moderate magnetic fields the same particle impacts the accel grid in the grid aperture. At high magnetic field strengths particle (70,170) impacts the accel grid aft surface.

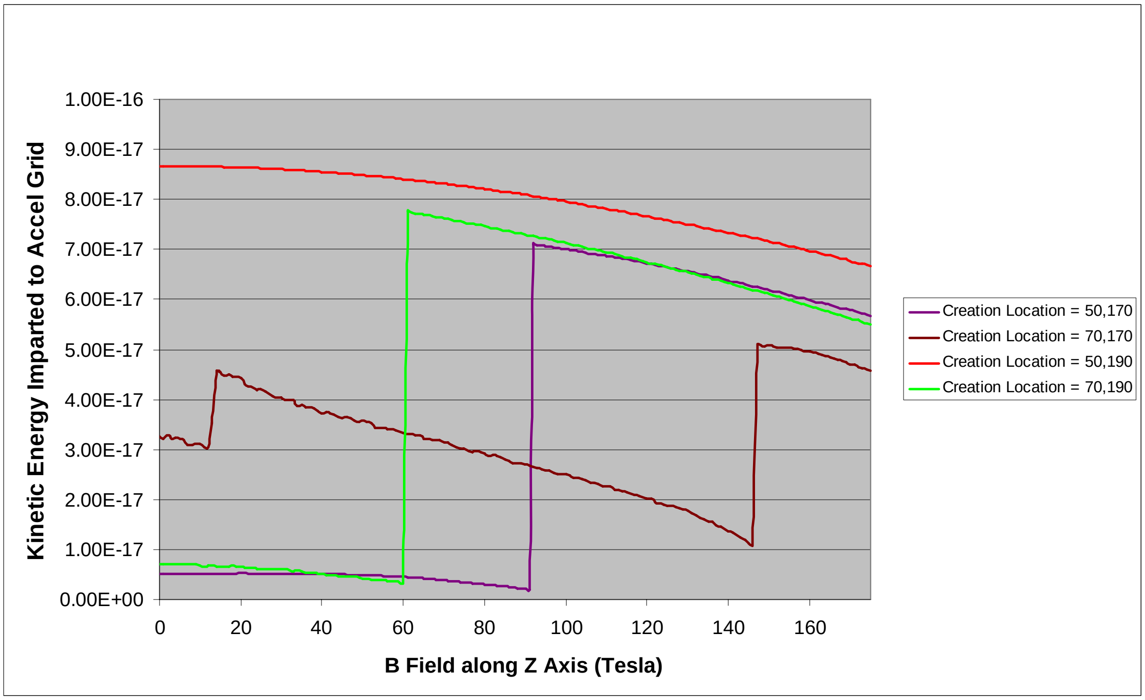

Figure 4.25: Impact Energies for Particles Created Outside of the Ion Beam and Aft of the Decel Grid for a Three Grid Thruster (Axial Locations 170 and 190)

Particles created aft of the decel grid and away from the ion beam impact the decel grid. Figure 4.26 shows the particles that impact the decel grid and their energies

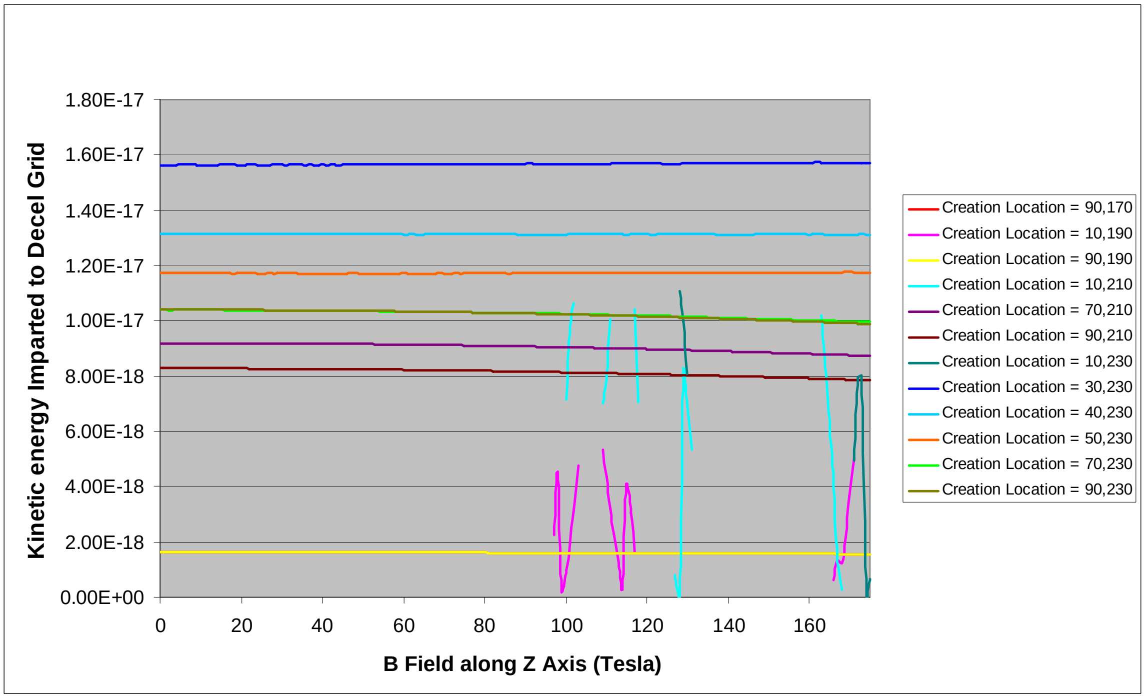

Figure 4.26: Decel Grid Impact Energies for Particles Created Aft of the Decel Grid for a Three Grid Thruster

No particles created at or aft of grid location 250 impacted either the accel or decel grid for a three grid thruster at any axial magnetic field strength.

4.1.7 Comparison of Individual Particle Results for Single and Multiple Current Loops

All of the test cases so far discussed for individual particle behavior in the presence of axial grid aperture embedded magnetic fields are for fields generated at the forward surface of the accel grid only. This is true for both the two and three grid test cases. The implications of using three current loops and thus having magnetic field generated at each grid will be discussed in more detail in Section 4.2; however some individual particle results will be described here.

Figure 4.27 shows a comparison of the accel grid impact energies for particle (10,120) for the three grid simulation described in Table 4.2 but for two different cases, one with grid embedded fields generated at each grid, and one with the embedded field generated only at the accel grid. In both of these cases the B field strength against which the impact energy is compared is the peak axial field strength. In both cases this is the field measured at the forward surface axial location and centerline of the accel grid aperture. For the 3 grid current loop case, the currents for all three loops (screen, accel, and decel) are the same. In other words if a one Amp current is running in the accel grid current loop, then a one Amp current is used in the screen grid current loop and a one Amp current is running in the decel grid current loop. This and the fact that the screen and decel current loops have larger radii than the accel grid loop allow for establishing that the peak axial field will be at the radial center of the accel grid current loop in the three current loop case just as it is for the accel grid current loop only case.

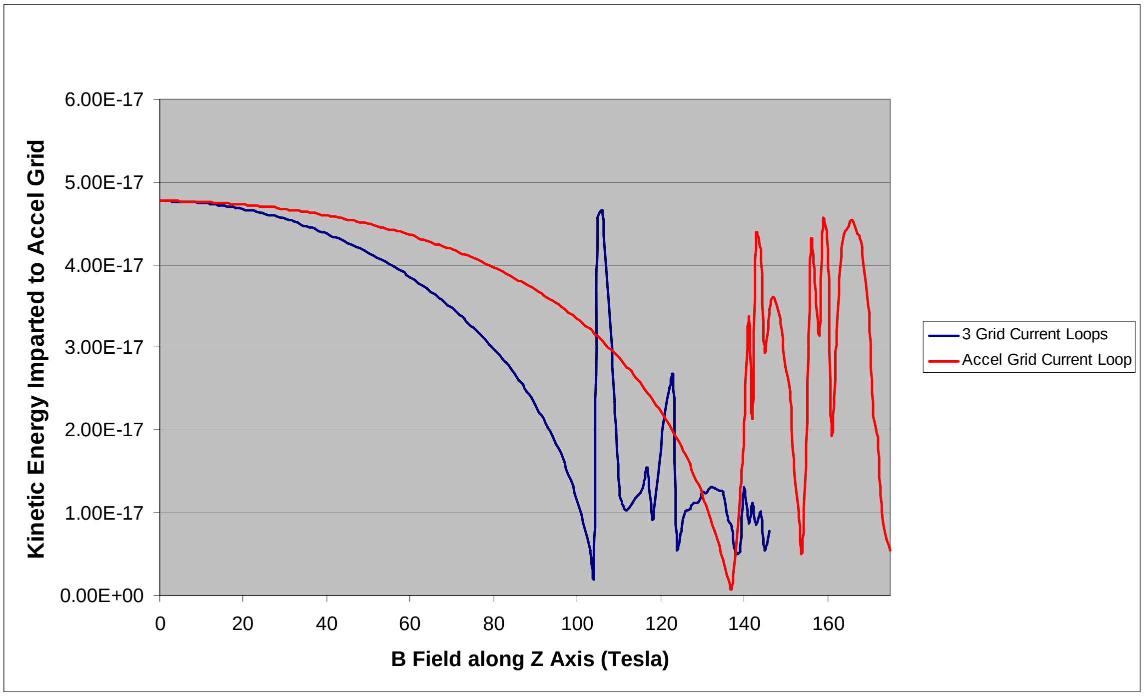

Figure 4.27: Accel Grid Impact Energies for Particle (10,120) With 3 Grid B Fields and Just Accel Grid Field

Figure 4.27 shows that for a particle originating within the accel grid aperture and near the axis of the ion beam the minimum impact energy is achieved at a lower axial field strength for a three current loop simulation.

Figure 4.28 shows that particles created near the centerline and within the decel grid aperture have similar behavior to those created within the accel grid aperture for the three grid current loop case.

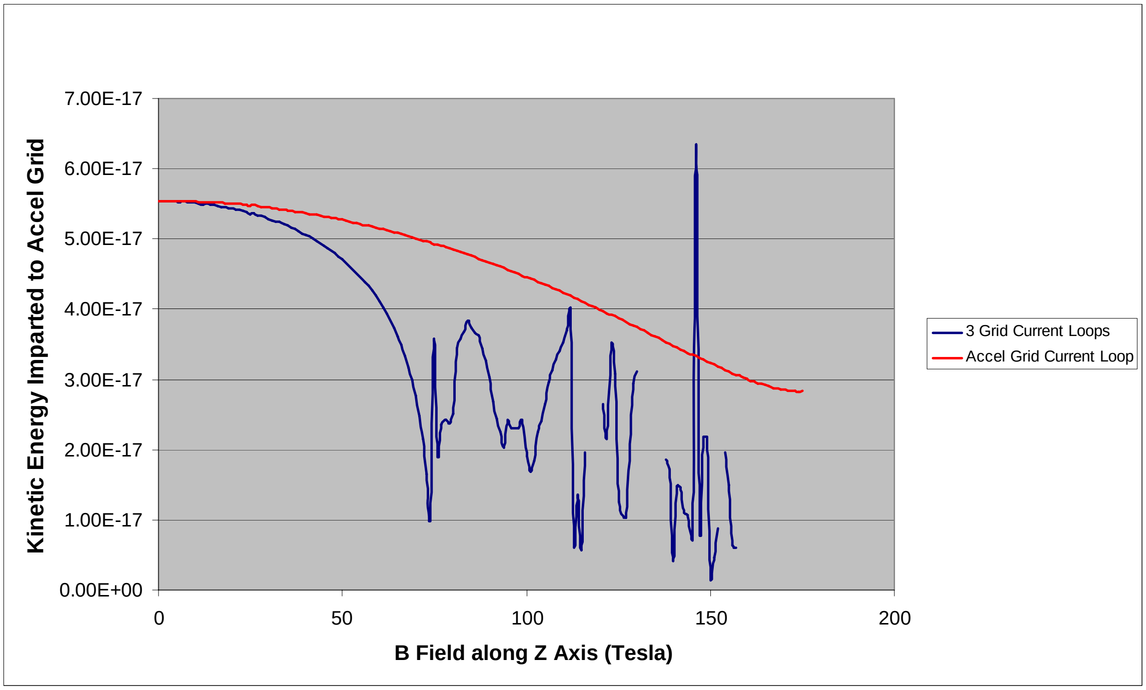

Figure 4.28: Accel Grid Impact Energies for Particle (10,147) With 3 Grid B Fields and Just Accel Grid Field

Figure 4.29 shows the resulting accel grid impact energies for a representative particle from aft of the decel grid in a three grid thruster, in this case particle (10,210). For the case of a single current loop at the accel grid the particle initially impacts the accel grid, but at some ranges of higher B field impacts the decel grid instead. This is not the case for the three current loop test run. For three current loops the particle always impacts the accel grid. Gaps in the data in some cases for the accel current loop test and in all cases for the three current loop case represents test runs where the particle exceeded the step count limitation of the simulation (i.e., more than 10,000 steps).

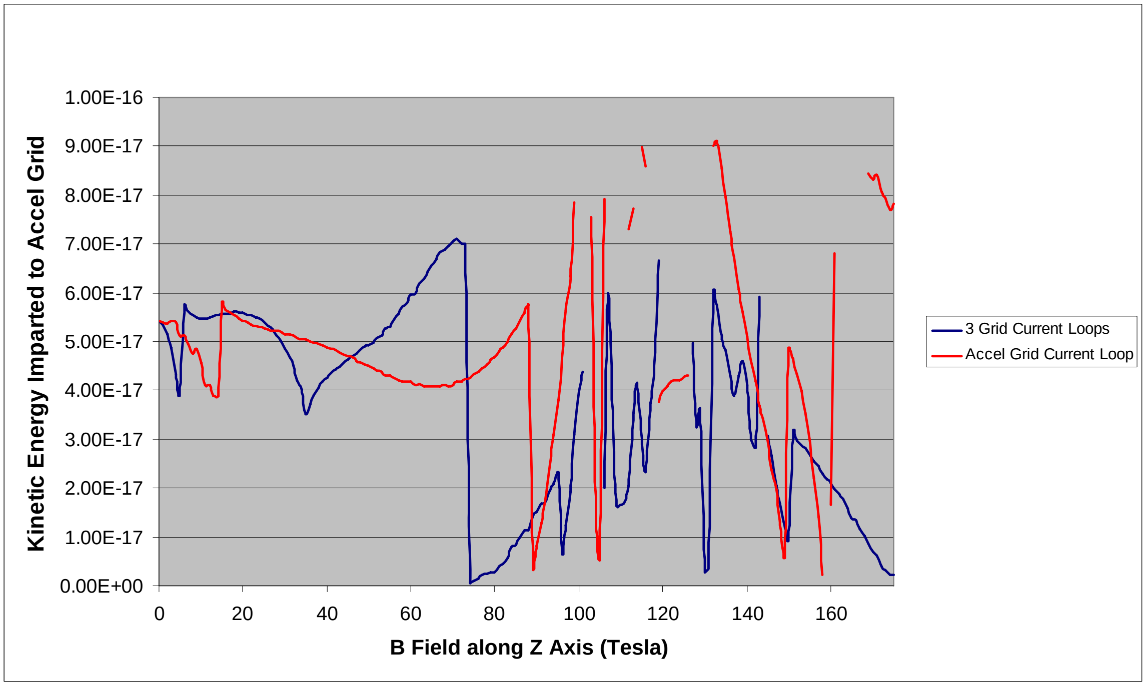

Figure 4.29: Accel Grid Impact Energies for Particle (10,210) With 3 Grid B Fields and Just Accel Grid Field

Once again, as with the earlier data, discontinuities indicate transitions where the particles go from impacting one surface or portion of the accel grid to a different surface or portion of the grid.

Particles created initially within the decel grid and near the edge of the beam have large discontinuities in their impact energies as was seen in Figure 4.22. Once again this is due to the change in their trajectories due to increasing magnetic field causing them to miss impacting the accel grid aft surface and take longer paths to a final impact on either the accel grid aperture side or forward side. The impact of including current loops in all three grids instead of just the accel grid on these particles is shown in Figure 4.30.

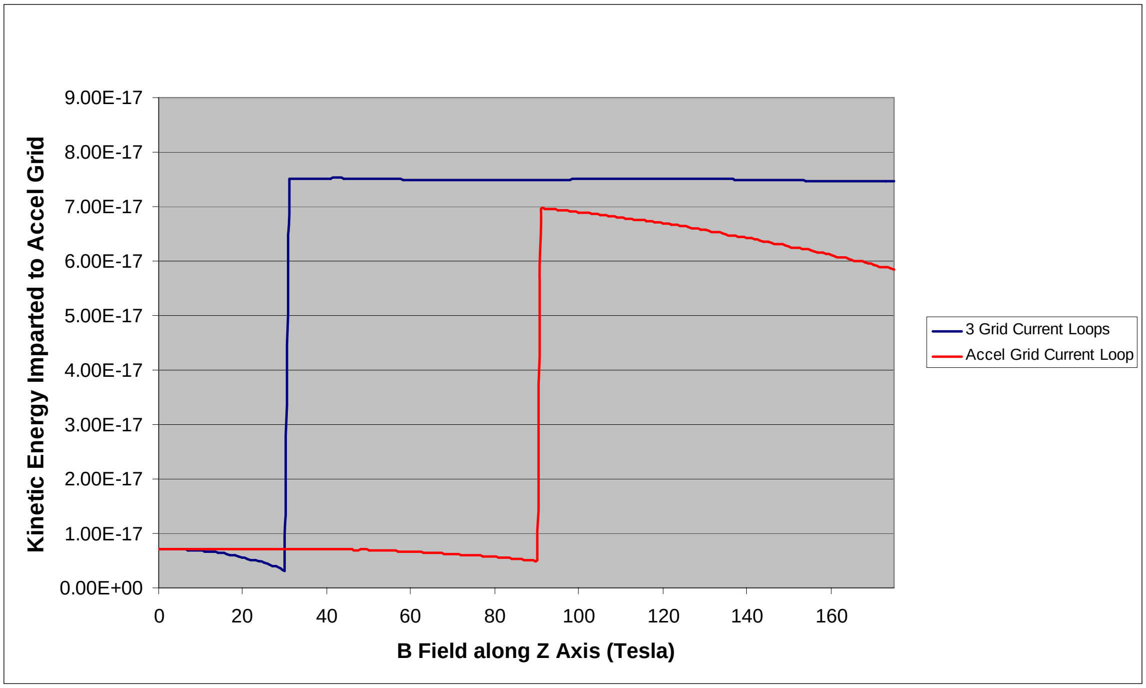

Figure 4.30: Accel Grid Impact Energies for Particle (40,170) With 3 Grid B Fields and Just Accel Grid Field

Figure 4.30 shows that using current loops on all grids causes the impact energy for particle (40,170) to decrease rapidly, but then jump to a higher level and at a lower axial magnetic field strength than for the single accel grid current loop run. The transition in impact energy occurs when the particle no longer impacts the accel grid in the aperture but instead impacts it on the aft surface. The fact that the particle impacts the accel grid aft surface instead of the side of the aperture has potential benefits which will be discussed in a later section.

4.2 Multiple Particle Run Test Case Description and Results

A more thorough examination of the impact on charge exchange ion induced grid erosion of the inclusion of grid embedded axial aligned magnetic fields is accomplished by creating sample charge exchange ions evenly distributed throughout the ion beam and comparing their cumulative grid impact energies over a wide range of applied magnetic fields. Comparisons can then be made by examining total energy imparted to all grids, total energy imparted to each grid, and total energy imparted to each grid region. These would be the ideal means of comparison except that many particles become trapped or nearly trapped and eventually exceed the step count limitations of the program. This limitation can be overcome by comparing each of the above metrics for energy per impacting particle. What is lost in doing this is that some of the particles that might impact the grids at low magnetic fields might not impact the fields at all at high magnetic fields, but are not counted because only those particles that do impact are compared.

For the multiple test particle runs the simulation was configured to represent a Boeing (now L3) 13cm Xenon Ion Thruster. This is a three grid ion thruster used for North-South Station-keeping for geosynchronous communications satellites. The details of the simulation setup and how this thruster is modeled are described in the next section.

The evaluation of grid embedded magnetic fields over multiple particle runs was done for both the case of a current loop embedded in the accel grid only and for current loops in all three grids. In both cases the particles sampled were created at the same points within the simulation ion beam. Particles were created every fifth axial and radial grid node within the ion beam. This gave a total of 481 test particles for each run. As with the individual particle evaluation a separate magnetic field loop was added around the particle loops within the ionLite code. This loop added a multiplier to the existing grid embedded current loop that was sized to iterate at 1 Tesla intervals from 0 to 175 Tesla. This means that for each test all 481 particles were run to completion at a specified magnetic field, then the field increased by 1 Tesla and the particle runs repeated. This resulted in 84656 particle runs to complete each evaluation (1 vs. 3 grid embedded fields).

4.2.1 The Boeing (L3 Communications) 13cm XIPS Thruster

To maximize the realism of the evaluation the simulation was configured to closely match an existing ion propulsion system. The Hughes/Boeing/L3 13cm Xenon Ion Propulsion System is used on the Hughes/Boeing 601HP geosynchronous commercial communications satellite for North-South station keeping. It has been flown on more than a dozen spacecraft and has been in operation for nearly a decade.

The simulation was configured using an input data file that closely matches the grid geometry of the 13cm thruster and the applied electrostatic potentials for the nominal thruster operation. One alteration was made for the decel grid potential in that the simulation uses a positive 30 Volts for the decel grid potential. This differs from the actual but not in a way that would significantly effect the outcome of the simulation. The actual decel grid potential is treated as Boeing proprietary data. The thruster grid parameters were obtained from open source literature. [35,36,37,38] The exact inputs are shown in Table 4.3 which lists the input file parameters.

Radius	1.1e-3	Radius of calculation space
Rsc	87	Radius of the Screen Grid aperture in whole grid nodes
Rac	52	Radius of the Accel Grid aperture in whole grid nodes
Rdc	69	Radius of the Decel Grid aperture in whole grid nodes
Zsc	30	Axial location of the Screen Grid forward surface in whole grid nodes
Zac	80	Axial location of the Accel Grid forward surface in whole grid nodes
Zdc	153	Axial location of the Decel Grid forward surface in whole grid nodes
Tsc	23	Thickness of the Screen Grid aperture in whole grid nodes
Tac	46	Thickness of the Accel Grid aperture in whole grid nodes
Tdc	23	Thickness of the Decel Grid aperture in whole grid nodes
Vplasma	780.0	Plasma Potential
Vsc	750.01	Screen Grid Potential
Vac	-300.01	Accel Grid Potential
Vdc	30.0	Decel Grid Potential
Vnetral	0.0	Neutralization Plane Potential
Isc	0	Screen Grid Loop Current
Iac	91.912	Accel Grid Loop Current
Idc	0	Decel Grid Loop Current
i_start	0	Radial (i) index of first test particle cell
i_inter	5	Radial (i) interval for the run
i_stop	0	Radial (i) index of last test particle cell
j_start	0	Axial (j) index of first test particle cell
j_inter	5	Axial (j) interval for the run
j_stop	298	Axial (j) index of last test particle cell
Temp	500.0	Neutral Particle Temperature (usually discharge chamber temp.)
Uinit_r	1	R component of the initial thermal velocity of all test particles
Uinit_z	0	Z component of the initial thermal velocity of all test particles
Uinit_t	0	θ component of the initial thermal velocity of all test particles
mainF	1	Write the MainOutput.txt file (1 = Yes, 0 = No)
runNumF	1	Write the runNum.txt file (1 = Yes, 0 = No)
velF	0	Write the RTZvelocity.txt file (1 = Yes, 0 = No)
runSumF	1	Write the RunSummary.txt file (1 = Yes, 0 = No)
RposF	0	Write the Rposition.txt file (1 = Yes, 0 = No)
ZposF	0	Write the Zposition.txt file (1 = Yes, 0 = No)
TposF	0	Write the Tposition.txt file (1 = Yes, 0 = No)
RZTposF	0	Write the RZTposition.txt file (1 = Yes, 0 = No)
diagF	1	Write the diagnosticFile.txt file (1 = Yes, 0 = No)
numPosF	0	Write the numbered particle position files (1 = Yes, 0 = No)
shthOn	1	Include plasma sheath (1 = Yes, 0 = No)
beamOn	1	Include Ion Beam (1 = Yes, 0 = No)
shthTh	1.1e-3	Sheath Thickness in grid points
charge	87	Particle charge state, 1 for singly charged ions, -1 for electrons
massNumber	52	Atomic number of the particle

Table 4.3: Input Data for Multiple Particle Runs

Table 4.3 shows that for the initial set of runs only a current loop for the accel grid aperture was included. The current shown, 91.912 Amps, produces a magnetic field strength of 0.1 Tesla at the center of the accel grid aperture.

The actual hardware version of the 13cm thruster produces a thrust of 17.8 mN at an Isp of 2585s. [38]

4.2.2 Varying B Field Strength – Accel Grid Only

In the initial set of multi-particle runs a grid embedded current loop was incorporated only in the accel grid. The current loop, and hence the source of the axial aligned B field was located at the leading (forward) surface of the accel grid. An initial current of 92.912 Amps was set for this current loop resulting in a Z component of magnetic field at the center of the current loop of 0.1 Tesla. The program was configured to loop over charge exchange ions starting at every fifth axial and radial grid node within the ion beam and with a multiplier applied to the accel grid current loop that incremented between 0 and 1750 with an increment value of 10. This resulted in test runs of all the sample particles at each integer magnetic field strength between 0 and 175 Tesla.

An initial review of the results for kinetic energy transfer to all grids over the range of magnetic fields tested indicates very little overall impact to the presence of the axial aligned magnetic field. The total kinetic energy imparted to the grids varies by approximately +7% to -12% over the magnetic fields tested. This can be seen in Figure 4.31 which shows the kinetic energy imparted to all grids for the complete set of particles over the range of magnetic fields from 0 to 175 Tesla.

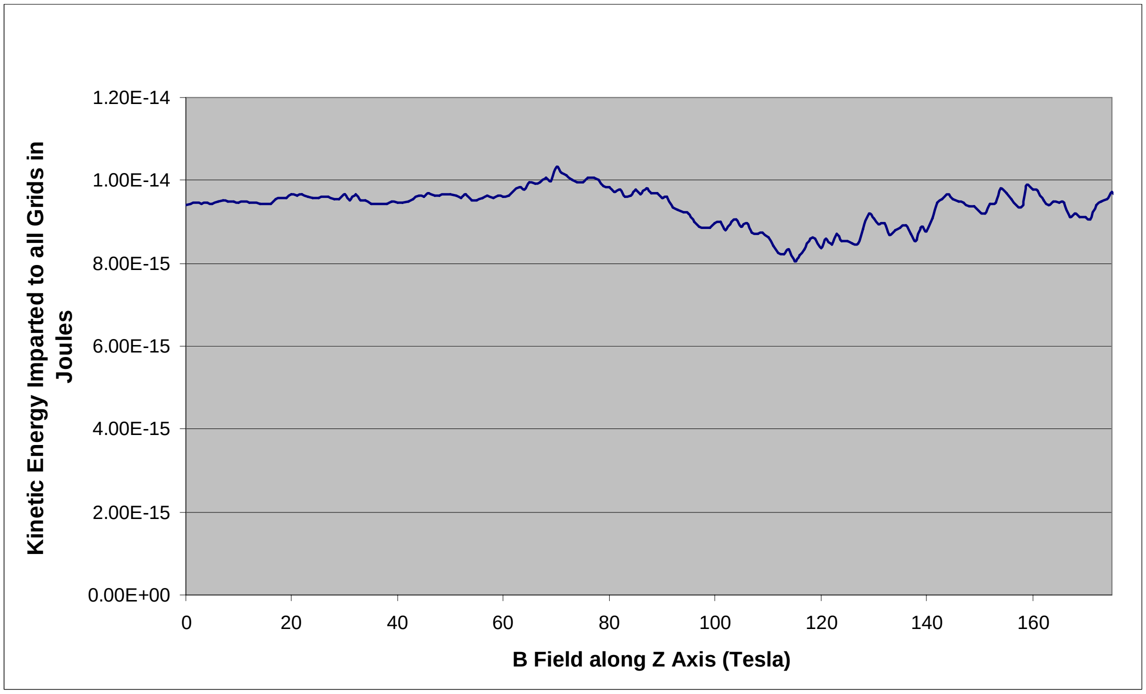

Figure 4.31: Kinetic Energy Imparted to all Grids as a Function of Z Axis B Field

One positive implication of the data indicated in Figure 4.31 is that between approximately 80 and 115 Tesla the kinetic energy imparted to all grids drops by approximately 11.6% from the initial zero B field value.

As stated in Section 1, the main life limiting factor in ion propulsion systems is erosion of the accel grid. It is therefore of great interest how the kinetic energy imparted to the accel grid changes by the addition of the grid embedded magnetic field. It would be expected that in a three grid thruster most of the charge exchange ions would impact the accel grid and that the plot of that energy over the range of magnetic fields being considered would bare a strong resemblance to the total energy profile shown in Figure

4.31, and that is the case. Figure 4.32 shows the total energy imparted to the accel grid for the range of magnetic fields being tested.

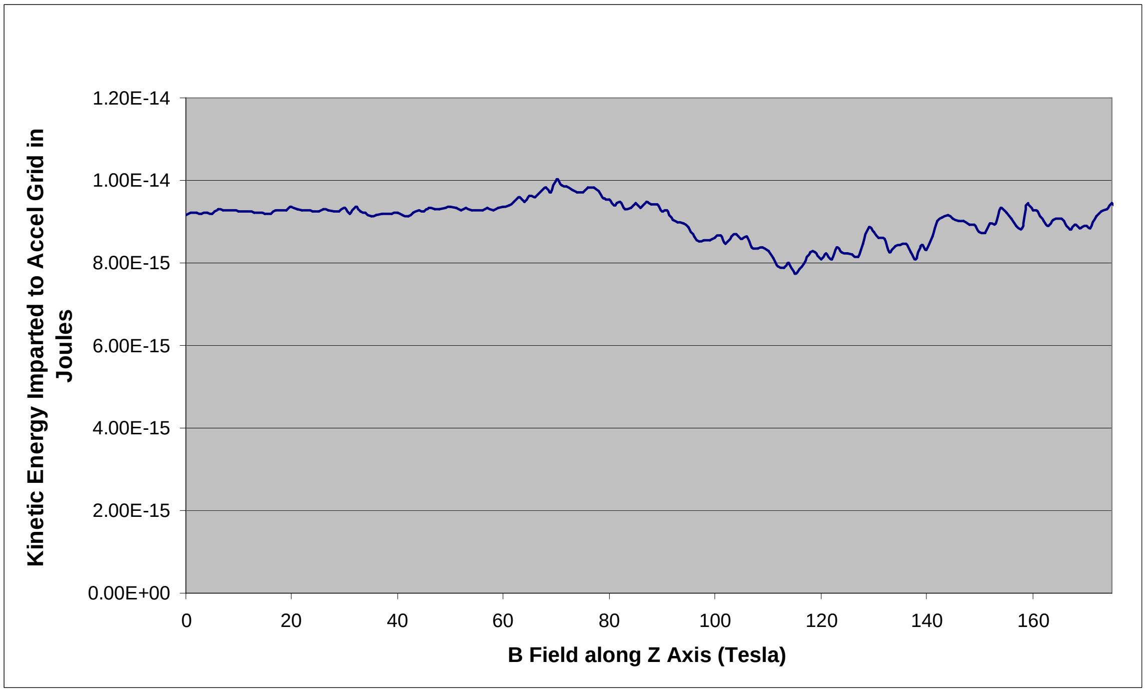

Figure 4.32: Kinetic Energy Imparted to Accel Grid as a Function of Z Axis B Field

Figure 4.32 can be seen to be almost identical to Figure 4.31 with the exception that the small amount of what might be nearly constant energy imparted to the decel grid is removed.

Figure 4.33 shows the energy imparted to the decel grid over the range of magnetic fields investigated for this analysis. It indeed shows that the energy absorbed by the decel grid due to particle impacts is relatively constant over the tested range of fields.

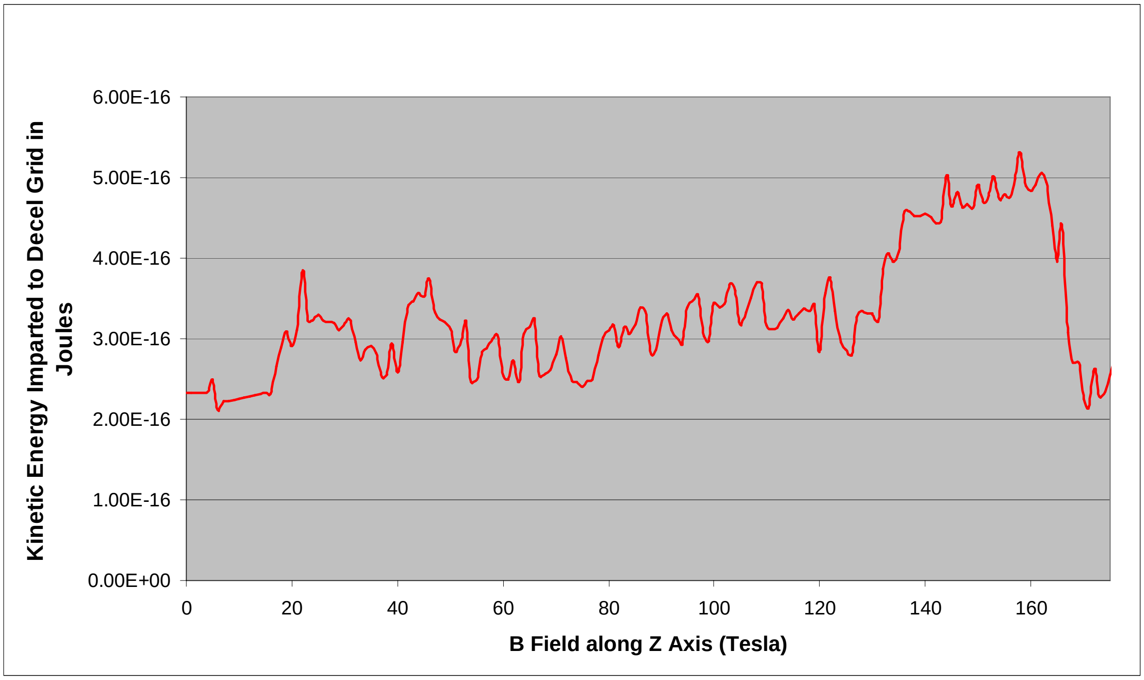

Figure 4.33: Kinetic Energy Imparted to Decel Grid as a Function of Z Axis B Field

The total kinetic energy imparted to the decel grid is more than an order of magnitude less than the energy imparted to the accel grid.

As the magnetic field is increased, more particles become trapped or nearly trapped. These particles end up on longer trajectories before contacting either the accel or decel grids and can eventually exceed the step count limitations of the simulation. In the configuration under consideration here for example, with no B field present no particles exceed the step count limitation, while at 175 Tesla 12 particles exceed the step count limit. For this reason it is useful to examine the impact energy per particle to ascertain the reduction in grid damage that might be obtained by inclusion of the grid embedded magnetic fields.

Figure 4.34 shows the energy per particle impact imparted to all grids. This is simply the total energy indicated in Figure 4.31 divided by the number of particles impacting the screen, accel, and decel grids.

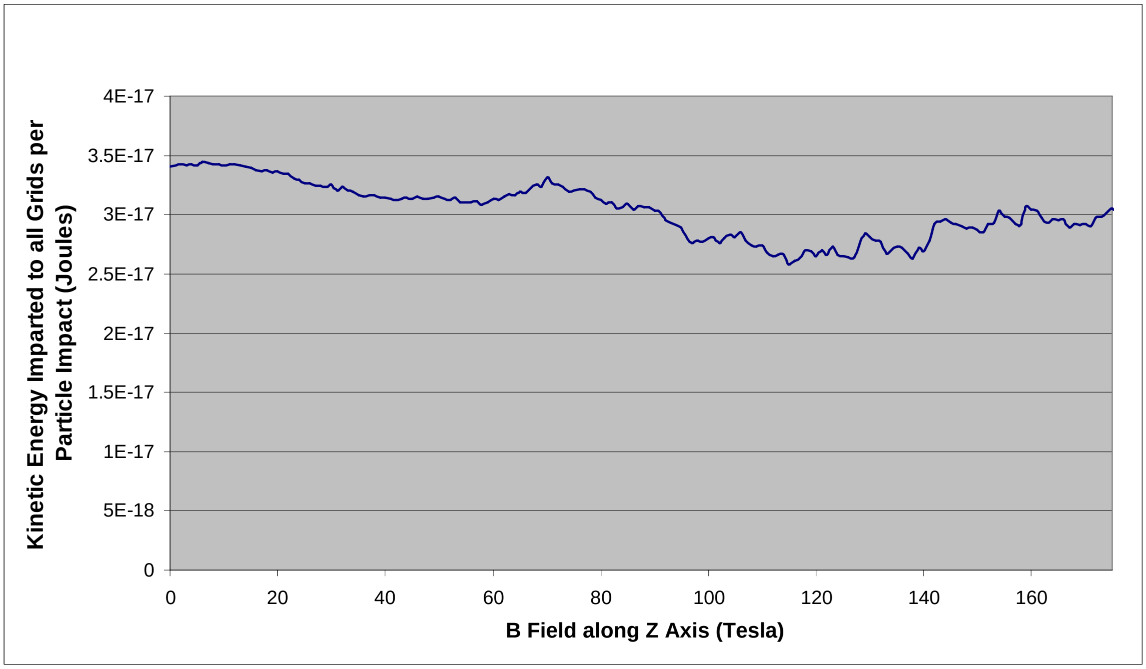

Figure 4.34: Kinetic Energy per Particle Impact for all Grids

Figure 4.34 shows a slight downward trend in the impact energy per particle as the Z axis B field increases, reaching a minimum around 115 Tesla. This represents an reduction in impact energy of approximately 23% between the value with no B field and that at a B field of 116 Tesla.

The kinetic energy imparted to the accel grid per particle impacting the grid is shown in Figure 4.35.

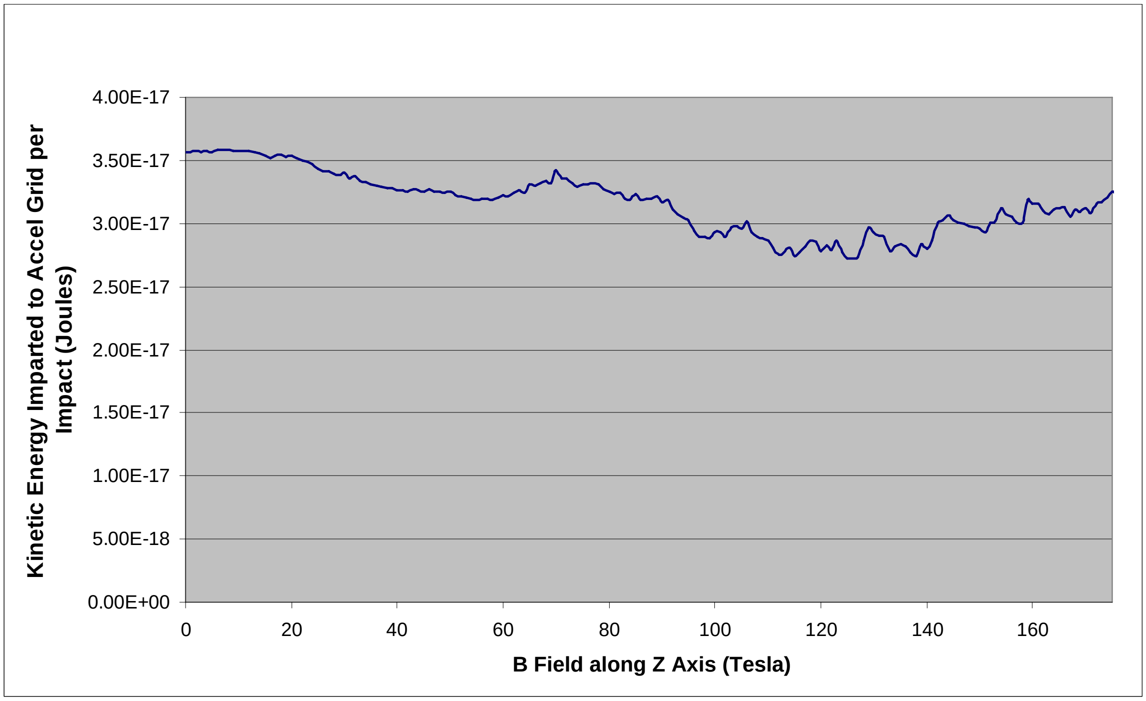

Figure 4.35: Kinetic Energy per Accel Grid Impact

Figure 4.35 shows that there is a 23% reduction in impact energy per particle impact with the accel grid over the range of Z axis magnetic fields from 0 to 126 Tesla.

Decel grid impacts are much less common during the course of the simulation than impact with the accel grid; however the data indicating the energy transfer to the decel grid per impact is a useful measure of the implications for decel grid erosion of inclusion of grid embedded magnetic fields in the accel grid aperture. Figure 4.36 shows the results for kinetic energy imparted to the decel grid per decel grid impact. It can be seen from Figure 4.36 that the impact energy per particle for the decel grid varies only moderately in response to the applied magnetic field. It is also interesting to note that in general the impact energy per particle is approximately half of the impact energy per particle for the accel grid.

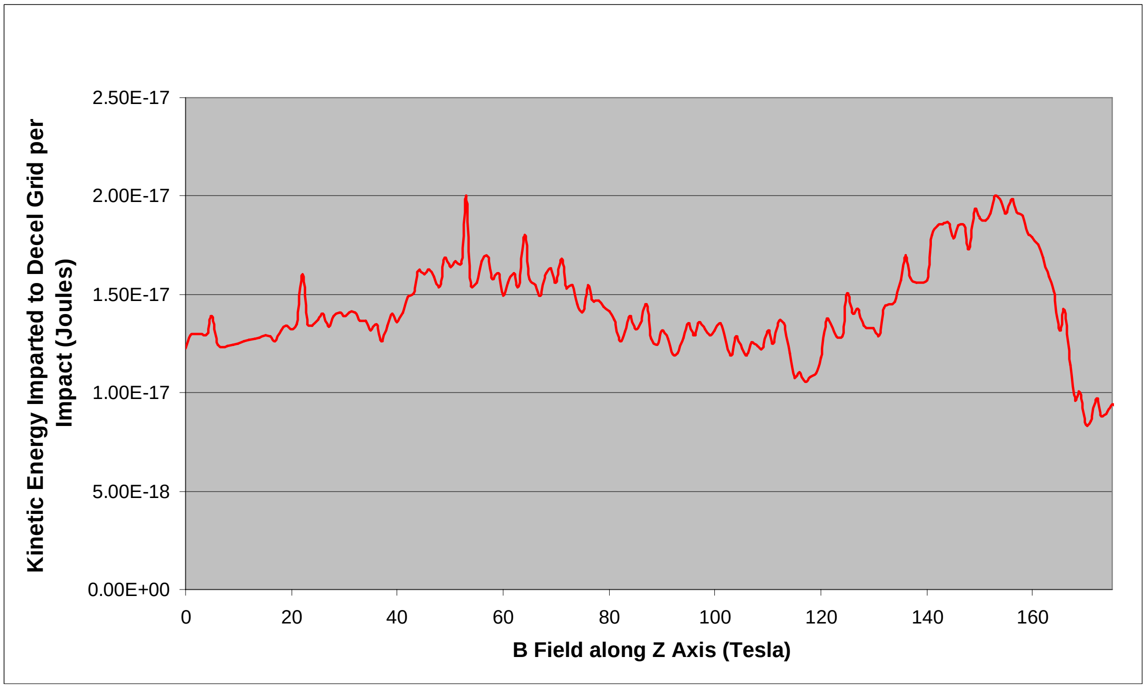

Figure 4.36: Kinetic Energy per Decel Grid Impact

The usefulness of the results contained in this section in predicting the benefits of adding a grid embedded magnetic field to the accel grid will in part be limited by the loss of particles due to the program step count limitation. It is therefore valuable to investigate the implications of these lost particles. Particles that exceed the step count limit are not counted as impacting any grid. Whatever energy they might have as a result of their velocity is therefore not tracked by the program in its current configuration. Their numbers are however tracked, as are the number of particles impacting each grid surface.

It is possible then to reconstruct to a certain degree how these lost particles might effect the results of the investigation of grid embedded magnetic fields by estimating how their energy would change the plots shown in the earlier part of this section.

Figure 4.37 shows the dropped particle count for each run over the range of B fields evaluated. It shows that compared to the total number of particles generated for the simulation, 481, the number of particles that exceed the step count is always less than 3%. This implies that the impact on the final evaluation will be within the range of accuracy of the simulation as discussed in Section 3.5.

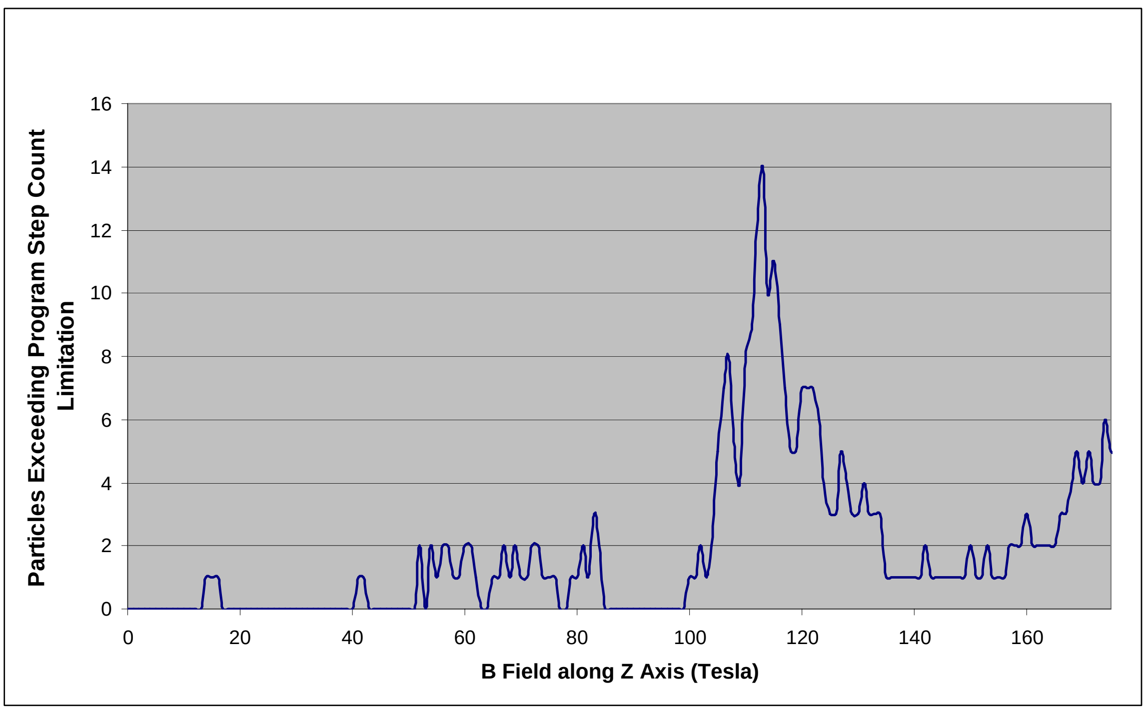

Figure 4.37: Particles Dropped From Computation Due to Exceeding the Program Step Count Limitation

An interesting metric can be generated by examining the total particle impacts for each grid surface over the range of Z axis B fields under consideration. If all of the dropped particles are then assumed to impact each grid surface in each case a worst case assessment can be made. Figure 4.38 displays the total number of particles that impact the accel grid and each grid surface (accel grid forward surface, accel grid aft surface, accel grid aperture) and assumes that in each case all of the dropped particles impact each surface.

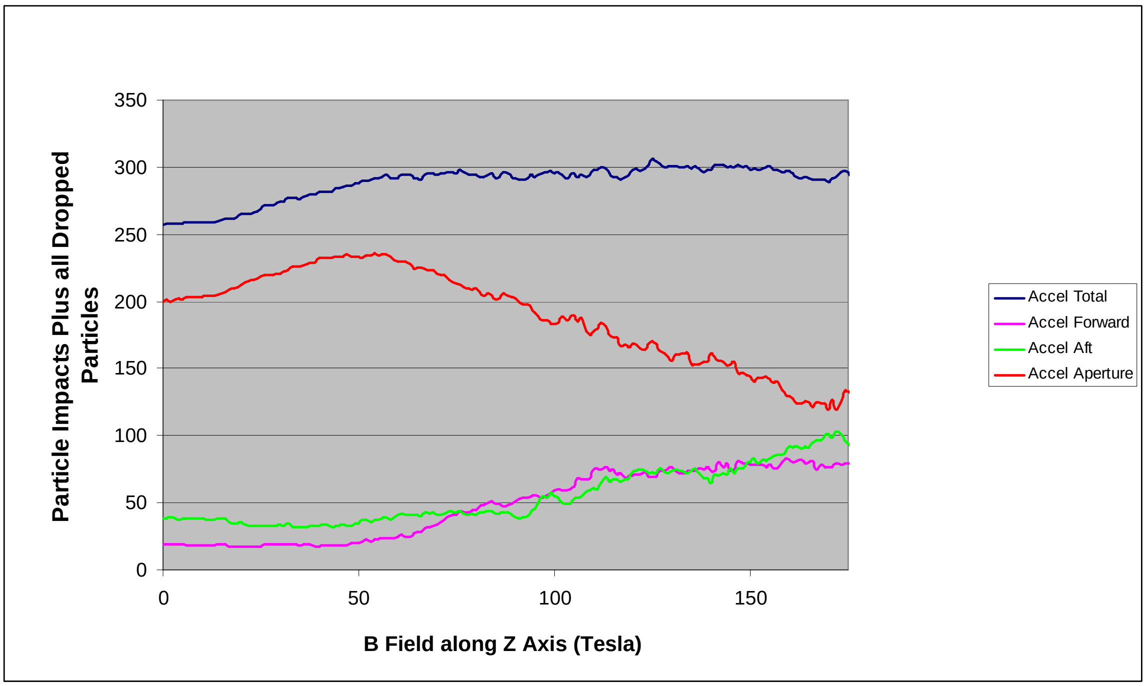

Figure 4.38: Particle Impacts with Each Grid Surface Including all Dropped Particles Impact That Surface

One key observation from Figure 4.38 is that while the total number of particles that impact the accel grid remains relatively constant over the range of Z axis B fields examined, the number of particles impacting within the accel grid aperture decreases significantly.

4.2.3 Varying B Field Strength – All Grids

In the second set of multi-particle runs grid embedded current loops were incorporated in all three grids. The three current loops, and hence the source of the axial aligned B fields were located at the leading (forward) surface of each grid. An initial current of 56.0315 A was set for each current loop resulting in a Z component of magnetic field at the center of the accel current loop of 0.1 Tesla. The program was once again configured to loop over charge exchange ions starting at every fifth axial and radial grid node within the ion beam and with a multiplier applied to all grid current loops that incremented between 0 and 1750 with an increment value of 10. This resulted in test runs of all the sample particles at each integer magnetic field strength between 0 and 175 Tesla.

The use of three current producing loops resulted in a much greater number of particles becoming trapped and exceeding the step count limitation of the program than was the case for a single current loop. This becomes particularly important as the peak axial field is increased above 85 Tesla. The implications of this for analysis of the results for this section are discussed later.

Initial examination of the results for impact energy imparted to all grids over the range of axial B fields examined show a significant improvement (i.e., decrease in total energy imparted to the grids) as the axial field is increased. This result is somewhat suspect however due to the large number of particles dropped from the calculation as the field is increased beyond 85 Tesla. Figure 4.39 shows the total energy imparted to all grids as a result of particle impacts.

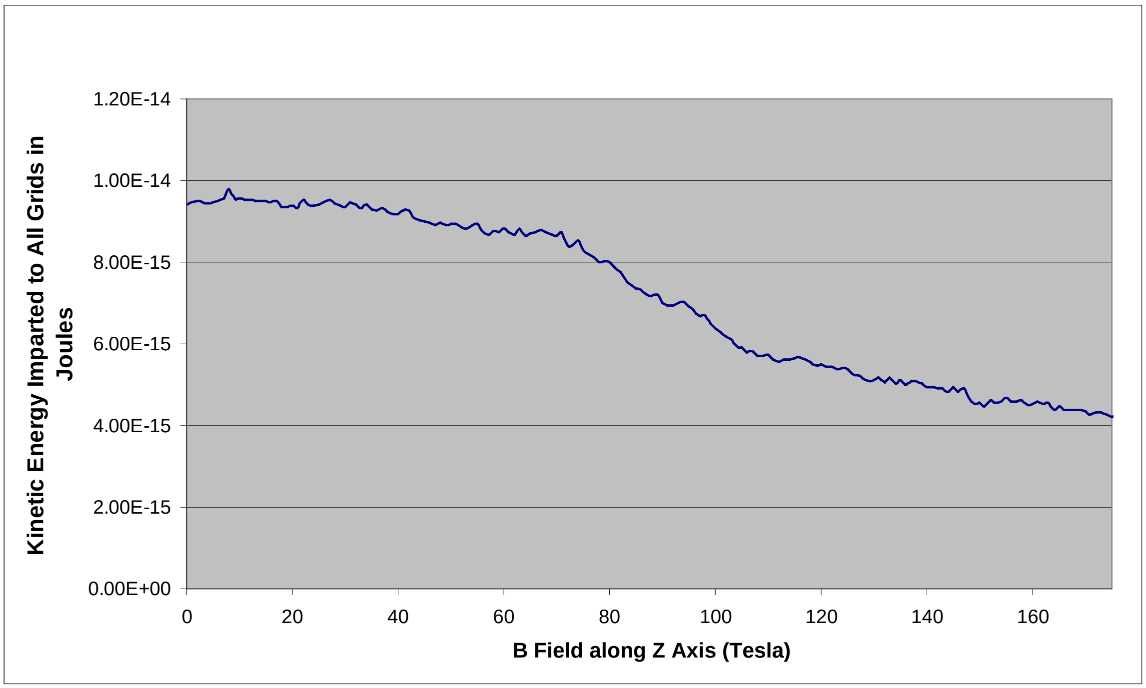

Figure 4.39: Kinetic Energy Imparted to all Grids as a Function of Z Axis B Field for the 3 Current Loop Case

Figure 4.39 shows that up to approximately 30 Tesla the impact of the axial B field is negligible, but above 30 Tesla the total kinetic energy imparted to all grids drops by about 21% by the point at which an 85 Tesla field is applied. This represents an improvement in total grid impact energy of twice what was observed for the accel current loop only case. For fields above 85 Tesla the total energy imparted to all grids continues to decline; however, the number of particles dropped from the calculation above 86 Tesla represents more than 5% of the total that are calculated to impact all grids.

An examination of the total energy imparted to the accel grid by all particle impacts shows that the impact energy profile closely matches the impact energy profile for all grids. This once again shows that the majority of charge exchange impacts are with the accel grid. Figure 4.40 shows the total impact energy imparted to the accel grid as a function of the peak Z axis B field.

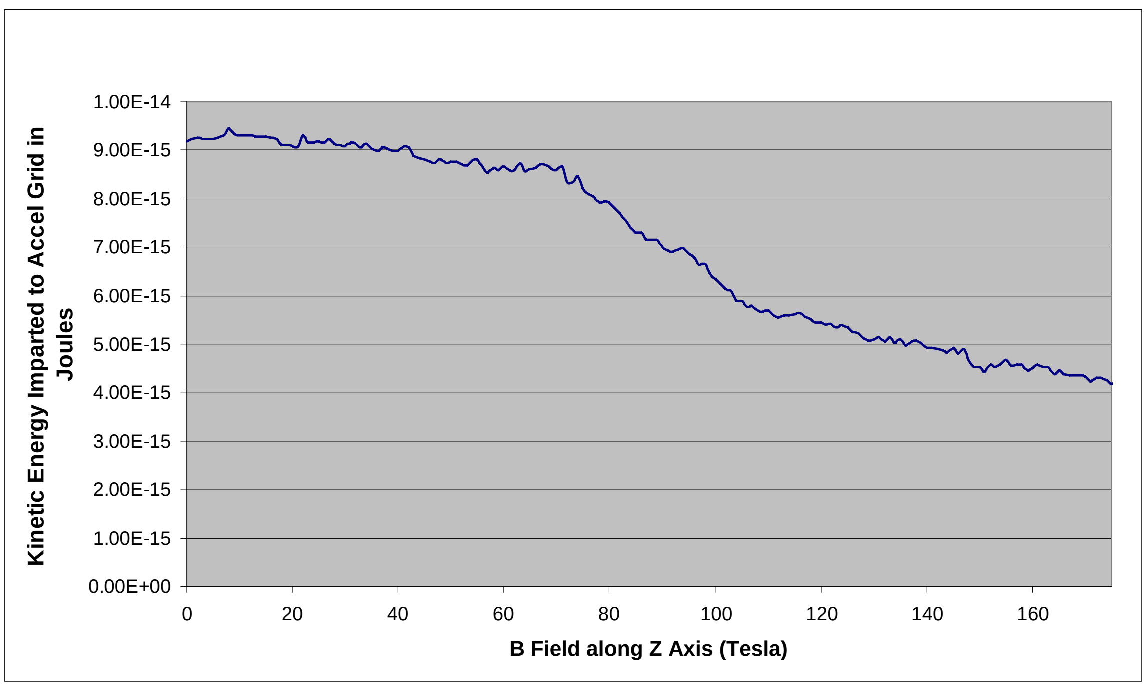

Figure 4.40: Energy Imparted to Accel Grid as a Function of Z Axis B Field for the 3 Current Loop Case

The impact energy profile for the accel grid is similar to that for all grids in that it remains level up to a Z axis B Field of approximately 30 Tesla, then drops off to a final value at 175 Tesla which is less than half the initial value.

The total impact energy for the decel grid is very different from the single current loop case. Figure 4.41 shows the total impact energy imparted to the decel grid for the three current loop configuration.

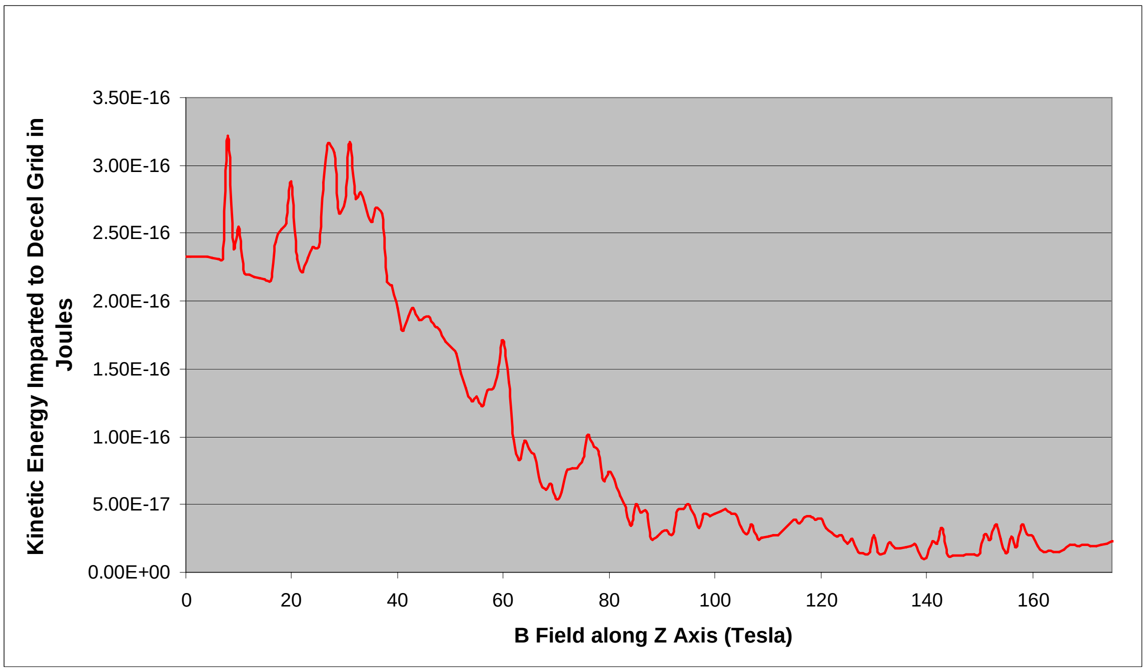

Figure 4.41: Energy Imparted to Decel Grid as a Function of Z Axis B Field for the 3 Current Loop Case

Unlike the accel grid current loop only case which had a relatively flat impact energy profile over the entire range of Z axis B fields under consideration, the impact energy profile for the three grid case drops off sharply above approximately 30 Tesla, well before the point at which dropped particles become important.

Due to the dropped particles and the impact they have on the resulting total impact energy it is once again useful to examine the impact energy per particle as was done in the single current loop case. Figure 4.42 shows the per particle impact energy for all grids.

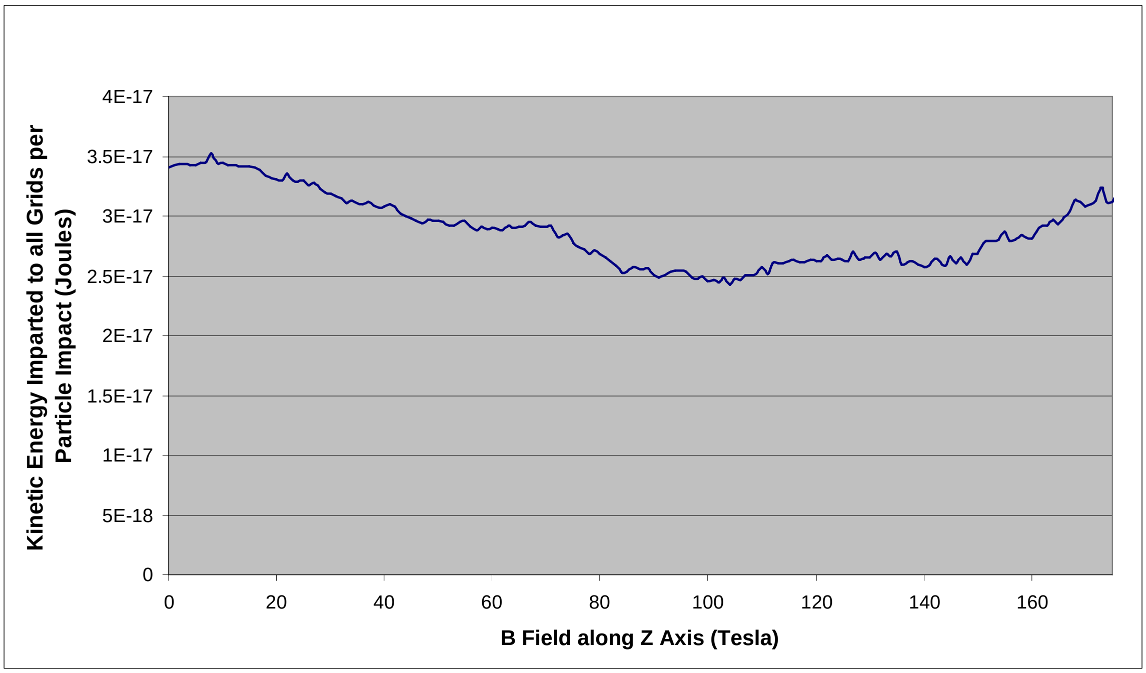

Figure 4.42: Kinetic Energy per Particle Impact for all Grids for the 3 Current Loop Case

Figure 4.42 shows that as the Z axis B field is increased the resulting kinetic energy per impact with all grids drops, reaching a minimum point around 100 Tesla. At this point (100 Tesla) the kinetic energy imparted to all grids with each particle impact is more than 28.7% lower than in the zero magnetic field case.

The kinetic energy per impact with the accel grid is shown in Figure 4.43. The kinetic energy imparted to the accel grid per particle impact provides a metric of the amount of material sputtered from the grid with each charge exchange ion impact.

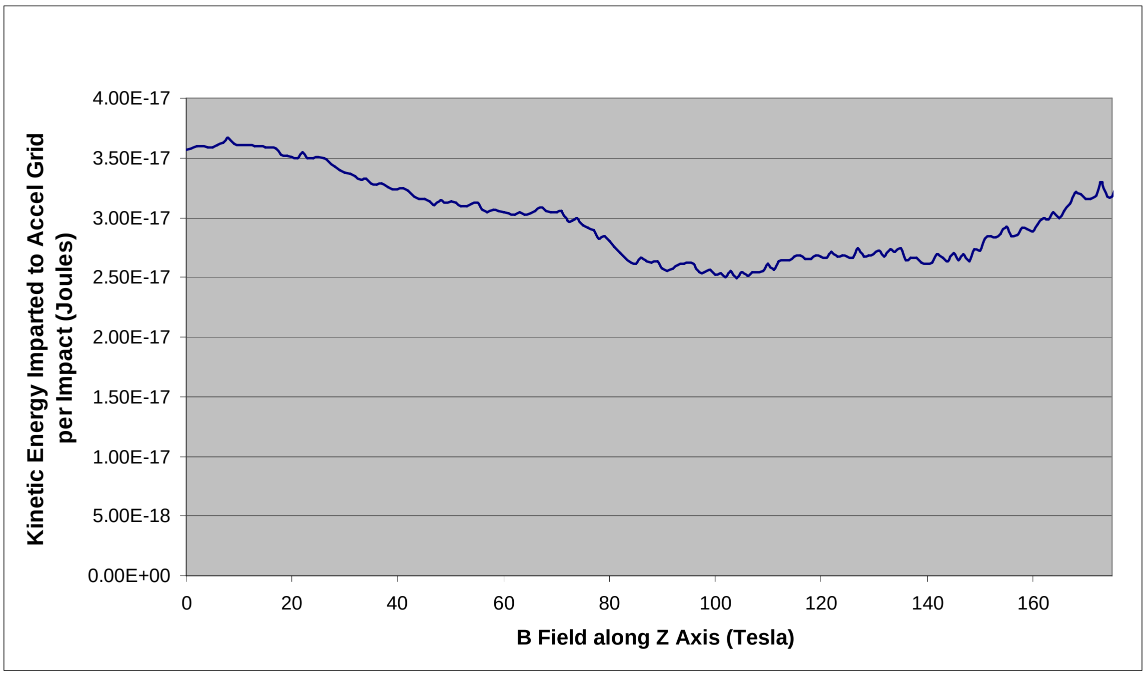

Figure 4.43: Kinetic Energy per Accel Grid Impact for the 3 Current Loop Case

Figure 4.43 shows that while the overall impact energy profile is similar to that for all grids, the actual improvement in impact energy per particle is larger than that seen for all grids. The minimum point in the impact energy imparted per particle is 30.25% lower than the impact energy per particle with no magnetic field.

The kinetic energy imparted to the decel grid per particle impact has a profile that indicates an even greater improvement in impact energy as a result of the additional magnetic field. Figure 4.44 shows the impact energy imparted to the decel grid per particle impact.

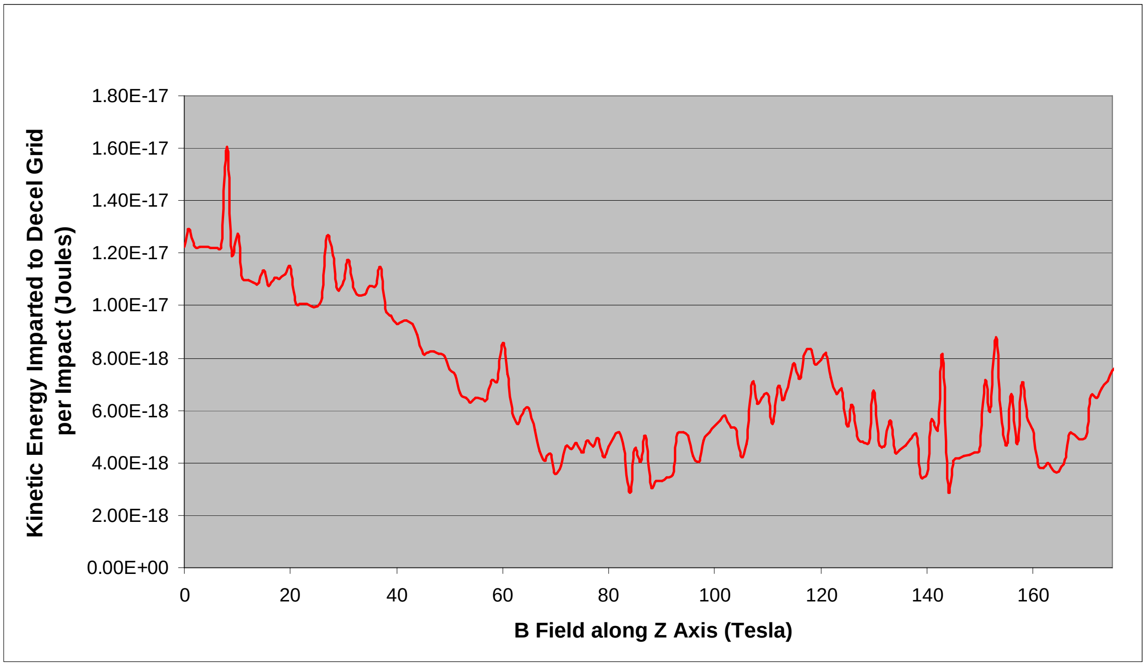

Figure 4.44: Kinetic Energy per Decel Grid Impact for the 3 Current Loop Case

Figure 4.44 shows that the individual particle impact energy drops off considerably for the decel grid as the Z axis B field strength increases to approximately 83 Tesla. By 83 Tesla the impact energy per particle has decreased by nearly 77% from its initial no magnetic field value.

As was discussed earlier in this section, the influence of particles dropped from the computation due to exceeding the program step limitation is much more significant for the three current loop case than for the one current loop case. Figure 4.45 shows the total number of particles dropped from the computation as a factor of the Z axis B field.

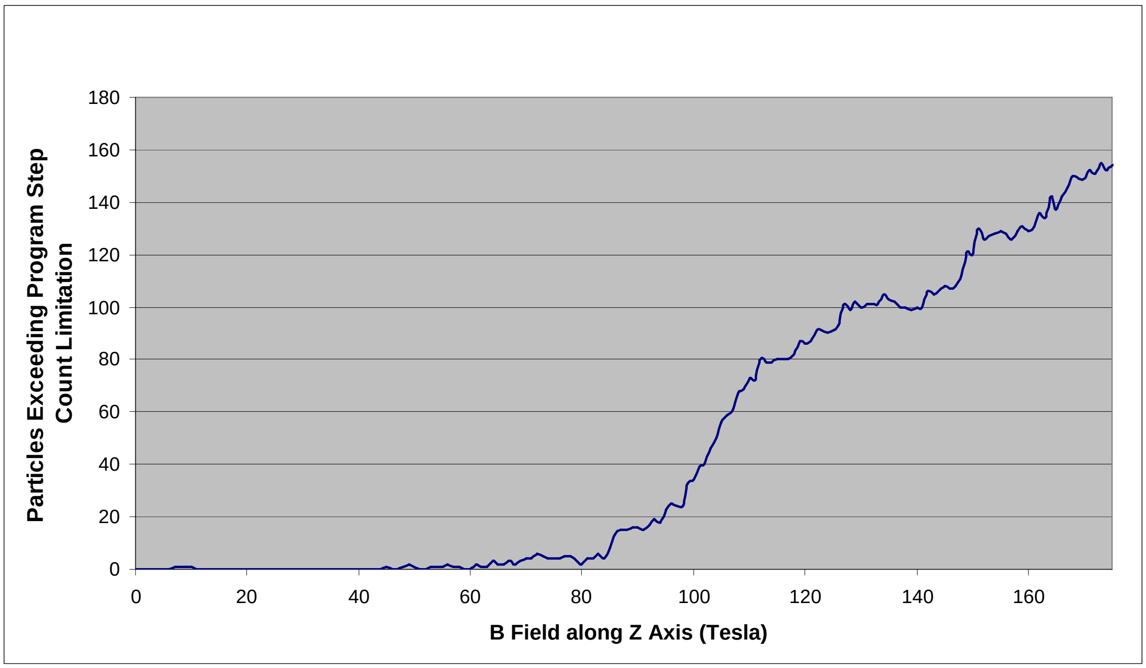

Figure 4.45: Particles Dropped From Computation Due to Exceeding the Program Step Count Limitation for the 3 Current Loop Case

Figure 4.45 shows that at Z axis B fields above approximately 85 Tesla the number of particles that exceed the step count limitation increases significantly to the point where by 175 Tesla more particles are dropped than impact all of the grids. This is significantly worse than the single current loop case.

As with the single current loop case it is useful to evaluate what the worst case implications of these dropped particles might be. If the number of particles impacting each area of the accel grid are examined, and it is assumed that all dropped particles impact each of these accel grid surfaces the worst case number of impacts can be examined. Figure 4.46 shows the number of particle impacts for the accel grid and each accel grid surface adjusted to include in each case all of the dropped particles.

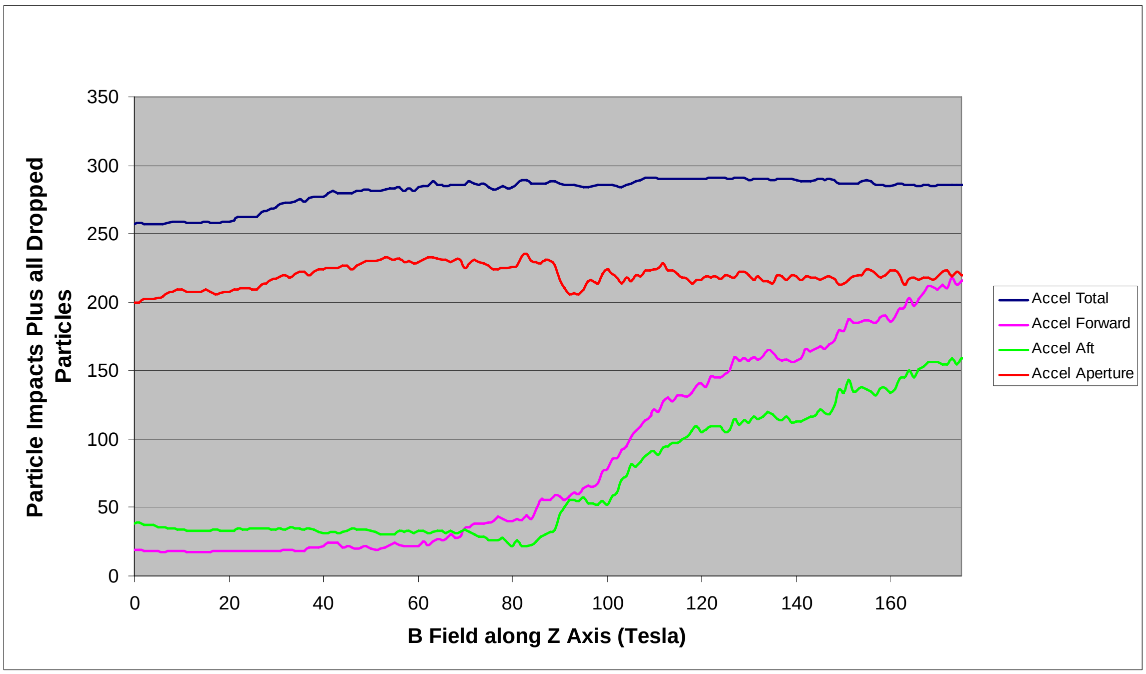

Figure 4.46: Particle Impacts with Each Grid Surface Including all Dropped Particles Impact That Surface for the 3 Current Loop Case

Figure 4.46 shows that if all of the dropped particles impact the accel grid, the total number of particles impacting the accel grid as the Z axis magnetic field is increased remains relatively constant. The same is true for the particles impacting within the grid aperture. On the other hand if all of the dropped particles are impacting either the forward or aft grid surface, then the number of impacts with those surfaces increases several fold as the Z axis B field increases above 83 Tesla. This suggests that the majority of the dropped particles are particles that otherwise would impact the accel grid in the aperture.

A further evaluation which looks at the implications of the dropped particles goes along with the preceding paragraph in that the implications for impact energy are postulated. If the number of particles impacting the accel grid are added to the number of dropped particles and this number multiplied by the per particle impact energy at any point in the B field range, then an estimation of the actual total impact energy imparted to the accel grid is achieved. Figure 4.47 shows the results for doing just that. The most important feature of Figure 4.47 is that it indicates a reduction in total impact energy of approximately 22% from the initial zero magnetic field value to the value observed at a Z axis B field of approximately 100 Tesla. This implies that even if all dropped particles impact the accel grid, there is still a 22% reduction in the kinetic energy imparted to the grid achievable by adding a grid embedded magnetic field with current loops at the forward surface of each grid.

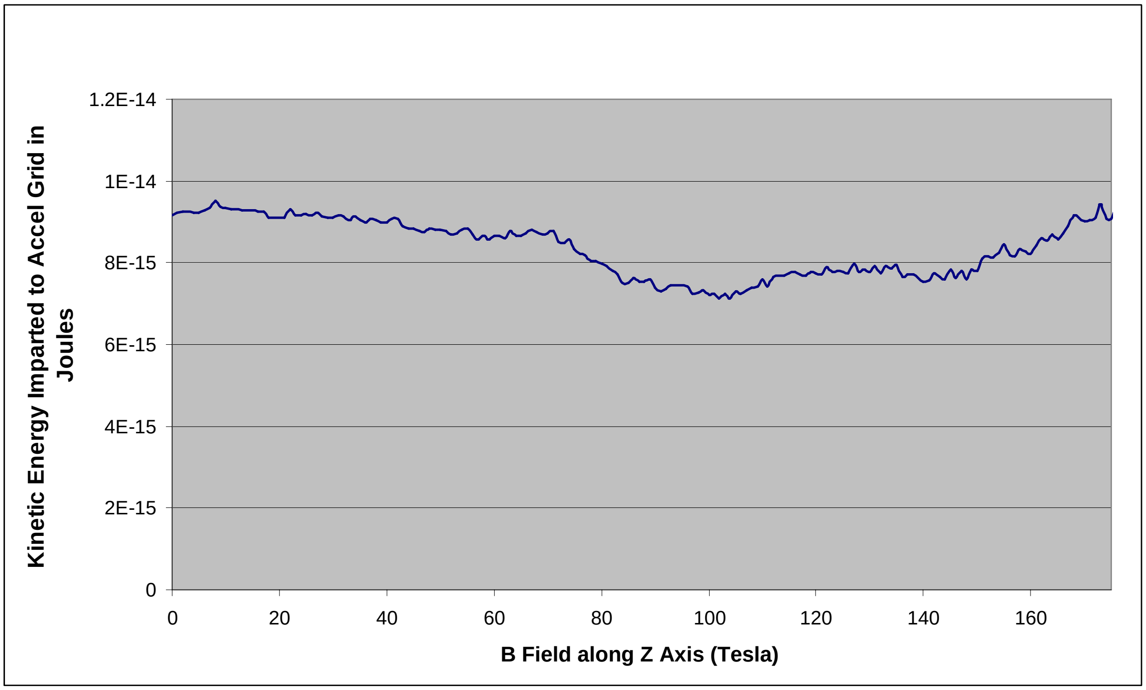

Figure 4.47: Potential Total Accel Grid Impact Energy if All Dropped Particle Impact the Accel Grid at per Particle Impact Energy

4.3 Alternatives to Large B Field Producing Currents

The analysis done to this point has involved the use of very large magnetic field strengths. While the use of these large fields has been shown to offer advantages in terms of reduced energy transfer to the grids, production of fields these magnitudes requires very large currents and is not practical for use in conventional ion propulsion systems. There are several possible alternatives to the use of such large currents however, which would ideally magnify the impact of the magnetic field and thus show an improvement in thruster life without the use of very large fields or conversely large currents. Two of these potential alternatives are discussed in the following sections.

4.3.1 Reduction of Grid Aperture Radius

The first alternative to the use of very large currents to produce magnetic fields is a modification of thruster geometry to reduce the radius of the grid apertures, and thus the B field producing current loops. The principle behind this idea can be seen by an examination of the basic equation for the B field produced by a current loop. If only the Z axis component is considered the equation for the field strength is given by equation 3.21 re-printed here as equation 4.1.

$$B_Z = \frac{\mu I}{2} \frac{a^2}{\left(a^2 + z^2\right)^{3/2}} \tag{4.1}$$

The value a in this equation is the radius of the current loop and the value z is the distance normal to the plane of the current loop at which the B field is to be measured. If the field strength at the center of the current loop is to be determined $z = 0$ and the equation reduces to:

$$B_Z = \frac{\mu I}{2a} \tag{4.2}$$

Equation 4.2 shows that the strength of the axial component of the magnetic field is inversely proportional to the radius of the current loop. This implies that large fields can be produced with less current if the aperture radius is small. There is clearly going to be an impact on the thrust produced by a single set of grid apertures if the apertures are small, but this can be made up for by increasing the density of the apertures in the grids. The full scope of implications for ion acceleration and thrust performance will not be discussed here.

To investigate the implications of reducing grid aperture radius as a means of achieving reduced grid erosion using lower magnetic field strength three test cases are considered. The first is a nominal baseline configuration which is the same as that used for section 4.2. The second considers a thruster geometry wherein the radius of each of the grid apertures is half the baseline. The third test case sets the grid aperture radius for each grid to one quarter of the baseline radius. The remaining elements of the simulation are the same in each case (grid thickness, grid separation, grid potential, particle mass, etc.).

Three particles were simulated and their impact energy with either the accel or decel grid calculated over a range of Z axis B fields from 0 to 100 Tesla. The first particle represent a charge exchange ion created within the accel grid aperture at approximately 38% of the accel aperture radius. The second particle represents a particle created between the accel and decel grids at approximately 38% of the accel grid aperture radius. The third particle represents a charge exchange ion created aft of the decel grid at approximately the edge of the ion beam or 115% of the accel grid aperture.

Because changing the diameter of the grid apertures changes the potential field and the distance the particles must travel before impacting the grid the impact energy at zero magnetic field is different in each test case. This makes a direct comparison of the implication of decreasing the grid diameter difficult. It is enlightening to compare the overall impact on the impact energy profile in each case of the increasing magnetic field.

The first particle test, the particle created within the accel grid, has impact energy profiles over the range of Z axis B fields from 0 to 100 Tesla as shown in Figure 4.48.

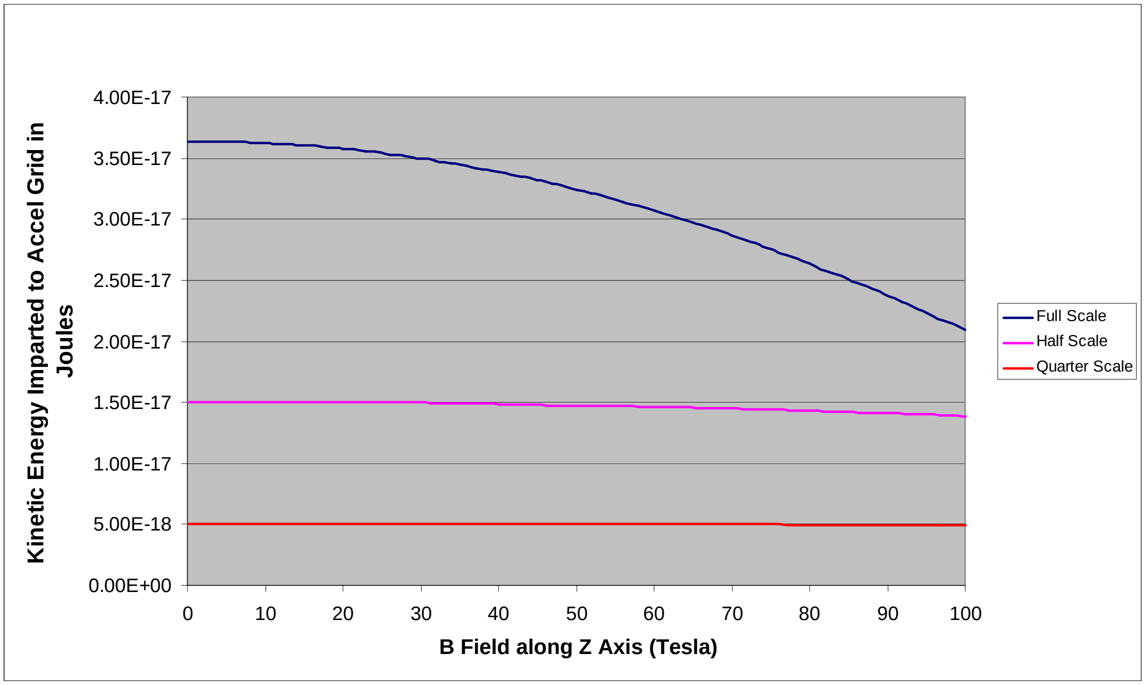

Figure 4.48: Energy Imparted to Accel Grid for Three Cases of Grid Aperture Radius for a Particle Initially Within the Accel Grid Aperture at 38% of the Aperture Radius

Figure 4.48 shows that as the radius of the grid apertures is decreased the energy imparted to the accel grid decreases; however, the influence of the additional grid embedded magnetic field also decreases. This is seen as a flattening of the impact energy profile. The implication of this result is that while a given current produces a stronger axial field in the grid aperture, the influence of the magnetic field in reducing grid impact energy is lessoned.

The second particle test, the particle created aft of the accel grid, has impact energy profiles over the range of Z axis B fields from 0 to 100 Tesla as shown in Figure 4.49.

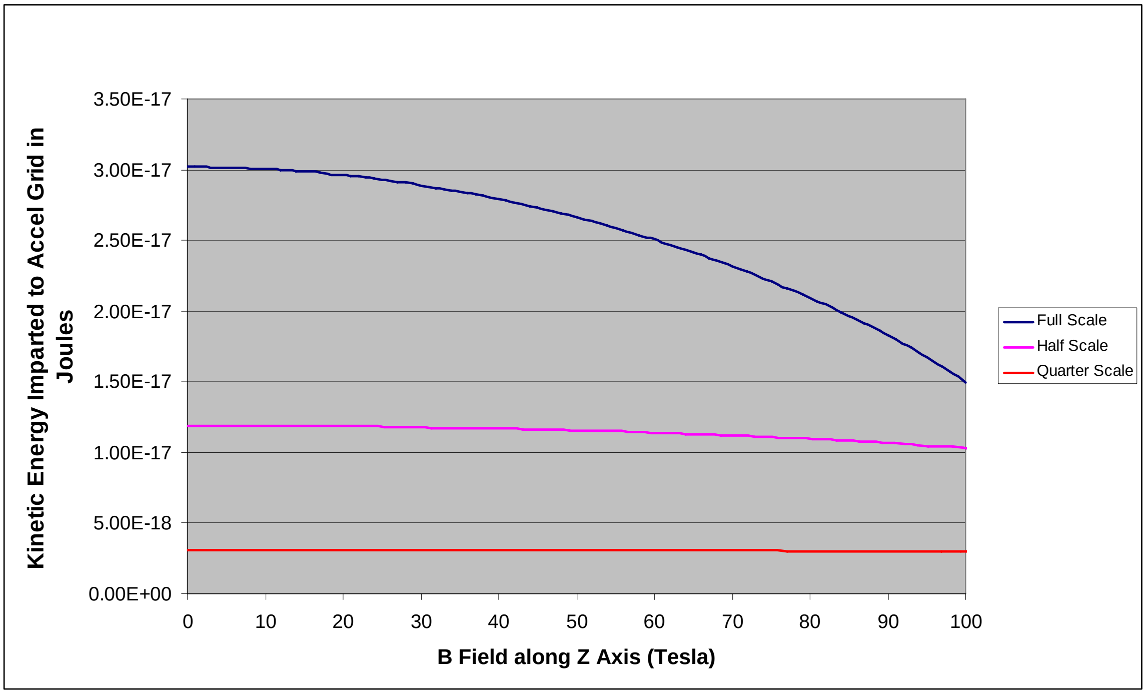

Figure 4.49: Energy Imparted to Accel Grid for Three Cases of Grid Aperture Radius for a Particle Initially Aft of the Accel Grid Aperture at 38% of the Aperture Radius

The behavior of the test particle shown in Figure 4.49 is similar to that for the particle starting in the accel grid aperture in that while the impact energy for smaller radius apertures is less, the influence of the magnetic field is also less.

The third particle test, the particle created aft of the decel grid, has impact energy profiles over the range of Z axis B fields from 0 to 100 Tesla as shown in Figure 4.50.

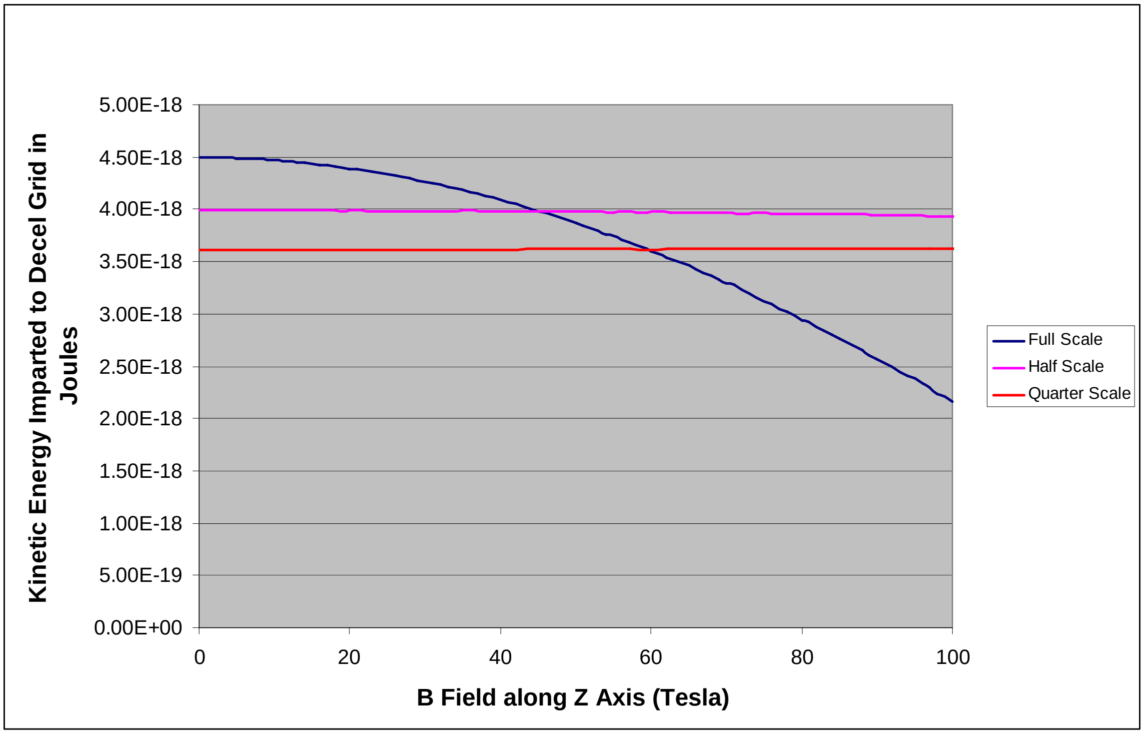

Figure 4.50: Energy Imparted to Decel Grid for Three Cases of Grid Aperture Radius for a Particle Initially Aft of the Decel Grid Aperture at 115% of the Accel Aperture Radius

The impact energy for particles created aft of the decel grid is not as strongly influenced by the grid aperture radius as was the case for the first two particle tests. The influence of the embedded magnetic field was however impacted in a similar way in that for the smaller radius cases the magnetic field shows minimal benefit. In the case of the smallest grid aperture the impact energy actually increases slightly over the range of magnetic fields tested.

4.3.2 Reduction of Propellant Ion Mass

The second alternative to the use of large currents is to magnify the impact of the magnetic field on the particle motion. The simplest way to do this is to reduce the particle mass. Charge exchange ions ultimately move under the influence of Newton's Second Law:

$$F = ma \tag{4.3}$$

If just considering the influence on the motion of the magnetic field, F is the force imparted to the particle by the magnetic field, m is the particle mass, and a is the resulting acceleration. It is clear that reducing m at constant F increases a.

As with the case of changing the grid aperture radius there are inevitable impacts on thruster performance due to changing the propellant mass. These will not be addressed here. Only the impact on kinetic energy of impact with any of the grids is considered.

Five cases of different propellant mass were examined. These five cases represent the Noble Gases through xenon, the most commonly used ion propulsion system propellant. The baseline thruster architecture is the same used in Section 4.2. Two particle examples were considered representing a charge exchange ion created within the accel grid aperture and a charge exchange ion created aft of the decel grid.

The first particle tested for varying propellant mass represents a charge exchange ion created within the accel grid aperture at approximately 58% of the accel grid aperture radius. Figure 4.51 shows the impact energy profile for the test particle over the range of axial magnetic fields from 0 to 100 Tesla for the five different propellant mass cases.

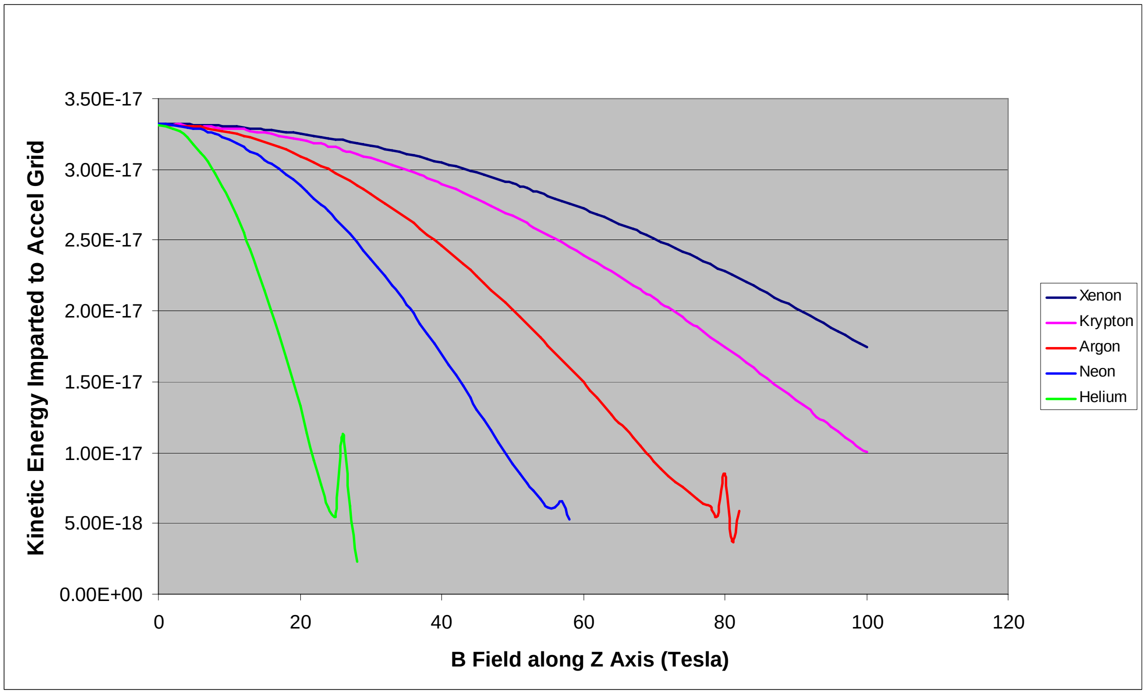

Figure 4.51: Impact Energy for Particles of Different Mass Initially Within the Accel Grid Aperture

One interesting feature immediately apparent from Figure 4.51 is that in spite of the different masses for each particle the impact energy with the accel grid for zero magnetic field is nearly identical. This implies that as the mass of the particles is decreased the square of the impact velocity increases in almost direct inverse proportion thus keeping the kinetic energy the same. This feature makes direct comparison of the influence of decreasing propellant mass fairly straight forward.

Figure 4.51 shows that for the first test particle, as the propellant mass decreases the influence of the magnetic field on the impact energy increases. The minimum impact energy is approximately the same in each case, around 5×10^{-18} Joules; however, the minimum occurs at a lower magnetic field strength for each reduction in propellant mass to the point that the impact minimum for helium occurs at approximately 100 Tesla less that for xenon.

The second test particle for comparing propellant mass represents a particle created aft of the decel grid at approximately 38% of the accel grid aperture radius. Figure 4.52 shows the impact energy results for different mass propellants.

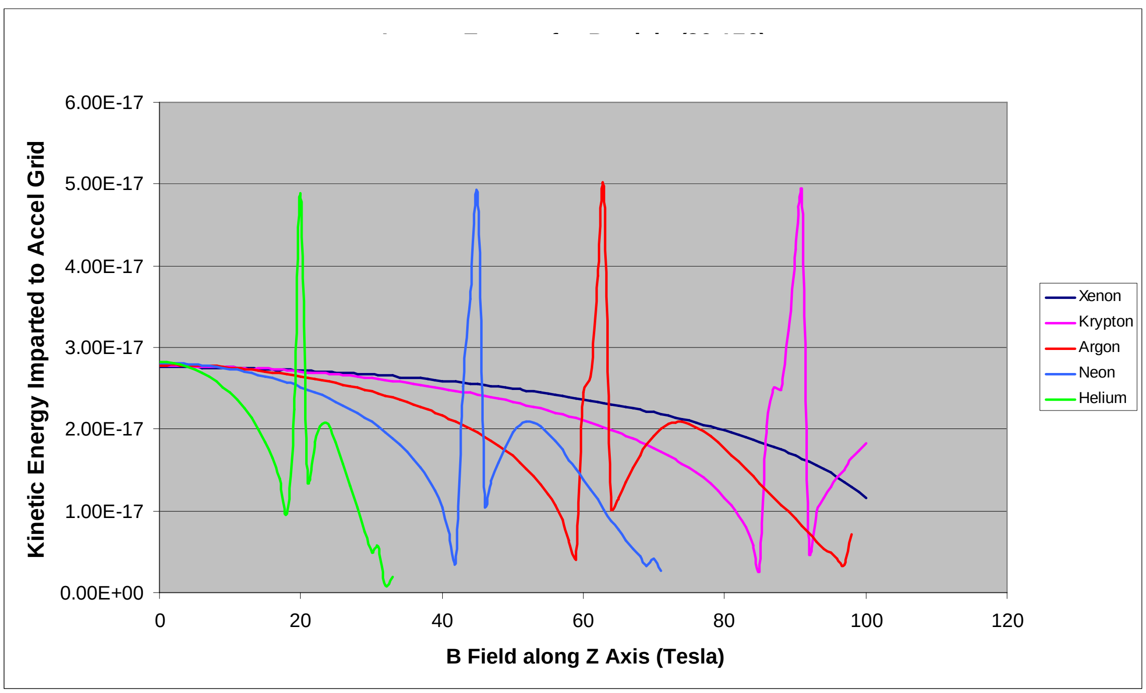

Figure 4.52: Impact Energy for Particles of Different Mass Initially Aft of the Decel Grid Aperture

As was the case for the particle initially within the accel grid aperture the impact energy for each propellant mass particle with no magnetic field is approximately the same. Figure 4.52 shows that as with the previous particle the impact of the magnetic field is always greater for a particle of lower mass. In this case however, the particles of lower mass start to behave erratically at a lower magnetic field than do their more massive counterparts. This implies that the particles reach a point in the magnetic field strength range where they become trapped or mirrored at a lower magnetic field strength if they are lighter.

CHAPTER 5

DISCUSSION OF RESULTS

This Chapter discusses two topics; (1) the results obtained in the previous Chapter for incorporation of micro-solenoid magnetic fields in the grid apertures of ion thrusters, and (2) the usefulness of the ionLite program in performing this analysis. The objective is to answer two questions. Specifically, for (1), did the inclusion of grid embedded micro solenoid fields show promise as a means of reducing charge exchange induced grid erosion? For (2), did the ionLite program accomplish its objective of providing a highly flexible, easily reconfigurable simulation that allows for high level evaluation of alternative thruster grid geometries and field configurations with the intention of finding innovative new techniques for increasing thruster performance and lifetime?

5.1 Effect of Grid Embedded Magnetic Fields on Thruster Grid Erosion

Two principle investigations were accomplished and reported in Chapter 4, the first being a study of individual charge exchange ions and their response to increasing embedded magnetic fields, and the second being a study of cumulative effects of many particles and the impact on total kinetic energy imparted to the grids over a range of embedded magnetic fields. The reason for breaking down the investigation of the impact of grid embedded magnetic field in this fashion is clear from the results for the multiple particle runs.

The multiple particle runs do not exhibit steady change in total impact energy imparted to the grids over the range of magnetic fields that were investigated. While Figure 4.43 shows that in the case of a three grid, three current loop configuration the impact energy per impact particle generally decreases between 0 and 100 Tesla axial field, this trend is not true for any range between those field strengths. The impact energy per impact at 65 Tesla is higher than the impact energy per impact at 60 Tesla for example. This basic behavior is exhibited in all of the multiple particle run results for all of the different configurations examined. While it was possible to obtain significant reductions in total impact energy and impact energy per particle at some field strengths, slightly different field strength, either higher or lower, produced higher impact energies.

The non-regular impact energy profile exhibited in all cases for the multiple particle runs can be traced directly back to the results observed for the individual particle behavior in the presence of the embedded magnetic fields. Some individual particles have very smooth, regularly changing impact energy profiles in response to large scale changes in Z axis B Field, as shown in Figures 4.1 and 4.2 in Chapter 4. Other particles show highly erratic, large scale changes in impact energy over relatively small changes in Z axis B Field, as can be seen in Figures 4.3 and 4.4 in Chapter 4. Since the impact energy results for the multi-particle runs are simply the sum of the impact energies of these two different type behaving particles, the results are understandably non-regular.

Why do some particles have regular response to the changing magnetic field while others do not? There are two principle sources of this dichotomy. They are the varying magnetic field and the varying electric field within the simulation space. These combine to make the particle's behavior in response to increasing axial magnetic field strength highly dependant on the particles starting location. The starting location determines what regions of fields inside the simulation the particle will visit along its trajectory. If the particle moves from regions of relatively constant fields, to regions where the fields are spatially highly variant, its motion will become more erratic. There are several reasons for this which will be discussed later.

In Chapter 4 all of the impact energy results were compared against the peak magnetic field strength observed along the axis of the apertures. This does not imply that the field throughout the simulation was a constant axial field. The magnetic field is far from uniform. When a particle moves near the region of the magnetic field source (the current loop) the field strength increases significantly. For the case of a three grid thruster with embedded current loops in all grids (as per the configuration used in Section 4.2.3) a maximum 1 Tesla field at the aperture axis still has regions where the field is as high as 10 Tesla near the current loop itself. At much higher axial field levels there can be large regions within the simulation where the field strength is several times greater than the axial field strength. There are two consequences that were observed in Chapter 4 that can be explained by this.

When the field strength becomes very high, the particle Larmor radius becomes small as was discussed in Chapter 2. [20] If the particle Larmor radius becomes small enough its motion through the simulation becomes more dependant on the motion of its guiding center. The more a particle's motion is dependant on its guiding center motion the more steps are required by the simulation to describe its motion. This leads inevitably to more particles exceeding the step count limits at higher magnetic fields, as was seen in Section 4.2.3. An example of this can be seen in the next few Figures. Figure 5.1 shows

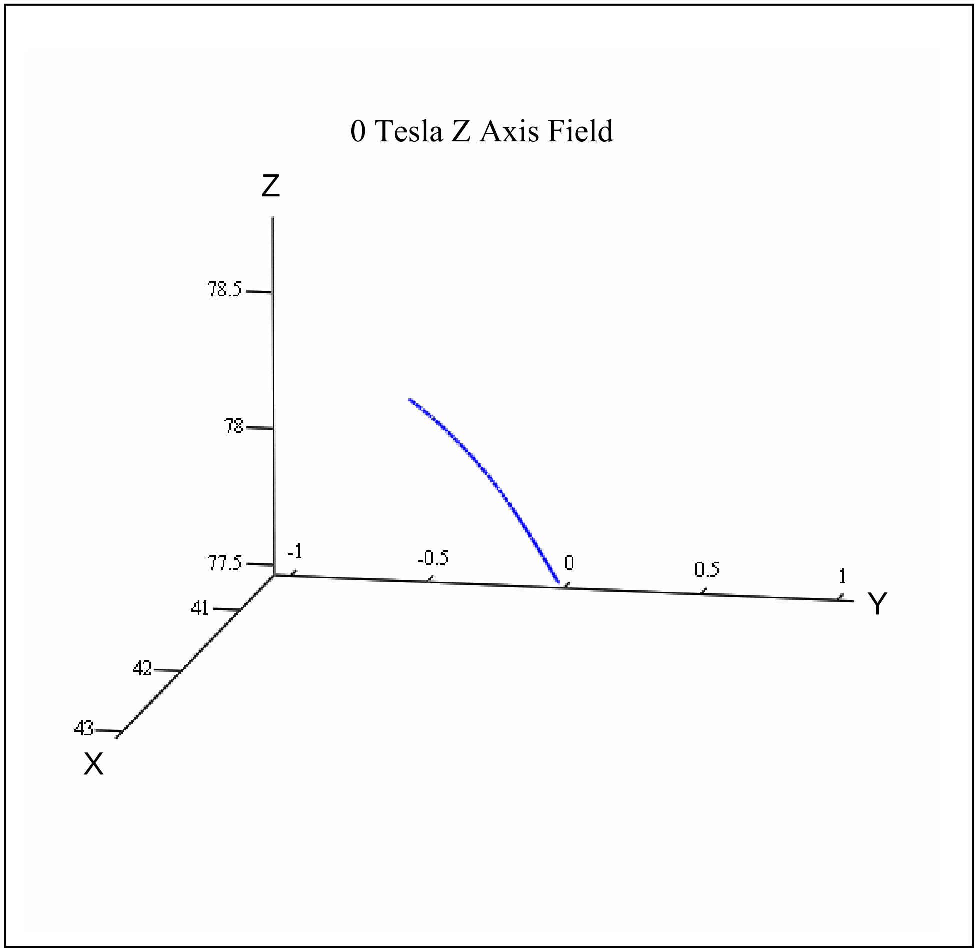

Figure 5.1: Particle 40,77 Trajectory With no Magnetic Field

particle (40,77) from section 4.1.1. The impact energy profile over the tested range of magnetic fields can be seen in Figure 4.5. It has a regular, decreasing impact energy up to approximately 72 Tesla, beyond which it has a highly erratic impact energy response to increasing magnetic field. At 0 Tesla Z axis field the particle moves only in X and Z to proceed to an impact in the accel grid aperture as can be seen in Figure 5.1. When the Z Axis Magnetic Field is increased to 50 Tesla the particle motion starts to show curvature in the Y axis as desired, and resulting in an impact in the accel grid aperture at a more oblique angle causing less energy transfer to the grid. This can be seen in Figure 5.2.

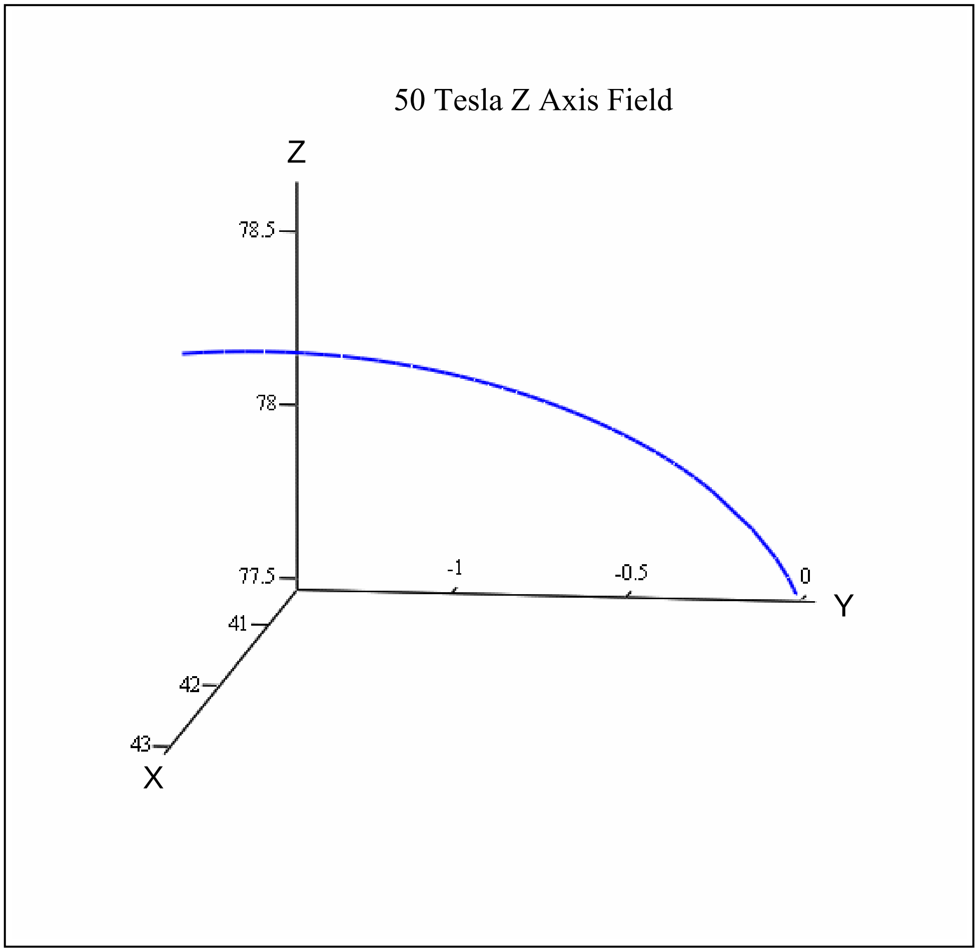

Figure 5.2: Particle (40,77) Trajectory at 50 Tesla Z Axis Field

At approximately 70 Tesla Z axis Field the particle motion is still regular, though it has started to turn around in X and Y, thus showing a nice regular curve as can be seen in Figure 5.3. The impact energy is nearing the minimum by this point. At 75 Tesla Z axis

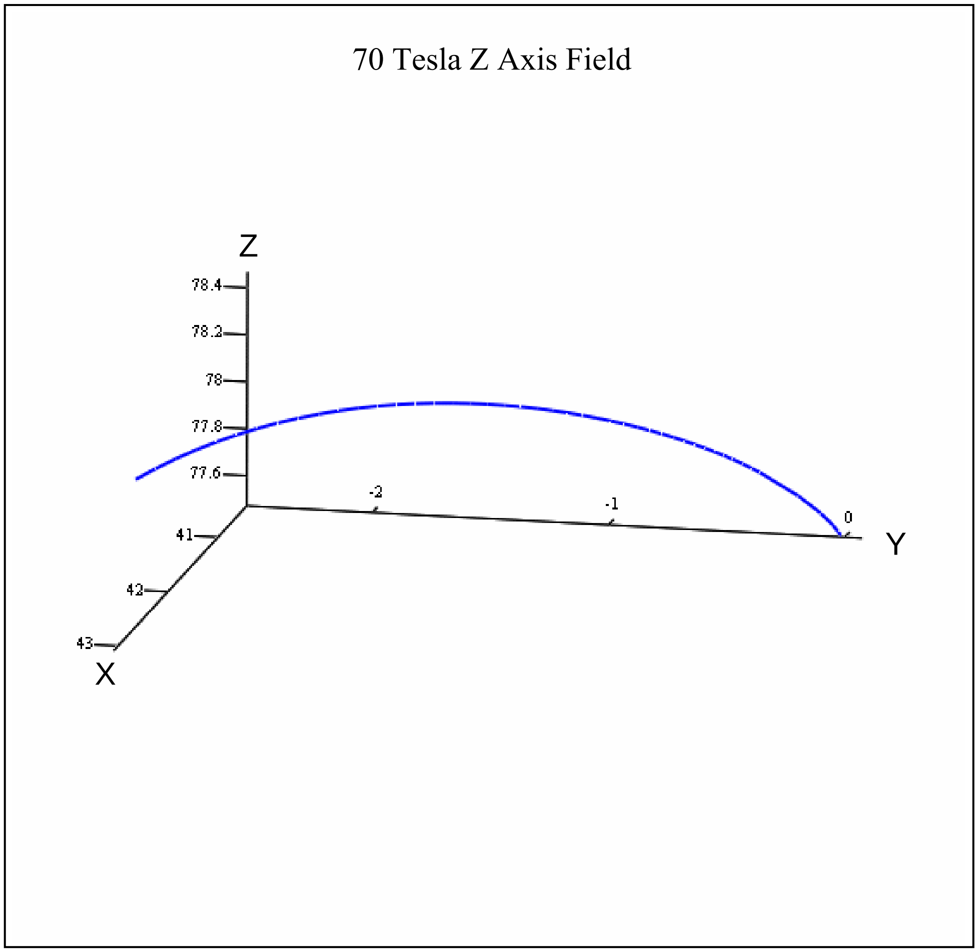

Figure 5.3: Particle (40,77) Trajectory at 70 Tesla Z Axis Field

The particle is just past the minimum point in its impact energy profile. The motion now appears erratic, contributing by that nature to the erratic impact energy response observed above 75 Tesla. Figure 5.4 shows the trajectory of the particle at an axial field peak of 75 Tesla.

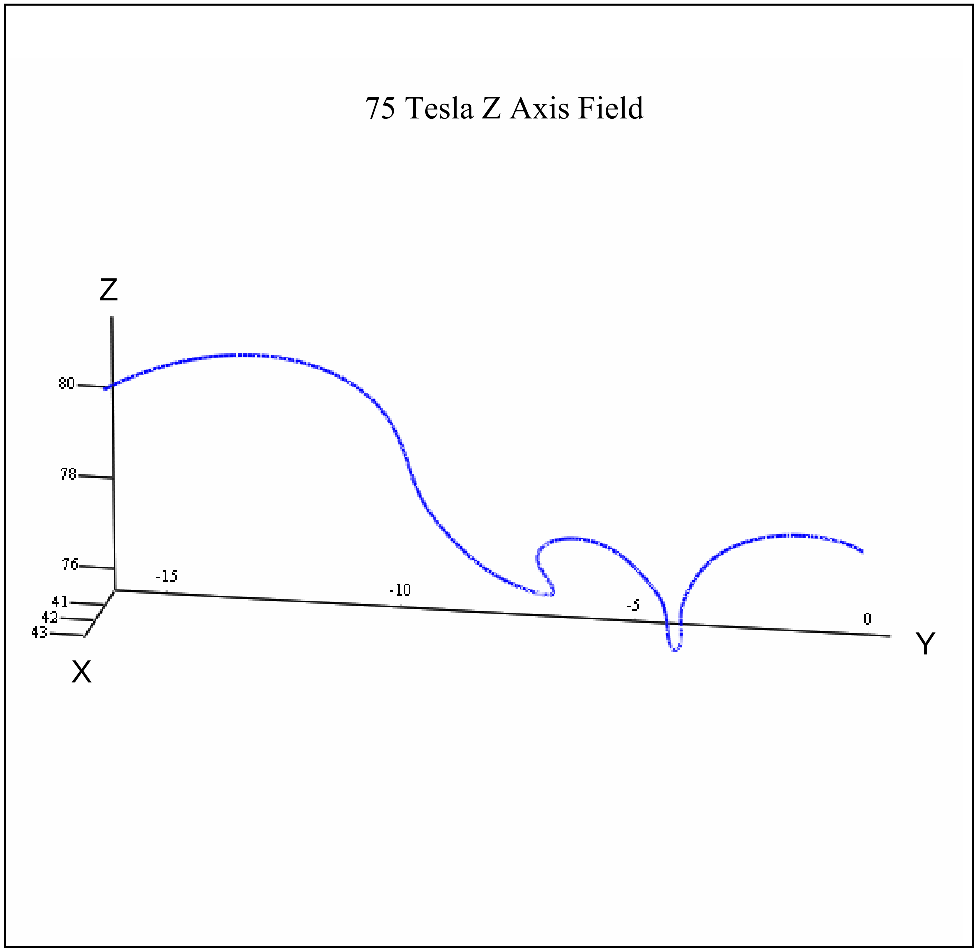

Figure 5.4: Particle (40,77) Trajectory at 75 Tesla Z Axis Field

Another cause of erratic particle behavior is magnetic mirroring and reflection. Magnetic mirroring occurs in regions of converging magnetic fields. [39] Magnetic mirroring will only come into play if the fields are high enough that the particle's motion is principally defined by its guiding center motion. Magnetic mirroring is a lossless phenomenon that occurs when a charged particle travels into a region of converging field lines. The particles guiding center motion will be reflected and travel back along the field lines to a second converging field point at which it is reflected back again. In the case of grid embedded magnetic fields, converging field points can be created when multiple current loops are used. [39] In the ion thruster grid current loop configuration however the particle can easily be reflected away a single converging field point and then travel into a region where the guiding center motion no longer predominates. The particle is then pulled back toward the current loop plane by electrostatic forces. This situation is analogous to a rubber ball bouncing on a floor. The floor represents the magnetic mirroring force and gravitational acceleration the electrostatic force. A case of magnetic mirroring can be seen in Figure 5.5. The particle in Figure 5.5 can be seen to be repeatedly covering the region between Z Axis locations of approximately 90 to 140 grid nodes and plus and minus 25 Y grid nodes. The outcome for this particle is that is exceeds the program step limit, however it can be seen that this type of trajectory can give rise to highly varying impact location for different particles at just slight variation of the field.

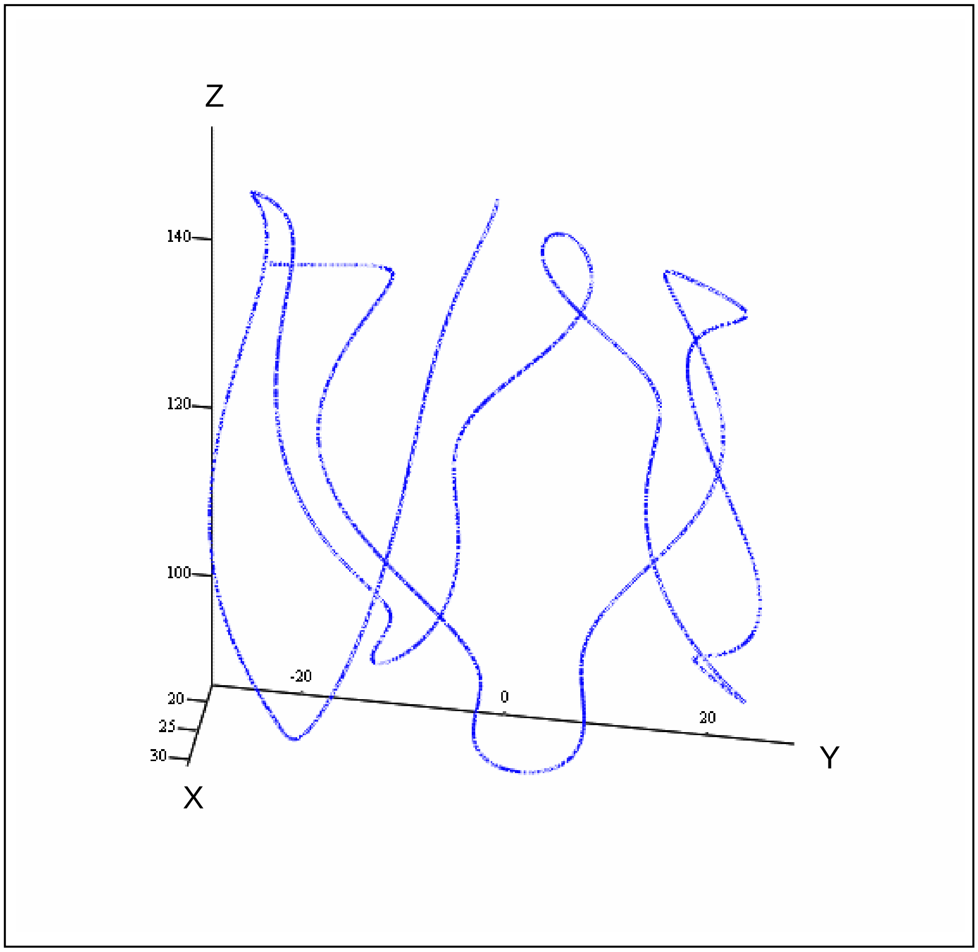

Figure 5.5: An Example of Magnetic Mirroring Effects on Particle Trajectory

The discussion above on the effects of magnetic mirroring begins to delve into the second cause of erratic particle motion, specifically the presence of a spatially varying electric field. Spatially varying electric fields can impact guiding center drift in much the same way that a spatially varying magnetic field can. [39] Long before the impact of varying E-fields in the form of guiding center drift comes into play, the basic directional nature of the electric fields inside the grid apertures limits the effectiveness of the grid embedded magnetic fields in reducing particle impact energy. In Chapter 1, in describing the basic concept behind the use of grid embedded magnetic fields, the examples used showed that the axial aligned B field gives rise to an additional force that acts to turn the velocity vector parallel to the grid surface, and to a lesser extent reduce the magnitude of the velocity vector component normal to the grid surface. What that high level discussion did not include is that, particularly inside the grid apertures, as the particle trajectory turns from one that is directly normal to the surface, the e-field component normal to the surface continues to accelerate the particle toward the surface. Until the B field becomes quite large the trajectory can turn considerably, but all that happens is that the e-field has longer to accelerate the particle. This results in a much larger velocity vector magnitude. The normal component of which is nearly the same, or even greater, than in the no magnetic field case. This is compounded by the fact that as the particles trajectory caries it more tangent to the grid aperture surface, the local e-field remains normal to the surface.

This behavior explains two important features of the multi-particle impact energy profiles; (1) they remain relatively constant until some fairly high level field is reached and (2) they reach a minimum at around 100 Tesla. The full meaning of this will be discussed later.

In summary, the combined impact energy profiles of particles that have regularly changing impact energies and particles impacted by mirroring in addition to particles that have trajectories that alter just enough between one Z axis B field level and the next to miss their previous impact surface and proceed to impact another surface at very different energy results in the irregular impact energy profiles observed for the multi-particle runs. Additionally, as the field is increased, particle mirroring and decreased Larmor radius due to increased magnetic field is the cause of an increasing number of particles being dropped from the calculation as a result of exceeding the program step count limit.

Overall the results for the multi-particle runs are very encouraging. There is a significant decrease in per particle impact energy, as well as in adjusted total impact energy when all dropped particles are assumed to impact at average impact energy. The reduction is more than 20% for the three current loop case. An important consideration for further design refinement comes from the fact that the impact energy profile for all of the cases evaluated occurs at nearly the same axial magnetic field strength. Figure 4.32 for example shows that total kinetic energy imparted to all grids remains nearly constant from 0 Tesla up to approximately 60 Tesla. From 60 Tesla to about 80 Tesla the total impact energy increases. Then from 80 Tesla until approximately 110 Tesla the total kinetic energy decreases to a minimum which is about 12% below the 0 field impact energy. This behavior can best be understood by examining the Larmor radius for a representative particle. For this test run the accel grid aperture radius was 0.645 mm. For a particle of xenon traveling at a nominal impact speed of 20,000 m/s the Larmor radius at a constant B field of 1 Tesla is 27.2 mm. At a constant B field of 80 Tesla the Larmor radius is reduced to 0.34 mm. At a constant B field of 100 Tesla the Larmor radius is 0.27 mm. The implication of this is clear, the minimum impact energy for all particles will occur when the configuration results in the Larmor radius being nearly equal to the grid aperture radius. As the axial B field is increased above this critical point the influence of guiding center motion becomes more prevalent and the benefits to employing the axial magnetic field start to decrease.

While the axial field strengths are very high (approximately 100 Tesla) the implication is that with further refinement a combination of grid geometry, grid voltages, and B field strength could eventually be identified which minimizes charge exchange grid erosion at a reasonable axial B field strength. Additionally, there are various alternative configurations and magnetic field generation mechanisms which could make the use of grid embedded fields practical. Two of these were investigated very briefly in Chapter 4, the use of reduced grid aperture radii to enhance the magnetic field strength and the use of lower mass propellants. It was observed that reducing the diameter of the grid apertures actually reduced the influence of the magnetic fields. This can easily be seen to be a consequence of the discussion above about the critical nature of the particle Larmor radius. It is probable that had the testing in this case have continued into even higher B field levels there would have been a point in the impact energy profile where a distinct minimum would have been reached, and that would have corresponded to the point where the Larmor radius of the particles was just inside the smaller aperture radius. The second method for achieving the benefit of grid embedded magnetic fields at lower field strength which was investigated was the use of lower mass propellants. The result of this investigation showed that there were definite reductions in the critical magnetic field strength (the field strength at which the impact energy is a minimum) for each lower mass propellant used. There are many other implications to using lower mass propellants in electrostatic thruster, both advantages and disadvantages, a discussion of which is beyond the scope of this work.

There are other potential methods for achieving the benefits of incorporating grid embedded magnetic fields that could potentially be implemented in the near future. These are potential techniques for achieving the large fields required without exotic material to produce the required fields. For example: a powerful solenoid around the grids themselves could impose a relatively even axial field. The grid embedded current loops would then be required to carry only modest current to impart a localized directionality to the field to form the mini-magnetic nozzle configuration. This could potentially have the additional benefit of reducing magnetic mirroring by limiting the regions where the magnetic field is converging.

5.2 Usefulness of the Simplified Ion Thruster Model – ionLite

The ionLite code was developed in order to evaluate not just the value of grid embedded magnetic fields, but as a tool to aid in finding many different optimizations of grid geometry and fields. The design objectives as described in Chapter 3 were to provide a simple to use particle simulation that by concentrating only on charge exchange ion induced grid erosion effects could be run and reconfigured many times very quickly.

The accuracy and validation of the code were covered in Chapter 3. It is a further statement on the accuracy of the simulation that the results do show that the minimum impact energy occurs at the field level that causes the particle Larmor radius to be just inside the aperture radius. Insofar as the goal of being able to be rapidly reconfigured and re-run is concerned, the examination of the grid embedded fields described in Chapter 4 fully validates the program's meeting that goal. To complete the test runs in section 4.2.3 for example the program was run for nearly 500 particles and reconfigured 150 times. This took approximately 3 days and was automated by virtue of an additional For Loop. The time quoted for duration was on a six year old Pentium 4 Laptop running at 1.7 GHz with 256 Meg of RAM. A more modern computer or a workstation would result in completing these 150 runs considerably faster. Since the code is fully portable and could easily be run on a mainframe it is obvious that these runs could probably be done in considerably less time with the proper resources.

Trying to accomplish this analysis on a full thruster simulation would have required a considerably more time. For example the "ibx" code which was developed to provide a faster code for evaluation of ion thruster grid erosion run on a similar computer would require approximately 6 hours per run or about 37 days for all 150 cases. [40] By using ionLite a relatively accurate and highly informative result was obtained for hundreds of different configurations of both grid geometry and magnetic field in a little over two weeks time. This verifies that the program has met its design goals and will be a useful tool in evaluating alternative active charge exchange grid erosion mechanisms.

CHAPTER 6

CONCLUSIONS

An analysis of the usefulness of incorporating axial aligned grid embedded magnetic fields as a means of reducing charge exchange ion imparted grid erosion in ion thrusters was undertaken. As part of this study a new simplified thruster simulation was developed with the intention of providing a tool that could rapidly model many different thruster grid configurations. Using the new program, ionLite, simulations of several different grid and magnetic field configurations were made at axial field strengths between 0 and 150 Tesla.

The result of the analysis is that axial aligned magnetic fields generated by current loops embedded in the thruster grid material shows promise as a technique for reducing charge exchange induced grid erosion. In the simulation it was observed that, for the configurations examined, kinetic energy imparted to the thruster grids could be reduced by more than 20%. The minimum total impact energy for all particles occurred at the point where the axial magnetic field strength was sufficient to cause the particle Larmor radius to be just inside the radius of the grid apertures. For the configurations under examination this required very high axial field strengths of approximately 100 Tesla. At axial field strengths above that required to reduce the Larmor radius to less than the grid aperture radius the total impact energy increased as the particle motion became more strongly defined by the guiding center motion. It can be concluded however based on the discussion in Chapter 5 that the grid configurations used in this evaluation were probably not optimum for taking advantage of the grid embedded magnetic fields and that alternative configurations could lead to even greater reduction in total impact energy. Other techniques were also briefly evaluated and one, the use of reduced mass propellants, showed promise as a means of achieving the benefit of the grid embedded magnetic fields at lower total field strengths.

The analysis performed here could not have been accomplished without the use of the ionLite thruster simulation. This simulation was developed for the purpose of evaluating charge exchange ion induced grid erosion and was conceived as a tool that could be simple enough to run quickly with the ability to be easily re-configured and re-run for very different configuration. This allowed for the evaluation of hundreds of different configurations of magnetic field and thruster grid geometries in a relatively brief period. This tool has proved accurate, flexible, and invaluable, and will be developed and refined further.

REFERENCES

1. Soulas, G. C., "Performance Evaluation of Titanium Ion Optics for the NASA 30 cm Ion Thruster," 27th International Electric Propulsion Conference, IEPC-01-092, Oct 2001.
2. Choueiri, E. Y., "Overview of U.S. Academic Programs in Electric Propulsion," 35th AIAA/ASME/SAE/ASEE Joint Propulsion Conference, AIAA-99-2163, Jun 1999.
3. Meserole, J. S., "Measurement of Relative Erosion Rates of Carbon-Carbon and Molybdenum Ion Optics," 30th AIAA/ASME/SAE/ASEE Joint Propulsion Conference, AIAA-94-3119, Jun 1994.
4. Soulas, G. C., "Improving the Total Impulse Capability of the NSTAR Ion Thruster with Thick-Accelerator-Grid Ion Optics," 27th International Electric Propulsion Conference, IEPC-01-092, Oct 2001.
5. Brewer, G. R., "Ion Propulsion Technology and Applications," Gordon and Breach Science Publishers, New York, NY, 1970.
6. Filliben, J. D., "Electric Thruster Systems," Chemical Propulsion Information Agency, The Johns Hopkins University, Whiting School of Engineering, Columbia, MD, Jun 1997.

7. Domonkos, M. T. and Stevens, R. E., "Assessment of Spectroscopic, Real-Time Ion Thruster Grid Erosion-Rate Measurements," 36th AIAA/ASME/SAE/ASEE Joint Propulsion Conference, AIAA 2000-3815, Jul 2000.

8. Crary, F. J., Young, D. T., Nordholt, J. E., "Charge Exchange Ions Produced by an Ion Propulsion System," 39th AIAA Aerospace Sciences Meeting, AIAA-2001-0968, Jan 2001.

9. Davis, V. A. et al, "Ion Engine Generated Charge Exchange Environment: Comparison Between NSTAR Flight Data and Numerical Simulations," 36th AIAA/ASME/SAE/ASEE Joint Propulsion Conference, AIAA 2000-3529, Jul 2000.

10. Kaufman, H. R., "Technology of Electron-Bombardment Ion Thrusters," Advances in Electronics and Electron Physics, V36, Academic Press, New York NY, 1974.

11. Shimada, et al, "Ion Thruster Endurance Test Using Development Model Thruster for ETS-IV," 23rd International Electric Propulsion Conference, IEPC-93-169, Sep 1993.

12. York, T. M., Jacoby, B. A., Mikellides, P.,"Plasma Flow Processes Within Magnetic Nozzle Configurations," Journal of Propulsion and Power, Vol 8, No. 5, Sep-Oct 1992.

13. Mikellides, I. G., Mikellides, P. G., Turchi, P. J., York, T. M., "Theoretical Design of a Magnetic-Nozzle Acceleration System for Fusion Propulsion," 36th AIAA/ASME/SAE/ASEE Joint Propulsion Conference and Exhibit, AIAA 2000-3367, Jul 2000.

14. Beattie, J. R. et al, "Xenon Ion Propulsion Subsystem," AIAA Journal of Propulsion and Power, Vol 5, No 4, Jul-Aug 1989.

15. Griffiths, D. W., "Introduction to Electrodynamics 3rd Ed.," Prentice Hall, 1999.

16. Makles, M. R. et al, "Experimental And Modeling Studies of Low Energy Ion Sputtering in Ion Thrusters," 39th AIAA/ASME/SAE/ASEE Joint Propulsion Conference, AIAA 2003-5160, Jul 2003.

17. Jahn, R. G., "Physics of Electric Propulsion", McGraw-Hill, 1998

18. Kraus, J. D., "Electromagnetics 4th Ed.," McGraw-Hill, 1992.

19. Tippler, P. A., "Physics for Scientists and Engineers 4th Ed.," W. H. Freeman and Company, 1999.

20. Chen, F. F., "Introduction to Plasma Physics and Controlled Fusion, Volume 1: Plasma Physics," Plenum Press, 1984.

21. Loh, W. H. T., et al, "Jet, Rocket, Nuclear, Ion and Electric Propulsion: Theory and Design," Springer-Verlag, 1968.

22. Killinger, R. Bassner, J. Muller, J., "Development of an High Performance RF-Ion Thruster," AIAA-1995-2445, 1999.

23. Beattie, J. R., Penn, J. P., "Electric Propulsion – A National Capability," AIAA/ASME/SAE/ASEE 25th Joint Propulsion Conference, AIAA-89-2490, Jul 1989.

24. Fearn, D. G., "The Future of Gridded Ion Engines," 39th AIAA/ASME/SAE/ASEE Joint Propulsion Conference and Exhibit, AIAA 2003-4714, July 2003.

25. Katz, I. Mikellides, I. G., Goebel, D. M., “Model of the Plasma Potential Distribution in the Plume of a Hollow Cathode,” 40th AIAA/ASME/SAE/ASEE Joint Propulsion Conference and Exhibit, AIAA 2004-4108, July 2004.

26. Siegfried, D. S., Wilbur, P. J., “A phenomenological Model Describing Orificed, Hollow Cathode Operation,” AIAA/JSASS/DGLR 15th International Electric Propulsion Conference, AIAA-81-0746, 1981.

27. Turchi, P. J., Sahi, A., “Low Power Plasma Thruster Based on Hollow Cathode Discharge,” 30th AIAA/ASME/SAE/ASEE Joint Propulsion Conference, AIAA-94-3126, June 1994.

28. Hiatt, J. M., Wilbur, P. J., “Ring Cusp Discharge Chamber Performance Optimization,” AIAA/DGLR/JSASS 18th International Electric Propulsion Conference, 1985.

29. Farnell, C. C., Williams, J. D., Wilbur, P. J., "Numerical Simulation of Ion Thruster Optics," 28th International Electric Propulsion Conference, NASA/CR-2003-212305, Jul 2003.

30. Okawa, Y., Takegahara, H., "Numerical Study of Beam Extraction Phenomena in an Ion Thruster," Japan Journal of Applied Physics, Vol. 40 Part 1 No. 1, Jan 2001.

31. Vincenti, W. G. and Kruger, C. H., “Introduction to Physical Gas Dynamics”, Krieger Publishing, 1965.

32. Eshbach, O. W. et al, “Handbook of Engineering Fundamentals,” John Wiley & Sons, 1975

33. Bohdansky, J., “Important Sputtering Yield Data for Tokamaks: A Comparison of Measurements and Estimates,” Journal of Nuclear Materials 93 & 94, 1980.

34. Smythe, W. R., "Static and Dynamic Electricity: Third Edition," Hemisphere Publishing, 1989.

35. Beattie, J. R., Williams, J. D., Robson, R. R., "Flight Qualification of an 18-mN Xenon Ion Thruster," AIAA/AIDAA/DGLR/JSASS 23rd International Electric Propulsion Conference, IEPC-93-106, Sep 1993.

36. Beatie, J. R. et al, “Xenon Ion Propulsion Subsystem,” AIAA/DGLR/JSASS 18th International Electric Propulsion Conference, AIAA-85-2012, Sep 1985.

37. Beatie, J. R., Matossian, J. N., Robson, R. R., “Status of Xenon Ion Propulsion Technology,” 19th AIAA/DGLR/JSASS International Electric Propulsion Conference, AIAA-87-1003, May 1987.

38. Beatie, J. R., Robson, R. R., Williams, J. D., “18-mN Xenon Ion Propulsion Subsystem,” AIDAA/AIAA/DGLR/JSASS 22nd International Electric Propulsion Conference, IEPC-91-010, Oct 1991.

39. Gurnett, D. A., Bhattacharjee, A., “Introduction to Plasma Physics, With Space and Laboratory Applications,” Cambridge University Press, 2005.

40. Nakayama, Y., Wilbur, P., “Numerical Simulation of High Specific Impulse Ion Thruster Optics,” 27th International Electric Propulsion Conference, IEPC-01-99, Oct 2001.